Spring 2021

Advanced battery modeling for interfacial phenomena and optimal charging

Yaqi Zhu
Missouri University of Science and Technology

Department: Mechanical and Aerospace Engineering

ADVANCED BATTERY MODELING FOR INTERFACIAL PHENOMENA AND OPTIMAL CHARGING

by

YAQI ZHU

A DISSERTATION

Presented to the Graduate Faculty of the

MISSOURI UNIVERSITY OF SCIENCE AND TECHNOLOGY

In Partial Fulfillment of the Requirements for the Degree

DOCTOR OF PHILOSOPHY

in

MECHANICAL ENGINEERING

2021

Approved by:

Jonghyun Park, Advisor
Robert G. Landers
Frank Liou
Jonathan W. Kimball
Daoru Han

To the memory of my grandfather, who serves as a role model for me and motivates me to be an upright, kind, and honest person.

PUBLICATION DISSERTATION OPTION

This dissertation consists of the following six articles, formatted in the style used by the Missouri University of Science and Technology:

Paper I, Pages 10-35, has been published in ACS applied materials & interfaces 11.42 (2019): 38719-38726.

Paper II, Pages 36-81, has been published in Journal of Power Sources 476 (2020): 228593.

Paper III (Pages 82-109), Paper IV (Pages 110-133), Paper V (Pages 134-163) and Paper VI (Pages 164-197) are intended for submission.

Additional information regarding material within the dissertation:

Paper III~Paper VI are based upon work supported by the Department of Energy Vehicle Technologies Office under Award Number DE-EE0008449. This report was prepared as an account of work sponsored by an agency of the United States Government. Neither the United States Government nor any agency thereof, nor any of their employees, makes any warranty, express or implied, or assumes any legal liability or responsibility for the accuracy, completeness, or usefulness of any information, apparatus, product, or process disclosed, or represents that its use would not infringe privately owned rights. Reference herein to any specific commercial product, process, or service by trade name, trademark, manufacturer, or otherwise does not necessarily constitute or imply its endorsement, recommendation, or favoring by the United States Government or any agency thereof. The views and opinions of authors expressed herein do not necessarily state or reflect those of the United States Government or any agency thereof.

ABSTRACT

Lithium ion batteries are one of the most promising energy storage systems for portable devices, transportation, and renewable grids. To meet the increasing requirements of these applications, higher energy density and areal capacity, long cycle life, fast charging rate and enhanced safety for lithium ion battery (LIBs) are urgently needed. To solve these challenges, the relevant physics at different length scale need to be understood. However, experimental study is time consuming and limited in small scale's study. Modeling techniques provide us powerful tools to get a deep understanding of the relevant physics and find optimal solutions. This work focuses on studying the mechanism in advanced battery engineering techniques and developing a new charging algorithm by model-based optimization. The research topics are divided into six topics and each topic is reported as a form of journal publication. Paper I provides a new aspect of how ALD coating improves the lithium ion diffusion at electrode particles. Paper II explains the mechanisms by which 3D electrodes enhance battery performance and reveals guidelines for optimized 3D electrode designs by a 3D electrochemical-mechanical battery model. Paper III investigates the electrolyte concentration impact on SEI layer growth and Li plating, especially under high charge rates. Paper IV proposes an optimized charging protocol for fast charging for reducing the charging time with minimal degradation. Paper V reports a comprehensive degradation model for degradation estimation and life predication of energy storage system (ESS). Paper VI is a study of temperature-dependent state of charge (SOC) estimation for battery pack.

ACKNOWLEDGMENTS

Firstly, I would like to thank my advisor, Dr. Jonghyun Park, for his invaluable supervision and consistent support for my research. I am deeply grateful for the great opportunities, supportive working environment and research resources offered by Dr. Park. Your expertise helped me to sharpen my thinking and brought my work to a higher level.

Secondly, I would like to express my sincere gratitude to all my committee members, Dr. Robert G. Landers, Dr. Frank Liou, Dr. Jonathan W. Kimball, Dr. Daoru Han and Dr. S. N. Balakrishnan for kindly offering suggestions and support for my research. I would particularly like to thank Dr. Landers for his insightful comments and suggestions in the regular meetings. Also, I would like to offer my special thanks to Dr. Balakrishnan for his guidance and encouragement when I extended my study in a new area.

Thirdly, I would like to thank my colleagues, Hiep Pham, Tazdik Patwary, Damola Ajiboye, Brody Riemann, Jie Li and Yufang He, for their assistance at every stage of my work. It is their kind help and support that have made my study in MST a wonderful time. I also appreciate all my friends for their help and support during my PhD journey.

Finally, I would like to thank my lovely family member my father, Aiqun Zhu, my mother, Guizhi Zhang, my grandfather Xingtian Zhu and my grandmother Wenshu Yang for their tremendous understanding, support, and love in my life.

TABLE OF CONTENTS

LIST OF ILLUSTRATIONS

PAPER I Page

PAPER II

PAPER V

PAPER VI

LIST OF TABLES

PAPER VI

SECTION

1. INTRODUCTION

Lithium-ion batteries (LIBs) are first introduced to market in 1991 by Sony and have become one of the most popular battery technologies in the world. Due to their high energy capacity, longer life time, light weight, low self-discharge rate, no memory effect, and environmentally friendly, LIBs are superior to other secondary batteries such as the lead acid (Pb-acid), nickel-cadmium (Ni-Cd) and nickel-metal hydride (Ni-MH) batteries. LIBs are not only widely used in a variety of portable electronic devices, but have recently entered the commercial electric vehicle market, resulting in a significant increase in battery requirements in terms of energy density, power density, cycle life, safety, and cost.

A LIB is made up of anode, cathode, separator, electrolyte and two current collectors (positive and negative). During charge process, lithium ions are formed from the lithium metal oxide in the cathode, diffuse across the electrolyte, and are finally inserted into the carbon/graphite anode. During the ion formation, the metal in the lithium metal oxide is reduced, producing a free electron to maintain charge neutrality. The free electrons will immigrate to anode from outside electric circuit and react with the inserted lithium ion. During discharge process, both lithium ion and electrons move in the opposite directions, while anode is reduced and cathode is oxidized.

In order to enhance batteries' performances, tailor architectural configurations toward optimal functioning of energy storage devices, shape new materials for larger capacity and power, computational simulations, based on theoretical modeling and coupled

to validation and quantification of uncertainties have been extensively studied. There are three main categories of battery models: mathematical models, electrochemical models and electrical equivalent circuit models. Among these models, electrochemical models are more sophisticated because they are based on chemical/electrochemical kinetics and transport equations, which can be used to simulate the batteries' characteristics and reactions and provide full information on the internal electrochemical dynamics of a battery. The Pesudo-two-Dimensional (P2D) model and the Single Particle Model (SPM) are the most widely used electrochemical models. P2D models are based on porous electrode theory, the concentrated solution theory and the kinetics equations. It can simulate both ion concentration and potential across the cell dimension and give accurate prediction. To reduce the computation time, SPM, a simplified version of P2D model, has been developed. In SPM, each electrode is represented by a spherical particle and the electrolyte dynamics in the potential are ignored. Despite P2D and SPM, the porous electrode model with the polynomial approximation (PP model), which incorporate the parabolic approximation of the concentration equations in the P2D model, is also employed in battery simulation. It retain the complexity of physics based on porous electrode theory, but mathematically simpler. Based on the framework of these models, they can be extended into more dimensions, e.g. two dimensional and three dimensional, or with more physics such as degradation features and mechanical properties in order to address specific problems.

One of the main challenges in lithium ion battery is degradation reaction taking place at the electrode/electrolyte interface. A substantial amount of work has been done to understand capacity fade through experiment and simulation. The battery degradation

results from various physical reactions, including current collector corrosion, electrolyte decomposition, solid electrolyte interface (SEI) layer formation, Li plating and so on. Among them, SEI layer formation and growth and Li plating on anode particles and the metal dissolution, electrolyte oxidation and salt decomposition on cathode material are the most critical processes leading to capacity degradation in lithium batteries. The formation of SEI layer on anode particles in initial cycles will consume a significant amount of cycable Li ion. It could serve as a protective layer of anode active materials. However, during cycling, SEI layer becomes unstable and continuously grows, leading to a further capacity fade. Intercalation is a diffusion-limited process. Deposition of lithium on the anode particles will take place when local anode potential become negative. In fast charge, the amount of ions accumulated on the anode surface could be much larger than the intercalation rate, leading to an occurrence of Li plating. Li plating is hazard to both the electrochemical performance and safety of cells. On one hand, plated lithium metal could react with electrolyte to form new SEI layer, causing a loss of reversible lithium ion. On the other hand, serious Li plating could form dendrite, which can penetrate the separated or break in the end, resulting in short circuits in the cell. Another key degradation physics is dissolution of transition metal. Metal dissolution could cause a structure change of active material, reducing the ability of accommodating inserted lithium ion of electrode. Also, metal ions with high oxidation ability will lead to a decomposition of electrolyte solvent.

This dissertation utilizes mathematical modeling tools to analyze interfacial phenomenon and degradation physics in lithium batteries. Paper I investigate the mechanism that how ALD coating on electrode materials enhance the Li diffusion. It is generally believed that Li diffusion enhancement is a result of the higher conductivity of

the coating layer, when compared to that of active materials. However, it is questionable that the ultra-thin coating layer could lead to such a significant improvement of the diffusivity of the whole electrode particle since the fraction of ALD coating layer is very small. In this paper, we proposed a new hypothesis about the role of ALD coating. Considering particles' surface are partially blocked in the agglomeration of electrode particles, intercalation is not uniform over the whole particle surface. The function of ALD coating is to provide a quick path to distribute Li ions over the whole surface and to Li ions intercalate uniformly and effectively. Simulations based a 2D SP model were conducted for both traditional belief and the proposed hypothesis for validation. The impact of coating layer on Li ion distribution and electrode capacity were investigated in models with Li ions intercalated uniformly and nonuniformly. The specific surface area of individual particles and lumped electrode were also inspected to verify the proposed hypothesis. A parametric study of coating thickness, flex angle, current density and particle size were conducted to provide a guidance for ALD coating and electrode design. The influence of coating layer on effective diffusivity was checked by s simulated GITT test for traditional explanation and proposed mechanism for further validation.

Paper II studied an optimization of 3D electrode architecture design by using a 3D electrochemical model. Optimized 3D electrode architectures are promising in improving battery performance compared with conventional laminated structures. In this paper, the mechanism that how 3D electrodes enhance battery performance was revealed by a 3D electrochemical model, which was validated by experiments on 3D micro-lattice electrodes prepared by Aerosol Jet printing. Electrode geometry was studied by comparing the electrochemical response of electrodes with block-, X-, cubic-structure, and a structure

formed by subtracting spheres from a solid block (called ‘sphere-structure’). Lithium concentration and potential distribution were mapped to reveal the impact of electrode geometries, electrode thickness, packing density and porosities on species transport during electrochemical process. The X- and cubic-structured electrodes demonstrated a larger capacity (35% higher at 0.5C) than the inverse sphere-structured electrodes as a result of more efficient electron transport enabled specifically by the change in electrode geometry. To further understand the coupled physics of ion and electron transport in the solid and liquid phase, the individual transport phenomena were analyzed by decoupling them and calculating the effective diffusivity for each. It was found that the primary reason for the superior performance of batteries with 3D electrode architectures is the fact that 3D structures facilitate species transport in the liquid phase. In addition, the main factors affecting battery performance are ion diffusion in the electrolyte and electron transport in the 3D electrode skeleton. Furthermore, the geometric parameters of each electrode architecture were studied to obtain the optimal electrode design. A competition between available volume for intercalation and easier electronic/ionic path was shown in the determination of electrodes’ areal/specific capacities. The maximum benefits of a 3D architecture are realized when the length of the structures’ truss members is of the order of the diffusion length for the ions in the electrode (~15-20 μm in the current study).

Paper III focused on the impact of electrolyte concentration on SEI layer growth and Li plating. Previous works showed that two main side reactions, SEI layer formation and Li plating, can be affected by electrolyte concentration. However, the mechanism by which electrolytes influence these reactions has not been fully understood. This paper developed a full order electrochemical model in which the degradation physics and their

dependence on electrolyte concentration were considered. The model was validated by experimental data of capacity fade under various C-rate and electrolyte concentration. The evolutions of side reaction constant, overpotential, current density, solvent concentration, ohmic voltage were investigated in various electrolyte concentration to reveal the mechanism how electrolyte concentration impact SEI layer formation and Li plating. It was found that a high salt concentration (1.5 mol/L and 2 mol/L of LiPF6 in EC: DMC) suppressed the SEI layer growth and promoted Li plating. The behavior of Li plating in simulations including and excluding SEI reaction was studied to explore the interaction between these two side reactions. It revealed that the existence of the SEI layer slowed the lithium plating rate by increasing its overpotential through ohmic resistance. Further, the C-rate impact on sides reactions was studied. As a result, both low electrolyte concentration and low charge current C-rate resulted in a more severe capacity degradation in the CC cycling process.

Paper IV studied the optimized extreme fast charging protocol for lithium ion battery. Charging protocol is critical to achieve the balance between cell degradation and charging time in fast charging of lithium ion batteries. The traditional constant current constant voltage (CCCV) cannot effectively shorten the charge time under high Crate and it will cause a sever Li plating in the charging process. Various new charge protocols were proposed towards fast charging. However, none of them controls cell degradation, in particular, Li plating, during charging process. This paper proposed a modeling-assisted fast charging algorithm CQtCV by regulating the Li plating current. The controlling variable, Li plating current, was provided by a full order electrochemical degradation model, which included degradation physics of SEI layer growth and Li plating. The model

parameters were classified into two groups, non-degradation related, and degradation related, and were identified using 1st cycle's voltage profile and capacity profile of C-rate test, respectively. The performance of CQtCV was compared with 3C CCCV based on fitted model in one cycle as well as in long cycling simulation. It was demonstrated that the proposed charging protocol can effectively reduce charge time (>20%) and improve capacity retention at the same time. In terms of degradation, CQtCV was able to suppress the SEI layer growth but slight promote Li plating.

Paper V focused on a problem of control oriented comprehensive degradation model for battery energy storage system. Battery energy storage systems (BESSs) are essential for electrical grids to yield smooth fluctuations in power generation. The power quality and economic performance of BESSs are highly dependent on battery degradation situations, which are impacted by its operation conditions. To accurately track cell degradation and predict battery life in real-time, this paper developed a comprehensive degradation model, in which key degradation physics, namely, SEI layer formation and growth, Li plating on the graphite anode, and Mn dissolution on cathode of nickel-cobalt-manganese oxide (NMC622) were considered. To make the model computationally efficient, the model was established based on a reduced-order single particle (SP) model that includes electrolyte phase dynamics. The model was validated against experiment data and was proved to be capable to capture the capacity degradation rate. The results of three degradation physics were investigated separately. It was revealed that the deposition rate of both SEI layer and Li plating increase as the charge voltage increase. At the cathode side, the solvent oxidation rate determined the proton concentration that triggers the Mn dissolution, and the loss rate of active material in the cathode kept increasing. Then, the

impact of degradation physics on capacity in long cycling test were studied. In 3000 cycles' simulation, the SEI growth played a main role in capacity fade in the first about 2000 cycles, and Mn dissolution had a significant impact after about 1000 cycles. The capacity loss caused by Mn dissolution not only came from the loss of active material in cathode, but also from the consumption of Li ions in electrolyte. The charge current impacts on the three degradation physics are also analyzed. High charge current slows down the reaction of Mn dissolution at cathode and speed up the SEI layer growth and Li plating at anode. Furthermore, a sensitivity study of degradation reaction constants against capacity fade were conducted to give a reference about the degradation situation in various battery material systems.

Paper VI deals with a model-based time-dependent SOC estimation for battery pack. In battery management system, an accurate estimation of SOC is the fundamental for the purpose of efficiently and safely use the batteries. A modern battery pack is usually composed of hundreds or even thousands of cells. Individual cells will be different in initial SOC, capacity and internal resistance due to fabrication process and material defects. How to estimate the SOCs of all the cells with low computation cost is a challenge. Also, temperature has a significant impact on cell's SOC though several temperature-dependent properties, such as open circuit voltage, electrode diffusivity and electrolyte conductivity. The temperature deviation between cells of a battery pack can further increase deviation of cells' SOCs. However, most works didn't consider the temperature impact and thermal behavior of in-pack cells. This paper employed a physics-based reduced-order single particle model along with a lumped thermal model to improve the accuracy and robustness of SOC estimation. To reduce the computational cost, an "average cell" SOC is firstly

estimated based on the physical model, and then SOCs of individual cells are estimated by incorporating the performance divergences between the average cell and each individual cell. The performances of extended Kalman filter (EKF) and unscented Kalman filter (UKF) as an average cell state estimator were evaluated. It was demonstrated that UKF has a better accuracy and convergence rate than EKF due to its superior advantage in highly nonlinear system. As for the individual cell state estimator, a discretized EKF was implemented and it was found that its stability and accuracy was significantly impacted by the estimation error of the average cell states. A holding time of 10 s was added for the individual cell state estimator to avoid large average cell states' error, and it showed a quick convergence in 15 s with a small error of <4% for SOC and <0.6 K for cell temperature. Moreover, the filter was computational efficiently with 0.16 ms for 1 s simulation time in 1 cell.

PAPER

I. A NEW ASPECT OF THE LI DIFFUSION ENHANCEMENT MECHANISM OF ULTRA-THIN COATING LAYER ON ELECTRODE MATERIALS

ABSTRACT

Atomic Layer Deposition (ALD) coating on active material particles has been widely considered as an effective and efficient strategy to improve the capacity and cycle life of lithium-ion batteries. One of the key roles of the ALD coating layer is to facilitate the Li ion transfer in electrode particles. Several recent studies demonstrated that an ALD coating layer could significantly improve the effective diffusion coefficients in cathode particles. As such, this enhanced transport property is generally believed to be a result of the higher conductivity of the coating layer, itself, when compared to that of active materials. However, since the fraction of ALD coating layer is very small, it is questionable that the ultra-thin coating layer could lead to such a significant improvement of the diffusivity for the whole particle. Thus, we proposed a new hypothesis about the role of ALD coating layer on Li ion transportation. Due to the agglomeration of particles in an electrode, the surface of the particles are partially blocked and, correspondingly, Li ion intercalation is not uniform over the whole surface. Herein, we propose that the ALD coating could provide a quick path to distribute Li ions over the whole particle surface and allow Li ions to spread uniformly and effectively, leading to improved effective diffusivity of the particles and their utilization. In this work, this hypothesis was validated by simulation and experimental study. It was proved that the particle with an optimal ALD coating thickness has the most uniform Li ion distribution, leading to an optimal discharge

capacity. Along with the validation of the hypothesis, a parametric study was conducted by consideration of the flux area, particle size and current density, which revealed the fundamental role of coating layer on charge transfer, Li ion diffusion and corresponding battery performance.

1. INTRODUCTION

Surface coatings have been employed as a widely used strategy to improve capacity, cyclability, rate capability and thermal stability of lithium-ion battery cathode materials. A coating layer usually functions by protecting the active material from side reactions with electrolytes[1-5]; accommodating the cyclic volume expansion and contraction of cathode particles during charge-discharge process [6-10]; improving the mechanical property of particles to avoid the generation of cracks [11-14]; working as hydrofluoric acid scavenger to reduce the dissolution of transition metal elements [2, 15-18]; and facilitating species transfer and diffusion at electrode/electrolyte interface [15, 19-21]. Conventionally, surface coatings are achieved by techniques such as chemical vapor deposition (CVD) [22, 23] or wet chemistry approach such as sol-gel [24-27] and precipitation [28-30]. However, these techniques lack a precise control of coating thickness, consistency and conformity, and, as a result, cracks and pinholes may exist in the resulting coating products. [31] One fabrication technique that can avoid these issues to create uniform coating layers is through atomic layer deposition.

Among the many techniques to create surface coatings, Atomic Layer Deposition (ALD) coating has been regarded as the most effective as it can avoid consistency and

conformity issues to create continuous and pinhole-free coating layers. ALD coatings are mostly implemented by a binary chemical reaction with a substrate surface at a finite number of surface sites with atomic level control. Because the two chemical reactions proceed in a sequential fashion and all surface sites are involved in the deposition reaction during one cycle, the ALD film tends to be smooth, conformal, pinhole-free, and in good contact with substrate materials. By controlling ALD process parameters such as temperature and working cycles, different thicknesses of the coating layer ranging from nanometer to submicrometer can be obtained, which can enable further functionality and optimization of coating layers. [32]

Recently, many studies investigating ALD coating of cathode materials have been reported [33-35]. For example, an ultrathin crystalline ZrO_2 nanofilm was deposited on $LiMnO_4$ particles via ALD [36, 37] where the nanofilm had two structures: an amorphous structure in the external layer with a thickness of ~2 nm and an epitaxial crystalline structure for the layer inside. The best property was achieved at 6 ALD cycles (1.6 nm) where capacity retention was 68% after 100 cycles while the bare ones exhibited 51.4% retention. Another study determined that the optimal thickness was 6 layers (1.02 nm), of which the capacity retention was 66.67% and 62.33% compared with 52% and 49% for the bared particles measured at 25 °C and 55 °C, respectively. [38] An Al_2O_3 ALD coating layer on $LiMn_2O_4$ was obtained by Waller et al [39], in which the capacity retention was enhanced by 2.5 times compared to the case of non-coated particles. Furthermore, a large shift of binding energy in Al 2p peak was observed, demonstrating the coating layer worked as a HF scavenger to reduce the degradation of $LiMn_2O_4$ particles by forming Al-O-F compound. The 10 ALD layer coated electrodes (~1 nm) showed the best performance in

which both the cyclability and rate capability were enhanced. Recently, an ultrathin CeO_2 film deposited onto $LiMn_2O_4$ particles by ALD technique was demonstrated [40, 41]. The CeO_2-coated LiMn2O4 possessed an extraordinary capacity retention that was 96% of the initial capacity after 1000 charge-discharge cycles. Its rate capability was also much better than the uncoated, ZrO_2-coated and Al_2O_3-coated particles. In that work, the optimal thickness of CeO_2 coating layer was larger than that of other ceramic oxide coating materials, which was determined to be around 3 nm with 50 ALD cycles and was attributed to the high ionic conductivity of CeO_2. Since most common metal oxide materials have low ionic conductivity, the ionic species transport is hindered when the coating thickness increases. [2, 42-44] However, a thick layer is needed to guarantee a sufficient distance between active material and electrolyte. [45] Therefore, a CeO_2 coating could solve this trade-off. Despite general benefits of ALD coating on stress generation and volume change, the CeO_2 ALD layer was able to facilitate species transfer and diffusion in electrode particles. But the mechanism of how CeO_2 ALD layer enhances the Li ion diffusion is still unclear and lacks validation.

Here, the majority of previous studies were based on the presumption that the enhanced transport property was caused by the high conductivity of CeO_2 coating layer, itself (Figure 1 (a)), in that it could work as a conductive layer to improve the overall diffusivity of the electrode particles [28, 46, 47]. But considering that the fraction of the CeO_2 layer was very small compared to the electrode particle (coating thickness was in the nm scale while the electrode particle diameter was in μm scale), there is reasonable doubt in whether it could lead to such a significant improvement based on high conductivity of the layer alone. Therefore, to better explain the role of CeO_2 layer in Li ion diffusion in

electrode particles, a new hypothesis is proposed in this work. We suggest that because particles tend to agglomerate in the porous electrode, the surface area of individual particles are partially blocked by neighboring particles and other additive and filler materials. As a result, the Li ion intercalation at these blocked regions would be limited, and overall, the lithium flux could be not uniform. Here, if there is a coating layer with high conductivity on the particle surface, Li ions could quickly spread throughout the coating layer first and then be distributed over the whole particle surface (Figure 1 (b)). It should be noted that in some coating materials with special structures, such as one dimensional structure [48-50], the agglomeration phenomenon of particles may not be severe, therefore, the hypothesis proposed here mainly points to conventional laminated electrode materials.

This paper examined this hypothesis through simulation and experimental study by comparing two mechanisms: one for the conventional explanation and the other one for the proposed hypothesis. The model was established based on Single Particle (SP) model, and the electrochemical reactions of non-coated and coated particles with different coating thickness were simulated. A Brunauer-Emmett-Teller (BET) test and Particle Size Analysis (PSA) were conducted to examine the surface area difference between lumped electrode and individual particles. Behavior of Li ion diffusion under different flux angle, particle size and current density was also investigated in order to capture their effects and a complete understanding of the mechanism. To further compare the two theories, a Galvanostatic Intermittent Titration Technique (GITT) experiment was simulated to calculate the effective diffusivity of electrode particles. The results of this work revealed a fundamental, previously unconsidered mode in which ALD coatings function to enhance

the performance of batteries and provides further understanding into the role of ALD coating layers.

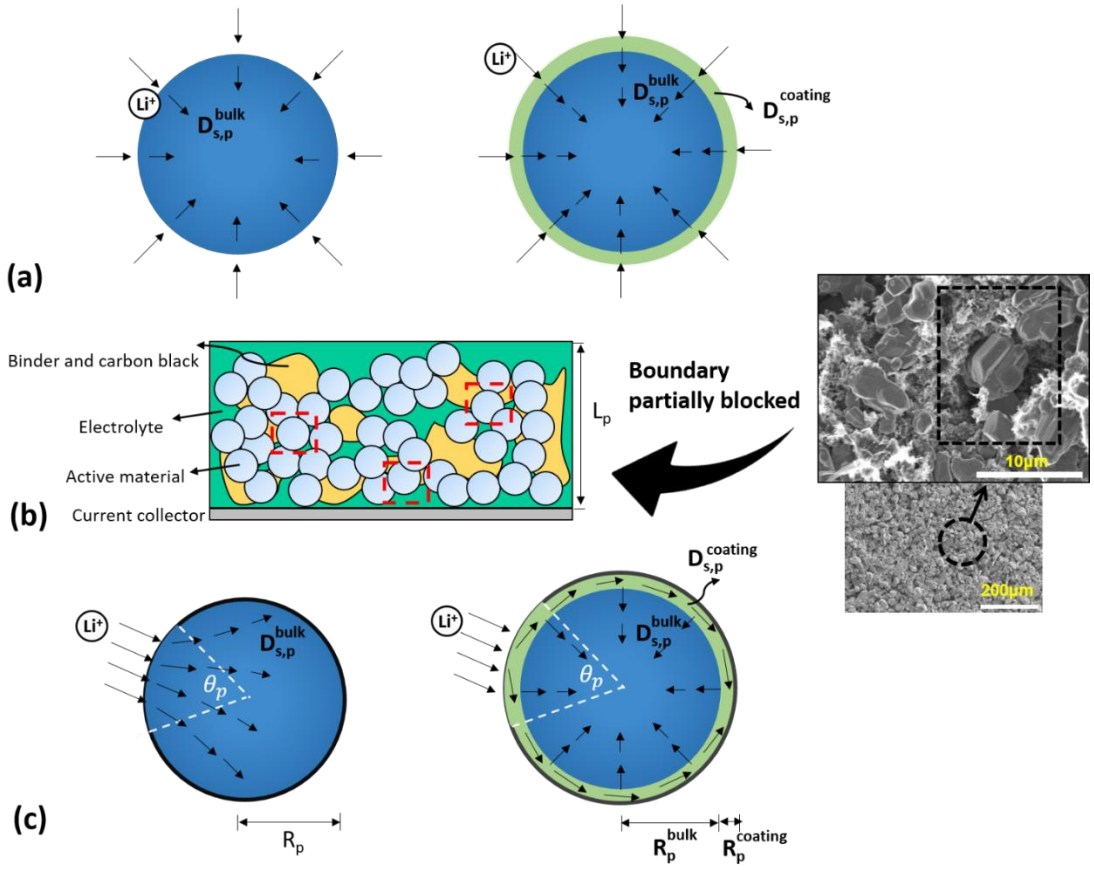

Figure 1. Schematic representation of SP model for uncoated and coated particle based on the traditional explanation (a), schematic and SEM images of an electrode (b), and the proposed hypothesis (c)

2. MATHEMATICAL MODEL

To examine these two mechanisms, we modified the SP model as shown in Figure 1(a) and (c). The coated particle is divided into two sections: an active material section with a particle radius R_p^{bulk} (blue) and a CeO_2 coating layer section with a thickness of $R_p^{coating}$ (green). The diffusion coefficients for these two sections are $D_{s,p}^{coating}$ and $D_{s,p}^{bulk}$, respectively. As only the effective diffusivity of the particle could be measured from experiments, we estimated the individual diffusivity values of the coating layer and active material by fitting the simulated voltage profiles to the measured values. The final fitted diffusivities are shown in Table 1.

Table 1. Effective Li ion diffusivity and individual Li ion diffusivities of CeO2 coating layer and active material at different thickness.

Thickness (nm)	Effective Li ion diffusivity (m^2/s)	Active material diffusivity (Ah/m^2)	Coating layer Li ion diffusivity (m^2/s)	Capacity (Ah/m^2)
0	4e-15[a]	4e-15[a]	/	36.8
2	1.2e-14[a]	4e-15[a]	3.2e-12[b]	39.6
3	1.7e-14[a]	4e-15[a]	4e-12[b]	40.1
5	4.5e-15[a]	4e-15[a]	5e-14[b]	37.1

[a] From ref. 43

[b] Calculated by new hypothesis SP model based on data from ref. 43

The governing equation of material balance for Li ion is in active solid material particles is:

$$\frac{\partial c_{s,p}^{m}}{\partial t} = D_{s,p}^{m} \frac{1}{r^2} \frac{\partial}{\partial r}\left(r^2 \frac{\partial c_{s,p}^{m}}{\partial r} \right) \qquad \text{on positive electrode} \tag{1}$$

$$\frac{\partial c_{s,n}}{\partial t} = D_{s,n} \frac{1}{r^2} \frac{\partial}{\partial r}\left(r^2 \frac{\partial c_{s,n}}{\partial r} \right) \qquad \text{on negative electrode} \tag{2}$$

where $\mathrm{m} = \text{bulk or coating}$ for the active material and the coating material in the positive electrode, respectively. $C_{s,p}^{m}$ and $C_{s,n}$is the concentration of lithium ions, $D_{s,p}^{m}$ and $D_{s,n}$ is the diffusion coefficient of lithium ions in cathode and anode particles, respectively. t is time and r is the radius direction coordinate.

For the traditional theory model, lithium ions could transfer through the entire surface area between the particle and the electrolyte (Figure 1(a)), while in the new hypothesis model, a flux angle of θ is implemented over which lithium ions could transfer. Therefore, the boundary conditions for Eq. 1 are

$$D_{s,p} \left.\frac{\partial c_{s,p}}{\partial r}\right|_{r=0} = 0 \qquad D_{s,p}^{m} \left.\frac{\partial c_{s,p}^{m}}{\partial r}\right|_{r=R_p} = -J_p \quad \text{on positive electrode (traditional theory)} \tag{3}$$

$$D_{s,p} \left.\frac{\partial c_{s,p}}{\partial r}\right|_{r=0} = 0 \qquad D_{s,p}^{m} \left.\frac{\partial c_{s,p}^{m}}{\partial r}\right|_{r=R_p,\theta=\theta_p} = -J_p \quad \text{on positive electrode (new hypothesis)} \tag{4}$$

$$D_{s,n} \left.\frac{\partial c_{s,n}}{\partial r}\right|_{r=0} = 0 \qquad D_{s,n} \left.\frac{\partial c_{s,n}}{\partial r}\right|_{r=R_n} = -J_n \qquad \text{on negative electrode} \tag{5}$$

where J_p and J_n is the molar flux of lithium ions at the surface of electrodes. The flux can be described as

$$J_p = \frac{I_{loc,p}}{F} = \frac{I_{applied}}{Fa_pL_p} \qquad J_n = \frac{I_{loc,n}}{F} = \frac{I_{applied}}{Fa_nL_n} \tag{6}$$

$$a_i = 3\frac{\varepsilon_i}{R_i} \tag{7}$$

where $I_{applied}$ is the applied current density and is defined as positive in the charge process and negative in the discharge process. a_i is the specific surface area of electrode material, ε_i is the solid phase fraction of electrodes, and L_i is the thickness of active material. The surface State of Charge (SOC) for positive and negative electrodes are defined as

$$x_{i,surf} = \frac{c_{s,i,avg}\big|_{r=R_i}}{c_{s,i,\max}} \qquad (i = p,n) \tag{8}$$

where $C_{s,i,aveg}$ is the average Li ion concentration along the electroactive arc of electrode particles.

The electrochemical reaction rate for the lithium ion intercalation/de-intercalation at the electroactive surface is assumed to follow the Butler-Volmer equation, so the flux J can be calculated as follows:

$$\frac{J}{F} = k_i\left(c_{s,i,\max}\right)^{0.5} c_e^{0.5}\left(1-x_{i,surf}\right)^{0.5} x_{i,surf}^{0.5}\left[\exp\left(\frac{0.5F\eta_i}{RT}\right)-\exp\left(-\frac{0.5F\eta_i}{RT}\right)\right] \tag{9}$$

where C_{e} is the Li^+ concentration in the liquid phase, k_i is the reaction rate constant that is related to the temperature. η_i is the overpotential, which is defined as

$$\eta_p = \varphi_{1,p} - \varphi_{2,p} - U_p - I_{loc,p}\cdot R_{coating}$$

$$\eta_n = \varphi_{1,n} - \varphi_{2,n} - U_n \tag{10}$$

where $\varphi_{1,p}$ and $\varphi_{1,n}$ is the potential at the surface of the solid, $\varphi_{2,p}$ and $\varphi_{2,n}$ is the potential of the solution, and U_p and U_n is open-circuit potential of the electrode that is a function

of surface SOC at constant temperature. $R_{coating}$ is the resistance of coating layer, which is calculated by:

$$R_{coating} = \frac{\delta}{\sigma} \tag{11}$$

δ is the thickness of coating layer, σ is the conductivity of the layer[46],

$$\sigma = \frac{q_p^2 c_{s,p} N_A}{k_B T} D_{s,p}^{coating} \tag{12}$$

where q_p is charge of lithium ion, c_p is average Li-ion concentration in the coating layer and $D_{s,p}^{coating}$ is diffusion coefficient of the coating layer. In this model, the solution concentration change is not considered. Therefore, the potential difference between anode and cathode could be expressed as

$$\varphi_{2,p} - \varphi_{2,n} = IR_{cell} \tag{13}$$

where R_{cell} is the electrolyte resistance. Therefore, the voltage for the full cell can be described as,

$$\begin{aligned} V_{cell} &= \varphi_{1,p} - \varphi_{1,n} \\ &= U_p - U_n + \frac{2RT}{F}\ln\left(\frac{\sqrt{m_p^2+4}+m_p}{2}\right) + \frac{2RT}{F}\ln\left(\frac{\sqrt{m_n^2+4}+m_n}{2}\right) + IR_{cell} + I_{loc,p}R_{coating} \end{aligned} \tag{14}$$

where

$$m_i = \frac{I}{Fk_i L_i c_{s,i,\max} c_e^{0.5} \left(1 - x_{i,surf}\right)^{0.5} x_{i,surf}^{0.5}} \tag{15}$$

3. EXPERIMENTAL

$LiMn_2O_4$ (LMO), Carbon Black (CB) and Poly(vinylidene fluoride) (PVDF) were purchased from MTI, Alfa Aesar, and Sigma Aldrich, respectively. To prepare the sample LMO-blend, 85 wt% $LiMn_2O_4$, 8 wt% carbon black and 7 wt% PVDF were mixed by a speedmixer (Flacktek Inc. speedmixer, DAC 150.1 FVZ) at room temperature and used as is. For samples of LMO-electrode, the same ratio of powder blend was mixed in the solvent 35 wt% N-methyl-2-pyrrolidone (NMP) by the speedmixer. The LMO-electrode mixture was then casted onto Al foil and dried at 120 °C for 18h under vacuum. The dried powders were carefully peeled off the Al-foil for the following experimental study. Surface area analysis for the samples was conducted using Brunauer-Emmett-Teller (BET) nitrogen absorption method (Quantachrome NOVA 2000e Surface Area). Particle size distribution was measured by laser diffraction (Microtrac S3500 Particle Size Analyzer).

Galvanostatic Intermittent Titration Technique (GITT) was conducted in the two models to extract the lithium diffusion coefficient of electrode particles. The test procedure was composed of a series of charge current pulses of 0.2 °C for 12min. After each charge period, the sample would be relaxed until the potential drift was less than 0.1 mV/h. Then, the effective diffusion coefficient D^{eff} was calculated by the equation below.

$$D = \frac{4L^2}{\pi\tau}\left(\frac{\Delta E_S}{\Delta E_t}\right)^2 \qquad \left(t \ll \frac{L^2}{D}\right) \tag{16}$$

where ΔE_S is the change of the steady-state voltage of cell for each step and ΔE_t is the total transient voltage change of the cell for applied current for time τ. L is the length of the electrode.

4. RESULTS AND DISCUSSION

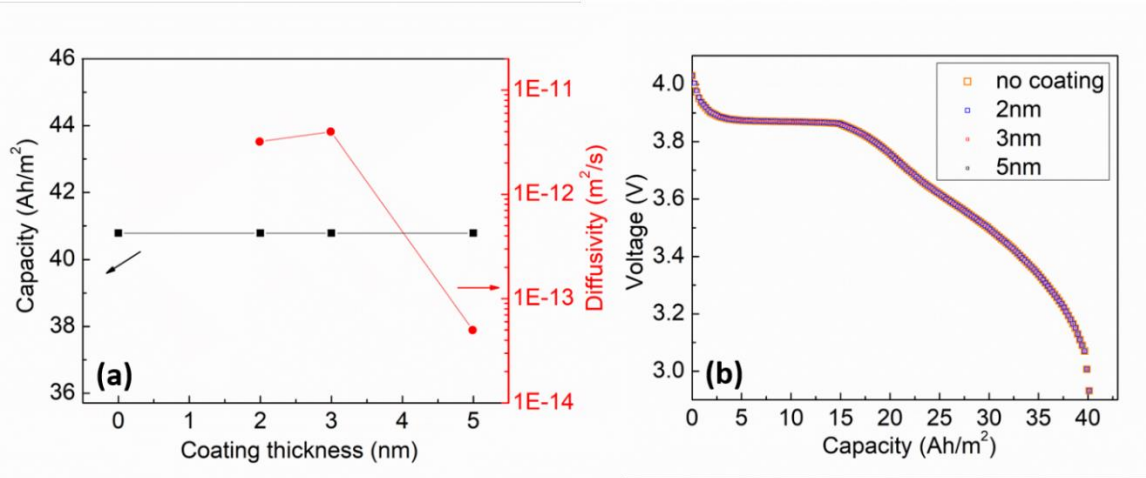

Figure 2. Calculated results of model based on traditional belief: (a) diffusivity parameters of CeO_2 coating layer and resulting capacity (b) voltage profile of cathode with different thickness coating layer.

Figure 2 shows the capacity and discharge profile of the SP model based on the traditional explanation. From this result, it can be confirmed that the discharge behavior does not change despite different diffusivity values at different coating thickness. In other words, the capacity was exactly the same for different samples, which is not consistent with experimental observations. Furthermore, the distribution of Li ion concentration in the non-coated and 3nm-coated particles is shown in Figure 3, where the arrows indicate the diffusion path of Li ion in the particles. This case considered the conventional explanation of ALD coating enhancement. It can be observed that the concentration distribution and diffusion path of Li ions are exactly same for non-coated and 3nm-coated particles, indicating that the coating layer has no impact on the Li ion diffusion. Therefore,

the traditional explanation on the role of CeO_2 coating layer cannot describe the observed phenomena correctly.

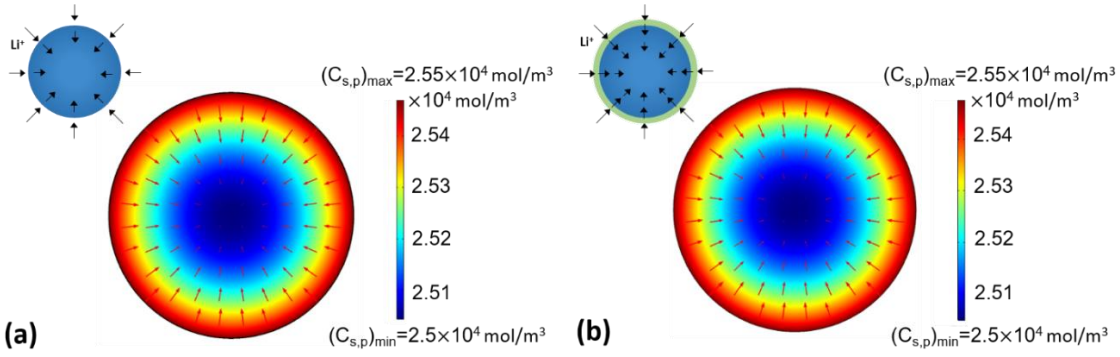

Figure 3. Diagram of Li-ion concentration distribution in (a) non-coated and (b) 3nm coated $LiMn_2O_4$ particle, based on the traditional explanation.

Figure 4 presents the simulation of the concentration distribution of non-coated and 3nm-coated particles based on the model of the proposed mechanism. The flux angles for both diagrams were assumed as 90 degrees as an example. As shown in the non-coated particle, the Li ion diffusion is unidirectional from the in-flux boundary. On the other hand, in CeO_2-coated particle, the diffusional behavior becomes more radial, which means that Li ions tend to spread throughout the highly conducting coating layer first, and then disperse from the coating layer to the active material in all directions. As a result, the distribution of Li ions takes on a radial transference path comparable to the traditional case with the uniform intercalation throughout the whole surface, in which a small gradient in concentration developed, and correspondingly, the active material utilization is enhanced.

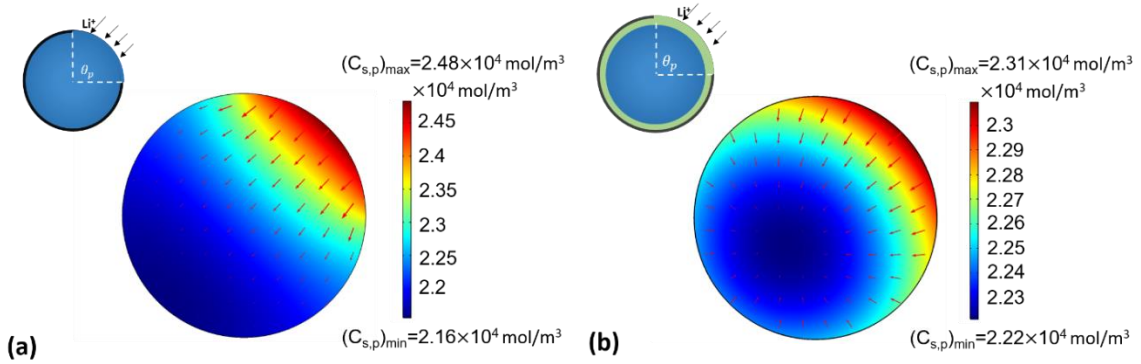

Figure 4. Diagram of Li-ion concentration distribution and diffusion path in (a) non-coated and (b) 3nm coated $LiMn_2O_4$ particle of model based on proposed mechanism.

The Li ion distribution of particles with different coating thickness are presented in Figure 5(a). From the experimental results in Table 1, it can be concluded that the diffusivity of CeO_2 coating layer is closely related to its thickness. This could be explained as a result of different dominant diffusion mechanisms. For CeO_2 coating layer with a thickness less than 3nm, the surface diffusion is dominant so that the diffusivity is higher, while the bulk diffusion becomes more significant for coating layers thicker than 3nm and thus lowers the diffusivity. It should be noted that when the thickness is less than 3nm, the coating layer itself may not evolve uniformly and, consequentially, affects the diffusivity[18]. As shown in Figure 5(a), the higher the diffusivity is, the more homogenous the Li ion concentration distribution becomes. Therefore, the minimal concentration gradient is obtained for 3nm-coated particle. The distribution of Li ion concentration determines the Li ion concentration at the surface of active material, which determines the open circuit voltage. Figure 5(b) plots the variation of surface Li ion concentration obtained from the model of the proposed mechanism as a function of time. It can be found that as the

diffusivity of the coating layer increases, the surface Li ion concentration decreases, leading to an increase in open circuit voltage of the positive electrode, according to Eq. 14. Another impact of the coating layer is its resistance. With the thickness increase, the ohmic resistance of the coating layer will increase. The voltage drop due to the ohmic resistance of coating layer is calculated and shown in Figure 5(c). It shows that because the thickness of coating layer is too thin, the ohmic voltage ranges from $1\times e^{-5}$ to $1\times e^{-8}$ V, which will not have a significant impact on the overall cell voltage. As a result, in the given voltage range, the discharge capacity of electrode particles will be higher for a coating layer of higher diffusivity. These results are consistent with the experimental result, indicating that the proposed mechanism can explain the experimental observation.

In the proposed hypothesis, a part of the particle boundaries was assumed to be blocked and no flux occurs at those parts. This means the exposed particle surface area in an electrode is smaller than the sum of the surface area of individual particles. To prove this, BET surface area analysis and PSA analysis of pure LMO, LMO-blend and LMO-electrode were conducted by measuring the surface area of lumped electrode and individual particles. First, the particle size distribution of pure LMO and LMO-blend were measured as shown in Figure 6. It can be observed that after mixing with CB and PVDF, the average size of powders increased, which may be caused by the adherence of the filler materials to the LMO particles. The specific surface area of individual particles was calculated from this result by Eq. 17.

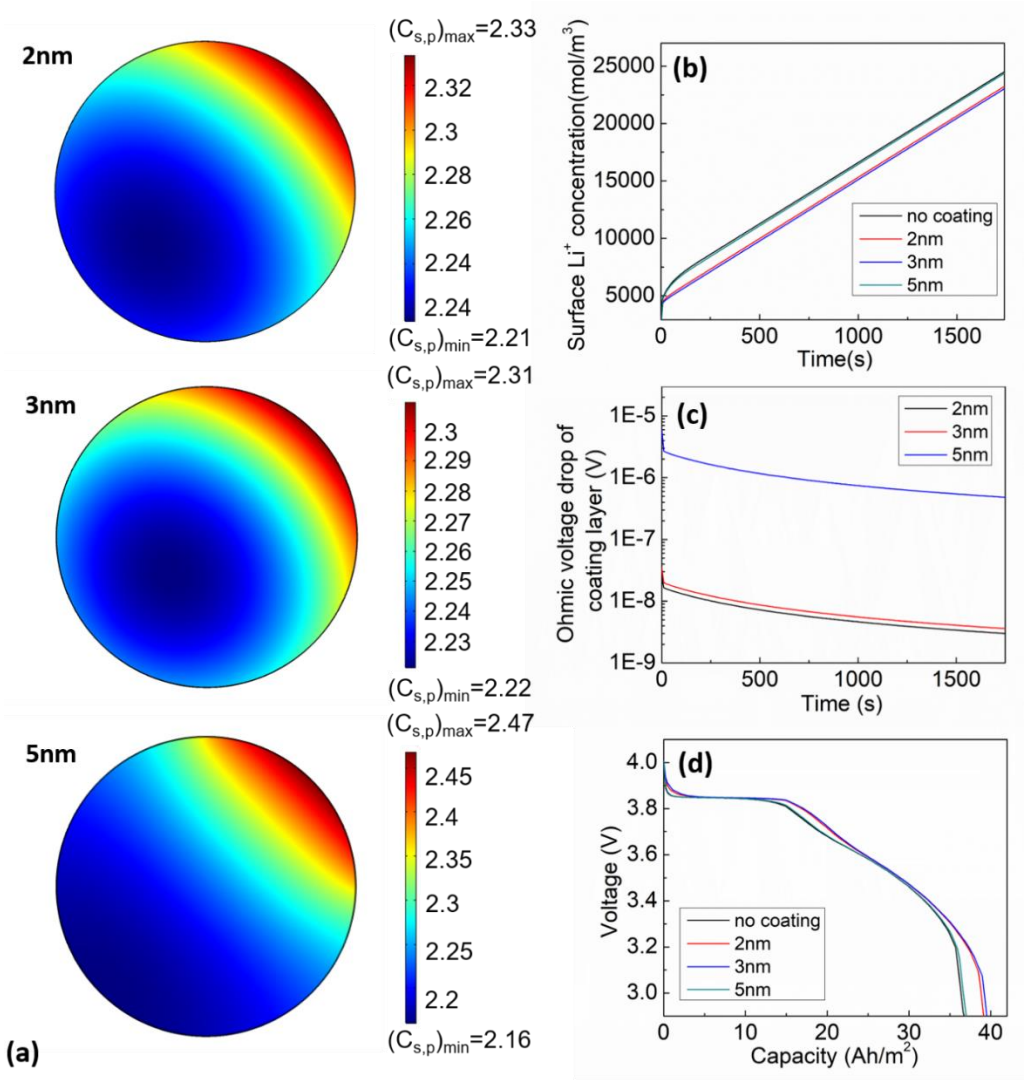

Figure 5. Diagram of (a) Li-ion concentration distribution ($\times 10^4$ mol/m^3), (b) surface Li ion concentration, (c) resistance of coating layer and (d) cell voltage profile for in non-coated, 2nm, 3nm and 5nm coated $LiMn_2O_4$ particle in the model based on proposed mechanism.

$$Specific\ surface\ area\ \ for\ individual\ \ particles = \sum \left(4\pi r^2 \times \frac{Volume\%}{\frac{4}{3}\pi r^3} \right) \times \frac{1}{\rho} = \frac{1}{\rho} \sum \left(\frac{3 \times Volume\%}{r} \right) \quad (17)$$

where r is the radium of particles, *Volume%* is the volume fraction of particle with particular radium and ρ is the density of particles. We uses the density of pure LMO particles for both samples, which is 4.5 g/cm^3. The results of BET test are shown in Table 2. It can be summarized as follows: The specific surface area of lumped samples are 0.729, 1.518, and 1.538 m^2/g, which is about 0.70%, 1.47% and 1.49% of the value of individual pure LMO particles, and about 3.80%, 7.90% and 8.02% of the value of individual LMO-blend particles. This indicates that a large portion of the particles' surface is blocked in which Li ions could not intercalate through.

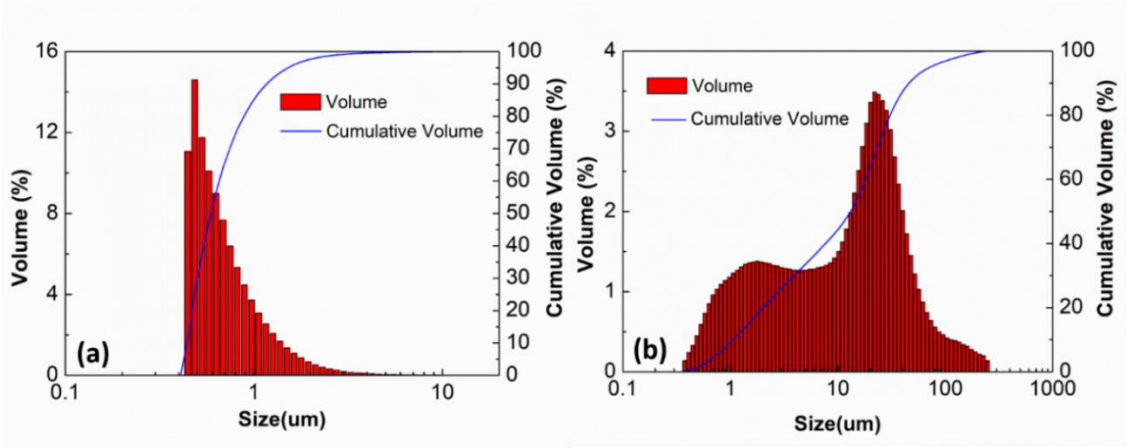

Figure 6. BET Specific surface area and specific surface area for individual particles of pure LMO, LMO-blend and LMO-electrode.

Table 2. BET Specific surface area and specific surface area for individual particles of pure LMO, LMO-blend and LMO-electrode.

	BET Specific Surface Area (m^2/g)	Specific surface area for individual particles (m^2/g)
Pure LMO	0.728	103.39
LMO-blend	1.516	19.18*
LMO-electrode	1.538	/

* Using the density of pure LMO

Through this series of modeling and experimental investigation, the proposed hypothesis is validated. Next, the impact of flux angle and current density on electrode capacity were investigated. As shown in Figure 7(a), with the increase of flux angle, the capacity of the electrode increases. This can be explained as a larger flux angle permits a larger boundary area for Li ion to disperse and transfer through, leading to more effective Li ion diffusion. However, the impact of flux angle is much smaller in particles with 2 nm and 3 nm coating. This is because a coating layer with 2 nm or 3nm thickness has higher diffusivity, which allows the coating layer to sufficiently distribute Li ions on the particle surface homogeneously. Figure 7(b) exhibits the influence of current density. As shown, and as expected, a larger current density causes a decrease in capacity. It can also be observed that the coating layer with high diffusivity is effective in improving the rate performance of electrode, especially under a high current rate. The impact of particle size on the electrochemical performance is shown in Figure 7(c). First, the overall capacities are higher for small particles than larger particles and the short diffusion path in the small

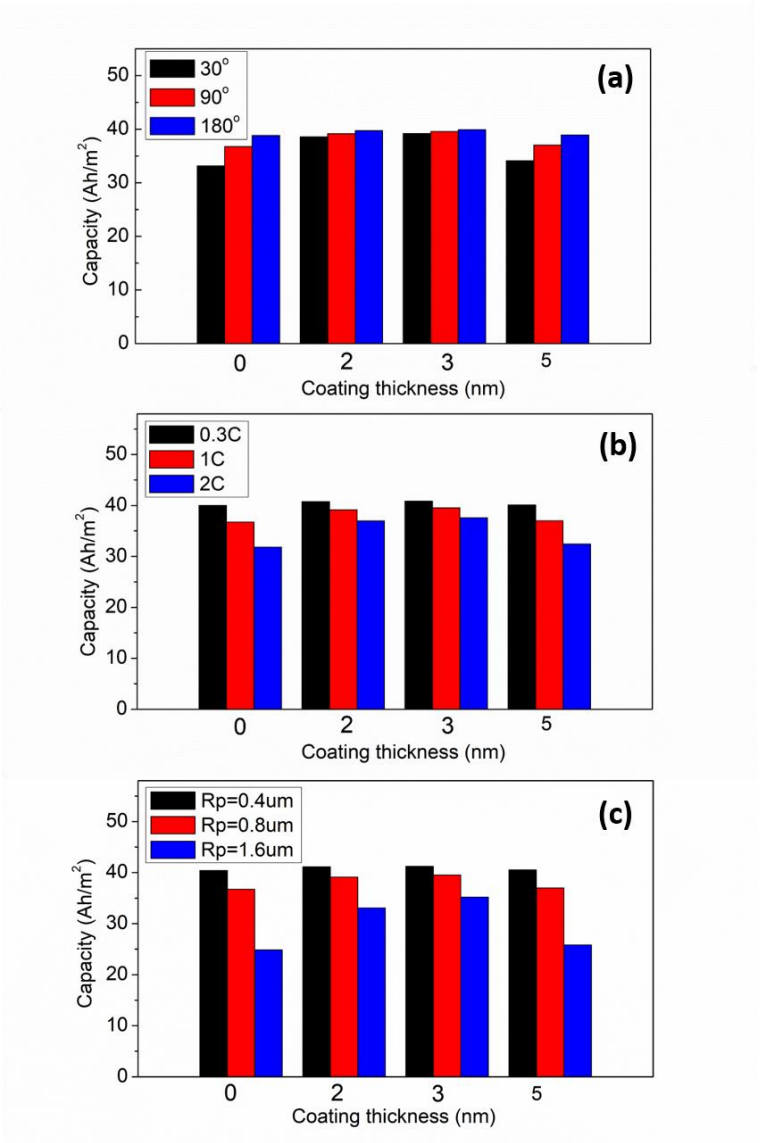

Figure 7. Capacity as a function of coating layer thickness for (a) different flux angle, (b) different current density in CeO_2 coated $LiMn_2O_4$ particle and (c) different active material particle size.

particles is the main reason for this. However, the capacity variation is more evident in larger particles. This is because the diffusion becomes more important limiting factor as the particle size increases, and the diffusion-enhancing coating layer has more impact on

larger particles. As a result, the capacity enhancement caused by coating layer become much more significant in large particles. As shown, the trade-off is clearly visible on larger particles. This understanding on the relationship between coating thickness, flux angle, current density, particle size and battery performance can provide a guidance for ALD coating and electrode design.

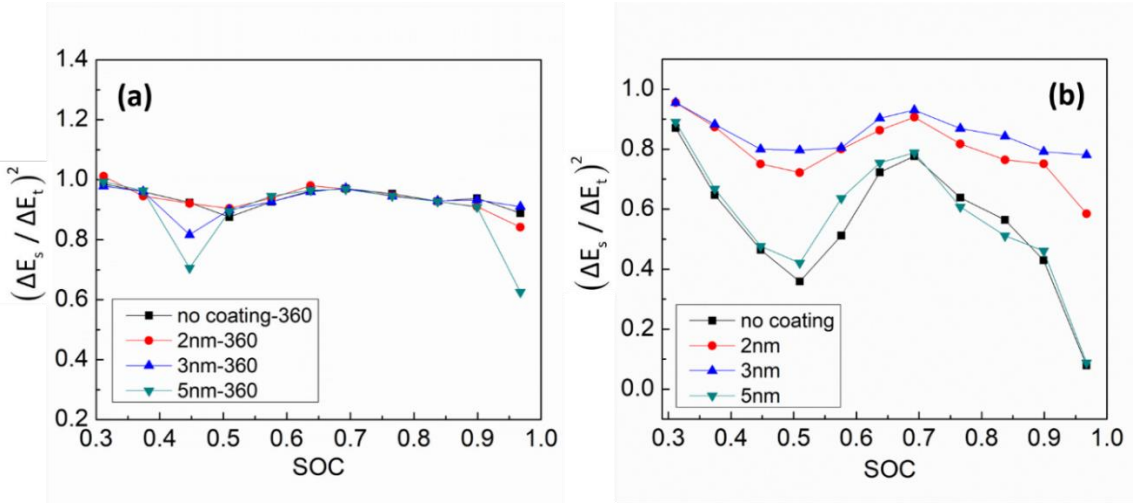

Figure 8. Square of slope of *Et* vs. *Es* as a function of state of charge (SOC) in models based on (a) traditional explanation and (b) proposed mechanism.

Another aspect of the validation of the proposed hypothesis can be considered from the effective diffusivity itself, measured from the experiment listed in Table 1. For this, a GITT experiment was simulated. Since the electrode length L in Eq. 16 is unknown and both L and time interval τ are constant in the measurement, we exclude this term and only calculate the square of the slope of E_s and E_t as a relative diffusivity. It can be observed in

Figure. 8 that for the model based on traditional explanation, all the effective diffusivities are not significantly different from each other for non-coated particle and coated particles with different coating layer thickness at most SOC points. However, in the model with the proposed hypothesis, the effective diffusivity is obviously improved by CeO_2 coating, and the 3nm-coated particle achieved the highest value. At the 0.92 SOC point especially, the diffusion coefficient of 3nm-coated particle is 4 times and 2nm-coated particle is 3 times that of the non-coated particle, which is very close to the corresponding experimental value. Therefore, this strengthens the position that the proposed hypothesis is correct.

5. CONCLUSIONS

In this work, it was proved that the enhanced transport property of ALD-coated particle was not attributed to the high conductivity of ALD coating layer, itself, as traditionally understood, but, rather, in the coating layer's role as a Li ion distributor enabling almost uniform intercalation through the entire particle surface despite physical blockings. The conducted simulation based on the conventional explanation showed that the CeO_2 coating layer could neither improve the capacity nor the effective diffusivity for $LiMn_2O_4$ particles when Li ion intercalation was ideally uniform. On the other hand, the model based on the proposed mechanism yielded consistent results with the experimental observation. The direct measurement of the surface area through BET and PSA indicated that the surface area of particles was partially blocked due to the agglomeration of particles and, as a result, Li ion intercalation was then limited in that region. The model confirmed that the existence of ALD coating can effectively distribute Li ions over the entire particle

surface despite the physical blockings. Finally, the analysis on the influence of flux angle, current density and particle size provides deeper understanding on relationship between the coating parameters, electrode configuration, battery operating condition, and battery performance, which serves as an importance guidance for electrode and coating design strategy.

REFERENCES

1. Chen, Z., et al., Role of surface coating on cathode materials for lithium-ion batteries. Journal of Materials Chemistry, 2010. **20**(36): p. 7606-7612.

2. Kim, J.W., et al., Surface chemistry of LiNi0. 5Mn1. 5O4 particles coated by Al2O3 using atomic layer deposition for lithium-ion batteries. Journal of power sources, 2015. **274**: p. 1254-1262.

3. Sun, Y.-K., et al., Significant improvement of high voltage cycling behavior AlF3-coated LiCoO2 cathode. Electrochemistry communications, 2006. **8**(5): p. 821-826.

4. Zheng, J., et al., The effects of AlF3 coating on the performance of Li [Li0. 2Mn0. 54Ni0. 13Co0. 13] O2 positive electrode material for lithium-ion battery. Journal of The Electrochemical Society, 2008. **155**(10): p. A775-A782.

5. Liu, H., et al., Cathode materials for lithium ion batteries prepared by sol-gel methods. Journal of Solid State Electrochemistry, 2004. **8**(7): p. 450-466.

6. Wang, H., et al., Graphene-wrapped sulfur particles as a rechargeable lithium–sulfur battery cathode material with high capacity and cycling stability. Nano letters, 2011. **11**(7): p. 2644-2647.

7. Ko, M., S. Chae, and J. Cho, Challenges in accommodating volume change of Si anodes for Li-ion batteries. ChemElectroChem, 2015. **2**(11): p. 1645-1651.

8. Li, X., et al., Hollow core–shell structured porous Si–C nanocomposites for Li-ion battery anodes. Journal of Materials Chemistry, 2012. **22**(22): p. 11014-11017.

9. Lu, S., et al., Significantly improved long-cycle stability in high-rate Li–S batteries enabled by coaxial graphene wrapping over sulfur-coated carbon nanofibers. Nano letters, 2013. **13**(6): p. 2485-2489.

10. Zou, L., et al., Modified natural flake graphite with high cycle performance as anode material in lithium ion batteries. Electrochimica Acta, 2009. **54**(15): p. 3930-3934.

11. Kim, H., et al., A new coating method for alleviating surface degradation of LiNi0. 6Co0. 2Mn0. 2O2 cathode material: nanoscale surface treatment of primary particles. Nano letters, 2015. **15**(3): p. 2111-2119.

12. Tan, G., et al., Coralline glassy lithium phosphate-coated LiFePO4 cathodes with improved power capability for lithium ion batteries. The Journal of Physical Chemistry C, 2013. **117**(12): p. 6013-6021.

13. He, Y., et al., Alumina-coated patterned amorphous silicon as the anode for a lithium-ion battery with high Coulombic efficiency. Advanced Materials, 2011. **23**(42): p. 4938-4941.

14. Wang, Z., et al., Structural and electrochemical characterizations of surface-modified LiCoO2 cathode materials for Li-ion batteries. Solid state ionics, 2002. **148**(3-4): p. 335-342.

15. Ha, H.-W., N.J. Yun, and K. Kim, Improvement of electrochemical stability of LiMn2O4 by CeO2 coating for lithium-ion batteries. Electrochimica Acta, 2007. **52**(9): p. 3236-3241.

16. Xiao, X., et al., Atomic layer coating to mitigate capacity fading associated with manganese dissolution in lithium ion batteries. Electrochemistry Communications, 2013. **32**: p. 31-34.

17. Park, S.-C., et al., The elevated temperature performance of LiMn2O4 coated with LiNi1− XCoXO2 (X= 0.2 and 1). Journal of power sources, 2002. **107**(1): p. 42-47.

18. Liu, D.-Q., X.-Q. Liu, and Z.-Z. He, The elevated temperature performance of LiMn2O4 coated with Li4Ti5O12 for lithium ion battery. Materials Chemistry and Physics, 2007. **105**(2-3): p. 362-366.

19. Wu, H., et al., Surface modification of LiNi0. 5Mn1. 5O4 by ZrP2O7 and ZrO2 for lithium-ion batteries. Journal of Power Sources, 2010. **195**(9): p. 2909-2913.

20. Hu, S.-K., et al., Cycle life improvement of ZrO2-coated spherical LiNi1/3Co1/3Mn1/3O2 cathode material for lithium ion batteries. Journal of Power Sources, 2009. **188**(2): p. 564-569.

21. Shi, J.Y., C.-W. Yi, and K. Kim, Improved electrochemical performance of AlPO4-coated LiMn1. 5Ni0. 5O4 electrode for lithium-ion batteries. Journal of Power Sources, 2010. **195**(19): p. 6860-6866.

22. Liu, P., et al., Fabrication of LiV2O5 thin-film electrodes for rechargeable lithium batteries. Solid State Ionics, 1998. **111**(1): p. 145-151.

23. Mantoux, A., et al., Vanadium oxide films synthesized by CVD and used as positive electrodes in secondary lithium batteries. Journal of The Electrochemical Society, 2004. **151**(3): p. A368-A373.

24. Cho, J., Y.J. Kim, and B. Park, LiCoO2 cathode material that does not show a phase transition from hexagonal to monoclinic phase. Journal of the electrochemical society, 2001. **148**(10): p. A1110-A1115.

25. Cho, J., Y.J. Kim, and B. Park, Novel LiCoO2 cathode material with Al2O3 coating for a Li ion cell. Chemistry of Materials, 2000. **12**(12): p. 3788-3791.

26. Zhao, H., et al., Improvement of electrochemical stability of LiCoO2 cathode by a nano-crystalline coating. Journal of power sources, 2004. **132**(1-2): p. 195-200.

27. Kim, Y.J., et al., Suppression of cobalt dissolution from the LiCoO2 cathodes with various metal-oxide coatings. Journal of The Electrochemical Society, 2003. **150**(12): p. A1723-A1725.

28. Cho, M.-Y., et al., Effects of CeO2 coating uniformity on high temperature cycle life performance of LiMn2O4. Materials Letters, 2011. **65**(13): p. 2011-2014.

29. Kannan, A.M. and A. Manthiram, Surface/Chemically Modified LiMn2 O 4 Cathodes for Lithium-Ion Batteries. Electrochemical and Solid-State Letters, 2002. **5**(7): p. A167-A169.

30. Liu, H., et al., A comparative study of LiNi0. 8Co0. 2O2 cathode materials modified by lattice-doping and surface-coating. Solid State Ionics, 2004. **166**(3-4): p. 317-325.

31. Shapira, A., et al., Robust AlF3 Atomic Layer Deposition Protective Coating on LiMn1. 5Ni0. 5O4 Particles: An Advanced Li-Ion Battery Cathode Material Powder. ACS Applied Energy Materials, 2018. **1**(12): p. 6809-6823.

32. George, S.M., Atomic Layer Deposition: An Overview. Chemical Reviews, 2010. **110**(1): p. 111-131.

33. Xiao, B., et al., Nanoscale Manipulation of Spinel Lithium Nickel Manganese Oxide Surface by Multisite Ti Occupation as High-Performance Cathode. Advanced Materials, 2017. **29**(47): p. 1703764.

34. Xiao, B. and X. Sun, Surface and Subsurface Reactions of Lithium Transition Metal Oxide Cathode Materials: An Overview of the Fundamental Origins and Remedying Approaches. Advanced Energy Materials, 2018. **8**(29): p. 1802057.

35. Zhao, Y., K. Zheng, and X. Sun, Addressing interfacial issues in liquid-based and solid-state batteries by atomic and molecular layer deposition. Joule, 2018.

36. Zhao, J. and Y. Wang, Atomic layer deposition of epitaxial ZrO2 coating on LiMn2O4 nanoparticles for high-rate lithium ion batteries at elevated temperature. Nano Energy, 2013. **2**(5): p. 882-889.

37. Zhao, J., et al., Low temperature preparation of crystalline ZrO 2 coatings for improved elevated-temperature performances of Li-ion battery cathodes. Chemical communications, 2012. **48**(65): p. 8108-8110.

38. Zhao, J. and Y. Wang, Ultrathin surface coatings for improved electrochemical performance of lithium ion battery electrodes at elevated temperature. The Journal of Physical Chemistry C, 2012. **116**(22): p. 11867-11876.

39. Waller, G., et al., Structure and surface chemistry of Al2O3 coated LiMn2O4 nanostructured electrodes with improved lifetime. Journal of Power Sources, 2016. **306**: p. 162-170.

40. Patel, R.L., et al., Significant Capacity and Cycle-Life Improvement of Lithium-Ion Batteries through Ultrathin Conductive Film Stabilized Cathode Particles. Advanced Materials Interfaces, 2015. **2**(8): p. 1500046.

41. Patel, R.L., J. Park, and X. Liang, Ionic and electronic conductivities of atomic layer deposition thin film coated lithium ion battery cathode particles. RSC Advances, 2016. **6**(101): p. 98768-98776.

42. Meng, X., X.-Q. Yang, and X. Sun, Emerging Applications of Atomic Layer Deposition for Lithium-Ion Battery Studies. Advanced Materials, 2012. **24**(27): p. 3589-3615.

43. Ma, L., et al., Atomic Layer Deposition for Lithium-Based Batteries. Advanced Materials Interfaces, 2016. **3**(21): p. 1600564.

44. Xu, S., et al., Lithium transport through lithium-ion battery cathode coatings. Journal of Materials Chemistry A, 2015. **3**(33): p. 17248-17272.

45. Jung, Y.S., et al., Ultrathin Direct Atomic Layer Deposition on Composite Electrodes for Highly Durable and Safe Li-Ion Batteries. Advanced Materials, 2010. **22**(19): p. 2172-2176.

46. Sarkar, S., et al., Unveiling the Role of CeO2 Atomic Layer Deposition Coatings on LiMn2O4 Cathode Materials: An Experimental and Theoretical Study. ACS Applied Materials & Interfaces, 2017. **9**(36): p. 30599-30607.

47. Michalska, M., et al., Influence of LiMn2O4 modification with CeO2 on electrode performance. Electrochimica Acta, 2014. **136**: p. 286-291.

48. Boukhalfa, S., K. Evanoff, and G. Yushin, Atomic layer deposition of vanadium oxide on carbon nanotubes for high-power supercapacitor electrodes. Energy & Environmental Science, 2012. **5**(5): p. 6872-6879.

49. Sopha, H., et al., ALD Al2O3-coated TiO2 nanotube layers as anodes for lithium-ion batteries. ACS omega, 2017. **2**(6): p. 2749-2756.

50. Kurttepeli, M., et al., Heterogeneous TiO2/V2O5/carbon nanotube electrodes for lithium-ion batteries. ACS applied materials & interfaces, 2017. **9**(9): p. 8055-8064.

II. TOWARDS HIGH-PERFORMANCE LI-ION BATTERIES VIA OPTIMIZED THREE-DIMENSIONAL MICRO-LATTICE ELECTRODE ARCHITECTURES

ABSTRACT

Optimized three-dimensional (3D) electrode architectures hold the promise of improving battery performance, a goal that cannot be obtained via conventional laminated structures. This paper reports on the mechanisms by which 3D electrodes enhance battery performance. The diffusion/migration of electrons/ions inside the battery was comprehensively analyzed via a 3D electrochemical model and subsequently validated by experiments on 3D micro-lattice electrodes made by Aerosol Jet printing. Lithium concentration and potential distribution were mapped to correlate battery performance with different shapes, thicknesses, packing density, and porosities. The study revealed that the main factors determining battery performance are ion diffusion in the electrolyte and electron transport in the 3D electrode skeleton. Further, the emergence of a competition between available volume for intercalation and an easier electronic/ionic path was shown, which determined their areal/specific capacities. In order to fully reap the benefits offered by 3D structures for both energy and power performance, the length scale of members forming electrode structures needs to be optimized at a scale of the order of the intercalation diffusion length, which is tens of micrometers. This study reveals highly useful guidelines for optimized 3D electrode designs and the possible manufacturing routes to realize them in order to achieve superior battery performance.

1. INTRODUCTION

Lithium ion batteries are one of the most important energy storage systems for portable devices, transportation, and renewable grids. To meet the increasing requirements by these applications, batteries with a higher energy and power density are urgently needed. Battery performance can be improved either by using higher capacity electrode materials or by improving the transport of the species during battery operations. Although significant progress has been made in these areas, most of the materials used in today's commercial Li-ion batteries are similar to those discovered about 20 to 30 years ago [1, 2]. A different route to increase battery capacity and power is to create well-defined, three-dimensional (3D) porosity within the electrodes [3-6]. For example, conventional laminated composite electrodes fabricated via a tape casting process show a trade-off between energy density and power density. To improve the energy density, more active material needs to be loaded by increasing the electrode thickness and packing density. This, however, limits the transport of ions and electrons, leading to poor power performance and inefficient utilization of the electrode materials. A 3D lattice electrode structure, on the other hand, allows an increase in surface-to-volume ratio, enabling the electrolyte to penetrate through the electrode volume. The free surface also reduces lithiation stress, enabling the use of high-capacity materials that undergo large volumetric changes during the battery's electrochemical cycles. Lastly, 3D-structured electrodes enable large specific surface area and short ion diffusion lengths which in turn enhance the energy density without much sacrifice of power density.

The manufacture of 3D-structured electrodes at microscales has been challenging because of the fact that most microfabrication methods have been largely planar. Recent

advances in 3D printing (i.e., additive manufacturing), however, have opened new pathways to realize geometrically optimized electrode architectures. The first 3D micro-battery was fabricated in an interdigitated structure with $Li_4Ti_5O_{12}$ (LTO) and $LiFePO_4$ (LFP) by an extrusion-based direct ink writing technique. The micro-battery showed a high areal energy density of 9.7 J/cm^2 with a power density of 2.7 mW/cm^2 [7]. Subsequently, electrode performance was enhanced by interdigitated structures of graphene oxide-based $LiFePO_4$ and $Li_4Ti_5O_{12}$ [8], $LiMn_{0.21}Fe_{0.79}PO_4$ [3], $LiMnO_4$ [9], reduced chemically-modified graphene (rCMG) [10], and CNF-based LFP/Li [11]. In addition, multilayered thick electrodes of different patterns, such as the grid [12] and Z patterns [13, 14], were developed. However, the use of interdigitated structures is limited in the further improvement of porosity and pore volume because of their simple geometry, which plays an important role in the electron transport and mechanical stress relief [15]. Other methods to create 3D-architected electrodes include self-assembled nanolattices of an electrolytically active material sandwiched between rapid ion and electron transport pathways that exhibit high charge-discharge rates [16, 17]. Si-electrodes with porosities at a length scale of >20 μm were shown to relieve strain and prevent pulverization of the anodes during electrochemical cycling [18]. Lastly, hollow gold tube electrodes, fabricated with periodic pores with sizes in the hundreds of nanometers using two-photon lithography followed by atomic layer deposition, were used in Li-ion batteries for fundamental electrochemical studies [19, 20].

Recently, complex 3D micro-lattice electrodes with a hierarchical porosity over several orders of magnitude in length scale were reported to be achieved by Aerosol Jet (AJ) 3D printing [21]. AJ is an innovative, noncontact printing process that deposits

aerosolized microdroplets of nanoparticles dispersed in a solvent onto a substrate to create 3D structures such as lattices [22]. Compared with traditional extrusion and inkjet printing, the AJ method facilitates the use of a large viscosity range for inks (up to 1000 cP) and a stand-off height of up to 5 mm between the substrate and nozzle, which enables printing on complex 3D substrates [23, 24]. The length scale of the truss members of the lattice structure is about 10 μm [21], a scale comparable to the characteristic diffusion length of Li ions in several host materials for reasonable charge-discharge times. Further, the sintering process creates an internal porosity within the truss members, which is of the order of a micron or less, thus forming a hierarchical porous structure [21].

For energy storage devices, a hierarchical electrode porosity in three dimensions provides several advantages [25-28]. For example, the electrochemical performance of the electrode material would be influenced not only by submicron scale porosity via parameters such as pore size, pore distribution, and pore morphology, but also by macroscale porosity that forms the electrode structure. During the AJ 3D printing process, the submicron scale porosity can be adjusted by sintering parameters and the macroscale electrode structure is determined by the initial design/printing program [22]. Theoretically, pores can facilitate the species transport from the electrolyte to the electrode surface. However, too small pores would impede species movement. On the other hand, volumetric energy density is reduced by the existence of large pores [29]. The macro-porous Sn-Cu alloy electrode has an average pore size of 180 nm, and it delivered a reversible capacity of 350 mAh/g in the 70^{th} cycle, improving on the 270 mAh/g attributed to an average pore size of 500 nm [30]. In 3D-ordered macro-porous $Li_4Ti_5O_{12}$ electrodes, a porous internal wall structures exhibited better rate capability and extremely high capacities [31]. In

mesoporous anatase TiO_2, the specific capacities of electrodes increased as the pore size of the surfactants used in the preparation increased from 5.7 nm to 7.0 nm [32]. The interconnectivity between pores is also critical for electrode performance because it affects the electrolyte distribution. For example, in mesoporous anatase TiO_2 a uniform pore size distribution was reported to be beneficial because it allowed an optimal open volume for best mass transport without wasted space [28]. In a study of 3D vanadium pentoxide aerogel, the tortuosity of the material was reduced by a hierarchically-ordered, inverted opal structure, leading to less polarization and a high capacity at high C-rate compared with bulk aerogels [33]. In addition, pore structure was shown to correlate with both surface area and pore wall thickness of the electrode material [34, 35]. Large specific surface area can effectively reduce the current density per unit surface area, alleviating the polarization at the interface and facilitating ion transfer [36]. Further, pore wall thickness determines the length of lithium ion diffusion during the intercalation and deintercalation process, impacting the capacity and rate capability of the material [37, 38]. It is notable that few studies have reported an experimental realization of electrodes with feature sizes of the order of 10s of micrometers [21, 39, 40]. Our previous work on Aerosol Jet printed electrodes [21] showed a significant improvement in areal capacity for X-structure compared to block structures of Ag electrodes (100% increase with electrode thickness increasing from 200 μm to 450 μm). A near-complete utilization of the electrode volume for micro-lattice scaffolds was also observed. Extrusion-based additive manufacturing [39] was used to fabricate 3D electrodes with feature sizes of tens of micrometers that exhibited improved electrochemical performance. Chemical etching was used to fabricate ‘sponge-

like' Si structures with feature sizes in tens of micrometers that showed a significant improvement in battery capacity with minimal capacity fade [40].

Although it has been shown that 3D-structured electrodes can improve battery performance, the extra freedom related to geometrical construction and its complex influence on electrochemical properties necessitates better understanding of the mechanisms of performance enhancement to allow the identification of optimized 3D electrode structures. Because it is too costly to use experimental trial and error methods, numerical modeling, validated by experiments for a few geometries, provides an effective way to predict the electrochemical properties of different sets of parameters while reducing time and cost. Over the past decades, several studies have been performed to include the features of electrode structure in battery performance simulations. For example, tortuosity was regarded as a key parameter to represent the impact of geometry on battery properties [41]. It was implemented as a correction factor for effective material properties such as mass transport, liquid phase diffusivity, and conductivity. Tomography was utilized as a way to input the microstructural information of the electrodes [15, 42]. The microstructure of electrodes can be meshed according to X-ray nano-CT images or SEM images [42] by using the finite volume method, thus allowing for the investigation of the spatial distribution of electrochemical properties in the model. Some works also implemented a 3D finite element scheme based on assumptions on particle size selection, arrangement, and material properties [43, 44]. In these works, microstructure was created by assembling particles in random or pre-set arrays in a unit cell with periodic boundary conditions. However, all the models mentioned above consider microstructural information only at the micro-scale while assuming a homogenous structure at the macro-scale. To take into

account the effect of both micro- and macro-scale pores in 3D electrode architectures, a model that is able to separately consider structural information at different scales needs to be developed.

Mechanical deformation and failure of the electrodes are important factors affecting battery electrochemical performance. The intercalation and de-intercalation of Li ions can cause an expansion and contraction of electrode volume, leading to micro and/or macro-scale stress generation in the electrode.[45, 46] This chemically induced stress is even more important for electrodes with 3D complex shapes, and can affect their mechanical stability during the charge-discharge cycles.[21] In addition, possible structural defects in such electrodes can amplify the stresses, adversely affecting their cyclic life and capacity.[45, 47] This effect can be studied by introducing an electromechanical-mechanical coupling term in the battery models. In few past studies, the impact of stress generation, particle deformation, crack propagation, and diffusion have been investigated in a single particle.[48-52] Several researchers also report macro-scale models that account for geometrical changes such as thickness increase and thermal swelling.[53-56] None of these studies,[48-56] however, considered complex 3D electrode architectures in their models.

In this paper, we analyze the effect of macro- and microscale structural features of 3D lattice-shaped electrodes on battery performance using a 3D electrochemical-mechanical model. In this model, the micro-scale structures are implemented based on a porous electrode theory, while the macro-scale structures are modeled by a 3D finite element scheme. The model is validated by experimental observation based on AJ printed 3D micro-lattice electrode Li-ion battery cells. The impact of two-level structural porosity on the electrochemical properties of the battery is analyzed by including different volume

fractions of the solid phase at the micro-scale and different electrode geometries and their electrode thicknesses at the macro-scale. This extensive study on the relationship between micro/macro electrode geometry and battery performance provides the scientific basis to facilitate high-capacity electrode designs that can be realized by additive manufacturing.

2. EXPERIMENTAL SETUP

A 40 ± 2 wt % Ag nanoparticle ink with a particle size of 30-50 nm and a viscosity of 1.5 cP (Perfect-TPS 50 G2, Clariant Group, Frankfurt, Germany) was adopted for printing. The ink was loaded into a commercial AJ printer (AJ-300, Optomec, Inc., Albuquerque, NM) to be deposited in a 3D geometry on a chromium-coated stainless steel connector disk of 11 mm diameter and 500 μm thickness under ambient conditions. The geometry of the electrode was drawn in AutoCAD by the software AutoLISP (AutoCAD 2015, Autodesk Inc., San Rafael, CA) and imported into the printer controller to guide the printing process. Subsequently, the printed pattern was sintered at 350 °C for 2 hours in a programmable oven (Neytech Vulcan furnace, Model 3-550, Degussa-Ney Dental Inc., Bloomfield, CT). The detailed preparation process of the 3D electrodes was presented in our previous paper [21].

A CR2032 coin cell (Wellcos Corp) was used to assemble a battery in an argon-filled glove box (Mbraun). A printed silver lattice was used as the working electrode (theoretical specific capacity 290 mAh/g). The counter electrode, separator, and electrolyte were Li foil (Sigma Aldrich), commercial PP/PE/PP membrane (Celgard), and 1M $LiFP_6$

EC:DMC 1:1 v/v (Sigma-Aldrich), respectively. The charge/discharge process was conducted from 0.02 to 2.8 V using a battery test station (IVIUMnSTAT, Ivium Tech).

3. ELECTROCHEMICAL MODEL

A 3D full-order electrochemical model was developed and implemented to evaluate the performance of the 3D lattice electrodes. The model is based on the porous electrode theory [57], where an electrode sketch is incorporated in the geometry and meshed by the finite element method. The Li ion concentration in the solid phase was evaluated via a fourth-order approximate analytic solution of the solid-phase diffusion equation [58]. Pore structure and then 3D geometry of the electrode that form the two-level porosity were treated as being at different scales: the pore structure was regarded as a homogenized system superimposed by electrode and electrolyte and the 3D geometry was simulated as if it were composed of individual solid and liquid phases [44]. To incorporate the 3D geometry of the electrode into the model, a half-cell model was developed as shown in Figure. 1. The mass conservation and charge conservation equations were evaluated in a 3D electrode according to the porous electrode theory, shown in Figure. 1(b). The equations used in the 3D model are summarized in Table 1. COMSOL 5.4 was used to implement all governing equations above into finite element simulation to determine the electrochemical behavior within the 3D electrodes schematized in Figure. 1(b). The material parameters used in the simulation are listed in Table 2.

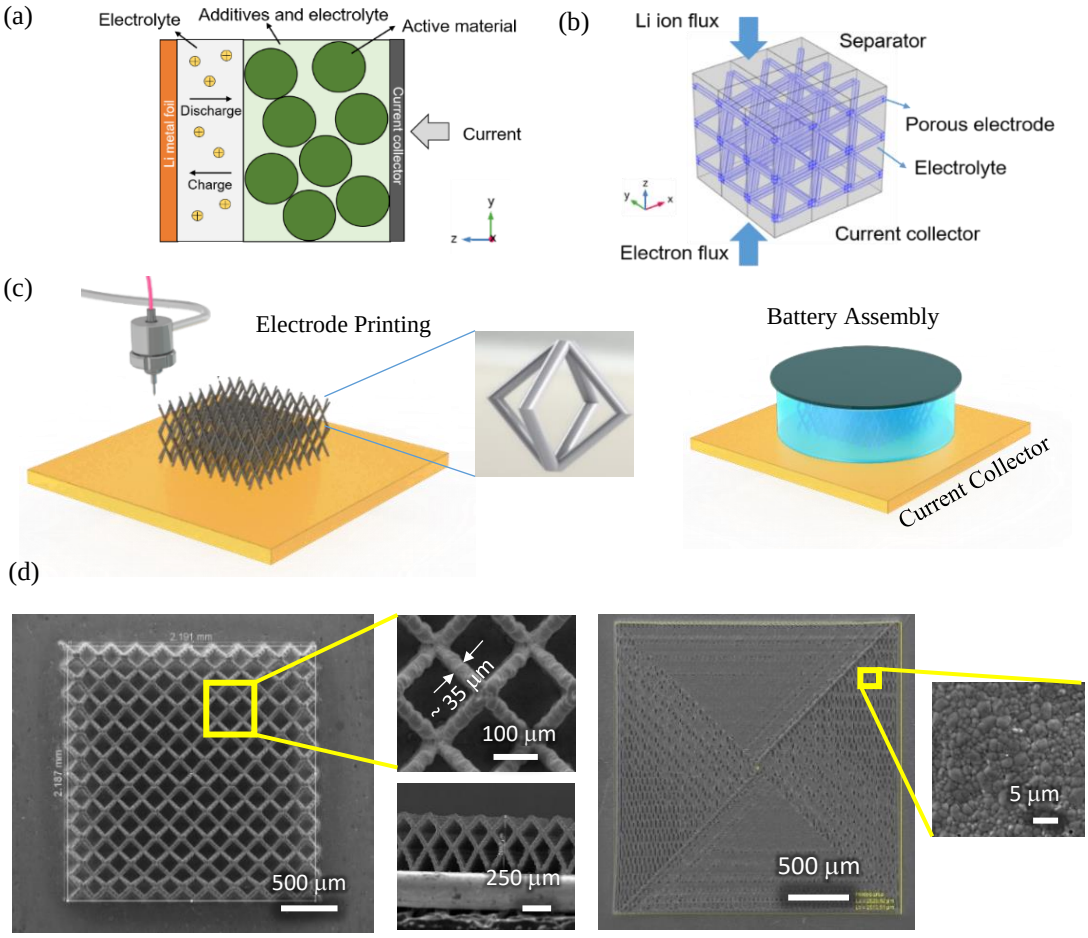

Figure 1. Half-cell and model description: (a) Illustration of half-cell with porous electrode, (b) 3x3x3 array of 3- dimensional open octahedral micro-lattice structure (called "X-structure") used to develop the electrochemical model; 3D micro-lattice battery electrode experiments and model validation. (c) Schematic of aerosol jet (AJ) printing process to fabricate 3D micro-lattice structures, along with a schematic of the battery assembly process, (d) AJ-printed open octahedral electrode architecture (called 'X-structure' in this paper, left) and block electrode architecture (right).

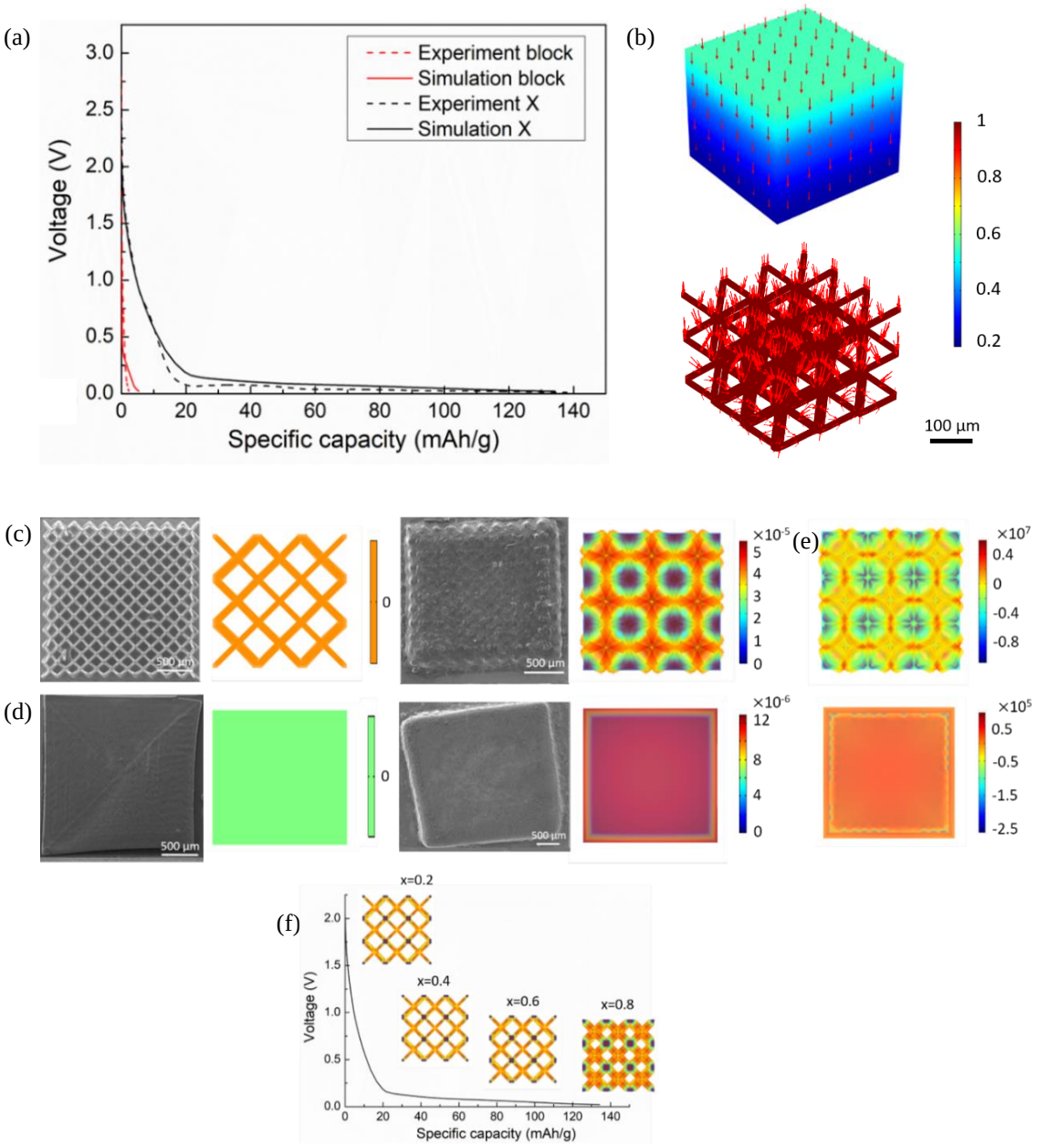

Figure 2. Model validation: (a) Comparison of battery performance for 3D printed electrodes with the model developed in the work demonstrating good agreement. (b) Spatial SOC distribution and flux distribution (red arrows) at 0.02 V for the open octahedral electrodes and block-structured electrodes. SEM image and simulated deformation of (c) X-structure electrode and (d) block-structure electrode in (left) as-fabricated state (0% capacity, x=0) and (center) fully lithiated state (100% capacity, x=1), (e) stress (Pa) of fully lithiated state in X-structure electrode and block-structure.

Table 1. Governing equations in 3D model.

Region	Governing Equation	Boundary conditions
Electrode	**Mass, solid phase** $$\frac{dc_{s,p,avg}(\mathbf{X},t)}{dt} = -\frac{J_p(\mathbf{X},t)}{3R_p} \quad (1)$$ $$\frac{dq_{s,p,avg}(\mathbf{X},t)}{dt} = -30\frac{D_{s,p}}{R_p^2}q_{s,p,avg}(\mathbf{X},t) - \frac{45}{2R_p^2}J_p(\mathbf{X},t) \quad (2)$$	$$c_{s,p,surf}(\mathbf{X},t) = c_{s,p,avg}(\mathbf{X},t) + \frac{8R_p}{35}q_{s,p,avg}(\mathbf{X},t) - \frac{R_p}{35D_{s,p}}J_p \quad (3)$$
	Charge, solid phase $$\sigma_{eff,p}\nabla\phi_{s,p}(\mathbf{X},t) = a_p F J_p(\mathbf{X},t) \quad (4)$$	Current collector/anode interface: $$-\sigma_{eff,p}\left(\frac{\partial\phi_{s,p}(t)}{\partial x} + \frac{\partial\phi_{s,p}(t)}{\partial y} + \frac{\partial\phi_{s,p}(t)}{\partial z}\right)\Bigg|_{z=0} = I_{app} \quad (5)$$
Electrode/ Separator	**Mass, liquid phase** $$\varepsilon_j\frac{\partial c_{e,j}(\mathbf{X},t)}{\partial t} = \frac{\partial}{\partial\mathbf{X}}\left(D_{eff,j}\frac{\partial c_{e,j}(\mathbf{X},t)}{\partial\mathbf{X}}\right) + a_j(1-t_+)J_j(\mathbf{X},t) \quad (6)$$	Separator/anode interface: $$-D_{eff,s}\frac{\partial c_{e,s}(t)}{\partial\mathbf{X}}\Bigg|_{z=L_p+L_s} = \frac{J_{Li}(t)}{F} \quad (7)$$

Table 1. Governing equations in 3D model. (Con't)

Region	Governing Equation	Boundary conditions
Electrode/ Separator	**Charge, liquid phase** $\kappa_{eff,j}\nabla\frac{\partial^2\phi_{e,j}(\mathbf{X},t)}{\partial\mathbf{X}^2}-\frac{2\kappa_{eff,j}RT(1-t_+)\partial^2\ln c_{e,j}(\mathbf{X},t)}{F\partial\mathbf{X}^2}\left(1+\frac{d\ln f_+}{d\ln c_{e,j}}\right)=$ (8)	Separator/anode interface: $\kappa_{eff,j}\nabla\frac{\partial\phi_{e,j}(\mathbf{X},t)}{\partial\mathbf{X}}-\frac{2\kappa_{eff,j}RT(1-t_+)\partial\ln c_{e,j}(\mathbf{X},t)}{F\partial\mathbf{X}}\left(1+\frac{d\ln f_+}{d\ln c_{e,j}}\right)\Bigg\|_{z=L_p+L_s}=$ (9)
Electrode kinetics	$J_p(\mathbf{X},t)=k_p c_{s,p,\max}c_e^{0.5}\left(1-\frac{c_{s,p,surf}(\mathbf{X},t)}{c_{s,p,\max}}\right)^{0.5}\left(\frac{c_{s,p,surf}(\mathbf{X},t)}{c_{s,p,\max}}\right)^{0.5}\left(\exp\left(\frac{0.5F}{RT}\eta_p(\mathbf{X},t)\right)-\exp\left(-\frac{0.5F}{RT}\eta_p(\mathbf{X},t)\right)\right)$ (10) $\eta_p=\phi_{s,p}-\phi_{e,p}-U_p$ (11) $J_{Li}(t)=0.85\left(\exp\left(-\frac{0.5F}{RT}\phi_{e,s}(\mathbf{X},t)\right)-\exp\left(\frac{0.5F}{RT}\phi_{e,s}(\mathbf{X},t)\right)\right)$ (12)	

Table 2. Model parameters used in simulation studies.

Parameter	Value	Description
$brug^{[44]}$	1.5	Bruggeman coefficient
$C_{e,k,0}^{[44]}$	2000	Initial electrolyte concentration (mol m^{-3})
$C_{\max,\, pos}$	102870	Maximum concentration of Li-ion in cathode (mol m^{-3})
$D_e^{[44]}$	7.5×10^{-11}	Diffusion coefficient in electrolyte (m^2s^{-1})
$D_{s,p}^{[44]}$	2.5×10^{-15}	Solid-phase Li diffusivity, positive electrode (m^2s^{-1})
F	96487	Faraday's constant (C mol^{-1})
$i_0^{[44]}$	0.85	Constant flux for half-cell
I	Variable	Applied current density (A m^{-2})
$K_{s,p}^{[44]}$	3.8	Solid phase conductivity (S m^{-1})
$k_p^{[44]}$	2×10^{-6}	Reaction rate coefficient, cathode ($m^{2.5}mol^{-0.5}s^{-1}$)
R	8.314	Universal gas constant (J mol^{-1} K^{-1})
$R_p^{[44]}$	13×10^{-6}	Particle radius, positive electrode (m)
$t_+^{[44]}$	0.363	Cationic transport number
ε_p	Variable	Solid phase volume fraction of cathode
$\varepsilon_s^{[44]}$	0	Solid phase volume fraction of separator
E	2.82×10^{6}	Effective Young's module (Pa)
v	0.37	Poisson's ratio
Ω	1.15×10^{-4}	Partial molar volume expansion of Ag~AgLi (m^3 mol^{-1})
	6.07×10^{-6}	Partial molar volume expansion of AgLi~$AgLi_{1.8}$ (m^3 mol^{-1})

4. RESULTS AND DISCUSSION

4.1. MODEL VALIDATION USING EXPERIMENTAL RESULTS

4.1.1. Voltage Profile. Schematics of the 3D electrodes' lattice structure used for model validation along with a unit cell are shown in Figure. 1(c). Two electrode structures fabricated by AJ printing – an open octahedral structure (called 'X-structure' in this paper) and a solid block-structure – are shown in Figure. 1(d). In the X-structure, the diameter of the electrode truss members of the micro-lattice was about 35 μm, which is on the same order of magnitude as the characteristic diffusion length ($\sqrt{Dt}$) for full lithiation at 0.5 C. The pore size in the printed micro-lattice structure was about 100 μm × 100 μm, which is sufficient for the electrolyte (viscosity <10 cP) to undergo capillary absorption [59]. The truss members of the electrode had an internal porosity ranging between 500 nm – 1 μm, also described in our previous work [21]. The block electrode and the X-structured electrode exhibited similar thicknesses of approx. 450 μm.

Figures 2(a) and (b) show a comparison between the measured discharge profiles of the two types of electrodes and the model prediction, respectively. The model predictions for both X-structure and block-electrode geometry show good agreement with the experimental data, which indicates that the modeling approach developed in this work can be used to capture the effect of electrode geometry on battery performance. The spatial distributions of state-of-charge (SOC) in the X- and the block structure are plotted in Figure. 21(b). When the capacity of a structure is larger, its SOC distribution is expected to be more uniform, and the average SOC is expected to be closer to 1, that is, a fully charged state. Note that the top surface in the Z-axis is the electrode/separator interface and

the bottom side is the electrode/collector interface. For the block structure, a limitation in species transport results in a maximum SOC of 0.54 along with a high concentration gradient from the electrode/separator interface to the electrode/current collector interface (ΔSOC being 0.32). This leads to a small average SOC for the entire electrode. By contrast, the SOC in the open octahedral structured electrode is larger than 0.99 at all positions, indicating a high utilization of the electrode material. This significantly improved behavior was attributed to the geometry of the 3D electrodes, which enhances the transport of the lithium ions. As indicated by the red arrows (representing flux), lithium ion flux was able to distribute at the surface of every unit lattice of the octahedral structure in various directions, rather than entering the electrode material only from the top surface in the block structure, which greatly improved the efficiency of lithium ion transfer.

4.1.2. Li-ion Intercalation Induced Electrode Displacement. It was observed in the experiments that the morphology of X-structured electrodes changed considerably after intercalation with Li-ions (Figures. 2(c) and 2(d)), which was caused by the volume change induced by the variation in the Li-ion concentration. To simulate this phenomenon, a stress model was developed by coupling the electrochemical-mechanical interaction at macro- and micro-scales. We note that since the battery model developed in this work is based on th ɔrous theory, the mechanical response of the electrode should be interpreted based on a multiscale perspective. The micro-scale stress model deals with the stress generated inside the particle induced by Li ion concentration change. The macro-scale stress model deals with the stress generated across the entire skeleton caused by the volume change of individual particles. In the micro-scale, the particles were assumed as spheres. Therefore,

the radial stress, σ_r, and tangential stress, σ_t, of individual particle can be be expressed as [49]

$$\sigma_r = \frac{2\Omega E}{3(1-\upsilon)}\left(\frac{1}{r_0^3}\int_0^{r_0} c_{s,avg} r^2 dr - \frac{1}{r^3}\int_0^{r} c_{s,avg} r^2 dr\right) \tag{13}$$

$$\sigma_t = \frac{\Omega E}{3(1-\upsilon)}\left(\frac{2}{r_0^3}\int_0^{r_0} c_{s,avg} r^2 dr + \frac{1}{r^3}\int_0^{r} c_{s,avg} r^2 dr - c_{s,avg}\right), \tag{14}$$

where r_0 is the radius of the particle, E is effective Young's modulus (considering porosity), υ is Poisson ratio, and Ω is the partial molar volume expansion of silver which is obtained from first-principles simulations and fitting of experimental data. The simulation data of $AgLi_x$ volume expansion and derivative process of Ω from a density functional theory (DFT) calculation are shown in Supplementary Material.

At particle surface ($r = r_0$)

$$\sigma_r = 0; \qquad \sigma_t = \frac{\Omega E}{3(1-\upsilon)}\left(c_{s,avg} - c_{s,surf}\right). \tag{15}$$

The tangential stress-strain relations and strain-displacement relations can be expressed as

$$\varepsilon_t = \frac{1}{E}\left(\sigma_t - \upsilon\left(\sigma_r + \sigma_t\right)\right) + \frac{\Omega}{3} c_{s,avg} \tag{16}$$

$$\varepsilon_t = \frac{u}{r} \tag{17}$$

By importing Eq. 15 into Eq. 16 and Eq. 17, the particle surface displacement can be obtained as

$$u_{surf} = \frac{\Omega r_0}{3}\left(c_{s,avg} - c_0\right) \tag{18}$$

In spherical particles, the micro-scale chemically induced eigenstrain $\boldsymbol{e}_s^{ch}$ is equal to the particles' volumetric strain, which is

$$\boldsymbol{e}_s^{ch} = \frac{1}{3}\left(\frac{\left(r_0 + u_{surf}\right)^3}{r_0^{\,3}} - 1 \right). \tag{19}$$

According to the Mori-Tanaka effective-field theory, the particle surface pressure is decided by the macro-scale total strain and the micro-scale volumetric strain. Therefore, the macro-scale eigenstrain $\boldsymbol{e}^{ch}$ can be computed as [56]

$$\boldsymbol{e}^{ch} = \boldsymbol{e}_m^{ch} + \varepsilon_s(\boldsymbol{e}_s^{ch} - \boldsymbol{e}_m^{ch}) + \varepsilon_s(\boldsymbol{C}_s^{-1} - \boldsymbol{C}_m^{-1})b_s \tag{20}$$

where ε_s is solid phase volume fraction, and $\boldsymbol{e}_m^{ch}$ is the chemically induced strain in the electrolyte, which is assumed to be 0 here. $\boldsymbol{C}_s$ and $\boldsymbol{C}_m$ are the stiffness matrices for the solid and liquid phase; while b_s is a function of $\boldsymbol{C}_s$ and $\boldsymbol{C}_m$.

The governing equation of macro-scale mechanical deformation is

$$\nabla \cdot \boldsymbol{\sigma} = 0 \tag{21}$$

$$\boldsymbol{\sigma} = \boldsymbol{C}_{eff} : (\boldsymbol{e} - \boldsymbol{e}_{ch}) \qquad e = \frac{1}{2}\left(\nabla \boldsymbol{u} + \nabla \boldsymbol{u}^T\right) \tag{22}$$

where $\boldsymbol{\sigma}$ is the macro-scale stress, $\boldsymbol{e}$ is the total macro-scale strain tensor and $\boldsymbol{u}$ is the total displacement, $\boldsymbol{C}_{eff}$ is the effective elasticity tensor can be calculated as

$$\boldsymbol{C}_{eff} = \boldsymbol{C}_m + \varepsilon_s(\boldsymbol{C}_s - \boldsymbol{C}_m)\boldsymbol{A}_s \tag{23}$$

$$\boldsymbol{A}_s = \boldsymbol{A}_D\left[(1-\varepsilon_s)\boldsymbol{I} + \varepsilon_s \boldsymbol{A}_D\right]^{-1} \tag{24}$$

$$\boldsymbol{A}_D = \left[\boldsymbol{I} + \boldsymbol{S}\boldsymbol{C}_m^{-1}\left(\boldsymbol{C}_s - \boldsymbol{C}_m\right)\right]^{-1} \tag{25}$$

$\mathbf{S}$ is Eshelby's tensor, which is a function of the aspect ratio of the particle and the Poison's ratio of the matrix phase.

A comparison of simulated deformation of the X-structured and block-structured electrodes with the experimental observations is shown in Figures. 2(c) and 2(d), respectively. For the X-structure, when the electrode was fully lithiated, the deformation resulted in complete filling of the spaces between truss members and the maximum displacement of the electrodes was located at the crosslinks, which matches quite well with the experiments (SEM images in Figure. 2(c)). For the block structure, the electrode shape did not change upon lithiation. This was because the SOC change in the block structure was not as large as that in the X structure as shown previously in Figure. 2(b), and, according to Eq. 15, the volume expansion was proportional to SOC changes. This result also matches with the experimental observations (SEM images in Figure. 2(d)). The corresponding spatial distribution of stress was shown in Figure. 2(e). As shown, the maximal stress in X-structure was around 5.93 MPa in the centers of truss members, while the maximal stress in block was 87.9 kPa at the edges of sides. The stress level of block structure is much less than in X-structure for two reasons. First, the SOC change from as-fabricated state to fully charged state in block structure is around 50% less than that in X-structure (Figure 2(f)). Secondly, the partial molar volume for Ag~AgLi (0~55.56% SOC) is less than that for AgLi~$AgLi_{1.8}$ (55.56%~100% SOC) according to the first-principles calculation and fitting of the experimental data (see section S2 of the Supplementary Material). Therefore, both the volume changes and stress in block structure is much less than that of X-structure.

The evolution of the X-structure as a function of SOC as predicted by our model is shown in Figure. 2(f). The volume expansion increased with the increasing of capacity ratio (x) under intercalation of Li ions. It is noted that the volume change from x=0 to x=0.6 was not as large as that from x=0.6 to x=1 due to the nonuniform of the partial molar volume at different SOC range. The excellent match between the SEM images and simulation results for volume expansion are a good validation for 3D model developed in this work. Further, by coupling the stress part, this electrochemical-mechanical model can also be applied to analyze the mechanical stability of other 3D electrodes in the future.

4.2. EFFECT OF MICRO-LATTICE GEOMETRY ON BATTERY PERFORMANCE

4.2.1. State of Charge for Different Electrode Geometries. First, to investigate the impact of microlattice structure on battery performance, three different 3D lattice architectures were considered because they can be fabricated by 3D printing techniques [21, 60]. The schematics of the unit cells of these structures are shown in Figure. 3(a). The first unit cell was formed by diagonally joining the corners of an octahedron without the horizontal elements; it was identified as the "X-structure" (same as the micro-lattice electrode in Figure. 1(d)). The second unit cell was constructed by solid square prisms perpendicular to each other in x, y, and z directions (i.e., "cubic-structure"). The third unit cell was constructed by subtracting a sphere from a solid cube (i.e., "inverse sphere-structure"). To exclude the influence of mass, the investigated structures were manipulated to be identical in mass in the same-sized box (330 μm × 330 μm × 305 μm). As shown in Figures. 3(b) and 3(c), the specific capacities of the X-s and the cubic-structure at 0.5 C discharge capacity were similar (at approx. 190 mAh/g), while the specific capacity for the

inverse sphere-structured electrode was lower (approx. 146 mAh/g). At a discharge current of 0.5 C and 0.8 C, the capacity of the cubic-structure was 1.8% and 2.2% higher than that of the X-structure, and the capacity of the inverse sphere-structure was 24.1% and 36.4% lower than that of the X-structure, respectively. This large difference in discharge capacity was attributed to the non-uniform distribution of lithium ions in these three structures, as shown in Figure. 3(d). It can be seen that at 0.02 V, the ranges of SOC in both the X- and the cubic-structure were 0.7~0.9, with a low SOC gradient. In the inverse sphere-structure, the SOC range increased and reached 0.54~0.68 (max), indicating low efficiency in material utilization.

4.2.2. Impact of Micro-lattice Structures on Species Transport. In the X- and cubic-structure, SOC reaches its maximum value at the separator/electrode interface and then gradually decreases towards the electrode/collector interface. In case of the inverse sphere-structure, however, the maximal SOC is seen at the electrode/collector interface, which is opposite to conventional laminated structures where the current is generally higher at the separator side. The observed phenomenon was attributed to the changes in electron and ion transport as a function of electrode geometry. To shed further light on this phenomenon, the spatial and temporal distribution of the lithium concentration were analyzed. They are affected by many factors, including Li ion diffusion in solid and liquid phases and electron transport in the solid phase. For solid phase diffusion, it turns out that the lithium ion diffusion is not the limiting factor in determining battery performance. When the Li ion diffusivity (D) in the solid phase is increased by a factor of 10, the battery capacity remains almost the same as the original D (D=2.5×10^{-15} m^{2}s^{-1}) (See Figures. S1 and S2). This indicates

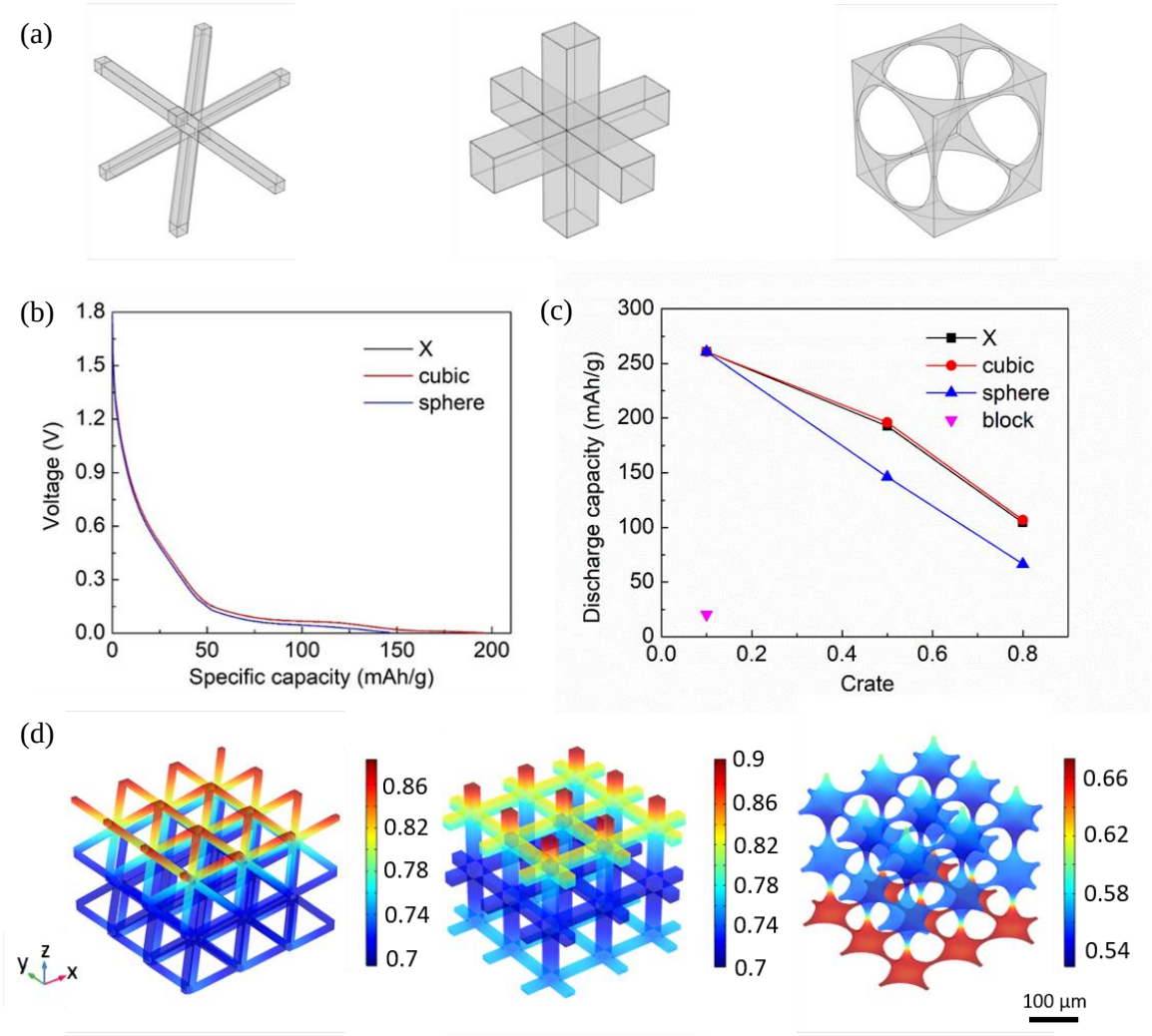

Figure 3. Comparison between three different lattice structures. (a) Unit cell of X-structure (left), cubic-structure (center), and inverse sphere-structure (right), (b) discharge voltage profile at 0.5 C, (c) discharge capacity at 0.1 C, 0.5 C, and 0.8 C, (d) spatial SOC distribution at the end of discharge.

that Li ion diffusivity is relatively large and not a limiting factor in the diffusion processes. It is thus concluded that Li ion diffusion in the liquid phase and electron transport in the solid phase are the two primary factors affecting the electrochemical processes through the 3D lattice structures. As shown in Figure. 1(b), electron transport occurs from the current

collector side to the separator side of the electrode so that the solid phase potential gradually increases from bottom to top. Meanwhile, Li ions diffuse from the separator to cathode section, decreasing the electrolyte concentration from top to bottom. According to Eq. (10), the intercalation flux is affected by electrolyte concentration and electric potential, which eventually affect lithium distribution and SOC.

The temporal evolution of the spatial distribution of SOC, electrolyte concentration, and solid phase potential in X- and inverse sphere-structures are plotted in Figure. 4(a) and Figure. 4(b), respectively. It can be seen that in the X-structure, at 0 s, both the electrolyte and solid phase potential gradients are very small (3.55 mol/L and 0.01 V), having a negligible impact on SOC distribution. Therefore, the maximal SOC is located at both the top and bottom side. However, the impact of electrolyte concentration becomes overwhelming as time evolves. As a result, the maximum SOC is distributed only at the top side at the end of the discharge. However, in the inverse sphere-structure (Figure. 4(b)), the difference of solid phase potential is larger than that in the X-structure (approx. 0.04 V from 0 s to 3900 s), while the electrolyte concentration gradient is almost the same for both. Therefore, the effect of the solid phase potential is dominant with respect to SOC distribution during the entire discharge process, and SOC is always maximal at the bottom. This significant potential gradient was attributed to the characteristic geometry of the electrodes. The comparison of potential gradients of the three structures is shown in Figure. 4(c). It can be seen that crosslinks or bottlenecks in the structures, such as the intersection of hexagonal prisms in the X-structure, the cubic column in the *z*-direction in the cubic-structure, and the thinnest part at the column in the sphere-structure, often occupy a larger potential gradient because the electron transport is impeded. The largest gradient of the

solid phase potential in the sphere-structure is about 1000 V/m, which is nearly 10 times that of the gradient in the other two geometries, indicating a severe limitation in electron transport caused by the geometry.

4.2.3. Mechanisms of Electron and Ion Transport. To further understand the coupled physics of ion and electron transport in the solid and liquid phase, the individual transport phenomena were analyzed by decoupling them and obtaining the effective diffusivity for each. The diffusion and conduction in the solid and liquid were examined by the ratio of effective diffusion coefficient or conductivity to the material diffusion coefficient or conductivity, which are expressed as p_s^{eff}, q_s^{eff}, p_2^{eff}, q_2^{eff} and defined as:

$$p_s^{eff} = \frac{D_{s,p}^{eff}}{D_{s,p}}$$

$$q_s^{eff} = \frac{K_{s,p}^{eff}}{K_{s,p}}$$

$$p_2^{eff} = \frac{D_2^{eff}}{D_2}$$

$$q_2^{eff} = \frac{K_2^{eff}}{K_2} \tag{13}$$

in which $D_{s,p}^{eff}$ is the effective solid phase diffusion coefficient which is evaluated using an equivalent model of one particle. The surface Li ion concentration gradient in the one particle model is matched with that in 3D model. $K_{s,p}^{eff}$, D_2^{eff} and K_2^{eff} are the effective solid phase conductivity, effective liquid phase diffusion coefficient, and effective liquid phase conductivity, respectively, which were evaluated in a 1D model with corresponding individual physics of Li ion diffusion or electron transport. The final effective transport properties were obtained when the gradient of Li ion concentration was matched with that

in a 3D model of the same physics. In particular, for the electrolyte, the relative characteristic times of electrolyte transport in relation to the discharge time, S_s, was analyzed further [47]:

$$S_s = \frac{\left(l_{sep} + l_{pos}\right)^2 I}{D_2 p_2^{eff} F \varepsilon_p c_{\max,pos} l_{pos}} \tag{14}$$

where l_{sep} and l_{pos} are the thickness of separator and positive electrode, respectively. I is the applied current density, D_2 is the electrolyte diffusion coefficient, and p_2^{eff} is the ratio of effective diffusion coefficient to the electrolyte diffusion coefficient given above. Note that the solid phase diffusion time is not considered as it is not a limiting factor as explained earlier.

As shown in Figures. 4(d) and 4(e), initially the values of p_s^{eff} exhibited almost no differences between different geometries, because $D_{s,p}^{eff}$ is mainly determined by the particle radius. If the flux is same, there is no critical difference inside single particles within an electrode. However, the values of $q_{s,p}^{eff}$ were 1, 0.035, 0.041, and 0.014 for block, cubic-, X-, and inverse sphere-structures respectively, indicating that 3D structures reduced electron transport in the solid phase compared with traditional laminated structures. This can be attributed to the reduction in solid phase by the 3D structures, leading to a reduction in path length for electron transport. In particular, the inverse-sphere structure showed a significant reduction, which can explain the phenomenon shown in Figures. 4(b) and (c).

On the other hand, the values of p_2^{eff} and q_2^{eff} were very similar between all three 3D geometries. Both were much larger than those of the block structure, indicating that 3D structures are effective in improving the species transport in the liquid phase. Unlike conduction in the solid phase, the removal of material to form a 3D structure enhanced the

transport in the liquid phase. As a result, S_s decreased from 16 in block structures to ~2.5 in 3D structures, indicating significantly improved Li ion diffusion, which makes the Li diffusion as a less-limiting factor compared to the electron transport (Figure. 4(f)).

4.3. OPTIMIZED ELECTRODE DESIGNS

4.3.1. Cubic-structured Electrodes. To obtain optimal electrode designs, we investigated the effect of different micro-lattice geometric parameters on the electrochemical performance of batteries. There are two factors determining the macro-scale porosity in the cubic structure: column width and distances between the columns. First, different column widths were investigated: 0.5 *w*, 0.75 *w*, 1 *w*, and 1.25 *w* (*w*=20.12 μm) (Figure. 5(a)). As shown in Figure. 5(b), as the column width increased, the SOC distribution became non-uniform and the electrode volume utilization decreased. Further investigation of the effect of column width on electrolyte concentration and solid phase potential showed that the concentration gradient of the electrolyte increased with a wider column. On the other hand, solid phase potential gradually decreased while the column width increased, see Figure. 5(b). This was attributed to the positive effect of the wider column on electron transport (as shown in Figure. 5(e)). Overall it was determined that electron transport was a main limiting factor in the case of 0.5 *w* width, and that the electrolyte concentration contributed more with increasing column width to become

(a) X-structure

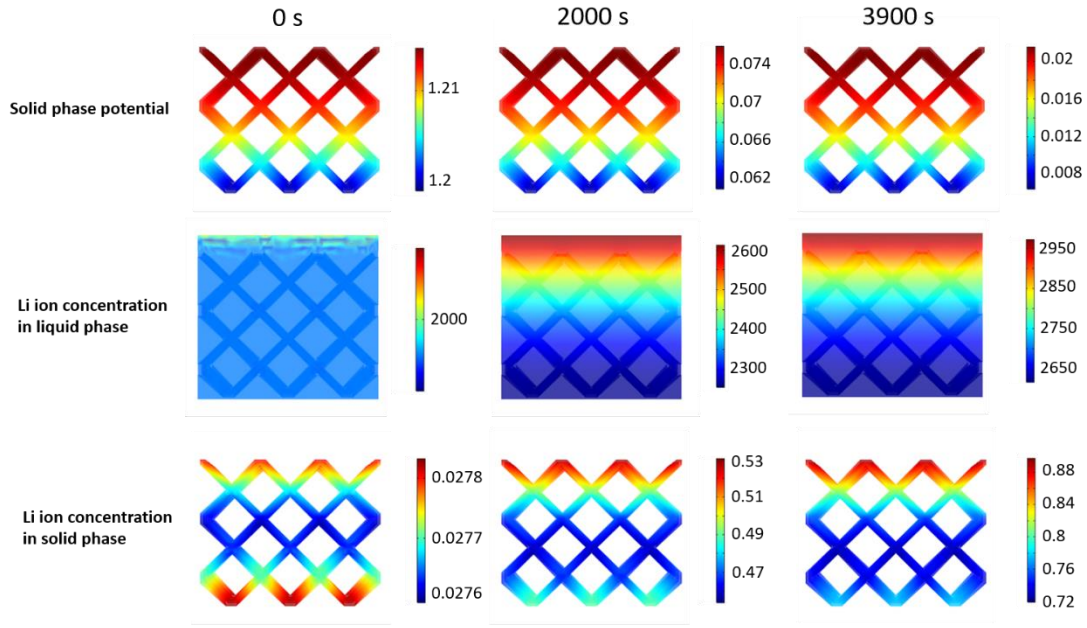

(b) Inverse sphere structure

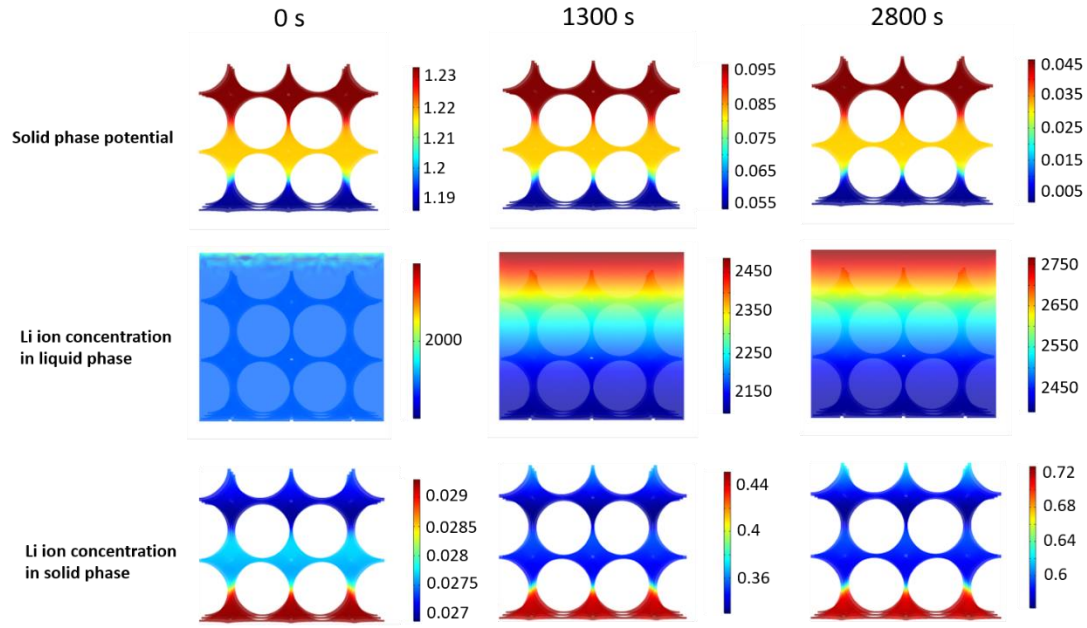

Figure 4. Temporal distribution of solid phase potential, Li ion concentration in the liquid phase and solid phase. (a) X-structure at 0 s, 2000 s, and 3900 s, and (b) inverse sphere-structure at 0 s, 1300 s, and 2800 s; Effect of geometry (c) The distribution of the gradient of solid phase potential in Z direction (V/m) at the end of the discharge process, (d) p_s^{eff} and q_s^{eff} , (e) p_2^{eff} and q_2^{eff} and (f) S_s of different structures.

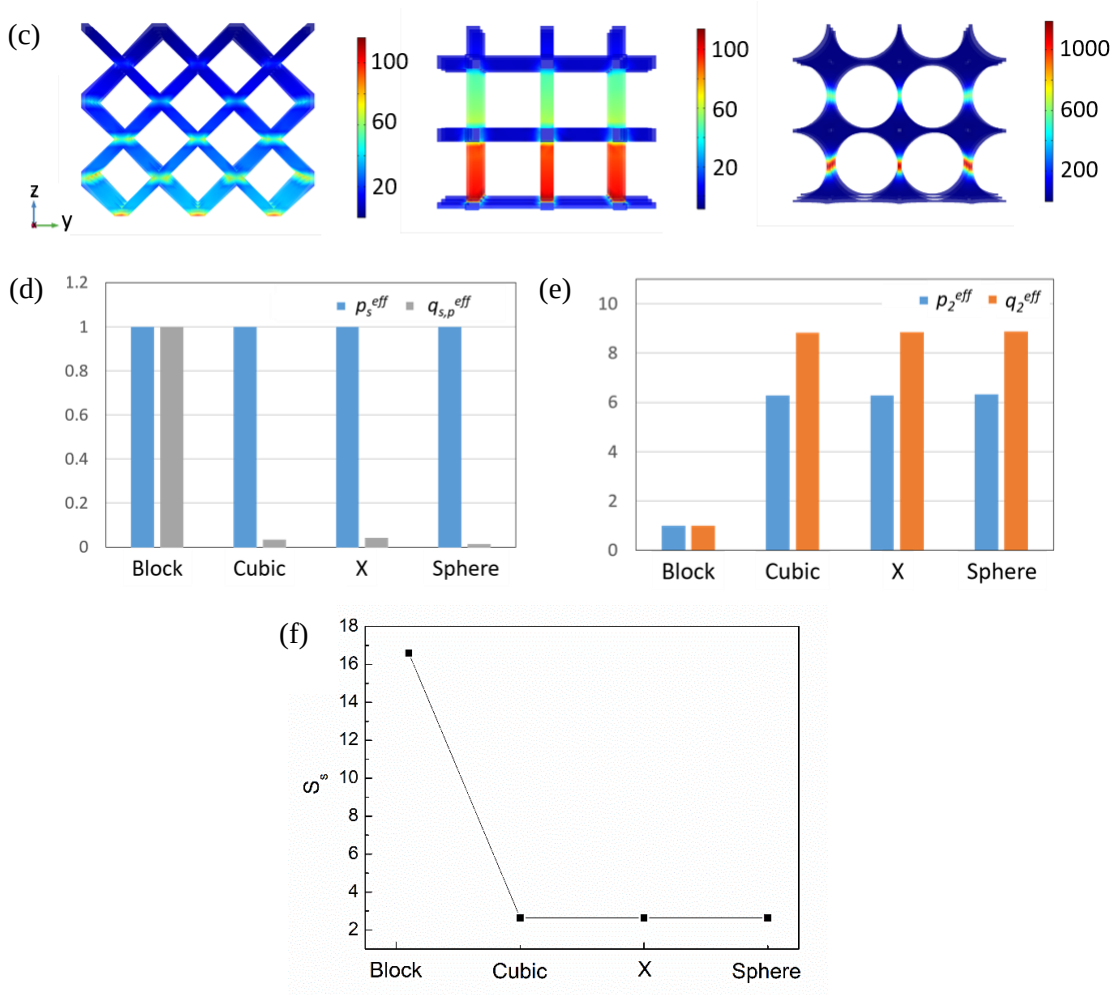

Figure 4. Temporal distribution of solid phase potential, Li ion concentration in the liquid phase and solid phase. (a) X-structure at 0 s, 2000 s, and 3900 s, and (b) inverse sphere-structure at 0 s, 1300 s, and 2800 s; Effect of geometry (c) The distribution of the gradient of solid phase potential in Z direction (V/m) at the end of the discharge process, (d) p_s^{eff} and q_s^{eff} , (e) p_2^{eff} and q_2^{eff} and (f) S_s of different structures. (Cont.)

dominant in the cases of 1 *w* and 1.25 *w*. Based on the above analysis, the increased areal flux is the primary reason for a more non-uniform distribution of SOC in cubic structures with wider columns compared to those with slender columns. As a result, the specific capacity decreased as the column width increased (Figure. 5(c)).

Areal capacity is another key performance attribute that needs to be considered in electrode design, as it characterizes the electrode's energy density. Although specific capacity decreased with column width, the total mass of the electrode increased as a result of denser packing of active material, leading to increased total capacity. This increase, however, tapered off at widths wider than 20 μm as seen in Figure. 5(d) (note that the projected areas of the electrodes are identical). As the specific capacity and areal capacity exhibited a trade-off in this case, the optimal value of column width needs to be chosen according to the target property of the electrode design. The characteristic transport properties are also illustrated in Figure. 5(e), (f), and (g). It is seen that the increase in column width enhanced electron transport in the solid phase. However, it also impeded species transport in the electrolyte (p_2^{eff} and q_2^{eff} decreased and S_s increased).

Next, the effect of the change in distance between columns in cubic structures on battery electrochemical performance was investigated. The column distance was manipulated by changing the number of columns in a unit cell from 2 to 5, as shown in Figure. 6(a). It can be seen in Figure. 6(b) that the solid phase potential difference for all numbers of column were around 0.009 V, indicating that the change in the number of columns has little impact on electron transport. On the other hand, the electrolyte concentration gradient increased as the number of columns increased because of the increase in flux at the current collector/cathode interface. Consequently, the electrolyte concentration became determining as the number of columns in the unit cell increased from 3 to 5. Because of the larger electrolyte concentration gradient, the SOC gradient increased for larger numbers of columns per unit cell, leading to a lower specific capacity, as shown

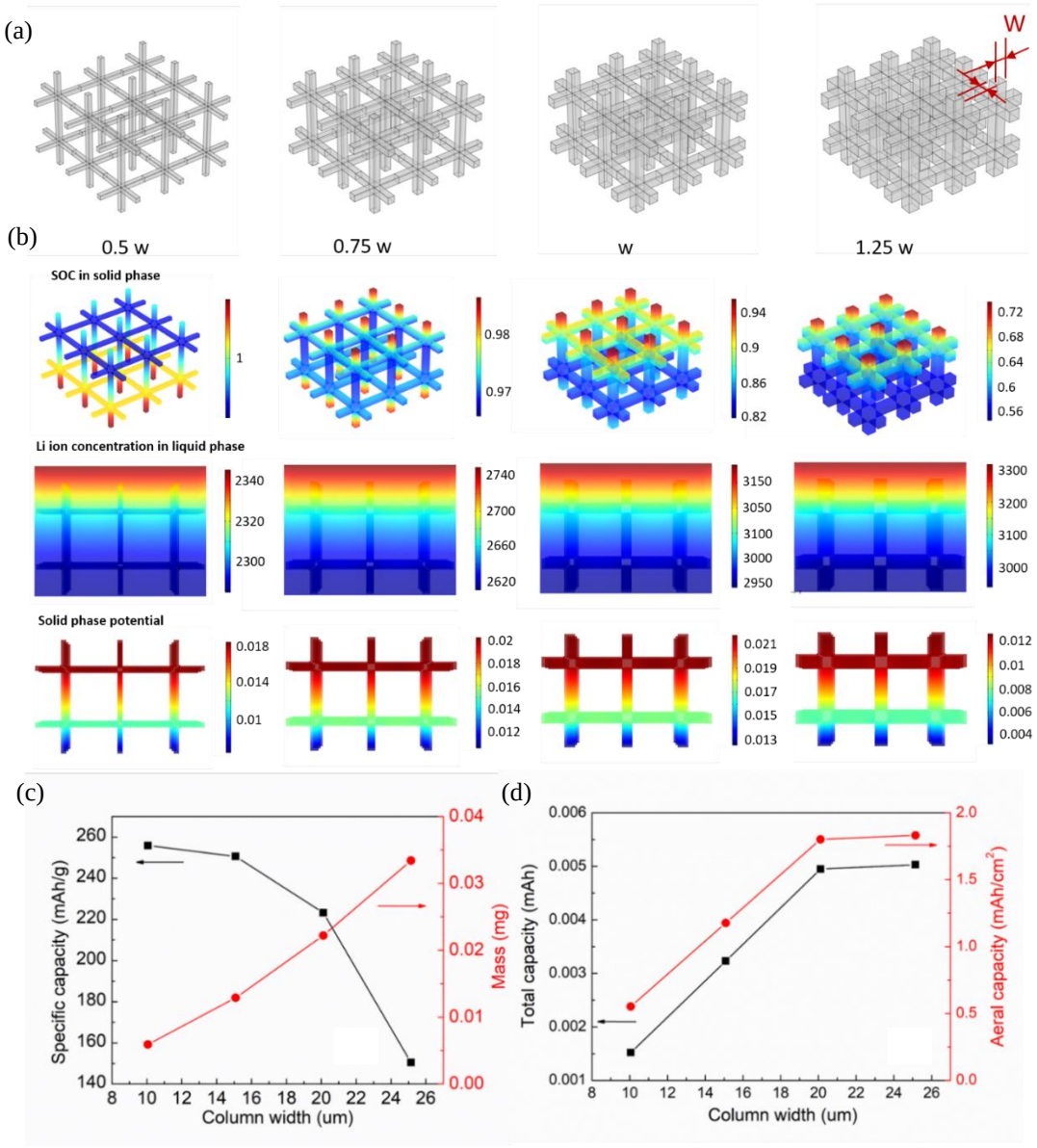

Figure 5. Effect of column width in cubic structures (a) Schematics of different cubic structures with different column widths, (b) distribution of SOC, electrolyte concentration, and solid phase potential at the end of the discharge in cubic structures with different column width. (c, d) Specific capacity and total mass, and total capacity and areal capacity, (e, f, g) p_s^{eff}, q_s^{eff}, p_2^{eff}, q_2^{eff} and S_s, as functions of column width in the cubic structure.

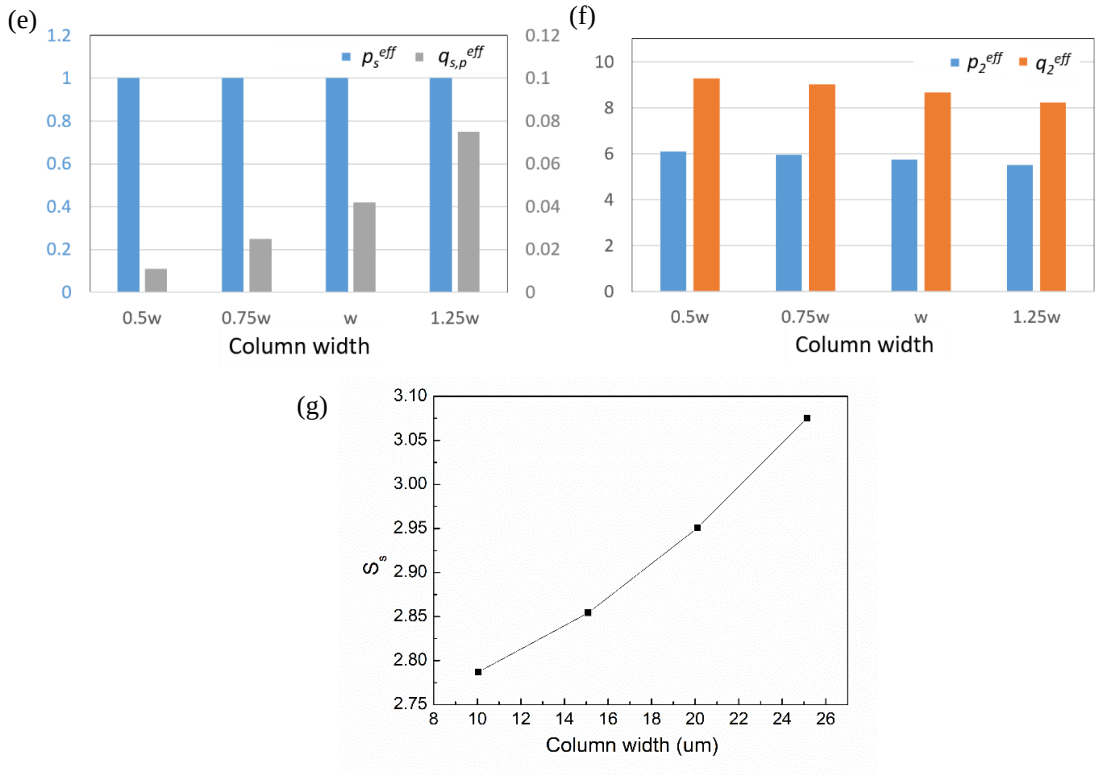

Figure 5. Effect of column width in cubic structures (a) Schematics of different cubic structures with different column widths, (b) distribution of SOC, electrolyte concentration, and solid phase potential at the end of the discharge in cubic structures with different column width. (c, d) Specific capacity and total mass, and total capacity and areal capacity, (e, f, g) p_s^{eff}, q_s^{eff}, p_2^{eff}, q_2^{eff} and S_s, as functions of column width in the cubic structure. (Cont.)

in Figure. 6(c). When the number of columns per cell number exceeded 4, the current density became too large for the electrode to reach a uniform distribution of lithium ion in the electrolyte as a result of limited ion conductivity. The efficiency of material utilization was reduced, leading to a low specific capacity, which further decreased the total capacity and areal capacity (Figure. 6(d)). The effect of number of columns on characteristic transport properties mirrors that of the number of columns, namely, the electron transport

in the solid phase was improved and species transport in electrolyte was reduced (Figure. 6(e), (f), and (g)).

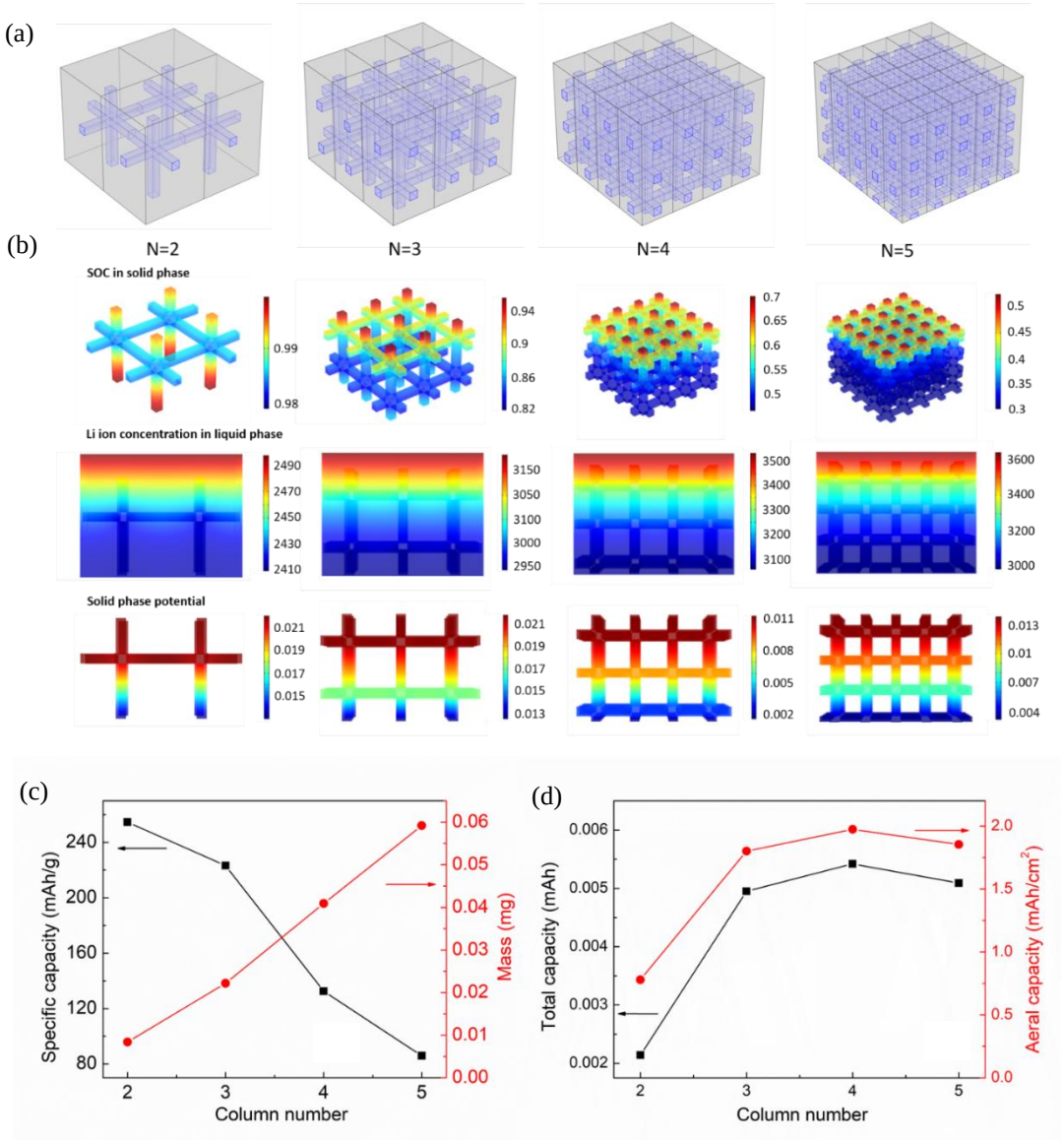

Figure 6. Effect of number of columns in cubic structures. (a) Schematic of cubic structure with different numbers of columns, (b) distribution of SOC, electrolyte concentration, and solid phase potential at the end of the discharge in cubic structures with different numbers of columns. (c, d) Specific capacity, total mass, total capacity, and areal capacity, (e, f, g) p_s^{eff}, q_s^{eff}, p_2^{eff}, q_2^{eff}, and S_s as functions of number of columns in cubic structures.

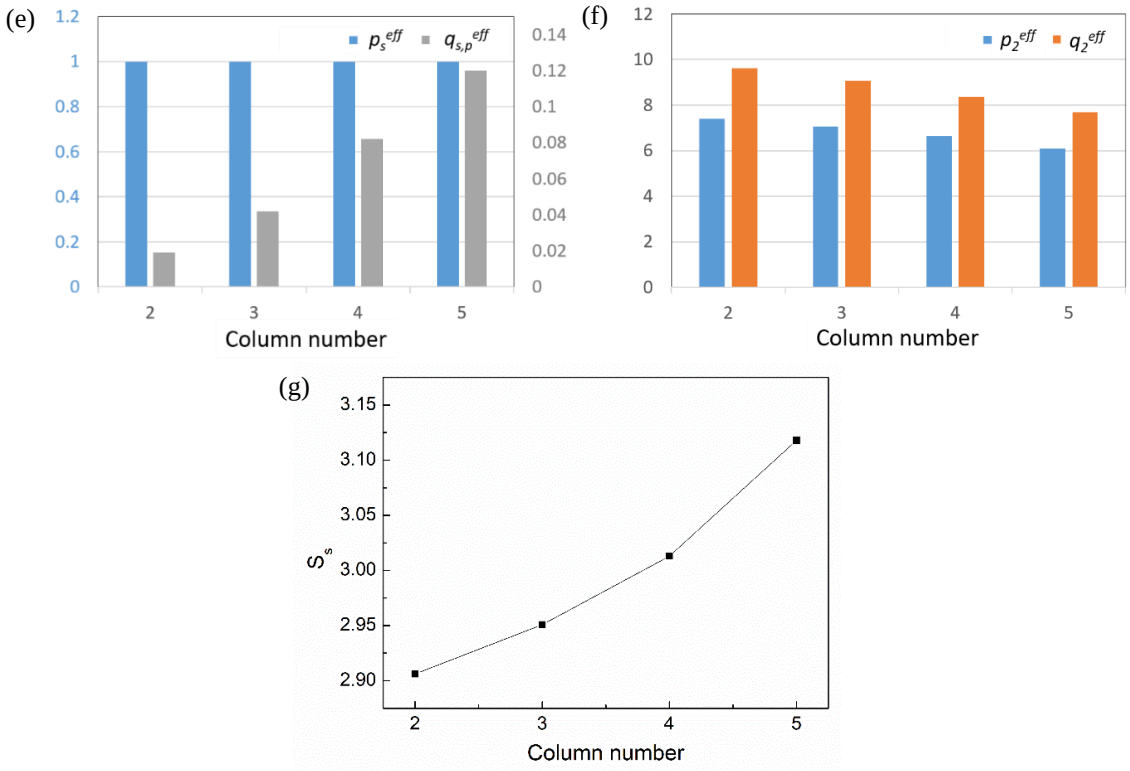

Figure 6. Effect of number of columns in cubic structures. (a) Schematic of cubic structure with different numbers of columns, (b) distribution of SOC, electrolyte concentration, and solid phase potential at the end of the discharge in cubic structures with different numbers of columns. (c, d) Specific capacity, total mass, total capacity, and areal capacity, (e, f, g) p_s^{eff}, q_s^{eff}, p_2^{eff}, q_2^{eff}, and S_s as functions of number of columns in cubic structures. (Cont.)

4.3.2. Inverse Sphere-structured Electrodes. The unit cell of the inverse sphere structure was constructed by subtracting a sphere from a cube, forming a bottleneck formed at the half-height of the unit cell. The effect of the bottleneck width was studied by changing the radius of the subtracted sphere, as shown in Figure. 7(a). It can be observed that the maximum SOC was located at both the bottom and top in the sample with a bottleneck width of 1 *w* (5.96 µm) (1st figure on the left) and at the top only for bottleneck widths of 5/3 *w* (9.43 µm), 7/3 *w* (13.21 µm), and 3 *w* (16.98 µm) (2nd, 3rd, and 4th figure

from left to right), indicating that the bottleneck was switching from electron transport limit in the solid phase to lithium ion diffusion limit in electrolyte. This result was consistent with those observed for the X-structure and the cubic-structure. However, because in inverse sphere structures the competing effects of specific capacity and total mass are much more evident, their areal capacity does not always increase with bottleneck width. The structure with a bottleneck size of 13.21 μm exhibited lower areal capacity than the structure with a 9.43 μm bottleneck. As shown in Figures. 7(e), (f), and (g), with increasing bottleneck width, electron transport in the solid phase was promoted significantly, while liquid phase diffusivity and conductivity were reduced.

These results showed that inverse sphere structures affected charge transport to a higher degree than the other two structures. This effect was further demonstrated when the number of columns in sphere-structures was investigated. As shown in Figure. 8(b), the solid phase potential decreased from ~0.05 V to ~0.02 V as the number of columns increased, while it was almost constant in cubic-structures (approx. 0.009 V), and exhibited only slight changes in the X-structure (from ~0.014 V to ~0.012 V). Because the bottleneck significantly restricts charge transport, the benefit of an increased bottleneck width is evident. This larger change in solid phase potential had a major effect on SOC distribution; in structures with 2 and 3 columns, the solid phase potential was the main barrier to a uniform distribution. Because the solid phase potential decreased with increasing number of columns, the SOC gradient also decreased from N=2 to N=3. Consequently, the maximum specific capacity was achieved for N=3 (Figure. 8(d)). Areal capacity was decreased with increased tap density in structures with higher numbers of columns and reached its maximum at N=4. The effect of the number of columns on species transport

was not as significant as that of bottleneck width; however, the effects of bottleneck width and number of columns on species transport were similar (Figure. 8(e), (f) and (g)).

4.4. POROSITY AND ELECTRODE THICKNESS

Two additional controllable parameters in electrode manufacture are thickness and porosity of the electrodes. The overall electrode thickness can be tailored by controlling the amount of electrode material dispensed during 3D printing. The porosity of the 3D electrodes [21] has a two-level hierarchical structure (i.e. micro and macro-scale porosity). The macro-scale porosity points to the spaces between truss members of the 3D structure, which is in the tens of micrometers. It is treated as a pure electrolyte phase. The micro-level pore structure is the internal porosity within the truss members and is determined by the sintering conditions and is of the order of one micrometer or less. The porosity used this section refer to the internal porosity within the truss members. Figure 8 shows the specific capacity and areal capacity of the three investigated structures with different thicknesses and levels of porosity.

Figures 9(a), 9(b), and 9(c) show that the specific capacity of all the structures decreased as the thickness and solid phase volume fraction (VF) increased. This was attributed to the fact that thicker and denser structures will limit the transport of lithium ions in the electrolyte. However, a thicker and denser structure also means more active material per unit area – in other words, a larger total electrode mass. Figures 9(d), 9(e), and 9(f) show that the changes in areal capacity are different with increasing electrode thickness and solid phase volume fraction for the three different structures. In a low solid phase

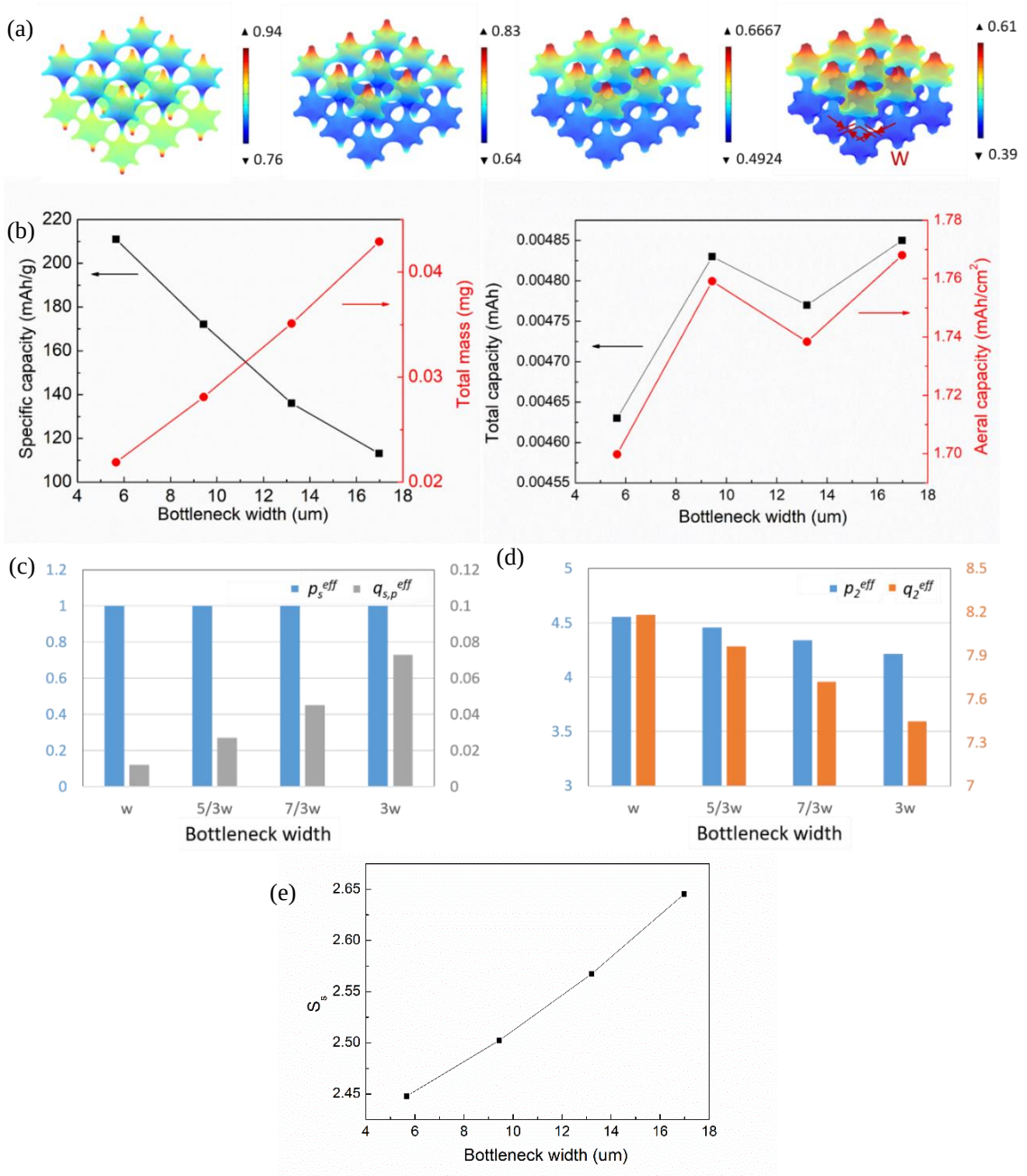

Figure 7. Effect of bottleneck width in inverse sphere structures. (a) Schematic of inverse sphere structure with different bottleneck widths, (b) Specific capacity, total mass, total capacity, and areal capacity, (c,d) p_s^{eff}, q_s^{eff}, p_2^{eff}, q_2^{eff}, and (e) S_s as functions of bottleneck width in inverse sphere structures.

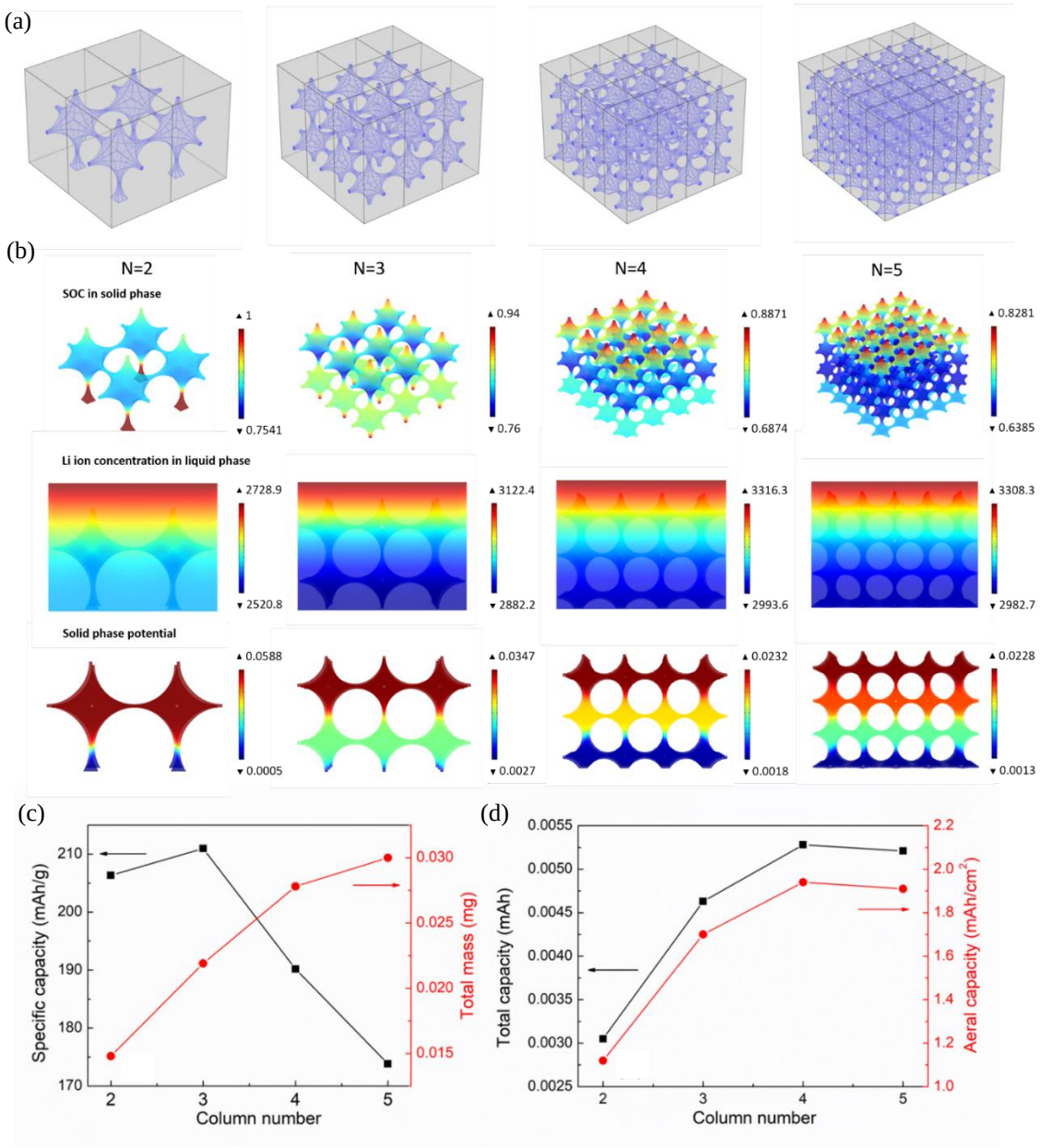

Figure 8. Effect of number of columns in inverse sphere structures. (a) Schematic of inverse sphere structures with different numbers of columns per unit length, (b) distribution of SOC, electrolyte concentration, and solid phase potential at the end of the discharge in sphere structures with different numbers of columns, (c) specific capacity and total mass, (d) total capacity and areal capacity (e, f, g) p_s^{eff}, q_s^{eff}, p_2^{eff}, q_2^{eff} and S_s as functions of number of columns.

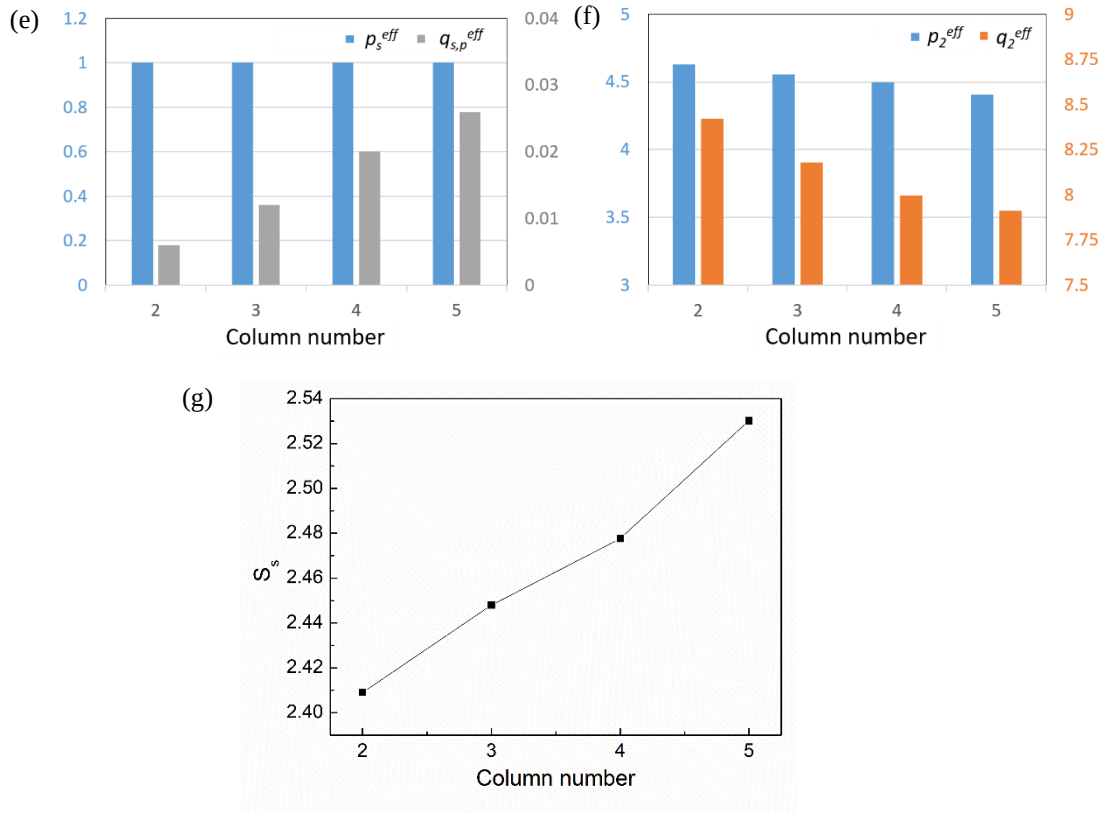

Figure 8. Effect of number of columns in inverse sphere structures. (a) Schematic of inverse sphere structures with different numbers of columns per unit length, (b) distribution of SOC, electrolyte concentration, and solid phase potential at the end of the discharge in sphere structures with different numbers of columns, (c) specific capacity and total mass, (d) total capacity and areal capacity (e, f, g) p_s^{eff}, q_s^{eff}, p_2^{eff} , q_2^{eff} and S_s as functions of number of columns. (Cont.)

volume (VF = 0.2), the effect of thickness was negligible because the large volume fraction of the electrolyte allowed sufficient diffusion of Li ions. In a high solid phase volume fraction (VF = 0.6), increasing thickness caused inefficient diffusion, leading to a decrease in both specific capacity and areal capacity. According to the simulation results shown in Figure. 9, the optimal parameters to obtain both high specific energy and high areal capacity, X-structure electrodes should have a thickness of 450 μm and VF = 0.2, cubic-

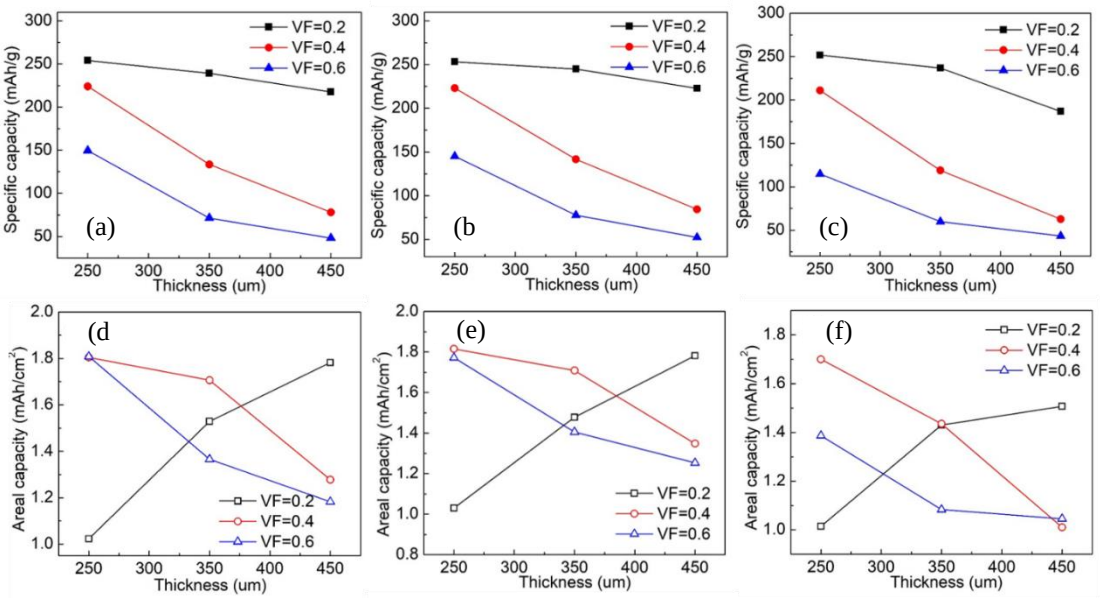

Figure 9. Effect of thickness and solid phase volume fraction (VF): specific capacity (0.5 C) of (a) X-, (b) cubic-, (c) inverse sphere-structured electrodes as a function of thickness and solid phase volume fraction (VF); areal capacity of (d) X-, (e) cubic-, (f) sphere-structured electrodes as a function of thickness and solid phase volume fraction.

structure electrodes should have a thickness of 250 μm and VF = 0.4, and sphere-structure electrodes should have a thickness of 250 μm and VF = 0.4.

5. CONCLUSIONS

We carried out an exhaustive study of the effect of 3-dimensional (3D) electrode architectures on the electrochemical performance of batteries and used the gained knowledge to determine optimized electrode structures (anodes and cathodes) for maximum areal and specific capacity. A 3-dimensional full-order electrochemical model, validated by Aerosol Jet printed open octahedral micro-lattice 3D electrodes with a two-

level porosity, was used for this analysis. The impact of the electrode geometry was studied by comparing the electrochemical response of electrodes with block-, X-, cubic-structure, and a structure formed by subtracting spheres from a solid block (called 'sphere-structure'). The study revealed that:

i) The primary reason for the superior performance of batteries with 3D electrode architectures is the fact that 3D structures facilitate species transport in the liquid phase. In addition, the main factors affecting battery performance are ion diffusion in the electrolyte and electron transport in the 3D electrode skeleton.

ii) In 3D electrode architectures, the competition between available volume for intercalation and an easier diffusion path for ion and electron transport determines areal/total and specific capacity. Because of this competition, the maximum benefits of a 3D architecture are realized when the length of the structures' truss members is of the order of the diffusion length for the ions in the electrode (~15-20 μm in the current study). In structures with truss members smaller than this scale, the total/areal capacity is too low and discharge rates are too high (undesirable for a battery). At larger length scales, the specific capacity is too low as a result of the increasing difficulty for ion transport through the liquid.

iii) Of the structures studied here, the X- and cubic-structured electrodes demonstrated a larger capacity (35% higher at 0.5C) than the inverse sphere-structured electrodes as a result of more efficient electron transport enabled specifically by the change in electrode geometry. The optimized parameters for these structures for a compromised high specific energy and high areal capacity were a thickness of 450 μm and a volume

fraction (VF) of 0.2, a thickness of 250 μm and VF of 0.4, and a thickness of 250 μm and VF of 0.4 for the X-structure, cubic-structure, and sphere-structured electrodes.

iv) If the electrode porosity is reduced, an insufficient diffusion of Li ions in the electrolyte causes a decrease in the electrode capacity even if the electrode volume increases. This was seen in cubic- and X-structured electrodes, where the specific capacity of 3D electrodes decreased with increasing column width and number (columns per unit length). This effect, however, becomes secondary when a bottleneck width emerges in the electrode structure which can impede electron transport through the electrode.

v) The requirement that the length scale of the truss members of optimum 3D architectures be of the order of tens of micrometers limits the availability of manufacturing methods to techniques such as aerosol jet, extrusion, or inkjet 3D printing.

REFERENCES

1. Padhi, A.K., K.S. Nanjundaswamy, and J.B. Goodenough, Phospho-olivines as positive-electrode materials for rechargeable lithium batteries. Journal of the electrochemical society, 1997. **144**(4): p. 1188-1194.

2. Goodenough, J., A. Manthiram, and B. Wnetrzewski, Electrodes for lithium batteries. Journal of power sources, 1993. **43**(1-3): p. 269-275.

3. Hu, J., et al., 3D-printed cathodes of LiMn1− xFexPO4 nanocrystals achieve both ultrahigh rate and high capacity for advanced lithium-ion battery. Advanced Energy Materials, 2016. **6**(18): p. 1600856.

4. Wei, T.S., et al., 3D printing of customized li-ion batteries with thick electrodes. Advanced Materials, 2018. **30**(16): p. 1703027.

5. Chen, L., et al., 3D printing of artificial leaf with tunable hierarchical porosity for CO2 photoreduction. Chemistry of Materials, 2018. **30**(3): p. 799-806.

6. Long, J.W., et al., Three-dimensional battery architectures. Chemical Reviews, 2004. **104**(10): p. 4463-4492.

7. Sun, K., et al., 3D printing of interdigitated Li-Ion microbattery architectures. Advanced materials, 2013. **25**(33): p. 4539-4543.

8. Fu, K., et al., Graphene oxide-based electrode inks for 3D-printed lithium-ion batteries. Advanced Materials, 2016. **28**(13): p. 2587-2594.

9. Li, J., et al., A hybrid three-dimensionally structured electrode for lithium-ion batteries via 3D printing. Materials & Design, 2017. **119**: p. 417-424.

10. Rocha, V.G., et al., Multimaterial 3D printing of graphene-based electrodes for electrochemical energy storage using thermoresponsive inks. ACS applied materials & interfaces, 2017. **9**(42): p. 37136-37145.

11. Cao, D., et al., 3D Printed High-Performance Lithium Metal Microbatteries Enabled by Nanocellulose. Advanced Materials, 2019. **31**(14): p. 1807313.

12. Liu, C., et al., Fabrication and Characterization of 3D-Printed Highly-Porous 3D LiFePO4 Electrodes by Low Temperature Direct Writing Process. Materials, 2017. **10**(8): p. 934.

13. Liu, C., et al., High mass loading ultrathick porous Li4Ti5O12 electrodes with improved areal capacity fabricated via low temperature direct writing. Electrochimica Acta, 2019. **314**: p. 81-88.

14. Liu, C., et al., Comparative study on the electrochemical performance of LiFePO4 cathodes fabricated by low temperature 3D printing, direct ink writing and conventional roller coating process. Ceramics International, 2019. **45**(11): p. 14188-14197.

15. Yan, B., et al., Three dimensional simulation of galvanostatic discharge of LiCoO2 cathode based on X-ray nano-CT images. Journal of The Electrochemical Society, 2012. **159**(10): p. A1604-A1614.

16. Kim, D.H., et al., Epidermal Electronics. Science, 2011. **333**(6044): p. 838-843.

17. Pikul, J.H., et al., High-power lithium ion microbatteries from interdigitated three-dimensional bicontinuous nanoporous electrodes. Nature communications, 2013. **4**: p. 1732.

18. Li, X., et al., Mesoporous silicon sponge as an anti-pulverization structure for high-performance lithium-ion battery anodes. Nature communications, 2014. **5**.

19. Xu, C., et al., Three-dimensional Au microlattices as positive electrodes for Li–O2 batteries. ACS nano, 2015. **9**(6): p. 5876-5883.

20. Schaedler, T.A., et al., Ultralight metallic microlattices. Science, 2011. **334**(6058): p. 962-965.

21. Saleh, M.S., et al., 3D printed hierarchically-porous microlattice electrode materials for exceptionally high specific capacity and areal capacity lithium ion batteries. Additive Manufacturing, 2018. **23**: p. 70-78.

22. Saleh, M.S., C. Hu, and R. Panat, Three-dimensional microarchitected materials and devices using nanoparticle assembly by pointwise spatial printing. Science Advances, 2017. **3**(3): p. e1601986.

23. Sukeshini, A., et al., Aerosol jet printing and microstructure of SOFC electrolyte and cathode layers. ECS Transactions, 2011. **35**(1): p. 2151-2160.

24. Goth, C., S. Putzo, and J. Franke. Aerosol Jet printing on rapid prototyping materials for fine pitch electronic applications. in 2011 IEEE 61st Electronic Components and Technology Conference (ECTC). 2011. IEEE.

25. Huang, X., et al., Ultrahigh Rate Capabilities of Lithium-Ion Batteries from 3D Ordered Hierarchically Porous Electrodes with Entrapped Active Nanoparticles Configuration. Advanced materials, 2014. **26**(8): p. 1296-1303.

26. Zhang, L., et al., High-performance hybrid supercapacitor with 3D hierarchical porous flower-like layered double hydroxide grown on nickel foam as binder-free electrode. Journal of Power Sources, 2016. **318**: p. 76-85.

27. Min, M., et al., Hydrous RuO2/carbon black nanocomposites with 3D porous structure by novel incipient wetness method for supercapacitors. Journal of The Electrochemical Society, 2006. **153**(2): p. A334-A338.

28. Ren, Y., L.J. Hardwick, and P.G. Bruce, Lithium intercalation into mesoporous anatase with an ordered 3D pore structure. Angewandte Chemie International Edition, 2010. **49**(14): p. 2570-2574.

29. Vu, A., Y. Qian, and A. Stein, Porous Electrode Materials for Lithium-Ion Batteries – How to Prepare Them and What Makes Them Special. Advanced Energy Materials, 2012. **2**(9): p. 1056-1085.

30. Ke, F.-S., et al., Electroplating synthesis and electrochemical properties of macroporous Sn–Cu alloy electrode for lithium-ion batteries. Electrochimica Acta, 2007. **52**(24): p. 6741-6747.

31. Sorensen, E.M., et al., Three-Dimensionally Ordered Macroporous Li4Ti5O12: Effect of Wall Structure on Electrochemical Properties. Chemistry of Materials, 2006. **18**(2): p. 482-489.

32. Saravanan, K., K. Ananthanarayanan, and P. Balaya, Mesoporous TiO2 with high packing density for superior lithium storage. Energy & Environmental Science, 2010. **3**(7): p. 939-948.

33. Dong, W., J.S. Sakamoto, and B. Dunn, Electrochemical properties of vanadium oxide aerogels. Science and Technology of Advanced Materials, 2003. **4**(1): p. 3-11.

34. Wang, D., et al., Synthesis and Li-ion insertion properties of highly crystalline mesoporous rutile TiO2. Chemistry of Materials, 2008. **20**(10): p. 3435-3442.

35. Ren, Y., et al., Influence of size on the rate of mesoporous electrodes for lithium batteries. Journal of the American Chemical Society, 2009. **132**(3): p. 996-1004.

36. Liu, H., et al., Highly ordered mesoporous NiO anode material for lithium ion batteries with an excellent electrochemical performance. Journal of Materials Chemistry, 2011. **21**(9): p. 3046-3052.

37. Jiang, C., et al., Preparation and rate capability of Li4Ti5O12 hollow-sphere anode material. Journal of Power Sources, 2007. **166**(2): p. 514-518.

38. Li, N., et al., Rate Capabilities of Nanostructured LiMn2 O 4 Electrodes in Aqueous Electrolyte. Journal of the electrochemical Society, 2000. **147**(6): p. 2044-2049.

39. Lacey, S.D., et al., Extrusion-Based 3D Printing of Hierarchically Porous Advanced Battery Electrodes. Advanced Materials, 2018. **30**(12): p. 1705651.

40. Li, X., et al., Mesoporous silicon sponge as an anti-pulverization structure for high-performance lithium-ion battery anodes. Nature communications, 2014. **5**: p. 4105.

41. Thorat, I.V., et al., Quantifying tortuosity in porous Li-ion battery materials. Journal of Power Sources, 2009. **188**(2): p. 592-600.

42. Less, G.B., et al., Micro-scale modeling of Li-ion batteries: parameterization and validation. Journal of The Electrochemical Society, 2012. **159**(6): p. A697-A704.

43. Wang, C.-W. and A.M. Sastry, Mesoscale Modeling of a Li-Ion Polymer Cell. Journal of The Electrochemical Society, 2007. **154**(11): p. A1035-A1047.

44. Li, J., et al., Enhanced Battery Performance through Three-Dimensional Structured Electrodes: Experimental and Modeling Study. Journal of The Electrochemical Society, 2018. **165**(14): p. A3566-A3573.

45. Wang, D., et al., Cracking causing cyclic instability of LiFePO4 cathode material. Journal of Power Sources, 2005. **140**(1): p. 125-128.

46. Bhattacharya, S., A.R. Riahi, and A.T. Alpas, A transmission electron microscopy study of crack formation and propagation in electrochemically cycled graphite electrode in lithium-ion cells. Journal of Power Sources, 2011. **196**(20): p. 8719-8727.

47. Wang, H., et al., TEM study of electrochemical cycling-induced damage and disorder in LiCoO2 cathodes for rechargeable lithium batteries. Journal of The Electrochemical Society, 1999. **146**(2): p. 473-480.

48. Yang, F., Interaction between diffusion and chemical stresses. Materials Science and Engineering: A, 2005. **409**(1-2): p. 153-159.

49. Zhang, X., W. Shyy, and A.M. Sastry, Numerical simulation of intercalation-induced stress in Li-ion battery electrode particles. Journal of the Electrochemical Society, 2007. **154**(10): p. A910-A916.

50. Verbrugge, M.W. and Y.-T. Cheng, Stress and strain-energy distributions within diffusion-controlled insertion-electrode particles subjected to periodic potential excitations. Journal of The Electrochemical Society, 2009. **156**(11): p. A927-A937.

51. Renganathan, S., et al., Theoretical analysis of stresses in a lithium ion cell. Journal of the Electrochemical Society, 2010. **157**(2): p. A155-A163.

52. Yang, X.-G., C. Bauer, and C.-Y. Wang, Sinusoidal current and stress evolutions in lithium-ion batteries. Journal of Power Sources, 2016. **327**: p. 414-422.

53. Fu, R., M. Xiao, and S.-Y. Choe, Modeling, validation and analysis of mechanical stress generation and dimension changes of a pouch type high power Li-ion battery. Journal of Power Sources, 2013. **224**: p. 211-224.

54. Oh, K.-Y., et al., A novel phenomenological multi-physics model of Li-ion battery cells. Journal of Power Sources, 2016. **326**: p. 447-458.

55. Sauerteig, D., et al., Electrochemical-mechanical coupled modeling and parameterization of swelling and ionic transport in lithium-ion batteries. Journal of Power Sources, 2018. **378**: p. 235-247.

56. Golmon, S., K. Maute, and M.L. Dunn, Numerical modeling of electrochemical–mechanical interactions in lithium polymer batteries. Computers & Structures, 2009. **87**(23-24): p. 1567-1579.

57. Newman, J. and W. Tiedemann, Porous-electrode theory with battery applications. AIChE Journal, 1975. **21**(1): p. 25-41.

58. Subramanian, V.R., V.D. Diwakar, and D. Tapriyal, Efficient Macro-Micro Scale Coupled Modeling of Batteries. Journal of The Electrochemical Society, 2005. **152**(10): p. A2002-A2008.

59. Ashraf, S. and J. Phirani, Capillary displacement of viscous liquids in a multi-layered porous medium. Soft matter, 2019. **15**(9): p. 2057-2070.

60. Kolan, K.C., et al. Effect of architecture and porosity on mechanical properties of borate glass scaffolds made by selective laser sintering. in Proceedings of the 24th Annual International Solid Freeform Fabrication Symposium. 2013. Austin.

III. STUDY ON HOW ELECTROLYTE CONCENTRATION IMPACTS ON SOLID ELECTROLYTE INTERPHASE (SEI) GROWTH AND LI PLATING IN LIHTIUM ION BATTERIES

ABSTRACT

Tuning salt concentration of electrolyte could be an efficient way to change the reactivity between electrolyte and both anode/cathode electrodes. Recently, several studies reveal that two main side reactions between electrolyte and anode, SEI layer formation and growth and Li plating, which count for the most cell degradation during fast charging, can be affected by electrolyte concentration. However, the mechanism by which electrolytes influence these reactions is not fully understood. In this work, a full order electrochemical model including physics of degradation at the anode and electrolyte impact depending on the electrolyte concentration is proposed and validated by experimental results. It proves that a high electrolyte concentration can suppress the SEI layer growth; while it promotes Li plating by enhancing its reaction rate. Furthermore, the coupling impact between the SEI layer and Li plating has been identified; the existence of SEI layer can slow down Li plating rate by developing its overpotential via the SEI film resistance. In terms of fast charging, Li plating would be greatly promoted by the high current rate, while SEI layer reaction is not sensitive to the charging current. Both low electrolyte concentration and high charging current result in a more severe capacity degradation. These results would be a useful guidance for electrolyte design for the fast charging batteries and operations.

1. INTRODUCTION

Lithium ion batteries (LIBs) are the main technical streams for electrical vehicles due to their high energy density, high voltage, low cost, and long cycle life [1]. However, the relatively long recharge time is a critical barrier for electrical vehicles to be adopted in place of gasoline vehicles. Therefore, the concept of extreme fast charging (XFC) has been proposed, which is to shorten the recharge time for electrical vehicles to approximate 15 min – similar to refueling conventional internal combustion engines for cells with energy density above 200 Wh/kg [2].

The key challenge for XFC in cell level is the requirement for the high rates of electrolyte mass transport and electrode charger transport [3]. The electrolyte transport properties are decisive in the ohmic voltage drop across the electrolyte, which can cause early hitting of the cut off voltage, leading to a reduction in available capacity [4, 5]. Also, a severe concentration polarization could be caused by poor electrolyte transport properties, especially under large current. As a result, the continuous high charge current in XFC may deplete Li ion at a certain depth of anode, meaning the active material beyond the depth cannot be utilized [6, 7]. Electrode charger-transfer overpotential is the main driving force in the Li plating overpotential, along with ohmic and concentration polarizations. Li plating occurs when the Li plating overpotential become negative (vs. Li/Li+) and is one of the main concerns during XFC due to its hazard to both the electrochemical performance and the cell safety. Plated Li metal causes electrolyte decomposition and a loss of lithium inventory, resulting in a decrease in cell capacity. Also, the formation of dendrites can affect the local transport properties of the anode, increase

Joule heating in the anode and cause short circuits and overheating in the cell if there is breaking in the end [8].

Extensive work has been done to improve the fast charge capability of Li ion batteries. The most common strategies were reducing the electrode particle size [9-11], and coating or incorporating conductive agents in anode materials [10, 12-17] to reduce the species transport distance at particle levels. Material modifications - such as doping foreign elements [18-21] or adjust stoichiometry of the active material [22, 23] proved to be effective in improving the Li ion diffusivity of electrode materials, thus enhancing their fast charge capabilities.

Recently, tuning salt concentration of electrolytes was proposed as another way to change the reactivity between electrolytes and both anodes and cathodes. Solid electrolyte interphase (SEI) layers are mainly derived from the decomposition of solvents. It was reported that salt concentration could alter the reactivity of solvents by binding the solvent molecules to the salts with different solvation numbers and solution structures [24, 25]. For example, at 1.2 M $LiPF_6$ in propylene carbonate (PC), the solvation number was mainly 4 with a solution structure of $Li^+(PC)_4/PF^-$, and continuous electrolyte reduction and no lithiation/delithiation on the graphite were observed. However, at 3.0~3.5 M $LiPF_6$ in PC, the main solvation number decreased to 3 ($Li^+(PC)_3PF_6^-$) and reversible lithiation/delithiation on graphite was detected [26]. Other salts such as LiClO4 and $LiN(SO_2C_2F_5)_2$ were reported to have similar behaviors in PC with $LiPF_6$ [27]. Moreover, in concentrated solutions of these salts (3.27 mol kg^{-1}), a thin and stable SEI film formed on the graphite surface, preventing the electrolyte composition and exfoliation of graphene layers from occurring in their dilute solutions (e.g., 1.23 mol kg^{-1}) [27, 28]. The

concentration impacts of $LiN(SO_2CF_3)_2$ on a series of solvents - such as dimethyl sulfoxide, 1,2-dimethoxyethane, acetonitrile, tetrahydrofuran, glyme ethers, and ethyl acetate - were also reported [29-32]. A high concentration of $LiN(SO_2CF_3)_2$ effectively reduced the electrolyte decomposition and allowed a reversible lithium intercalation into graphite with these solvents.

Li plating can be impacted by salt concentration, especially between the SEI layer and the plated Li metal. Plated Li metal was thermodynamically instable in the electrolyte and a SEI layer formed unavoidably on Li surfaces. The insulated SEI layers altered the electrical field distribution and the deposition reactivity of the anode surface, thus influencing the Li plating [33-35]. For example, it was observed that Li/Li symmetric cells were shorted earlier in 4M $LiPF_6$ EC/DMC than in 1M $LiPF_6$ EC/DMC during cycling tests, which corresponded to a decrease of SEI layer resistance as the salt concentration increased in the electrolyte [33]. Plated Li metal had needle-like morphology with lengths of several micrometers in dilute $LiN(SO_2C_2F_5)_2$ EC/DMC electrolyte, and as dense and uniform structures only a few nanometers long in concentrated $LiN(SO_2C_2F_5)_2$ EC/DMC electrolyte, in which the SEI layer of concentrated $LiN(SO_2C_2F_5)_2$ EC/DMC electrolyte contain more LiF contributed by the reduction of $N(SO_2C_2F_5)_2^-$, which had high interfacial energy and prevented Li dendrite growth [36]. Although lots of researches have reported the experiment results of the salt concentration impacts on side reactions, such as SEI growth and Li plating of Li ion battery, there was no comprehensive analysis of its mechanisms in theoretical aspects.

In this paper, a full order electrochemical model including SEI layer growth and lithium plating was applied to analyze the electrolyte concentration impact on side

reactions and cell properties. The change of reactivity between electrolyte and anode by salt concentration was explained by Gibbs free energy of SEI layer reaction from the first principle simulation. The interaction between the SEI layer and the Li plating rate was investigated by comparing models with and without SEI layer reaction. The model was validated with experimental results. The performance of cells with various electrolyte concentrations at high charge C-rates were also presented as guidance for electrolyte concentration for fast charge applications.

2. EXPERIMENT SETUP

Experimental validation of the proposed model was conducted based on a CR2032 coin cell test. It used MesoCarbon MicroBeads (MCMB) as the anode, NMC622 as the cathode, and LiPF6 dissolved in EC/DMC (1:1) by wt.) as electrolyte. An NMC622 paste was prepared by mixing 85.5 wt% NMC622 powder (MSE Supplies, 13 μm particle size) with 6.5 wt% carbon black (CB, Alfa Aesar) and 8 wt% Polyvinylidene fluoride (PVDF, Sigma-Aldrich), followed by dispersing the mixture in N-Methyl-2-pyrrolidone solvent (NMP, Sigma-Aldrich). The MCMB paste was prepared by mixing MCMB powder with 5 wt% CB and 10 wt% PVDF in NMP. The electrode thickness was 40 μm for cathode and 30 μm for anode. The diameter is 14 mm and 16 mm for cathode and anode, respectively. The coin cell was assembled in an argon-filled glove box. A PP/PE/PP membrane (Celgard) of 25 μm thickness was used as the separator. The electrolyte was prepared by dissolve 0.5 M/1 M/1.5 M/2 M in EC:DMC 1:1 (Sigma-Aldrich). The cell was put into cycling test by using battery testing station (Neware Battery Tester). The cycling test was

designed as constant current charge and discharge of 1C/2C/3C for 20 cycles, respectively, with a voltage range of 2.8-4.2 V. Then a long cycling test of 1C charge /discharge of 100 cycles was conducted.

3. MODEL DESCRIPTION

In this work, a physics-based model was developed to investigate the behavior of lithium plating and SEI layer growth under electrolytes with various salt concentrations. The modeling approach was based on the concentrated solution and the porous electrode theory proposed by Fuller and Newman, which is known as a pseudo-two-dimensional (P2D) model [37].

Both lithium plating and SEI layer growth were considered to take place at the surface of the anode particle. In this work, it was assumed that the lithium deposition was irreversible. The reaction of plating can be written as:

$$Li^{+} + e^{-} \rightarrow Li(s)\,. \tag{1}$$

The cathodic Tafel expression was used to describe the rate expression assuming the deposition reaction was irreversible. Therefore, a cathodic Tafel expression was incorporated in the model to describe the reaction current of lithium plating as:

$$i_{lp} = -i_{0,lp} \exp\left(-\frac{\alpha_{c,lp} F}{RT} \left(\phi_s - \phi_e - i_{tot} R_{film} \right) \right), \tag{2}$$

where ϕ_s and ϕ_e are solid and liquid phase potential at the anode particle surface, $\alpha_{c,lp}$ is the kinetic parameter, i_{tot} is the total current density, R_{film} is the resistance of deposited film and $i_{0,lp}$ is the exchange current density defined by

$$i_{0,lp} = FK_{Li}(c_{Li})^{1-\alpha}, \tag{3}$$

where K_{Li} is the lithium deposition rate coefficient and c_{Li} is the salt concentration in electrolyte.

The SEI formation continuously took place between the lithiated anode and the electrolyte solvent, which led to a continuous consumption of reversible Li ions and an increase in film resistance. In EC-based electrolyte, the main reaction of SEI formation was a process of one electron reduction of EC molecule, with a product of lithium ethylene dicarbonate $(CH_2OCO_2Li)_2$ and ethylene gas. The reaction process is:

$$nEC + Li^+ \rightarrow (EC)_n \bullet\bullet\bullet Li^+ \tag{4}$$

$$(EC)_n \bullet\bullet\bullet Li^+ + e^- \rightarrow \left[(EC)^{e^-}\right] \bullet\bullet\bullet Li^+ \bullet\bullet\bullet (EC)_{n-1} \tag{5}$$

$$2(EC)^{e^-} \bullet\bullet\bullet Li^+ \bullet\bullet\bullet (EC)_{n-1} \rightarrow (EC)_{n-1} \bullet\bullet\bullet Li^+ (CO_3)^- (CH_2)_2 (CO_3)^- Li^+ \bullet\bullet\bullet (EC)_{n-1} \downarrow + C_2H_4 \uparrow, \tag{6}$$

where n is solvation number. The radical anion formation process in Eq. 5 is the rate-determining step and its reaction rate can be expressed as:

$$i_{SEI} = -Fk_{SEI}c_{EC}^s \exp\left(-\frac{\alpha_{c,SEI}F}{RT}\left(\phi_s - \phi_e - i_{tot}R_{film} - U_{SEI}\right)\right), \tag{7}$$

where $\alpha_{c,SEI}$ is the kinetic parameter, k_{SEI} is SEI reaction constant, U_{SEI} is the equilibrium potential of SEI reaction and c_{EC}^s is the EC concentration on the anode particle surface. The radical anion formation occurred on the anode particle surface, and because of that the decay of EC concentration from the bulk electrolyte through anode surface film must be considered. The decayed concentration was calculated according to the diffusion law:

$$-D_{EC}\frac{c_{EC}^{s}-c_{EC}^{0}}{\delta_{film}}=-\frac{ai_{SEI}}{F}, \quad (8)$$

where D_{EC} is the diffusion coefficient of EC solvent, c_{EC}^{0} is the EC concentration in bulk electrolyte, δ_{film} is the thickness of surface film, and a is the specific surface area of anode particles.

Based on density functional theory, solvation number n determines the reductive reactivity of reactions in Eqs. 5 and 6, that is, the SEI formation. The corresponding Gibbs free energy of each solvation number is presented in Table 1 [38].

Table 1. Gibbs free energy of SEI reaction with different solvation number [38].

n	ΔG_n (Kcal/mol)
0	-7.5
1	-56.8
2	-47.4
3	-49
4	-51.7

Due to the formation energy in Eq. 5 with a small solvation number is lower than that with larger solvation number, Li ion tended to combine first with the EC solvent with low solvation number [38]. Based on this rule, the composition of solvation numbers with different salt compositions can be derived (Table 2), and the corresponding SEI reaction energy per mole of salt can be calculate as:

$$\Delta G = \frac{\sum_n \Delta G_n \times c_n}{c_{Li}} . \quad (9)$$

Table 2. SEI reaction energy of electrolyte with different salt concentration [38].

Salt concentration (mol/L)	EC concentration (mol/L)	Supermolecule (mol/L)	Gibbs free energy (Kcal/mol)
0.5	4.429	0.5 Li+(EC)4 2.429 EC	-88.14
1	4.429	1 Li+(EC)4 0.429 EC	-54.92
1.5	4.429	1.429 Li+(EC)3 0.071 Li+(EC)2	-48.94
2	4.429	0.429 Li+(EC)3 1.571 Li+(EC)2	-47.75

The SEI reaction constant k_{SEI} is proportional to SEI reaction energy. Therefore, it can be written as:

$$k_{SEI} \propto k_{0,SEI} \exp(-\frac{\Delta G}{RT}) \quad (10)$$

where $k_{0,SEI}$ is the reaction constant for Li concentration of 1 mol/L (as reference), ΔG is the Gibbs free energy of SEI formation reaction vs. reference. Fitted to measurements, the values of k_{SEI} in electrolyte of different salt concentrations were obtained, as shown in Table 3. Overall, k_{SEI} decreased as salt concentration increased, which agrees with the trend of SEI reaction energy. The equilibrium potential equations for electrodes, electrolyte

Table 3. Kinetic parameters of side reaction in electrolyte in different salt concentrations.

Salt concentration (mol/L)	0.5	1	1.5	2
[b] k_{SEI} (m/s)	9.45×10^{-15}	5.45×10^{-15}	3.5×10^{-15}	2.5×10^{-15}

transport, and side reaction are in Table 4. A brief overview of all used physicochemical parameters are listed in Table 5.

4. RESULTS AND DISCUSSION

The accuracy of the model was validated by comparing it with experimental data. Figure 1 shows the variance of discharge capacity versus cycle number during constant current charge and discharge cycling processes. The charge and discharge currents were 1C for the first 10 cycles and 2C for the 11~20th cycles. To analyze the discharge capacity degradation rate, the data were scaled according to the capacity of the first cycle of corresponding experimental currents. As observed, the capacity degradation rates were accelerated in the electrolyte with low salt concentration. Comparing the results of 1C and 2C, it was unexpectedly found that the capacity degradation rate was slower in 2C. This was caused by the dominate impact of charge time in the cell degradation which was explained in Figure 6. The simulated cycling capacities matched the experimental data for both the impact of salt concentration and the impact of applied current very well (RMS<9.3%).

Table 4. Governing equations.

Region	**Governing Equation**	
Electrode	**Mass, solid phase** $$\frac{\partial c_s}{\partial t} = \frac{1}{r^2}\frac{\partial}{\partial r}\left(D_s r^2 \frac{\partial c_s}{\partial r} \right)$$ $$\left.\frac{\partial c_1}{\partial t}\right\vert_{r=R} = -\frac{j_{\text{int}}}{F}$$	**Charge, solid phase** $$\nabla \cdot \left(\sigma_s^{eff} \nabla \phi_s \right) = j_{tot}$$
Electrode/ **Separator**	**Mass, liquid phase** $$\frac{\partial \left(\varepsilon c_e \right)}{\partial t} = \nabla \cdot \left(D_e^{eff} \nabla c_e \right) + \frac{1 - t_+}{F} j_{tot}$$	**Charge, liquid phase** $$\nabla \cdot \left(\kappa_e^{eff} \nabla \phi_e \right) + \nabla \cdot \left(\kappa_D^{eff} \nabla \ln c_e \right) = -j_{tot}$$
Electrode **kinetics**	$$j_{\text{int}} = a i_{0,\text{int}} \left(\exp\left(\frac{\alpha_{a,\text{int}} F}{RT} \eta_{\text{int}} \right) - \exp\left(-\frac{\alpha_{c,\text{int}} F}{RT} \eta_{\text{int}} \right) \right)$$ $$\eta_{\text{int}} = \phi_s - \phi_e - \frac{j_{tot}}{a} R_{film} - U_{\text{int}}$$	

Table 4. Governing equations. (Cont.)

<table>
<tr><th>Region</th><th colspan="2">Governing Equation</th></tr>
<tr><td rowspan="2">Side reactions</td><td>SEI reaction
$$j_{SEI} = -aFk_{0,SEI}c_{EC}^{s}\exp\left(-\frac{\alpha_{c,SEI}F}{RT}\left(\phi_s-\phi_e-\frac{j_{tot}}{a}R_{film}-U_{SEI}\right)\right)$$
$$-D_{EC}\frac{c_{EC}^{s}-c_{EC}^{0}}{\delta_{film}} = -\frac{j_{SEI}}{F}$$
$$\frac{\partial c_{SEI}}{\partial t} = -\frac{j_{SEI}}{2F}-\frac{j_{lpl}}{2F}\beta$$</td><td>Li plating
$$j_{lpl} = -ai_{0,lpl}\exp\left(-\frac{\alpha_{c,SEI}F}{RT}\left(\phi_s-\phi_e-\frac{j_{tot}}{a}R_{film}\right)\right)$$
$$\frac{\partial c_{Li}}{\partial t} = -\frac{j_{lpl}}{F}(1-\beta)$$</td></tr>
<tr><td colspan="2">$$\delta_{film} = \frac{1}{a}\left(\frac{c_{SEI}\cdot M_{SEI}}{\rho_{SEI}}+\frac{c_{Li}\cdot M_{Li}}{\rho_{Li}}\right)$$
$$R_{film} = \omega_{SEI}\frac{\delta_{film}}{\kappa_{SEI}} = \frac{1}{a\cdot\kappa_{SEI}}\frac{c_{SEI}\cdot M_{SEI}}{\rho_{SEI}}$$
Porosity $$\frac{d\varepsilon_l}{dt} = -a\frac{d\delta_{film}}{dt}$$</td></tr>
</table>

Table 5. Model parameters.

Parameter	Anode (Graphite)	Separator	Cathode (NMC622)
[a]Thickness (μm)	47.6	23	23.80
[b]Initial porosity	0.408	0.4	0.4
[b]Particle radius (μm)	4	/	8
[a]Diffusion coefficient in solid (m^2/s)	3.49×10^{-14}	/	1.85×10^{-14}
[a]Matrix conductivity (S/m)	100	/	10
[b]Reaction rate constant ($m^{2.5}/(mol^{0.5}\cdot s)$)	1.78×10^{-7}	/	1.25×10^{-7}
[37]Maximum Li ion concentration (mol/m^3)	26390		49000
[a] c_{EC}^0 (mol/m^3)	4429		
[39] M_{SEI} (kg/mol)	0.162		
[39] ρ_{SEI} (kg/m^3)	1690		
[39] κ_{SEI} (S/m)	5×10^{-6}		
[39] $\alpha_{c,SEI}$	0.5		
[b] D_{EC} (m^2/s)	1.5×10^{-18}		
[39] $\alpha_{c,lpl}$	0.5		
[39] M_{Li} (kg/mol)	6.94×10^{-3}		
[39] ρ_{Li} (kg/m^3)	534		
[b] K_{Li} ($mol/(m^{0.5}s)$)	5.18×10^{-9}		
[b]Initial SEI layer film thickness (m)	1.22×10^{-9}		
[39]Equilibrium potential of SEI layer (V)	0.4		

[a] Measured

[b] Fitted with experiment

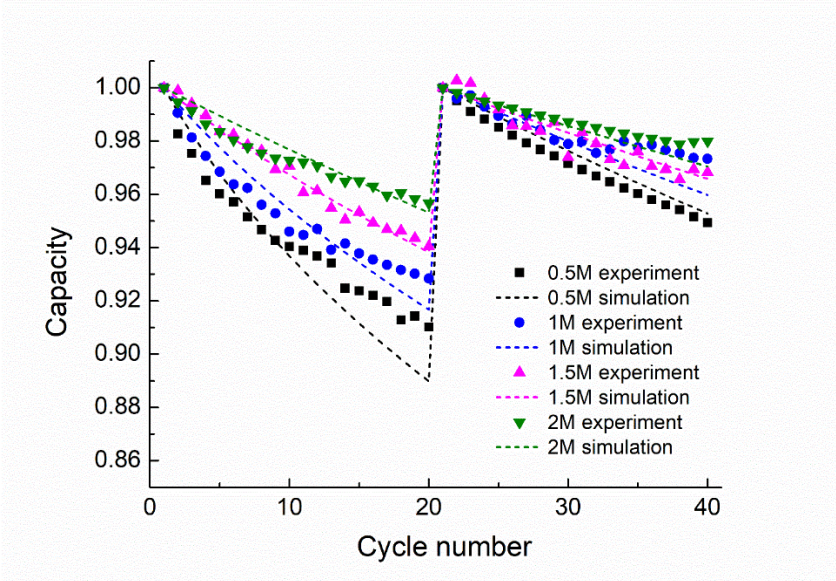

Figure 1. Comparison of experiment and simulation result of capacity degradation in 1C and 2C cycling.

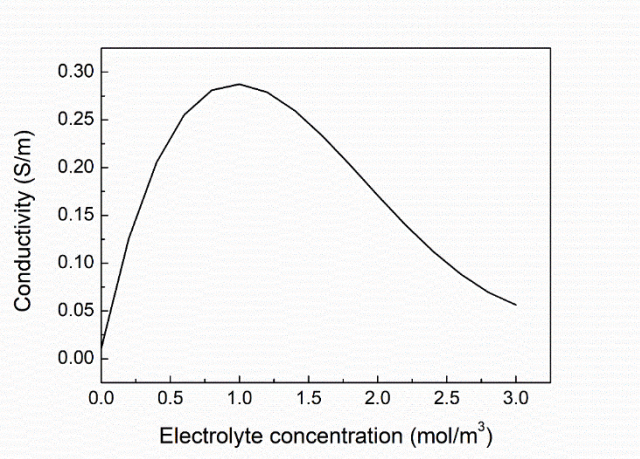

Figure 2. Electron conductivity as a function of electrolyte concentration.

Generally, electrolyte concentration is closely related to the mobility of Li ions in electrolytes. As shown in Figure 2, the electrolyte conductivity was a function of

concentration, which turned at 1 mol/L. In this study, the investigated electrolyte concentrations were 0.5, 1, 1.5 and 2 mol/ L, correspondingly, the liquid phase conductivities were 0.228, 0.2873, 0.2457 and 0.171 S/m, respectively. Among them, the electrolyte of 1 mol/L had the highest conductivity and 2 mol/L had the lowest. Liquid phase conductivity is closely related to charge immigration in electrolyte and charge transfer on electrode particle surfaces. With a high conductivity, both the potential gradient and Li ion concentration gradient were reduced, leading to a smaller polarization in interface and bulk electrolytes.

Despite the impact on electrolyte conductivity, salt concentration had an influence on SEI reaction constant k_{SEI} , as shown in Figure 3(a). To study the electrolyte concentration in SEI layer growth, the SEI layer behavior was investigated with salt concentrations of 0.5, 1, 1.5 and 2 mol/L during 1C constant current charge processes. The corresponding voltages and applied charge current C-rates are shown in Figure 3(b). First, the SEI reaction was analyzed numerically. According to Eq.7, the main impact factors of SEI reaction rate were the SEI reaction constant, EC concentration at anode particle surface, and local overpotential. EC concentration at anode particle surface also depends on SEI reaction rate, meaning it can be eliminated by importing Eq.8 into Eq.7. Consequently, SEI reaction current can be written into the following expression:

$$i_{SEI} = \frac{c_{EC}^{0}}{\dfrac{1}{\exp\left(-\dfrac{\alpha_{c,SEI}F}{RT}\left(\phi_s - \phi_e - \dfrac{j_{tot}}{a}R_{film} - U_{SEI}\right)\right)} \cdot \dfrac{1}{-Fk_{SEI}} - \dfrac{a\delta_{film}}{FD_{EC}}} \cdot \tag{10}$$

Electrolyte concentration mainly had impacts on two terms in Eq. 10: the SEI layer overpotential $\phi_s - \phi_e - \frac{j_{tot}}{a} R_{film} - U_{SEI}$ and SEI reaction constant k_{SEI}, which have reverse influences on SEI reaction currents. As shown in Figure 3(c), with increased electrolyte concentration, the SEI reaction overpotential increased less than 2e-4 V. However, its change was negligible compared with the variance of SEI reaction constants. The SEI reaction constant dominated the change in the SEI reaction currents with electrolyte salt concentrations. As a result, the SEI reaction current decreased (Figure 3(d)) along with a reduced thickness of deposited SEI film (Figure 3(e)) in concentrated electrolytes, indicating a suppression of SEI growth by high salt concentrations. Regarding physics, the concentration of the EC solvent at the anode particle surface was also a critical factor that influenced SEI layer growth. As known, the reduction process of solvated EC (Eq. 5) occurs at the interface between the anode particle and the electrolyte. Therefore, solvated EC molecules must transport through the formed surface film of deposited SEI components and lithium metal to take part in the reaction. As shown in Figure 3(f), the growing surface film caused a drastic reduction in EC concentration at the anode particle surface, due to a increased diffusion path.

According to Eq. 2, lithium plating reaction current depended on two components, exchange current density and local overpotential, in which local overpotential can be decomposed into solid phase potential ϕ_s, liquid phase potential ϕ_e, and ohmic potential caused by surface film $i_{tot} R_{film}$.

$$\eta_{lp} = \phi_s - \phi_e - i_{tot} R_{film} \tag{11}$$

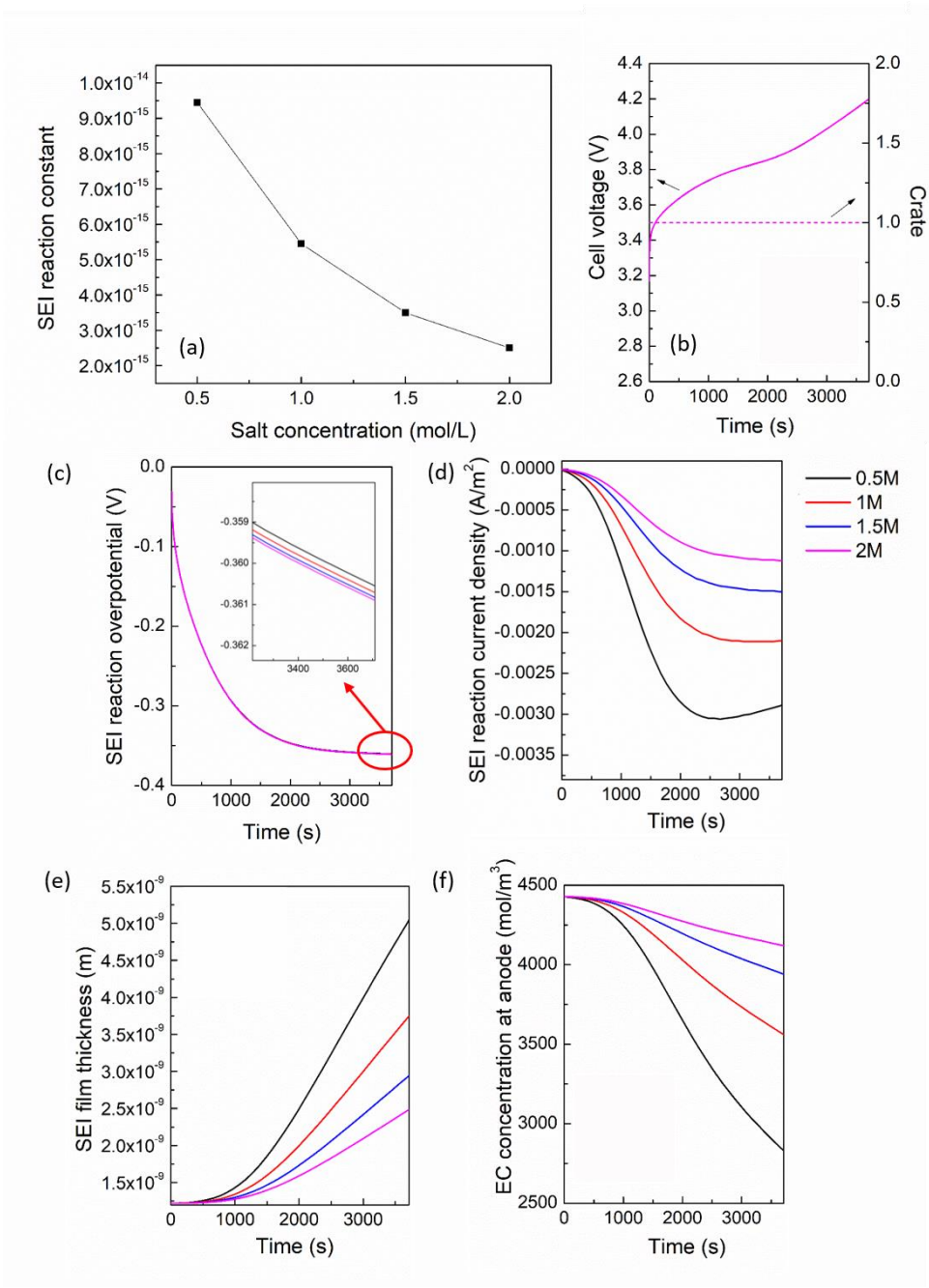

Figure 3. (a) SEI reaction constant as a function of salt concentration, (b) cell voltage and applied current C rate, (c) SEI layer growth overpotential, (d) SEI layer reaction current density (e) SEI film thickness and (f) EC concentration at anode particle surface for electrolyte of different salt concentrations.

Lithium plating exchange current density was proportional to salt concentration, as shown in Figure 4(a). To identify the difference between each salt concentration clearly, a constant current charge process of 5C was implemented for all the cells. The corresponding voltage and current profile are shown in Figure 4(b). The initial potential in liquid phase is 0. The liquid potential is derived from Li ion concentration gradient in electrolyte. In high salt concentration, the concentration gradient will be lower than low salt concentration if same amount of Li ion participates in the reversible reaction. Therefore, the liquid potential decreases as the salt concentration increases as shown in Figure 4(c). In the model, the surface film resistance was only contributed to by SEI film. As presented in the previous section (Figure 3(e)), the SEI film thickness decreased as the salt concentration increased. Consequently, the ohmic drop of surface film was much larger in low salt concentration electrolyte than in the high salt concentration electrolyte (Figure 4(d)). However, the change in liquid phase potential is about 0.05 V in 0.5 mol/L and 2 mol/L, which is larger than the change in ohmic potential which is about 5e-4 V. Therefore, for the local overpotential for lithium deposition the salt concentration increased, and the local overpotential decreased (Figure 4(e)) in agreement with the liquid phase trend. The impact of plating local potential is opposite with the impact of Li plating constant on plating current. As a compromised result, the Li plating current of 1.5 mol/L salt concentration is highest, resulting in a fastest deposition rate. Another point need to be noted is that the charge time of high salt concentration is longer because its polarization is lower at terminal voltage. Therefore, the total amount of the Li metal film for 1 cycle is slightly larger as salt concentration increases. Furthermore, it can be observed in Figures 4(f) and (g) that lithium plating occurred continuously once the charge began, not only when local potential was

negative, but also when positive. However, in the negative overpotential region, the lithium plating current decreased rapidly (-4E-6 V/s) and caused a faster growth (1.3E-13 m/s vs. 2.5E-14 m/s) of Li metal film with narrower overpotential change when compared with the positive overpotential region. Therefore, the starting point of lithium plating was usually set to zero in references.

The interaction between SEI layer growth and Li plating was investigated by including and excluding the physics of the SEI reaction in simulations. The main impact of the SEI reaction on lithium plating was on its deposition overpotential. Therefore, similar to the previous section, the liquid phase and the ohmic voltage are plotted in Figures 5(a) and (b). It was observed that the liquid phase potential is approximately 2e-4 V higher in the model with SEI reaction than without SEI reaction. This was because the SEI reaction consumed additional lithium ions from electrolytes, resulting in an extra voltage rise in the liquid phase. Also, the non-conductive SEI film caused a voltage drop of approximately 4.5e-4 V, which eliminated the change caused by liquid phase potential and leads to an increased lithium plating overpotential. As a result, cells with SEI reactions had a smaller lithium plating current and less deposited Li film. From this comparison, it was concluded that the existence of a SEI layer can alleviate Li plating overpotential because of its resistance, thus suppressing the occurrence of lithium plating.

Degradation physics is highly dependent on charge current; therefore the degradation effects of different salt concentration electrolytes were analyzed under different charge currents. In this study, a constant current (CC) charge and discharge cycling process of 1C and 5C with a cur of voltage of 4.2 V were investigated. The results

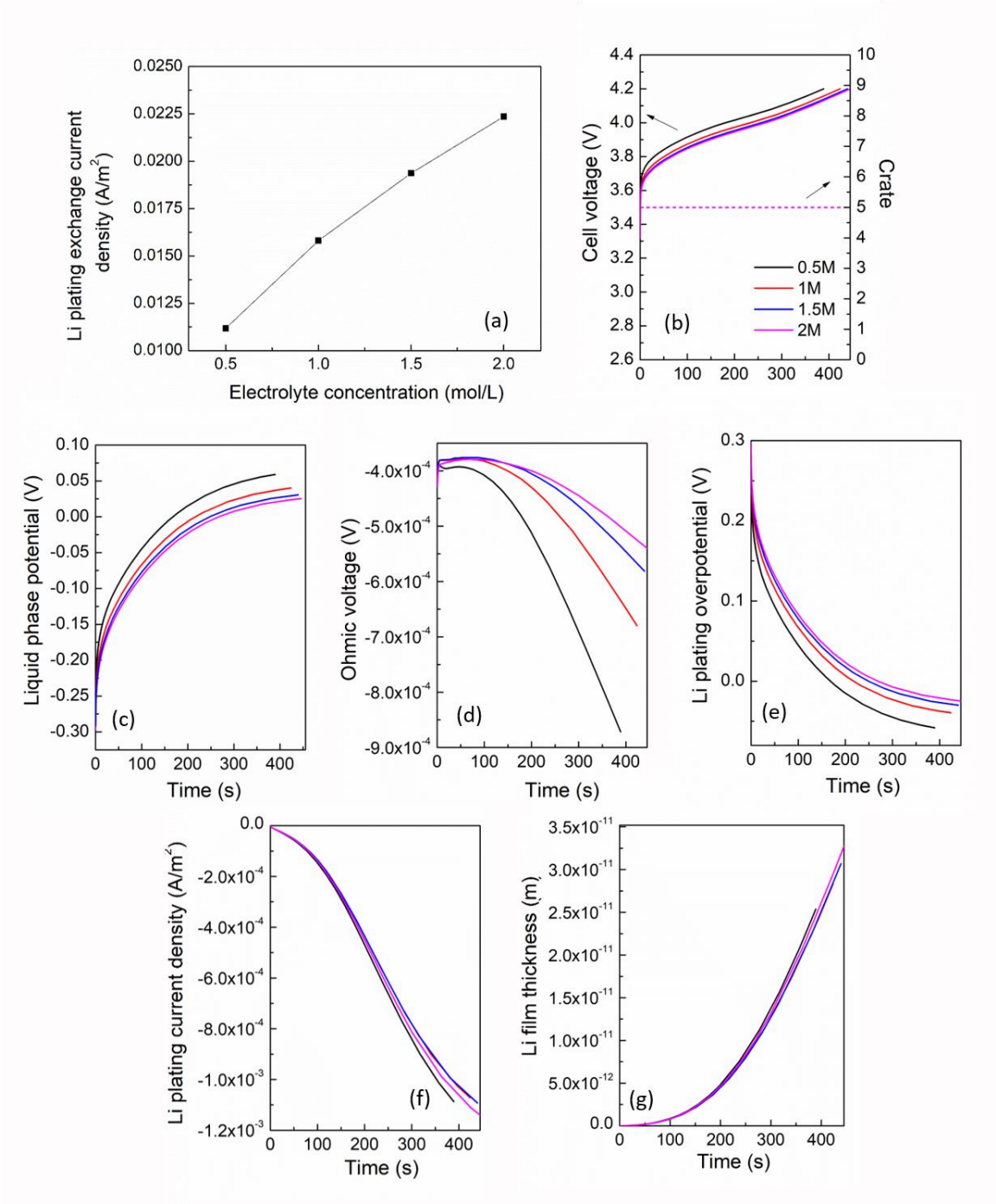

Figure 4. (a) Li plating exchange current density as a function of salt concentration, (b) cell voltage and applied current C rate, (c) liquid phase potential, (d) ohmic voltage, (e) Li plating overpotential, (f) Li plating current density and (g) Li metal film thickness for different salt concentration electrolyte.

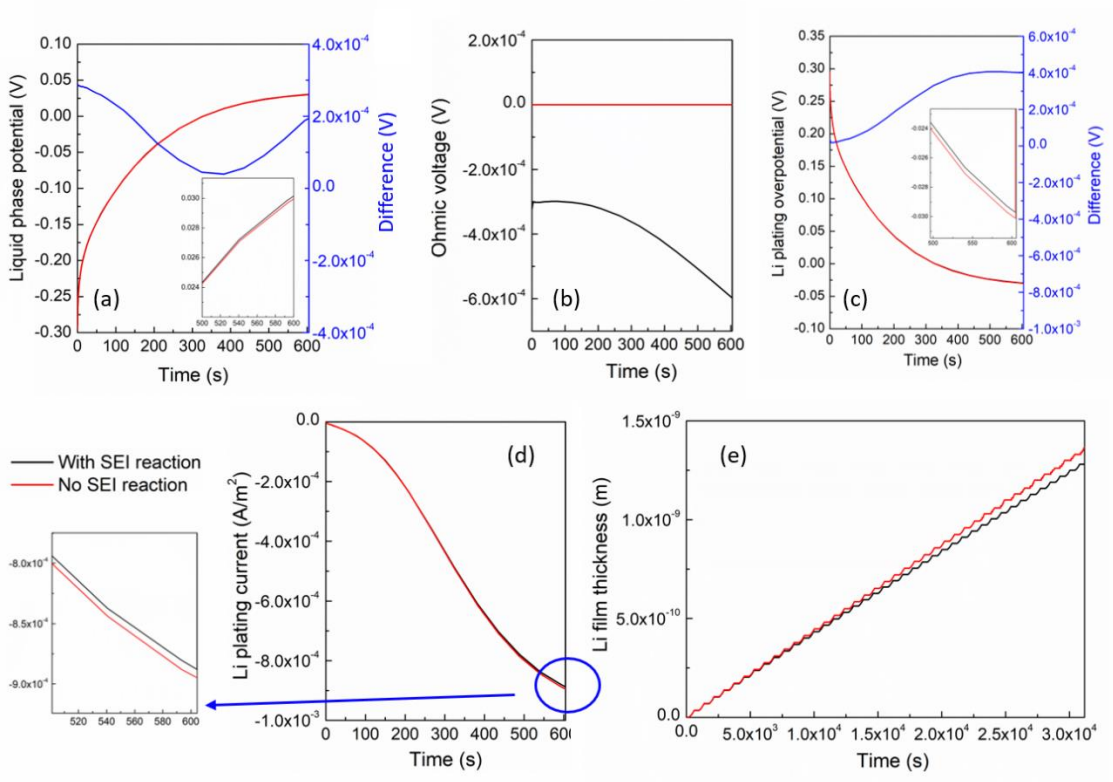

Figure 5. Comparison of simulation results with (black line) and without (red line) SEI layer growth. (a) liquid phase potential, (b) ohmic voltage, (c) Li plating overpotential, (d) Li plating current and (f) Li metal film thickness of 20 cycles.

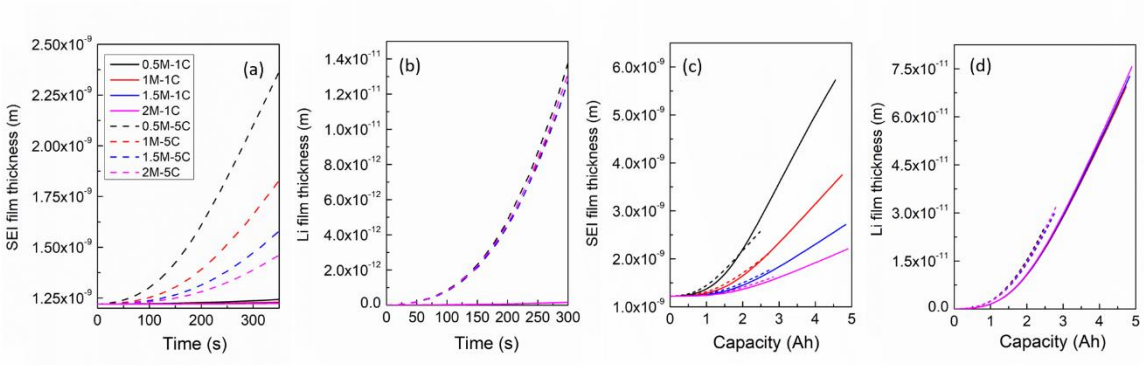

Figure 6. (a) SEI film thickness vs. time, (b) plated Li film thickness vs. time, (c) SEI film thickness vs. capacity, (d) plated Li film thickness vs. capacity.

are shown in Figure 6. It is evident in Figures 6(a) and (b) that the growth rates of the SEI layer and the Li metal layer were accelerated by high C- rate charging, in which the sensitivity of SEI layer growth was also improved by high C-rates, indicating that high salt concentration suppressed the SEI layer growth when fast charging. In contrast, lithium plating was not sensitive to different salt concentrations. Also, charge capacity was another critical criterion in the application. Cell degradation in terms of capacity in one cycle is shown in Figures 6(c) and (d). It was observed that because of the potential polarization in the high current charge, the charge capacity of 5C was only 65.3% of 1C. Therefore, the total amounts of SEI layer and deposited lithium metal per cycle were smaller in high C-rate charging. The SEI layer growth rate, in terms of capacity, was a compromise of charge time and growth rate, in terms of time. Therefore, it varied with salt concentration under various charge currents. In electrolyte with 1.5 mol/L and 2 mol/L, the SEI growth rate was close in 1C and 5C charge current, while in the electrolyte of 0.5 mol/L and 1 mol/L, the SEI growth rate become lower in 5C than in 1C as time increased. The rate of lithium deposition was larger under high charge current than that in low charge current, although the gap shrank.

One of the most important effects of the previous two side reactions was the capacity degradation. The results of capacity degradation under various salt concentrations and charge currents are presented in Figure 7. It was seen that the capacity degradation rate was reduced in the concentrated electrolyte due to its suppression of the SEI layer growth. However, the increase in charge current resulted in a slower capacity degradation, which was cause by a reduced charge time. These results are consistent with previous analysis of two sides reactions. Experiment results of cycling tests with 1C/2C/3C procedure are

presented in Figure 7(c). It was seen that the capacity degradation rate decreased as the salt concentration increased. Comparing different C-rates, the capacity degradation in 1C cycling was the fastest, and the difference between 2C and 3C was not evident. This may be caused by the variance in operation times and degradation rates in the same periods. Overall, the results matched well with the simulation.

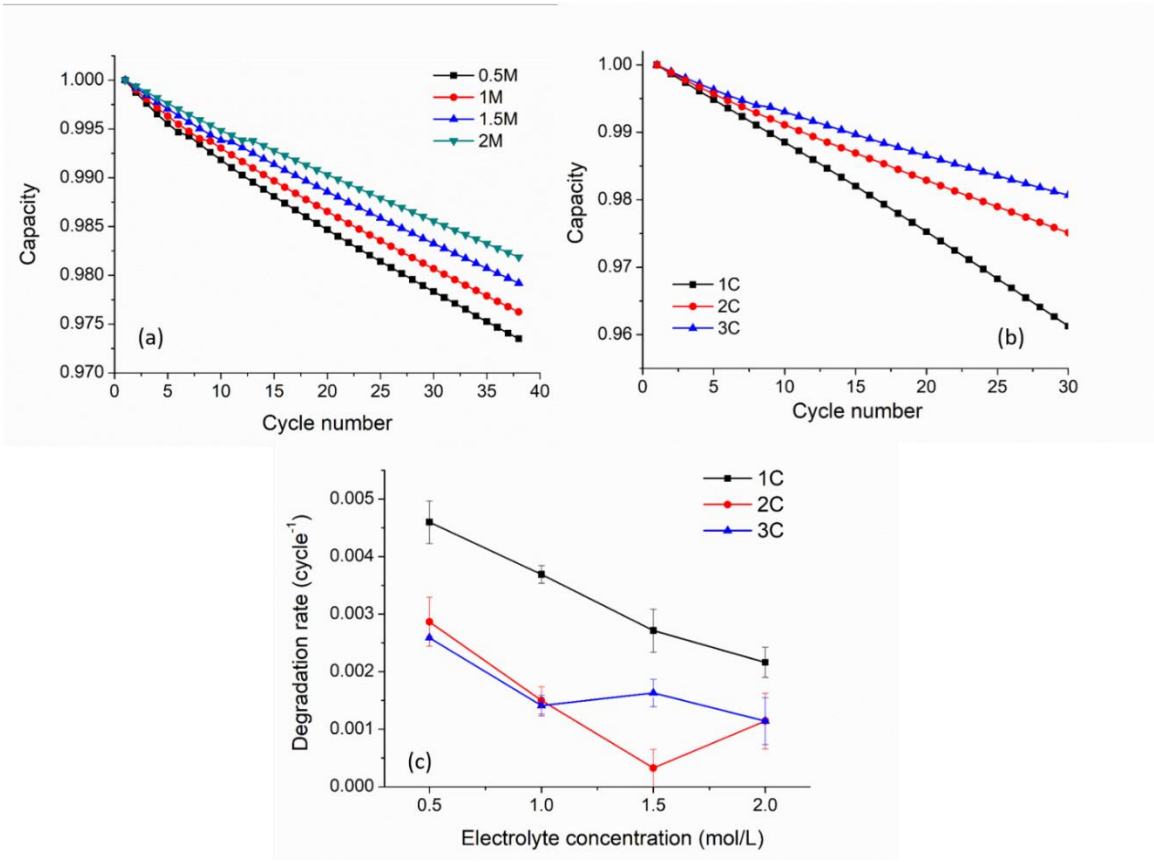

Figure 7. Comparison of capacity degradation in 100 cycles (a) different electrolyte concentration 1.5 M and 1.75 M (b) different charge Crate 1C and 7C.

5. CONCLUSIONS

A full order electrochemical model including two degradation physics at anode, SEI layer growth and lithium plating, was established and validated by the experiment results. The model captured the electrolyte concentration impact on both side reactions, as well as the total capacity degradation. The mechanism for how electrolyte concentration worked on each side reaction was investigated. It was found that the electrolyte concentration influenced the SEI layer and the Li plating mainly through their reaction constants and deposition overpotentials. A high salt concentration (1.5 mol/L and 2 mol/L of $LiPF_6$ in EC: DMC) suppressed the SEI layer growth and promoted Li plating. The mechanism for the interplay between the two side reactions was also analyzed. The existence of the SEI layer slowed the lithium plating rate by increasing its overpotential through ohmic resistance. In terms of charge current C-rates, a high C-rate (4C) accelerated both lithium plating and SEI layer reaction rates in terms of time. However, this acceleration was not evident when considering charge capacity in the CC process. Comprehensively, both low electrolyte concentration and low charge current C-rate resulted in a more severe capacity degradation in the CC cycling process.

REFERENCES

1. Ahmed, S., et al., Enabling fast charging – A battery technology gap assessment. Journal of Power Sources, 2017. **367**: p. 250-262.

2. Colclasure, A.M., et al., Requirements for enabling extreme fast charging of high energy density Li-Ion cells while avoiding lithium plating. Journal of the Electrochemical Society, 2019. **166**(8): p. A1412.

3. Liu, Y., Y. Zhu, and Y. Cui, Challenges and opportunities towards fast-charging battery materials. Nature Energy, 2019. **4**(7): p. 540-550.

4. Nyman, A., et al., Analysis of the polarization in a Li-ion battery cell by numerical simulations. Journal of The Electrochemical Society, 2010. **157**(11): p. A1236.

5. Smart, M., B. Ratnakumar, and S. Surampudi, Use of organic esters as cosolvents in electrolytes for lithium-ion batteries with improved low temperature performance. Journal of the Electrochemical Society, 2002. **149**(4): p. A361.

6. Doyle, M., T.F. Fuller, and J. Newman, The importance of the lithium ion transference number in lithium/polymer cells. Electrochimica Acta, 1994. **39**(13): p. 2073-2081.

7. Gallagher, K.G., et al., Optimizing areal capacities through understanding the limitations of lithium-ion electrodes. Journal of The Electrochemical Society, 2015. **163**(2): p. A138.

8. Perez, H.E., et al., Optimal charging of Li-ion batteries with coupled electro-thermal-aging dynamics. IEEE Transactions on Vehicular Technology, 2017. **66**(9): p. 7761-7770.

9. Jung, H.-G., et al., A high-rate long-life Li 4 Ti 5 O 12/Li [Ni 0.45 Co 0.1 Mn 1.45] O 4 lithium-ion battery. Nature communications, 2011. **2**(1): p. 1-5.

10. Kucinskis, G., G. Bajars, and J. Kleperis, Graphene in lithium ion battery cathode materials: A review. Journal of Power Sources, 2013. **240**: p. 66-79.

11. Wang, C., et al., A robust strategy for crafting monodisperse Li4Ti5O12 nanospheres as superior rate anode for lithium ion batteries. Nano Energy, 2016. **21**: p. 133-144.

12. Wang, Y.-Q., et al., Rutile-TiO2 nanocoating for a high-rate Li4Ti5O12 anode of a lithium-ion battery. Journal of the American Chemical Society, 2012. **134**(18): p. 7874-7879.

13. Yuan, L.-X., et al., Development and challenges of LiFePO 4 cathode material for lithium-ion batteries. Energy & Environmental Science, 2011. **4**(2): p. 269-284.

14. Shen, L., et al., Carbon-Coated Li3VO4 Spheres as Constituents of an Advanced Anode Material for High-Rate Long-Life Lithium-Ion Batteries. Advanced Materials, 2017. **29**(33): p. 1701571.

15. Kim, H., et al., A new coating method for alleviating surface degradation of LiNi0. 6Co0. 2Mn0. 2O2 cathode material: nanoscale surface treatment of primary particles. Nano letters, 2015. **15**(3): p. 2111-2119.

16. Li, C., et al., Cathode materials modified by surface coating for lithium ion batteries. Electrochimica Acta, 2006. **51**(19): p. 3872-3883.

17. Liu, H.-p., et al., High rate cycling performance of nanosized Li4Ti5O12/graphene composites for lithium ion batteries. Electrochimica Acta, 2016. **192**: p. 38-44.

18. Bai, Y.J., et al., Excellent long-term cycling stability of La-doped Li4Ti 5O12 anode material at high current rates. Journal of Materials Chemistry, 2012. **22**(36): p. 19054-19060.

19. Xu, W., et al., Simply AlF3-treated Li4Ti5O12 composite anode materials for stable and ultrahigh power lithium-ion batteries. Journal of Power Sources, 2013. **236**: p. 169-174.

20. Ni, H., et al., Enhanced rate performance of lithium titanium oxide anode material by bromine doping. Ionics, 2015. **21**(12): p. 3169-3176.

21. Zhang, P., et al., High rate capability of lithium chromium titanium oxide hierarchical mesoporous microspheres anode materials synthesized by a one-pot co-precipitation for lithium ion batteries. Journal of the Electrochemical Society, 2016. **163**(9): p. A1920-A1926.

22. Tian, J., et al., High-rate and cycling-stable nickel-rich cathode materials with enhanced Li+ diffusion pathway. ACS applied materials & interfaces, 2016. **8**(1): p. 582-587.

23. Jin, Y.-C., C.-Y. Lin, and J.-G. Duh, Improving rate capability of high potential LiNi0. 5Mn1. 5O4− x cathode materials via increasing oxygen non-stoichiometries. Electrochimica acta, 2012. **69**: p. 45-50.

24. Wang, D.Y., J. Burns, and J. Dahn, A systematic study of the concentration of lithium hexafluorophosphate (lipf6) as a salt for licoo2/graphite pouch cells. Journal of The Electrochemical Society, 2014. **161**(9): p. A1278.

25. Xu, K., Nonaqueous liquid electrolytes for lithium-based rechargeable batteries. Chemical reviews, 2004. **104**(10): p. 4303-4418.

26. Nie, M., et al., Role of solution structure in solid electrolyte interphase formation on graphite with LiPF6 in propylene carbonate. The Journal of Physical Chemistry C, 2013. **117**(48): p. 25381-25389.

27. Jeong, S.-K., et al., Interfacial reactions between graphite electrodes and propylene carbonate-based solutions: Electrolyte-concentration dependence of electrochemical lithium intercalation reaction. Journal of Power Sources, 2008. **175**(1): p. 540-546.

28. Jeong, S.-K., et al., Electrochemical intercalation of lithium ion within graphite from propylene carbonate solutions. Electrochemical and Solid State Letters, 2002. **6**(1): p. A13.

29. Yamada, Y., et al., Electrochemical lithium intercalation into graphite in dimethyl sulfoxide-based electrolytes: Effect of solvation structure of lithium ion. Journal of Physical Chemistry C, 2010. **114**(26): p. 11680-11685.

30. Yamada, Y., et al., Unusual stability of acetonitrile-based superconcentrated electrolytes for fast-charging lithium-ion batteries. Journal of the American Chemical Society, 2014. **136**(13): p. 5039-5046.

31. Yamada, Y., et al., General observation of lithium intercalation into graphite in ethylene-carbonate-free superconcentrated electrolytes. ACS Applied Materials and Interfaces, 2014. **6**(14): p. 10892-10899.

32. Petibon, R., et al., The use of ethyl acetate as a sole solvent in highly concentrated electrolyte for Li-ion batteries. Electrochimica Acta, 2015. **154**: p. 287-293.

33. Wu, B., et al., The interplay between solid electrolyte interface (SEI) and dendritic lithium growth. Nano Energy, 2017. **40**: p. 34-41.

34. Jeong, S.-K., et al., Suppression of dendritic lithium formation by using concentrated electrolyte solutions. Electrochemistry Communications, 2008. **10**(4): p. 635-638.

35. Masia, M., M. Probst, and R. Rey, Ethylene Carbonate− Li+: A Theoretical Study of Structural and Vibrational Properties in Gas and Liquid Phases. The Journal of Physical Chemistry B, 2004. **108**(6): p. 2016-2027.

36. Fan, X., et al., Highly fluorinated interphases enable high-voltage Li-metal batteries. Chem, 2018. **4**(1): p. 174-185.

37. Chen, L., et al., Modulation of dendritic patterns during electrodeposition: A nonlinear phase-field model. Journal of Power Sources, 2015. **300**: p. 376-385.

38. Wang, Y. and P.B. Balbuena, Theoretical studies on cosolvation of Li ion and solvent reductive decomposition in binary mixtures of aliphatic carbonates. International journal of quantum chemistry, 2005. 102(5): p. 724-733.

39. Yang, X.-G., et al., Modeling of lithium plating induced aging of lithium-ion batteries: Transition from linear to nonlinear aging. Journal of Power Sources, 2017. 360: p. 28-40.

IV. AN OPTIMIZED EXTREME FAST CHARGING PROTOCOL FOR LIHTIUM ION BATTERIES VIA CONTROLLING OF LI PLATING CURRENT

ABSTRACT

Charging protocol is critical to achieving a balance between cell degradation and charging time in fast charging of lithium ion batteries. The traditional constant current constant voltage (CCCV) cannot effectively shorten the charging time under high Crate and causes a sever Li plating in the charging process. Although various new charging protocols were proposed, none of them specifically controls cell degradation, especially Li plating. In this work, a modeling-assisted fast charging algorithm is proposed by regulating the Li plating current, named CQtCV, along with SEI growth and its impact on Li plating. The full order electrochemical model was used to find an optimal current to minimize the Li plating current, whose parameters were identified by experimental data as two groups of parameters: degradation-independent and degradation-related. The proposed algorithm enables that the Li plating rate can be well controlled with a short charging time without sacrificing capacity compared to CCCV. Based on results, the CQtCV protocol decreases the total charging time more than 20% with a reduced capacity loss (0.21 %~0.46 %) compared to a CCCV at 3C charging rate.

1. INTRODUCTION

Fast charging technology is critical for lithium batteries to achieve widespread commercial application in electric vehicles (EVs). To compete with the conventional

internal combustion engine vehicles, the United States Department of Energy (DOE) proposed a goal for fast charging, that is, a recharge time of 15 min for high energy density cells (>200Wh/kg). [1]

However, frequently utilization of fast charging could accelerate the degradation of batteries' electric properties. The intercalation of lithium ion into electrode is a diffusion-limited process. Only a certain amount of lithium can enter electrode materials per unit time at a given temperature. As the charging current increase, the amount of lithium ion transported to anode surface increases. Once it become larger than the amount of lithium ion can intercalate, lithium metal can be deposited on the surface of anode, so-called lithium plating. [2-6] Lithium plating can take place when the local potential at anode is below 0 V (vs. Li/Li^+). [7, 8] The plated lithium metal will react with the electrolyte and form new passivating films, reducing the inventory of cyclable lithium ion and increasing the internal resistance in the cell. This is known to be the main cause of the accelerated aging rate and cell capacity fade in fast charging. Serious lithium plating can also form dendrite, which may penetrate the separator, cause an internal short of the cell, and even lead to a thermal runaway. [4, 9-11] The high charging current will also cause an accelerated formation and growth of a solid electrolyte interphase (SEI) layer. At anode surface, Li ion can be reduced by electrolyte solvent and forms a thin film adhering to anode. The film will continuously grow during the battery charging since the anode potential is always outside the stable window of electrolyte component. The growth of SEI layer could lead to an increase of cell ionic resistance and a reduction of porosity, inducing a capacity degradation. [12, 13] In addition, a large non-uniform strain distribution can be caused by the rapid intercalation or extraction of Li ion from electrode during the fast

charging, leading to particle cracking of active to be passivated and result in local mechanical failure in electrode. [9, 11, 14-17]

To overcome the sever degradation brought by fast charging, a proper charging protocol is essential to achieving a balance between a short charging time and a long cycle life. The most widely used charging protocol in commercial lithium ion battery chargers is a constant current-constant voltage (CCCV) charge protocol. [18, 19] There are two charge stages in a CCCV. Firstly, a constant charge current is implemented on the cell until the cell voltage reaches an upper limit pre-defined according to battery chemistry. Then, the cell transfers to a constant voltage (CV) stage, in which the cell voltage is maintained at the upper limit until the charge current reduce to a pre-defined cut off value. In this way, the cell could avoid being overcharge, assuring a safe operation. In a fast charging, the constant current in CC stage will be lifted, leading to a high cell polarization and early switch to CV stage. Since the charging current in CV stage is small, more charging time is in need to obtain the required capacity if the end state of charge (SOC) in CC stage is low. [12, 20] Therefore, CCCV charge protocol cannot significantly increase the charge rate. On the other hand, higher cell polarization can cause a more sever Li plating. [21-26]

Instead of CCCV, some other charging protocols have been proposed to reduce the charging time and cell degradation. For example, a multi-stage constant current (MCC) charging method has been considered in many studies. By utilizing several different levels of constant current, the cell can be charged at a high current in the beginning and a low current in the end, avoiding reaching the cut-off voltage too early. [27, 28] As reported, a ten-level MCC charging method can achieve both a 11% charging time reduction and a 16% reduction of capacity loss per cycle as compared to 1C CCCV in a commercial pouch

cell of nickel-manganese-cobalt-lithium oxide (NMC) cathode and graphite anode. [29] Current decay charging method is another way to decrease the charging voltage increase compared to CCCV. A linear current decay (LCD) charging protocol was developed with an empirical charging current equation $I = I_0 - k_1 t$. The proper slope k_1 and the initial current I_0 need to be chosen to prevent overcharging and to attain a maximum utilization. LCD can reduce the charge time by 2.5 times at the same charge depth compared with CC charging. [30] However, a cut-off voltage cannot be maintained at the end of charge because of too small charge current. Therefore, a varying current decay (VCD) charging protocol was proposed, in which the charging current is in the form $I(t) = (I_0 + k_1 t^{0.5}) / \left(1 + k_2 t^{0.5} + k_3 t\right)$. Compared with CCCV protocol, VCD showed a lower capacity fade with same end SOC for the same period. [31] Pulse charging protocol is also being widely considered for fast charging.

In pulse charging, resting and negative pulses are included periodically between charging pulses, speeding up relaxation of ion gradients and the concentration overpotential in the anode and alleviating lithium plating. [12, 23] The removal of the need for CV stage in pulse charging also effectively lower its charge time. [32, 33] However, a higher interfacial resistance was reported in pulse charging compared with direct current (DC) charging. [34] Boost charging protocol was developed according to the theory that close-to-fully discharged batteries can be recharged with very high currents for a short period of time without introducing any detrimental effects. Therefore, before traditional CCCV charging, a short period of high average charge current was introduced as boost stage in this protocol. It was reported that boost charging with 5 min of 4.5C can reduce

the charge time by 30%-40% compared to 1C CCCV without evident change in capacity degradation in 500 cycles for cylindrical batteries. But in prismatic batteries, boost charging lead to a faster degradation. [35]

Cell degradation is one of the main limiting factors for fast charging protocol. However, it is not easy to fully understood via experimental study only. It is not easy to exactly measure the amount of lithium plating and SEI layer under different charging condition. The fundamental relationship between lithium plating and transport properties in electrolyte and solid phase is not well-known. In addition, the parameters in fast charging protocols are usually needed to be optimized because the battery responses are strongly affected by the cell's geometry and its material system. [23, 36] Therefore, a proper battery model is essential in enabling a fast charging protocol. The common battery models for this purpose include equivalent circuit model (ECM) [36-40], single particle model (SP) [41-45], and pseudo-two-dimensional (P2D) model [46-52]. ECM uses an electric circuit to approximate the charge/discharge process in batteries, which cannot explain the mechanism of electrochemical response, especially the degradation reactions. SP model is established based on physical equations, but it simplifies the electrode into one particle and ignores the electrolyte dynamics, which results in some errors at high current loading conditions.

In this work, a physics-based P2D model with two key side reactions, lithium plating and SEI growth, is used to find an optimal charging protocol. The model parameters are identified by experiment data. The key to developing a new charging protocol is to control the rate of lithium plating in hotspots in the cell, where lithium plating is most severely encountered. This proposed new charging algorithms is called CQtCV. Based on

the CQtCV protocol, the voltage, current, deposited Li metal film thickness, SEI film thickness, and capacity are compared with the ones based on CCCV with long cycling results.

2. EXPERIMENT SETUP

Experimental validation of the proposed model was conducted based on a CR2032 coin cell test. It used MCMB as the anode, NMC622 as the cathode, and 1M LiPF6 dissolved in EC/DMC (1:1) as electrolyte. An NMC622 paste was prepared by mixing 85.5 wt% NMC622 powder (MSE supplies, 13 μm) with 6.5 wt% carbon black (CB, Alfa Aesar) and 8 wt% Polyvinylidene fluoride (PvdF, Sigma-Aldrich), followed by dispersing the mixture in N-Methyl-2-pyrrolidone solvent (NMP, Sigma-Aldrich). The MCMB paste was prepared by mixing MCMB powder with 5 wt% CB and 10 wt% PvdF in NMP. The electrode thickness was 40 μm for cathode and 30 μm for anode. The diameter is 14 mm and 16 mm for cathode and anode, respectively. The coin cell was assembled in an argon-filled glove box. A PP/PE/PP membrane (Celgard) of 25 μm thickness was used as the separator. The cell was firstly charge and discharge at 1C for 1 cycle and then put into a C rate test of 0.2C, 0.5C, 1C, 3C, 0.2C with 5 cycles for each C rate for model validation using battery testing station (Neware battery tester). After C rate test, a CCCV test is conducted in the cell in which the cell was charged using a constant current (CC) step at the rate of 3C to a cut-off voltage of 4.2 V, followed by a constant voltage (CV) step at 4.2 V until the charge current dropped below C/10. After getting the current profile of proposed

charging protocol from simulation, the profile will be imported into the test station and implemented on cell to run the CQtCV test.

3. MODEL DESCRIPTION

The model is based on the basic P2D model with modification to describe the lithium plating and SEI growth [53]. In this model, the thermal impact is ignored. The main governing equations are presented in Table 1.

The capacity degradation can be derived from the amount of Li ion consumed from these reactions separately as below.

$$\frac{dQ}{dt} = \frac{dQ_{SEI}}{dt} + \frac{dQ_{Li}}{dt} = i_{SEI} + i_{Li} \tag{16}$$

$$\frac{dQ_{SEI}}{dt} = i_{SEI} \tag{17}$$

$$\frac{dQ_{Li}}{dt} = i_{Li} \tag{18}$$

in which, Q_{SEI} and Q_{Li} are the capacity fade caused by SEI layer growth and Li plating. i_{SEI} and i_{Li} is the reaction current of SEI growth and Li plating. According to Eq. (18), i_{Li} is the main factor determining the capacity loss caused by Li plating. Therefore, in the new charging protocol, Li plating rate $\frac{dQ_{Li}}{dt}$ would be controlled directly to minimize charge time and cell degradation during charge process. The charge protocol is named as CQtCV.

Table 1. Governing equations in optimized charging model.

Region	**Governing Equation**	
Electrode	**Mass, solid phase** $\frac{\partial c_s}{\partial t} = \frac{1}{r^2}\frac{\partial}{\partial r}\left(D_s r^2 \frac{\partial c_s}{\partial r}\right)$ (1) $\left.\frac{\partial c_1}{\partial t}\right\|_{r=R} = -\frac{j_{\text{int}}}{F}$ (2)	**Charge, solid phase** $\nabla\cdot\left(\sigma_s^{eff}\nabla\phi_s\right) = j_{tot}$ (3)
Electrode/ **Separator**	**Mass, liquid phase** $\frac{\partial\left(\varepsilon c_e\right)}{\partial t} = \nabla\cdot\left(D_e^{eff}\nabla c_e\right) + \frac{1-t_+}{F} j_{tot}$ (4)	**Charge, liquid phase** $\nabla\cdot\left(\kappa_e^{eff}\nabla\phi_e\right) + \nabla\cdot\left(\kappa_D^{eff}\nabla\ln c_e\right) = -j_{tot}$ (5)
Electrode kinetics	$j_{\text{int}} = a i_{0,\text{int}}\left(\exp\left(\frac{\alpha_{a,\text{int}}F}{RT}\eta_{\text{int}}\right) - \exp\left(-\frac{\alpha_{c,\text{int}}F}{RT}\eta_{\text{int}}\right)\right)$ (6) $\eta_{\text{int}} = \phi_s - \phi_e - \frac{j_{tot}}{a}R_{film} - U_{\text{int}}$ (7)	

Table 1. Governing equations in optimized charging model. (Cont.)

Region	**Governing Equation**	
Side reactions	**SEI reaction**	**Li plating**
	$j_{SEI} = -aFk_{0,SEI}c_{EC}^{s}\exp\left(-\frac{\alpha_{c,SEI}F}{RT}\left(\phi_s - \phi_e - \frac{j_{tot}}{a}R_{film} - U_{SEI}\right)\right)$ (8)	$j_{lpl} = -ai_{0,lpl}\exp\left(-\frac{\alpha_{c,SEI}F}{RT}\left(\phi_s - \phi_e - \frac{j_{tot}}{a}R_{film}\right)\right)$ (11)
	$-D_{EC}\frac{c_{EC}^{s} - c_{EC}^{0}}{\delta_{film}} = -\frac{j_{SEI}}{F}$ (9)	$\frac{\partial c_{Li}}{\partial t} = -\frac{j_{lpl}}{F}(1-\beta)$ (12)
	$\frac{\partial c_{SEI}}{\partial t} = -\frac{j_{SEI}}{2F} - \frac{j_{lpl}}{2F}\beta$ (10)	
	$\delta_{film} = \frac{1}{a}\left(\frac{c_{SEI}\cdot M_{SEI}}{\rho_{SEI}} + \frac{c_{Li}\cdot M_{Li}}{\rho_{Li}}\right)$ (13)	
	$R_{film} = \omega_{SEI}\frac{\delta_{film}}{\kappa_{SEI}} = \frac{1}{a\cdot\kappa_{SEI}}\frac{c_{SEI}\cdot M_{SEI}}{\rho_{SEI}}$ (14)	
	Porosity $\frac{d\varepsilon_l}{dt} = -a\frac{d\delta_{film}}{dt}$ (15)	

4. RESULTS AND DISCUSSION

4.1. PARAMETER IDENTIFICATION

P2D model contains many physical parameters which are determined by the fabrication specs and battery material properties. The model parameters can be classified into two groups: non-degradation parameters and degradation parameters. Non-degradation parameters are the parameters independent to degradation reactions, which includes geometry parameters (e.g., battery component thickness and electrode particle size), initial conditions (e.g., initial SOC and initial SEI film thickness), and the current corresponding to 1C current. Degradation parameters are closely related to side reactions, including SEI reaction constant and Li plating exchange current density. The first step in the parameter identification process is to fit electrode particle size according to charge current in constant voltage (CV) charging process. The current decay rate in CV process is determined by Li ion diffusion at electrode particle surface, which is mainly impacted by electrode particle size and Li ion diffusivity in solid phase. Li ion diffusivity in solid phase is obtained by experiment in this work. Therefore, the electrode particle size can be specifically identified by CV current profile as shown in Figure 1(a). Then, other non-degradation parameters are fitted against the voltage profile of the first test cycle in experiment. The fitting results of two experiment cells are shown in Figure 1(b) and (c). The root mean square errors (RMSEs) between experimental and simulated voltage profiles are 0.061 V and 0.072 V for cell 1 and cell 2, respectively. The identified parameters are summarized in Table 2. Lastly, the degradation parameters in the model are identified by the capacity profile of C-rate test. The degradation parameters are assumed to be same for

cell 1 and cell 2 because it is mainly decided by battery materials. Therefore, the fitted values are 5.202e-15 m/s and 1.311e-5 A/m^2 for SEI reaction constant and Li plating exchange current density, respectively, with capacity RMSEs of 0.0024 and 0.0080 in cell 1 and cell 2 (Figure 2).

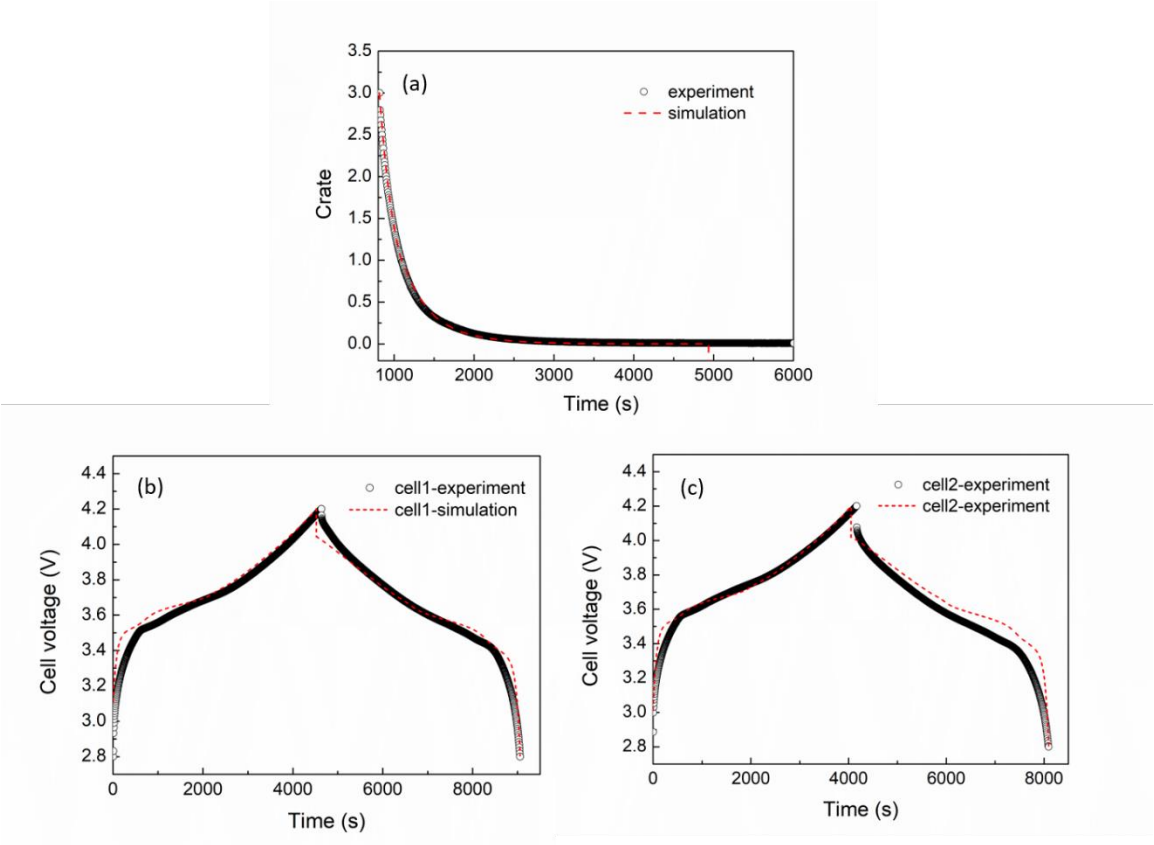

Figure 1. (a) Charge current C-rate in CV charging process, comparison of experimental and simulated voltage profile of the first test cycle in (b) cell1 and (c) cell2.

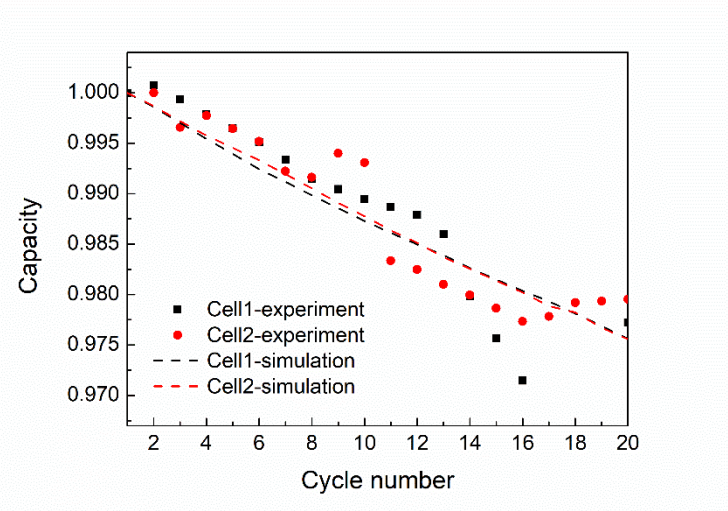

Figure 2. Comparison of experimental and simulated capacity profile of C-rate test in cell 1 and cell 2.

Table 2. Identified parameters.

		Cell1	Cell2
Non-degradation parameter	1C current (A)	6.3987	6.4961
	Initial SEI layer (m)	4.063e-09	4.063e-09
	Initial SOC Anode	0.0120	0.0080
	Initial SOC Cathode	0.9434	0.9396
	Cathode thickness (m)	3.782e-05	3.500e-05
	Anode thickness (m)	2.803e-05	2.500e-05
	Separator thickness (m)	2.599e-05	2.400e-05
Degradation parameter	SEI reaction constant (m/s)	5.202e-15	
	Li plating exchange current (A/m^2)	1.311e-5	

4.2. OPTIMIZED CHARGING ALGORITHM - CQTCV

The proposed CQtCV is to optimize cell degradation and charge time by controlling Li plating rate (Li plating current). As shown in Figure 3, there are four steps in CQtCV process: first, the cell is charged with a constant current with a upper current limit for 30s to avoid the charge voltage exceeds certain bound; secondly, a constant slope $\frac{d^2Q_{Li}}{dt^2}$ is implement until the $\frac{dQ_{Li}}{dt}$ reaches a threshold; thirdly, the cell is charged with the threshold value of $\frac{dQ_{Li}}{dt}$ until the voltage reaches a pre-determined value (4.2 V); Lastly, the cell is charged under constant voltage until the cell capacity reaches pre-determined value, for example, 80 %.

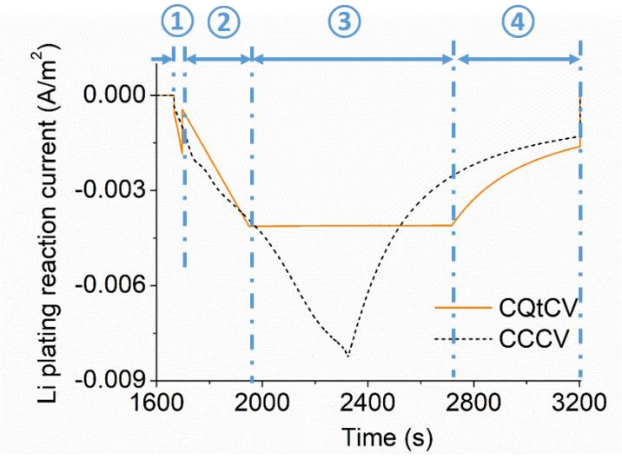

Figure 3. Li plating current as a function of time in CCCV and CQtCV in charge process.

With the obtained parameters in section 4.1, the battery model of cell 1 and cell 2 can be applied to generate charge current by implementing CQtCV algorithm. The comparison of the simulation results of CCCV and CQtCV algorithm in two experiment cells are shown in Figures 4 and 5. Take cell 1 as an example. As shown in Figure 4(a), the cell voltage of CQtCV increases faster than CCCV and it stops at 4.18 V when cell capacity reaches 80%, while CCCV stops at 4.16 V. Average charge current C-rate in CQtCV is around 4.25 C, and in consequence, the charge time in CQtCV is 29% less than CCCV. Regarding cell degradation, as shown in Figure 4(c) and (d), both the Li plating rate and SEI layer growth rate are faster in CQtCV than in CCCV. However, compared with CCCV, the total amount of deposited Li metal film thickness increases 0.008 % and SEI film thickness reduces 0.323 %. The capacity shown in Figure 4(f) is the ratio of remaining amount of reversible Li ion, which can be expressed as

$$Q_{rev} = 1 - \frac{c_{Li} + 2 \cdot c_{SEI}}{\int_{1st\ cycle} \frac{1}{a}\left(j_{\text{int}} + j_{SEI} + j_{lpl} \right) dt} \tag{19}$$

As a result, the remaining capacity in CQtCV is 0.011 % higher than CCCV after 1 cycle of 1C/1C test. The implementation of CQtCV shows a similar result in cell 2 as shown in Figure 5. In cell 2, CQtCV reduces the charge time by 21.7% in comparison of CCCV algorithm. The deposited Li film thickness increases 0.016 % and SEI layer thickness decreases 0.23 % in CQtCV, along with a 0.006 % improvement in capacity retention. The effect divergence between cell 1 and cell 2 is caused by the different initial condition and geometry parameters as shown in Table 2.

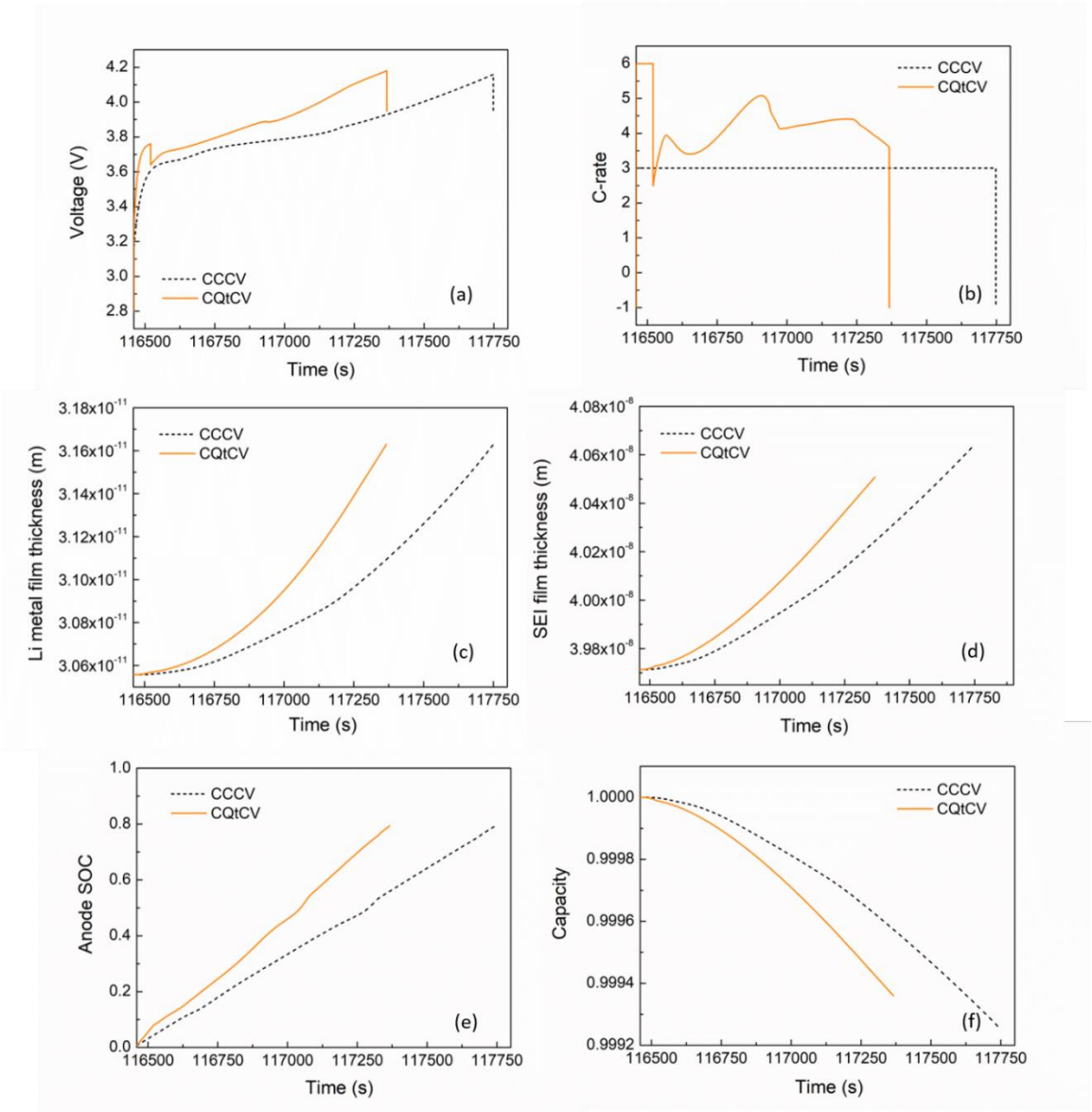

Figure 4. Comparison of (a) cell voltage (b) applied current C-rate (c) plated Li metal film thickness (d) SEI film thickness (e) anode SOC (f) capacity for 3C CCCV and CQtCV simulated based on battery model of cell 1.

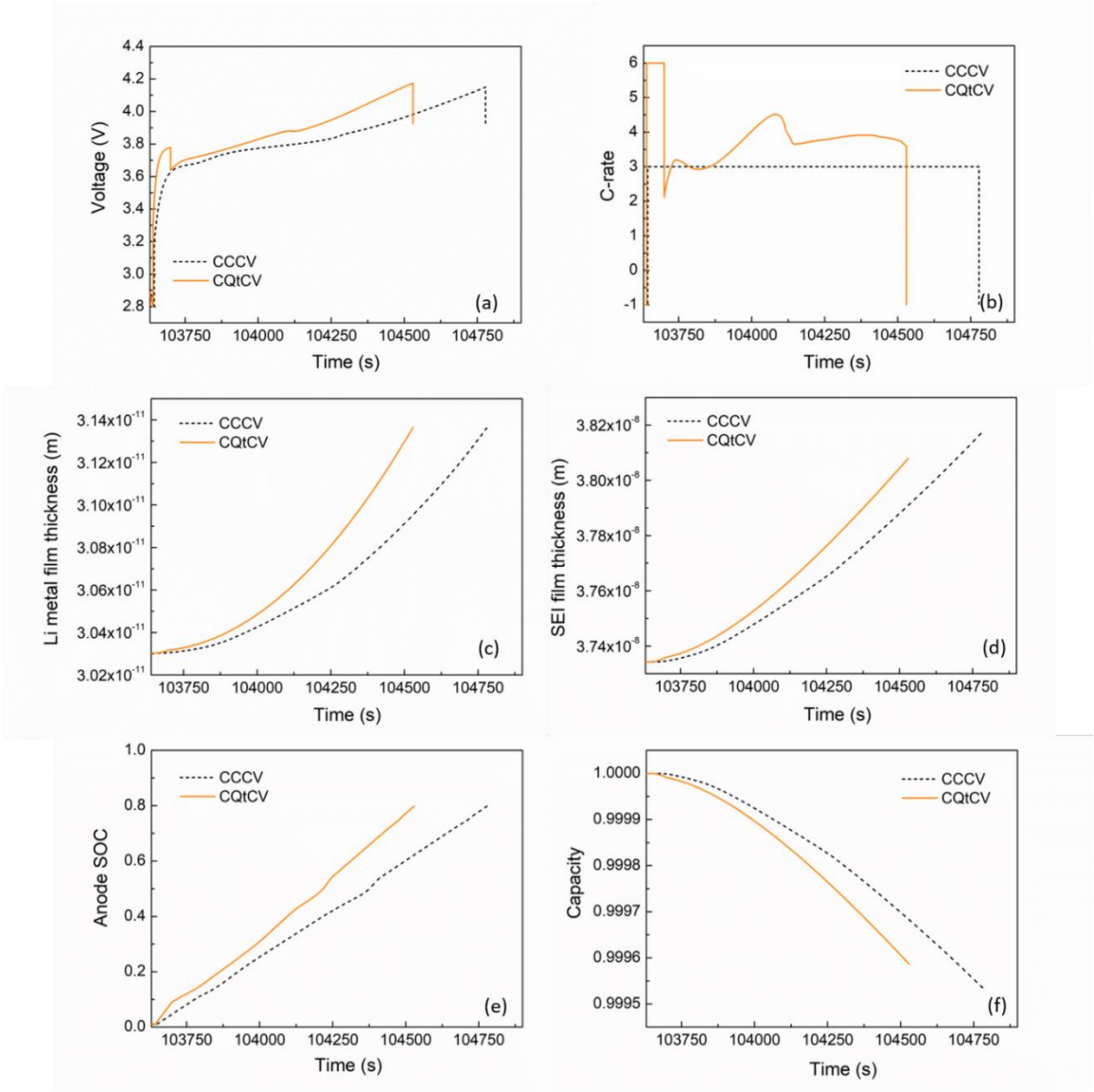

Figure 5. Comparison of (a) cell voltage (b) applied current C-rate (c) plated Li metal film thickness (d) SEI film thickness (e) anode SOC (f) capacity for 3C CCCV and CQtCV simulated based on battery model of cell 2.

The long cycling performance of two charge algorithms are investigated as shown in Figure 6 and Figure 7. The CCCV implemented as a reference here is of 3C charge and 1C discharge. Figure 6 (a) shows the charging time of two charging algorithms in 50 cycles

in cell 1. The average charging time is 1,285 s of CCCV, while is 906 s of CQtCV, that is about 29.5 % reduction in charging time via CQtCV. Figure 6 (b) and (c) show the growth of Li film and SEI film as a function of time in 50 cycles. As shown, the CQtCV accelerates Li plating but suppress the growth rate of SEI film compared with CCCV. As a result, the total thickness of plated Li metal film increases 0.2 %, and the thickness of SEI film decreases 7.1 % in CQtCV. In terms of the capacity fade caused by Li loss in Li plating and SEI reaction, the capacity retention after 50 cycling test is 0.46% higher in CQtCV than that of CCCV. The simulation results of two algorithms in cell2 are shown in Figure 7. The results are in the same trend with that in cell 2, where CQtCV shorten the charge time by 21 %, increases Li metal film thickness by 0.26 % and decreases SEI film thickness by 5.23 % in comparison with CCCV. After 50 cycles, the total capacity retention is improved 0.21 % by CQtCV. Therefore, it can be concluded that CQtCV is effective in reducing the charging time and reform capacity degradation compared with traditional charge algorithm CCCV.

5. CONCLUSIONS

An optimized charging protocol CQtCV based on regulating Li plating current has been proposed. Li plating current is provided by a full order electrochemical model in which two main side reaction during charge process: SEI layer growth and Li plating are included. Physical parameters in the model were classified as degradation-independent and degradation-dependent ones, and were identified by 1st cycle's voltage profile and capacity profile of C-rate test, respectively. The performance of two charging algorithms was

evaluated based on the fitted model. It was proved that the proposed charging protocol can effectively reduce charge time (>20%) and improve capacity degradation at the same time. The capacity improvement in CQtCV mainly comes from the suppression of SEI layer growth, however, Li plating would be slightly promoted in this process.

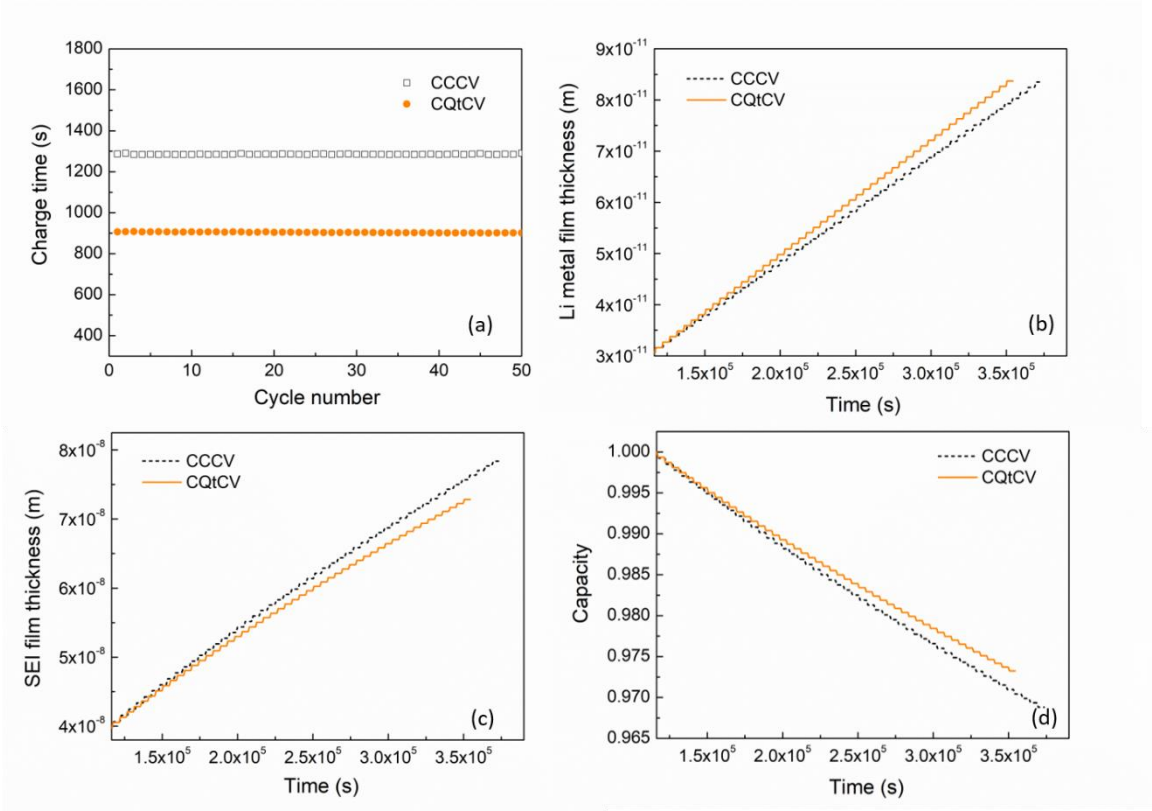

Figure 6. Comparison of (a) charge time vs. cycle number (b) Li metal film thickness (c) SEI film thickness and (d) capacity fade in 3C CCCV and CQtCV in cell 1.

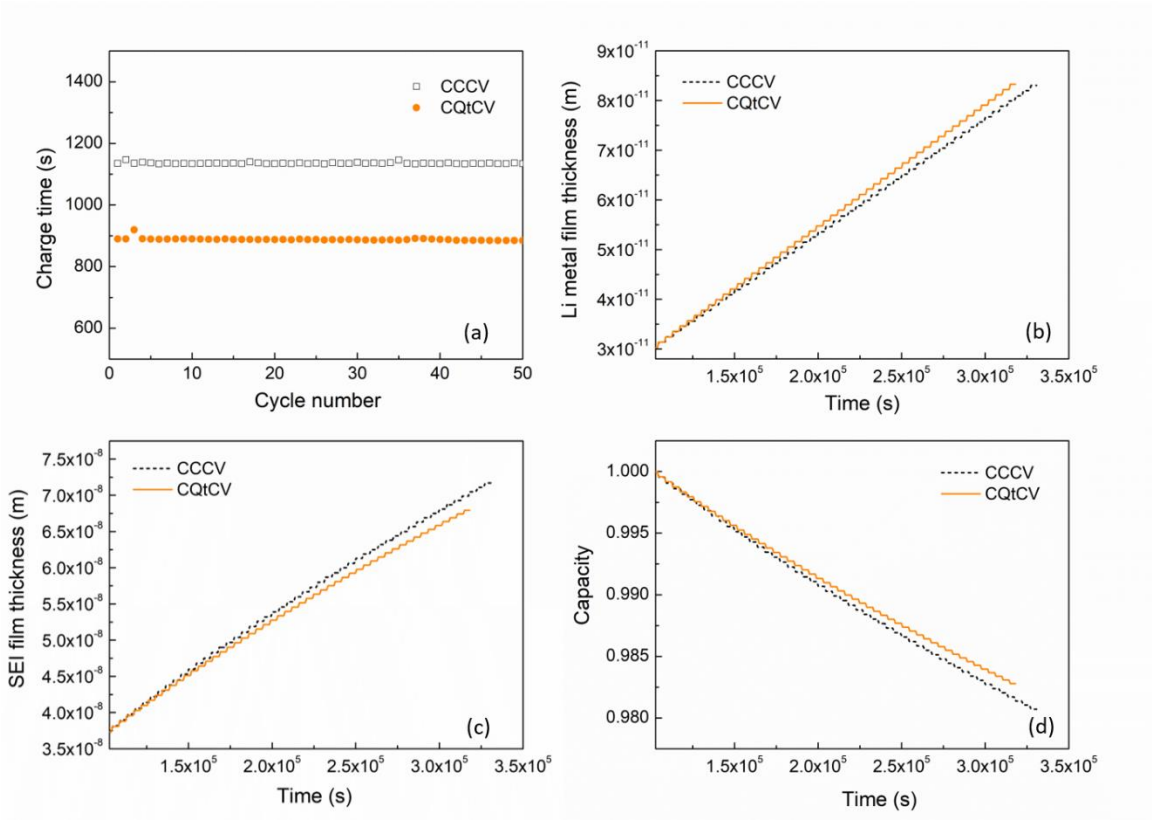

Figure 7. Comparison of (a) charge time vs. cycle number (b) Li metal film thickness (c) SEI film thickness and (d) capacity fade in 3C CCCV and CQtCV in cell 2.

REFERENCES

1. Colclasure, A.M., et al., Requirements for enabling extreme fast charging of high energy density Li-Ion cells while avoiding lithium plating. Journal of the Electrochemical Society, 2019. **166**(8): p. A1412.

2. Vetter, J., et al., Ageing mechanisms in lithium-ion batteries. Journal of Power Sources, 2005. **147**(1): p. 269-281.

3. Ahmed, S., et al., Enabling fast charging – A battery technology gap assessment. Journal of Power Sources, 2017. **367**: p. 250-262.

4. Burns, J., D. Stevens, and J. Dahn, In-situ detection of lithium plating using high precision coulometry. Journal of the Electrochemical Society, 2015. **162**(6): p. A959.

5. Waldmann, T., B.-I. Hogg, and M. Wohlfahrt-Mehrens, Li plating as unwanted side reaction in commercial Li-ion cells – A review. Journal of Power Sources, 2018. **384**: p. 107-124.

6. Waldmann, T., et al., Temperature dependent ageing mechanisms in Lithium-ion batteries – A Post-Mortem study. Journal of Power Sources, 2014. **262**: p. 129-135.

7. Pramanik, S. and S. Anwar, Electrochemical model based charge optimization for lithium-ion batteries. Journal of Power Sources, 2016. **313**: p. 164-177.

8. Suthar, B., et al., Optimal charging profiles for mechanically constrained lithium-ion batteries. Physical Chemistry Chemical Physics, 2014. **16**(1): p. 277-287.

9. Epding, B., et al., Aging-Optimized Fast Charging of Lithium Ion Cells Based on Three-Electrode Cell Measurements. Energy Technology, 2020: p. 2000457.

10. Fleischhammer, M., et al., Interaction of cyclic ageing at high-rate and low temperatures and safety in lithium-ion batteries. Journal of Power Sources, 2015. **274**: p. 432-439.

11. Raj, A., M.-T.F. Rodrigues, and D.P. Abraham, Rate-Dependent Aging Resulting from Fast Charging of Li-Ion Cells. Journal of The Electrochemical Society, 2020. **167**(12): p. 120517.

12. Yin, Y., et al., New fast charging method of lithium-ion batteries based on a reduced order electrochemical model considering side reaction. Journal of Power Sources, 2019. **423**: p. 367-379.

13. Verma, P., P. Maire, and P. Novák, A review of the features and analyses of the solid electrolyte interphase in Li-ion batteries. Electrochimica Acta, 2010. **55**(22): p. 6332-6341.

14. Xia, S., et al., Chemomechanical interplay of layered cathode materials undergoing fast charging in lithium batteries. Nano Energy, 2018. **53**: p. 753-762.

15. Tanim, T.R., et al., Extreme Fast Charge Challenges for Lithium-Ion Battery: Variability and Positive Electrode Issues. Journal of The Electrochemical Society, 2019. **166**(10): p. A1926-A1938.

16. Xu, R., et al., Heterogeneous damage in Li-ion batteries: Experimental analysis and theoretical modeling. Journal of the Mechanics and Physics of Solids, 2019. **129**: p. 160-183.

17. Liu, H., et al., Intergranular Cracking as a Major Cause of Long-Term Capacity Fading of Layered Cathodes. Nano Letters, 2017. **17**(6): p. 3452-3457.

18. Cope, R.C. and Y. Podrazhansky. The art of battery charging. in Fourteenth Annual Battery Conference on Applications and Advances. Proceedings of the Conference (Cat. No. 99TH8371). 1999. IEEE.

19. Chu, Z., et al., Non-destructive fast charging algorithm of lithium-ion batteries based on the control-oriented electrochemical model. Applied energy, 2017. **204**: p. 1240-1250.

20. Hasan, M.F., et al., Analysis of the implications of rapid charging on lithium-ion battery performance. Journal of the Electrochemical Society, 2015. **162**(7): p. A1382.

21. Xu, M., et al., Modeling the effect of two-stage fast charging protocol on thermal behavior and charging energy efficiency of lithium-ion batteries. Journal of Energy Storage, 2018. **20**: p. 298-309.

22. Keil, P. and A. Jossen, Charging protocols for lithium-ion batteries and their impact on cycle life—An experimental study with different 18650 high-power cells. Journal of Energy Storage, 2016. **6**: p. 125-141.

23. Mai, W., A.M. Colclasure, and K. Smith, Model-Instructed Design of Novel Charging Protocols for the Extreme Fast Charging of Lithium-Ion Batteries Without Lithium Plating. Journal of The Electrochemical Society, 2020. **167**(8): p. 080517.

24. Zhang, S.S., K. Xu, and T. Jow, Study of the charging process of a LiCoO2-based Li-ion battery. Journal of power sources, 2006. **160**(2): p. 1349-1354.

25. Dung, L., C. Chen, and H. Yuan. A robust, intelligent CC-CV fast charger for aging lithium batteries. in 2016 IEEE 25th International Symposium on Industrial Electronics (ISIE). 2016.

26. Zhang, S.S., The effect of the charging protocol on the cycle life of a Li-ion battery. Journal of power sources, 2006. **161**(2): p. 1385-1391.

27. Vo, T.T., et al., New charging strategy for lithium-ion batteries based on the integration of Taguchi method and state of charge estimation. Journal of Power Sources, 2015. **273**: p. 413-422.

28. Spingler, F.B., et al., Optimum fast charging of lithium-ion pouch cells based on local volume expansion criteria. Journal of Power Sources, 2018. **393**: p. 152-160.

29. Anseán, D., et al., Fast charging technique for high power lithium iron phosphate batteries: A cycle life analysis. Journal of Power Sources, 2013. **239**: p. 9-15.

30. Sikha, G., et al., Comparison of the capacity fade of Sony US 18650 cells charged with different protocols. Journal of power sources, 2003. **122**(1): p. 67-76.

31. Chung, S., et al., On charge conditions for Li-ion and other secondary lithium batteries with solid intercalation electrodes. Journal of power sources, 1999. **79**(2): p. 205-211.

32. Aryanfar, A., et al., Dynamics of lithium dendrite growth and inhibition: Pulse charging experiments and Monte Carlo calculations. The journal of physical chemistry letters, 2014. **5**(10): p. 1721-1726.

33. Amanor-Boadu, J.M., A. Guiseppi-Elie, and E. Sánchez-Sinencio, Search for optimal pulse charging parameters for Li-ion polymer batteries using Taguchi orthogonal arrays. IEEE Transactions on Industrial Electronics, 2018. **65**(11): p. 8982-8992.

34. Li, J., et al., The effects of pulse charging on cycling characteristics of commercial lithium-ion batteries. Journal of Power Sources, 2001. **102**(1-2): p. 302-309.

35. Notten, P.H., J.O. het Veld, and J. Van Beek, Boostcharging Li-ion batteries: A challenging new charging concept. Journal of Power Sources, 2005. **145**(1): p. 89-94.

36. Rai, R., et al. Multi-Level Constant Current Based Fast Li-Ion Battery Charging Scheme With LMS Based Online State of Charge Estimation. in 2020 IEEE Kansas Power and Energy Conference (KPEC). 2020. IEEE.

37. Zhang, L., et al., Comparative research on RC equivalent circuit models for lithium-ion batteries of electric vehicles. Applied Sciences, 2017. **7**(10): p. 1002.

38. Liaw, B.Y., et al., Modeling of lithium ion cells—A simple equivalent-circuit model approach. Solid state ionics, 2004. **175**(1-4): p. 835-839.

39. Hariharan, K.S. and V.S. Kumar, A nonlinear equivalent circuit model for lithium ion cells. Journal of power sources, 2013. **222**: p. 210-217.

40. Liao, C., H. Li, and L. Wang. A dynamic equivalent circuit model of LiFePO 4 cathode material for lithium ion batteries on hybrid electric vehicles. in 2009 IEEE Vehicle Power and Propulsion Conference. 2009. IEEE.

41. Zhang, X., A.M. Sastry, and W. Shyy, Intercalation-induced stress and heat generation within single lithium-ion battery cathode particles. Journal of The Electrochemical Society, 2008. **155**(7): p. A542-A552.

42. Zhang, D., B.N. Popov, and R.E. White, Modeling Lithium Intercalation of a Single Spinel Particle under Potentiodynamic Control. Journal of The Electrochemical Society, 2000. **147**(3): p. 831-838.

43. Li, J., et al., A Single Particle-Based Battery Degradation Model Including Chemical and Mechanical Degradation Physics. ECS Transactions, 2017. **77**(11): p. 1003-1014.

44. Guo, M., G. Sikha, and R.E. White, Single-Particle Model for a Lithium-Ion Cell: Thermal Behavior. Journal of The Electrochemical Society, 2011. **158**(2): p. A122-A132.

45. Pals, C.R. and J. Newman, Thermal Modeling of the Lithium/Polymer Battery: I . Discharge Behavior of a Single Cell. Journal of The Electrochemical Society, 1995. **142**(10): p. 3274-3281.

46. Grazioli, D., M. Magri, and A. Salvadori, Computational modeling of Li-ion batteries. Computational Mechanics, 2016. **58**(6): p. 889-909.

47. Akolkar, R., Mathematical model of the dendritic growth during lithium electrodeposition. Journal of Power Sources, 2013. **232**: p. 23-28.

48. Wang, C.-W. and A.M. Sastry, Mesoscale modeling of a Li-ion polymer cell. Journal of the Electrochemical Society, 2007. **154**(11): p. A1035-A1047.

49. Safari, M., et al., Multimodal physics-based aging model for life prediction of Li-ion batteries. Journal of The Electrochemical Society, 2009. **156**(3): p. A145-A153.

50. Jokar, A., et al., Review of simplified Pseudo-two-Dimensional models of lithium-ion batteries. Journal of Power Sources, 2016. **327**: p. 44-55.

51. Newman, J. and W. Tiedemann, Porous-electrode theory with battery applications. AIChE Journal, 1975. **21**(1): p. 25-41.

52. Doyle, M., T.F. Fuller, and J. Newman, Modeling of Galvanostatic Charge and Discharge of the Lithium/Polymer/Insertion Cell. Journal of The Electrochemical Society, 1993. **140**(6): p. 1526-1533.

53. Chen, L., et al., Modulation of dendritic patterns during electrodeposition: A nonlinear phase-field model. Journal of Power Sources, 2015. **300**: p. 376-385.

V. A CONTROL ORIENTED COMPREHENSIVE DEGRADATION MODEL FOR BATTERY ENERGY STORAGE SYSTEM LIFE PREDICTION

ABSTRACT

In order to ensure that stationary battery energy storage systems (BESSs) provide reliable energy buffering, both for power quality and economic purposes, degradation must be considered. Cell degradation involves various side reactions and is highly dependent on its operating conditions. To accurately track cell degradation and predict its impact on battery behavior, a comprehensive physics-based degradation model based on an electrolyte phase-enhanced single particle (SP) model was developed. Key degradation physics, namely solid electrolyte interphase (SEI) layer formation and growth, Li plating on the graphite anode, and Mn dissolution on cathode of nickel-cobalt-manganese oxide (NMC622) were considered. The model was validated against experimental capacity data. The results revealed that the deposition rates of both SEI layer and Li metal increased as the charge voltage increased. At the cathode side, the solvent oxidation rate determined the Mn dissolution rate. As a result, the volume fraction of NMC622 in the cathode continually decreased at a gradually rising rate. The impacts of three key degradation physics were analyzed. It was found that SEI layer growth played a main role in capacity fade in initial about 2000 cycles while Mn dissolution has a significant impact after about 1000 cycles. Furthermore, current is a critical impact factor in side reactions. High charge current was revealed slowing down the Mn dissolution and speed up the SEI layer growth and Li plating, and high discharge current accelerates Mn dissolution. A sensitivity study of side

reaction coefficients was conducted as a guidance for simulating degradation behavior of various material systems.

1. INTRODUCTION

Battery energy storage systems (BESSs) are essential for electrical grids to yield smooth fluctuations in power generation from various sources such as wind and solar [1]. Lithium ion batteries (LIBs) are generally applied in BESSs due to their advantages in low cost, high energy and power density and long cycle life [2, 3]. However, the performance of LIBs changes as degradation occurs during charging and discharging cycles. The degradation rate depends on many factors, e.g., depth-of discharge (DOD), charge and discharge currents, state of charge (SOC), lower and upper voltage limits, and environmental temperature [4-6]. To ensure the optimized utilization and work life of BESSs for power quality and economic purposes, the degradation of BESSs under different operation conditions must be well-managed. [1, 7]

The aging mechanisms of lithium ion batteries have various explanations and are not thoroughly understood at present. Some physics reactions were proposed that can impact battery life including, but not limited to, current collector corrosion, electrolyte decomposition, solid electrolyte interphase (SEI) layer formation, Li plating, structural changing in cycling, phase transformation, and chemical decomposition or dissolution [8-15]. The primary cause of batteries' performance deteriorations is typically SEI formation and growth. In graphite-based anode, the working voltage is around 0.05 V, which is outside the stabilized voltage window of common liquid organic electrolytes 1V~ 4.5V

[16-18]. Therefore, the graphite-based anode was unstable against electrolyte. The solvent in electrolytes can be reduced on the anode surface, and it forms a passivation protective layer, that is, a SEI layer [19-21]. The SEI layer is mainly formed in the initial a few cycles and it can restrict further anode corrosion and electrolyte reduction. The expansion and contraction of anodes during charge and discharge process generate cracks in the SEI film, leading to an exposure of lithiated anode surface to electrolyte and a continuous growth in the SEI layer [22, 23]. The reaction rate of later SEI growth slows down, compared with initial stage, because of the limitation of solvent molecule diffusion and the kinetics of decomposition reaction [24, 25]. The formation and continuous growth of the SEI film consume reversible Li ions, increase the cell's impedance, and reduce the electrodes' porosity, which is the main cause for capacity degradation.

Lithium plating is recognized as another hazardous aging mechanism in lithium ion batteries. It occurs at the anode surface when the local potential is less than 0 V (vs. Li/Li+) [24, 26, 27]. For example, at low temperature, the intercalation rate is too slow so that overpotential is needed to retain the given net current, which could induce the lithium plating. Under a high charge current, the mass transport rate is much larger than the intercalation speed that lots of Li ion accumulated on the anode surface, resulting in a large polarization, in which lithium deposition easily occurs [28-31]. Lithium plating consumes lithium ions inventory, leading to a capacity loss. Moreover, serious lithium deposition could form lithium dendrite, which can cause the penetration of separator, subsequent internal short circuit, and cell failure [23].

The NMC (lithium nickel manganese cobalt oxide) cathode is a promising material for lithium ion batteries due to its high energy density and low price. A primary aging

mechanism for NMC cathode is the dissolution of active material, which is a common phenomenon in Mn-based electrodes [24]. At elevated temperatures and charged states, the structural component Mn3+ is unstable and tend to disproportion into Mn2+ and Mn4+, in which Mn2+ dissolves in the electrolyte and Mn4+ stays in solid structure [23]. The dissolution of NMC material will cause a reduction of Li ion insertion sites, leading to a capacity fade. The dissolved manganese ions can also migrate to the anode side and deposit onto the electrode surface, which will further intensify electrolyte decomposition and increase the electrode impedance [23, 32-37].

To quantify the impact of aging physics on cell property, physics-based models are introduced to describe the battery performance evolution and analyze physical and chemical phenomena during battery utilization. To simulate the behavior of SEI formation and growth, most researchers use a kinetically limited SEI growth model with a Tafel equation on a basis of pseudo-two-dimensional (P2D) model [38-41]. Then, the diffusion of the electrolyte solvent in the SEI film was included as another limitation for SEI reaction [42-45]. The porosity reduction caused by SEI deposits was also considered as a side effect in some of these models [46]. Another common method to simulate SEI reaction is to write solid phase concentration as a function of the cycle according to Li-ion loss. In these models, the SEI growth process was divided into several stages: SEI formation om initial anode surface, SEI formation due to crack propagation and SEI thickness growth on cracked surface. Then, the capacity loss could be derived on a basis of cycle number [44, 47, 48]. Lithium plating was usually treated following standard Butler-Volmer or Tafel kinetics [49-52]. The degradation effects of lithium plating in simulations were similar with that of SEI growth. The deposited film grew thicker, clogging the anode pores and

consuming total exchange current. Some studies simulated lithium plating as a partially reversible process during which stripping occurs when local overpotential is positive with a ratio against the plating amount [53, 54]. Most mathematic models for Mn dissolution were established according to a Mn3+ disproportionation mechanism. Two acid generation reactions, solvent oxidation, and salt decomposition were usually considered trigger reactions for Mn dissolution [55, 56]. Furthermore, as a main side reaction at cathode, the comprehensive degradation effects of Mn dissolution was studied coupled with SEI reaction occurring at anode [57, 58].

Most of the physics-based degradation models belong to full order electrochemical model, which is too complex and computational expensive to be implemented in control system. To simplify the simulation, a single particle (SP) model is widely used as a reduced order electrochemical model to map the Li ion concentrations under various operation conditions. Jie et al. developed a comprehensive degradation model based on a SP model, and included side reactions of SEI growth and Mn dissolution [57]. The capacity loss caused by SEI reaction was counted by cycle, and several side effects in the Mn dissolution, such as diffusion of H^+, Mn^{2+} and H_2O and deposition of H^+, Mn^{2+} on anode surface were ignored.

In this work, a comprehensive degradation model that includes side reactions such as SEI layer growth, Li plating in the anode, and Mn dissolution in cathode was developed. To make the model computationally efficient, it is established based on a reduced-order single particle (SP) model that includes electrolyte phase dynamics. The model parameters are validated against the experimental data. Based on this model, the relationship among the deposition rate of SEI layer, Li metal, and charge voltage on anode degradation is

found. Also, on the cathode side, the correlation among solvent oxidation, proton concentration, and Mn dissolution reaction rate is identified. The Crate impact on each degradation physics are investigated, and the degradation parameters' sensitivity on capacity fade are studied.

2. MODEL DESCRIPTION

In the SP model, the active material in each electrode is represented by a particle. All the side reactions are assumed to take place uniformly on the particles' surface. The concentration and potential distribution are as assumed to be uniform in the solid phase; however, their gradients in the electrolyte phase are taken into consideration to improve model accuracy. The details of electrolyte-phase enhanced SP model are presented in previous work [57].

At the anode side, the SEI reaction and Li plating currents, respectively, are expressed using the following cathodic Tafel expressions:

$$i_{SEI} = -Fk_{0,SEI}c_{EC}^{s}\exp\left(-\frac{\alpha_{c,SEI}F}{RT}\left(\phi_{s,n}-\phi_{e,n}-i_{loc,n}R_{film}-U_{SEI}\right)\right) \quad (1)$$

$$i_{lpl} = -i_{0,lpl}\exp\left(-\frac{\alpha_{c,lpl}F}{RT}\left(\phi_{s,n}-\phi_{e,n}-i_{loc,n}R_{film}\right)\right) \quad (2)$$

where $k_{0,SEI}$ is the kinetic rate constant, c_{EC}^{s} is the concentration of EC at anode particle surface, $\alpha_{c,SEI}$ and $\alpha_{c,lpl}$ are the charge transfer coefficient, $i_{loc,n}$ is the total exchange current density, R_{film} is the ohmic resistance of surface film, U_{SEI} is the equilibrium potential of SEI deposition, $i_{0,lpl}$ is the exchange current density of Li deposition and $\phi_{s,n}$

and $\phi_{e,n}$ are solid phase potential and liquid phase potential for anode, respectively. The diffusion of solvent in surface film on anode surface is described as:

$$-D_{EC}\frac{c_{EC}^{s}-c_{EC}^{0}}{\delta_{film}}=-\frac{j_{SEI}}{F} \tag{3}$$

in which D_{EC} is the EC diffusivity, c_{EC}^{0} is the EC concentration in bulk electrolyte and δ_{film} is the surface film thickness. The molar concentration of deposited SEI layer and Li metal per unit volume of the electrode can be obtained from:

$$\frac{\partial c_{SEI}}{\partial t}=-\frac{i_{SEI}\cdot a_{s}^{neg}}{2F} \tag{4}$$

$$\frac{\partial c_{Li}}{\partial t}=-\frac{i_{lpl}\cdot a_{s}^{neg}}{F}\ , \tag{5}$$

where a_{s}^{neg} is the specific surface area of anode. The film resistance is only counted for SEI layer, which is calculated as:

$$R_{film}=\frac{1}{a_{s}^{neg}\cdot\kappa_{SEI}}\frac{c_{SEI}\cdot M_{SEI}}{\rho_{SEI}} \tag{6}$$

where κ_{SEI} is ionic conductivity, M_{SEI} is molar weight and ρ_{SEI} is the density of SEI film. The surface film thickness is:

$$\delta_{film}=\frac{1}{a_{s}^{neg}}\left(\frac{c_{SEI}\cdot M_{SEI}}{\rho_{SEI}}+\frac{c_{Li}\cdot M_{Li}}{\rho_{Li}}\right) \tag{7}$$

in which M_{Li} and ρ_{Li} are molar weight and density of Li metal film. The surface film growth can lead to a porosity decrease in anode particle, so the liquid phase volume fraction in anode can be expressed as:

$$\frac{d\varepsilon_{e,n}}{dt} = -a_n \frac{d\delta_{film}}{dt} \tag{8}$$

in which $\varepsilon_{e,n}$ is the volume fraction of liquid phase. The total volumetric current density at anode side is the sum of the current densities of intercalation reaction, SEI layer formation and Li plating:

$$i_{loc,n} = i_{\text{int},n} + i_{SEI} + i_{lpl} \tag{9}$$

At the cathode side, Mn dissolution is induced by acid attack. There are two sources of acid generation, solvent decomposition and $LiPF_6$ decomposition. The solvent decomposition reaction is expressed as:

$$Solvent \xrightarrow{Oxidation} Sl_o + H^+ + e^- \tag{10}$$

where Sl_o represents the overall products of the solvent oxidation, including soluble species and solid species. Its reaction rate can be written as:

$$R_{s,1}(t) = \frac{a_p i_{0,ox}}{F} \exp\left(\frac{0.5F}{RT}\eta_{ox}(t)\right) \tag{11}$$

where $i_{0,ox}$ is the exchange current density, η_{ox} is the overpotential for the solvent oxidation, which is:

$$\eta_{ox}(t) = \phi_{1,p}(t) - \phi_{2,p}(t) - U_{ox}^{eq}, \tag{12}$$

where U_{ox}^{eq} is the equilibrium potential for solvent oxidation. The number of protons generated from the $LiPF_6$ salt decomposition is given by:

$$\begin{aligned} &LiPF_6 \rightarrow LiF + PF_5 \\ &PF_5 + H_2O \rightarrow POF_3 + 2H^+ + 2F^- \end{aligned} \tag{13}$$

The salt decomposition rate is:

$$R_{s,2}(t) = k_{decom} c_{H_2O}^2(t) c_{LiPF_6}(t) \tag{14}$$

where c_{LiPF_6} is the concentration of $LiPF_6$, c_{H_2O} is the concentration of H_2O, and k_{decom} is the salt decomposition coefficient. The active material in cathode in this work is considered as $LiNi_{0.6}Mn_{0.2}Co_{0.2}O_2$ (NMC622). Mn dissolution reaction of NMC622 is given by:

$$\begin{aligned} &LiNi_{0.6}Mn_{0.2}Co_{0.2}O_2 + (3.2+2x)H^+ \rightarrow \\ &Li^+ + \frac{x}{2}Mn^{2+} + \left(0.1-\frac{x}{4}\right)Mn_2O_4 + (0.2-x)A^{2+} + (0.6+x)A^{3+} + (1.6+x)H_2O \end{aligned} \tag{15}$$

where A is Ni or Co element, x is the molar of Mn^{3+} in 1 molar $LiNi_{0.6}Mn_{0.2}Co_{0.2}O_2$ because the chemical valence of Mn is a mixture of +3 and +4 and the chemical valence of Ni and Co is a mixture of +2 and +3 in $LiNi_{0.6}Mn_{0.2}Co_{0.2}O_2$. In this work, x is assumed as 0.1. It is assumed that the reaction rate of the acid attack on the cathode, as shown in Eq. 13, is dominated by the acid concentration in the solution. Therefore, the reaction rate for the reaction in Eq. 13 is given by:

$$R_{s,3}(t) = k_{dis}c_{H^+}(t), \tag{16}$$

where k_{dis} is the reaction rate constant for the acid attach on the active material, and c_{H^+} is concentration of H^+. In addition, the produced H^+ could deposited at anode particle surface as H_2, which is described by:

$$H^+ + e^- \rightarrow \frac{1}{2}H_2(g). \tag{17}$$

Its deposition current is given by:

$$i_{H_2} = -e^{-\lambda_{H_2}\delta_{SEI}}Fk_{H_2}c_{H^+}\exp\left[-\frac{\alpha_c^{H_2}F}{RT}(\phi_1-\phi_2)\right]. \tag{18}$$

Considering the diffusion law of each by-product, the concentration of protons and water, respectively, in the cathode and anode are:

$$\varepsilon_{e,p}\frac{\partial c_{H^+}(t)}{\partial t}=\nabla\cdot\left(D_{eff,H^+}\nabla c_{H^+}\right)+\frac{1}{F}\left(R_{s,1}(t)+R_{s,2}(t)-3.4a_s^{pos}R_{s,3}(t)\right) \tag{19}$$

$$\varepsilon_{e,n}\frac{\partial c_{H^+}(t)}{\partial t}=\nabla\cdot\left(D_{eff,H^+}\nabla c_{H^+}\right)+\frac{1}{F}\left(R_{s,2}(t)+a_s^{neg}i_{H_2}\right) \tag{20}$$

$$\varepsilon_{e,p}\frac{\partial c_{H_2O}(t)}{\partial t}=\nabla\cdot\left(D_{eff,H_2O}\nabla c_{H_2O}\right)+\frac{1}{F}\left(-R_{s,2}(t)+2a_s^{pos}R_{s,3}(t)\right) \tag{21}$$

$$\varepsilon_{e,n}\frac{\partial c_{H_2O}(t)}{\partial t}=\nabla\cdot\left(D_{eff,H_2O}\nabla c_{H_2O}\right)-\frac{R_{s,2}(t)}{F}\quad . \tag{22}$$

To simplify the computation, Eqs. 19~22 are transformed into ordinary differential equations by a polynomial approximation [59]. Finally, the dissolution of active material at cathode could cause a change in cathode porosity and diffusivity. The cathode porosity is given by:

$$\frac{\partial\varepsilon_{s,p}(t)}{\partial t}=-a_s^{pos}(t)R_{s,2}(t)V_m\,. \tag{23}$$

The cathode diffusivity is given by:

$$D_{s,p}(t)=D_{s,p,0}(t)\left[1-\left(\frac{\varepsilon_{s,p}^0(t)-\varepsilon_{s,p}(t)}{\varepsilon_{s,p}^0(t)}\right)^{m1}\right], \tag{24}$$

where V_m is molar volume of NMC622, and $m1$ is an empirical coefficient. Li ion concentration in electrolyte will be affected by salt decomposition and Mn dissolution, thereby the equations for liquid phase Li ion concentration are:

$$\varepsilon_{e,p}\frac{dc_{e,p,avg}(t)}{dt}=2n_6D_{e,p}^{eff}c_{e,n,avg}(t)+2p_6D_{e,p}^{eff}c_{e,p,avg}(t)-\frac{J_e(t)}{l_p}+\frac{a_s^{pos}(t)\cdot Rs_3l_p-Rs_2}{F} \tag{25}$$

$$\varepsilon_{e,n}(t)\cdot\frac{dc_{e,n,avg}(t)}{dt}=2n_1D_{e,n}^{eff}(t)\cdot c_{e,n,avg}(t)+2p_1D_{e,n}^{eff}(t)\cdot c_{e,p,avg}(t)+\frac{J_e(t)}{l_n} \tag{26}$$

in which $D_{e,p}^{eff}$ and $D_{e,n}^{eff}$ are effective diffusivity in liquid phase at cathode and anode, n_1, n_2, p_1 and p_2 are coefficients, J_e is the liquid phase flux which is equal to $\frac{i_{app}(t)}{F}(1-t_-)$.

Table 1. Model parameters.

Parameter	Anode (Graphite)	Separator	Cathode (NMC622)
[a]Thickness (μm)	47.6	23	23.80
[a]Initial porosity	0.408	0.4	0.4
[b]Particle radius (μm)	0.8	/	1.03
[a]Matrix conductivity (S/m)	100	/	10
[b]Reaction rate constant ($m^{2.5}/(mol^{0.5}\cdot s)$)	1.78×10^{-7}	/	1.25×10^{-7}
[51] Maximum Li ion concentration (mol/m^3)	26390		49000

Table 2. Parameters of side reaction.

Parameter	Value	Parameter	Value
[a] c_{EC}^0 (mol/m^3)	4.429	[57] $a_p i_{0,ox}$ (A/m^3)	10
[51] M_{SEI} (kg/mol)	0.162	[57] U_{ox}^{eq} (V)	4.1
[51] ρ_{SEI} (kg/m^3)	1690	[57] k_{decom} (m^6/mol^2s)	7.13×10^{-10}
[51] κ_{SEI} (S/m)	5×10^{-6}	[b] k_{dis} (m/s)	5.147×10^{-9}
[51] $\alpha_{c,SEI}$	0.5	[57] λ_{H_2} (1/m)	2×10^{5}
[b] D_{EC} (m^2/s)	1.175×10^{-18}	[57] k_{H_2} (m/s)	2.07×10^{-8}

Table 3. Parameters of side reaction. (Cont.)

[51] $\alpha_{c,lpl}$	0.5	[57] $\alpha_c^{H_2}$	0.5
[51] M_{Li} (kg/mol)	6.94×10^{-3}	[57] D_{eff,H^+} (m^2/s)	1×10^{-10}
[51] ρ_{Li} (kg/m^3)	534	[57] D_{eff,H_2O} (m^2/s)	3×10^{-11}
[b] $i_{0,lpl}$ (mol/($m^{0.5}$s))	3×10^{-4}	[57] V_m (m^3/mol)	1.4×10^{-4}
[b] Initial SEI layer film thickness (m)	2.8×10^{-8}	[[51] Equilibrium potential of SEI layer (V)	0.4

[a] Measured

[b] Fitted with experiment

3. RESULTS AND DISCUSSION

Experimental validation of the proposed model was conducted based on a CR2032 coin cell fabricated in the laboratory. It is composed of meso carbon micro beads (MCMB) as anode and NMC622 as cathode, and LiPF6 dissolved in EC/DMC (1:1) by wt. as electrolyte. In the model, several physical parameters - such as SEI reaction constant, EC diffusivity, Li plating constant, Mn dissolution reaction constant, salt decomposition reaction constant, and solvent oxidation current density - are unknown and highly dependent on battery material system. Therefore, the cycling capacity profile of cell 1 (Figure. 1(a)) was used to estimate these parameters. Then the cycling capacity profile of cell 2 was used to compare with the simulated data as a validation. Figure. 1(a) shows the experimental capacity for constant current (CC) charge constant current (CC) discharge cycling of 20 cycles each at 1C, 2C, and 3C, followed by 50 cycles at 1C. It can be observed

that the degradation rate in the initial 10 cycles is 0.60%, which is much faster than the degradation rate of 0.12% in the following cycles, indicating that these cycles belong to the initial formation reaction of the SEI layer. Therefore, the initial 10 cycles were not included in the parameter identification and model validation. A linear fit has been conducted for the remaining cycles. By using the data from 11^{th} to 110^{th} cycles, the degradation physics parameters in the model have been identified, and their fitted values are shown in Table 2. The comparison of experiment and simulation results is shown in Figure. 1(b). The root-mean-square-error (RMSE) between simulation and cell 2 data was 0.098, indicating that the predicted result was able to capture the capacity degradation from the experiments. Note that the cycling test paused after 3C cycling for 20 hours and then resumed for 1C cycling. That was why a larger capacity fade was observed at $60^{th} \sim 70^{th}$ cycle (Figure. 1 (a)).

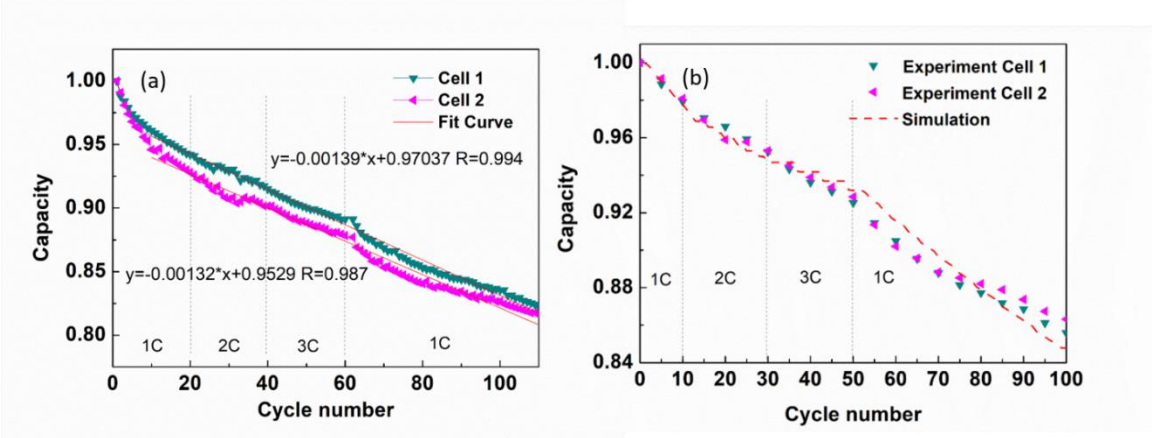

Figure 1. CC charge/discharge cycling of 20 cycles each at 1C, 2C, and 3C, followed by 50 cycles at 1C (a) capacity versus cycle of two cells (b) comparison of simulated and experimental capacity profiles.

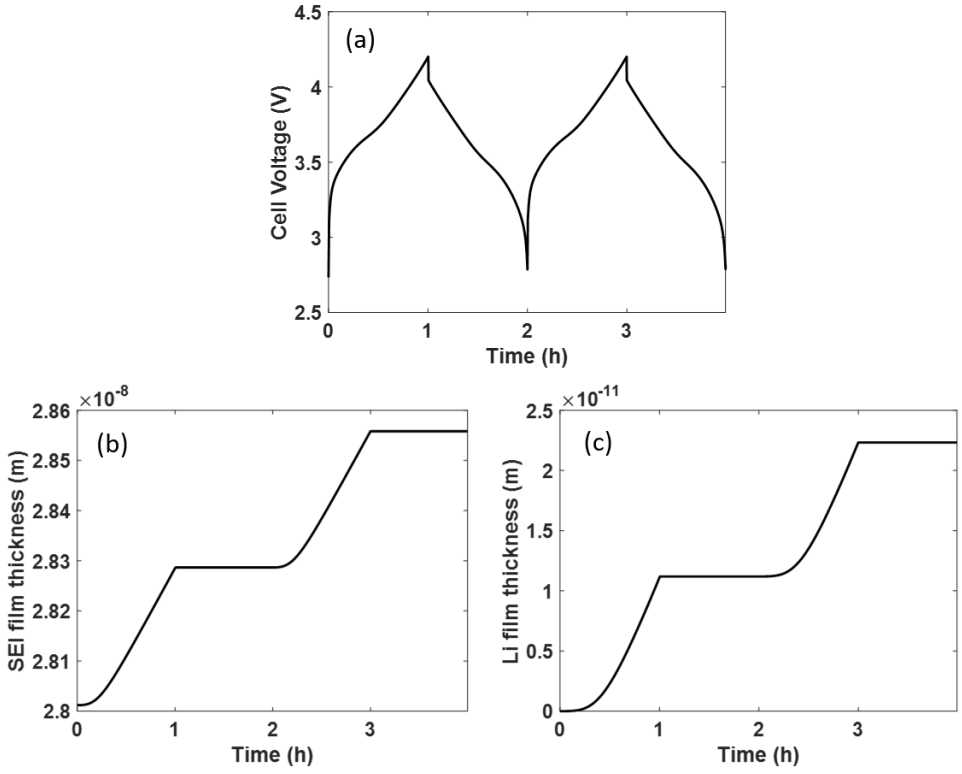

Figure 2. (a) cell voltage, (b) SEI film thickness and (c) plated Li metal film thickness at anode particle surface in 1C charge/discharge process.

A 1C constant current charge and discharge is implemented on the model with a voltage range of 2.8 V - 4.2 V. The corresponding cell voltage is shown in Figure. 2(a). Figures. 2(b) and (c) present the evolution of deposited SEI film and Li metal film, respectively. In this model, the SEI layer and Li metal deposition are assumed to only occur during the charge process. According to Eq. 1 and Eq. 2, the anode side reaction current could be negligible when their reaction overpotential is positive. During the discharge process, the overpotentials of both reactions at anode particle surfaces are usually positive, leading to a negligible increase of the SEI and Li metal films. It can be observed that the

deposition rates of both the SEI layer and the Li metal increase as the charge voltage increases, which is due to the high overpotential at the particle surface in the high cell voltage region. Therefore, high voltage accelerates the degradation in the anode. Moreover, the Li metal film thickness only increases 0.01 nm in the first cycle, which is very small compared with the SEI film (0.29 nm). This is because the charge current (1C) used here is not very high so that Li plating occurs at a lower rate than SEI reaction. High charge current could lead to a high overpotential at the anode surface, which will accelerate the deposition rate of Li metal (Eq. 2). Low cell temperature is another possible cause for serious Li plating because it slows down the ion transfer at anode particle. Except for these two conditions, SEI growth plays the main role in anode degradation.

The degradation results on the cathode side are shown in Figure. 3. It can be observed that the solvent oxidation mainly occurs at the cathode when the cell voltage is high (>3.8 V), while salt decomposition occurs in both electrodes during the entire cycling process. The reaction rate of the latter decreased due to the continuous consumption of H_2O (Eq. 16). Solvent oxidation and salt decomposition are two main sources for proton generation, and the concentration of proton determinates the dissolution rate (Eq. 14). According to Figures. 3(a) and (b), the solvent oxidation rate reaches 2,283 mol/(s·m^3), which is much higher than the maximal salt decomposition rate (~0.35 mol/(s·m^3)). Therefore, H^+ concentration has a drastic rise around the change-discharge transition point and stays stable when the cell voltage is low (<3.8 V) (Figure. 3(d)). Also, the Mn dissolution rate has the same trend with H^+ concentration (Figure. 3(c)). As a result, volume fraction of NMC622 in the cathode keeps decreasing at a gradually rising rate (Figure. 3(e)).

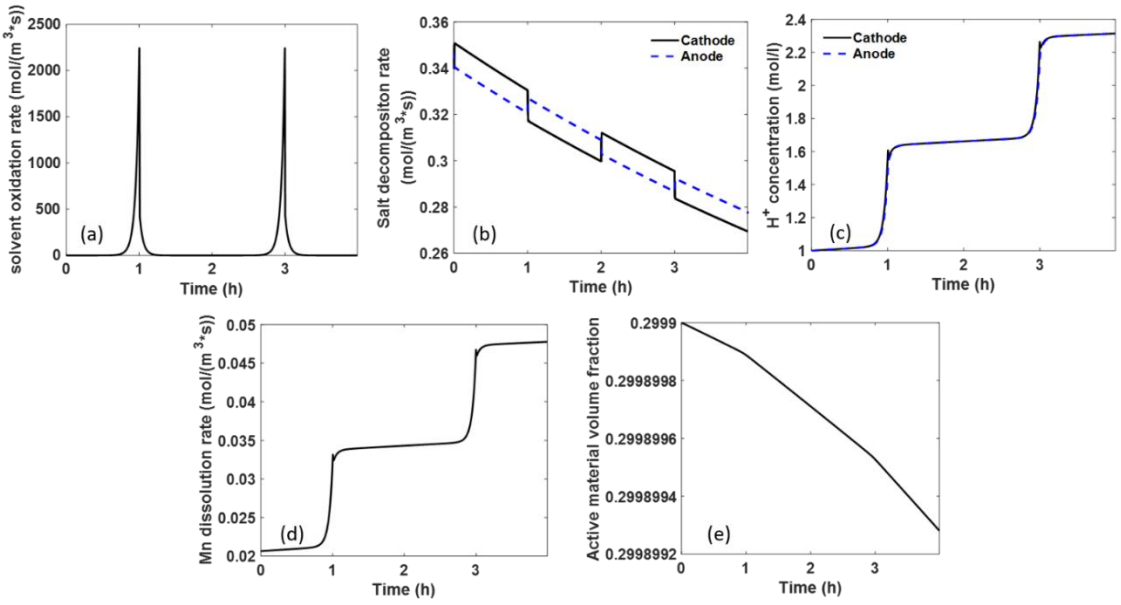

Figure 3. (a) Solvent oxidation rate, (b) salt decomposition rate on both electrodes, (c) proton concentration on both electrodes, (d) Mn dissolution rate and (e) evolution of active material volume fraction in cathode in 1C charge/discharge process.

This model considers three degradation physics, namely, SEI growth, Li plating and Mn dissolution. The effects of these degradation physics in 1C charge/discharge cycling are simulated as shown in Figure. 4(a). Both SEI growth and Li plating consumes Li ion inventory (Eq. 9). As observed in the simulation, the ratio of Li loss in the total amount of reversible Li ion is 85.65 %, in which SEI growth consumes 73.72 % and Li plating consumes 11.93 %. On the other hand, Mn dissolution leads to a reduction of active material in the cathode, with volume fraction reduction from 0.3 to 0.13, that is nearly 56.67% loss. To better explain the impact of active material loss in cathode, the capacity degradation is compared in models include and exclude Mn dissolution (Figure. 4(b)). As a result, the capacity loss induced by Mn dissolution is 6.5%. Also, the impact of Mn dissolution is negligible in the initial 200 cycles and then become more and more

significant, which is due to the increasing dissolution rate as cycled. Another effect of Mn dissolution is the consumption of Li ion in salt decomposition reaction. As shown in Figure. 4(c), the electrolyte concentration decreases from 980 mol/m^3 to 297 mol/m^3, which results 43% drop in electrolyte conductivity.

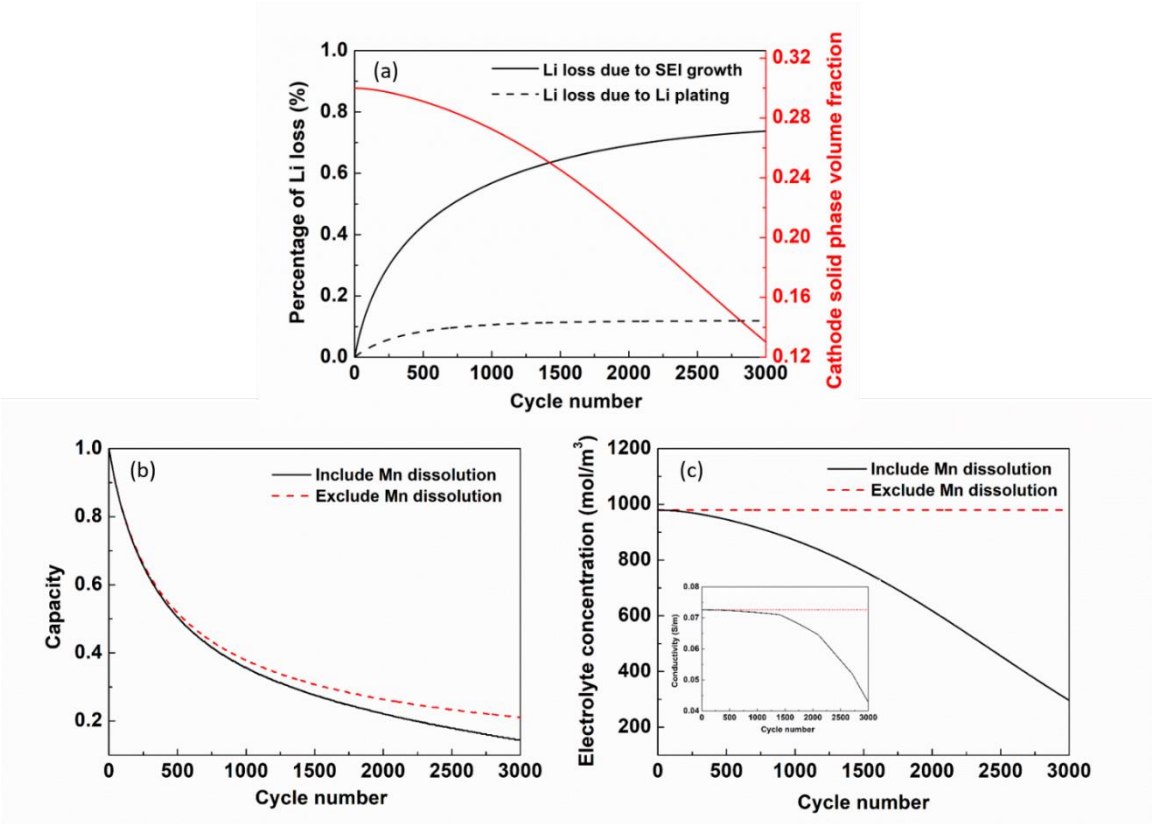

Figure 4. (a) Evolution of Li loss amount caused by SEI growth and Li plating, respectively and active material volume fraction, Comparison of (b) capacity degradation (c) electrolyte concentration (inset) electrolyte conductivity in 1C charge/discharge cycling test.

C-rate is an important impact factor in degradation rate. The influences of three test procedures - 1C/1C, 4C/1C and 4C/4C charge discharge - on three physics was analyzed separately. Figure. 5(b)~(c) presents the C-rate impact in Mn dissolution. As shown in Figure. 3, the solvent oxidation rate determines the reaction rate of Mn dissolution. The solvent oxidation rate is plotted in Figure 5(b). It can be observed that the maximal reaction rate of solvent oxidation is higher in 1C/1C test than the other two C-rates, which is around 2,283 mol/(s·m^3), while the maximal solvent oxidation rate is only 549 mol/(s·m^3) in tests 4C/1C and 4C/4C. This result indicates that the solvent oxidation rate is highly related to charge currents. In Figure 5 (a) and (b) the solvent oxidation only occurs when voltage is higher than 3.8 V, and because this region is much shorter in 4C charge process than that in 1C charge, the maximal rate of solvent oxidation is much less in the 4C charge. Consequently, the reaction rate of Mn dissolution is less in 4C/1C and 4C/4C than in 1C/1C (Figure. 5(c)). In the first cycle, the Mn dissolution rate is ~2.65e-3 mol/(s·m^3) in 4C charging, about 64.6% of that in 1C charging (~4.1e-3 mol/(s·m^3)). Regarding active material loss, its rate is maximal in the 1C/1C test with a value of 3.792e-7 h^{-1}. Then, the active material loss rate in 4C/1C is ~1.138-7 h^{-1}, which is slightly less than 1.1588e-7 h^{-1} in 4C/4C. This is because a high discharge current of 4C brings a faster rise in the Mn dissolution rate than 1C, which leads to a higher average Mn dissolution rate during the same time. Therefore, it can be concluded that the high charge current can slow Mn dissolution while high discharge current has a reverse effect. However, the impact of discharge current is less than charge current. The current impacts on anode side reaction, SEI film growth, and Li plating are plotted in Figures. 5 (e) and (f). It can be observed that both SEI film growth and Li plating are accelerated in 4C charging. For the SEI layer, its

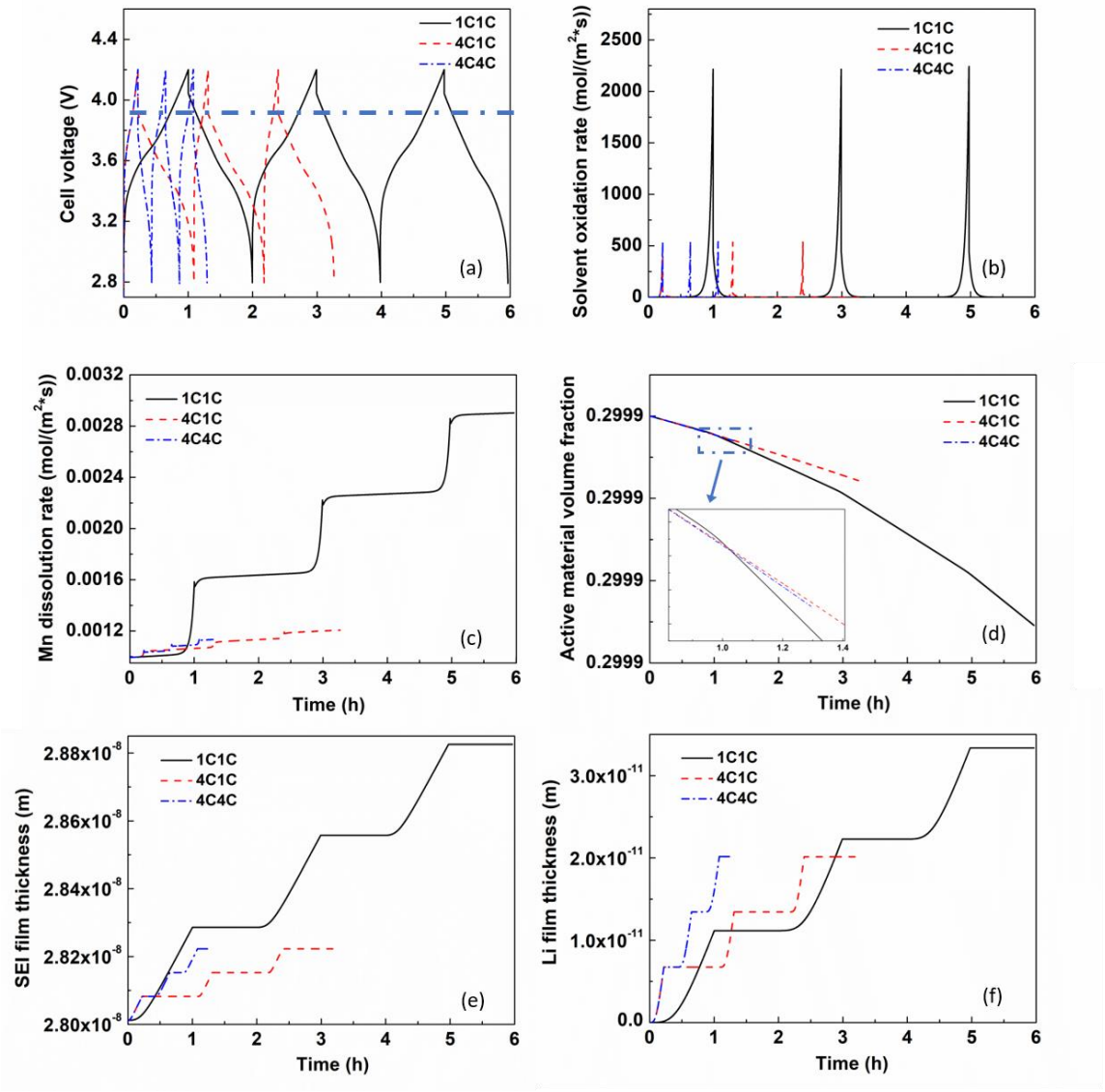

Figure 5. (a) Cell voltage (b) solvent oxidation rate (c) Mn dissolution rate (d) active material volume fraction (e) SEI film thickness (f) Li metal film thickness of 1C/1C, 4C/1C and 4C/4C charge discharge tests.

growth rate is 0.315 nm/h in 4C charging and 0.269 nm/h in 1C charging. The growth rate of deposited Li metal film is 0.029 nm/h in 4C and 0.011 nm/h in 1C charging. High charge current causes a polarization at the particle surface, leading to high overpotential.

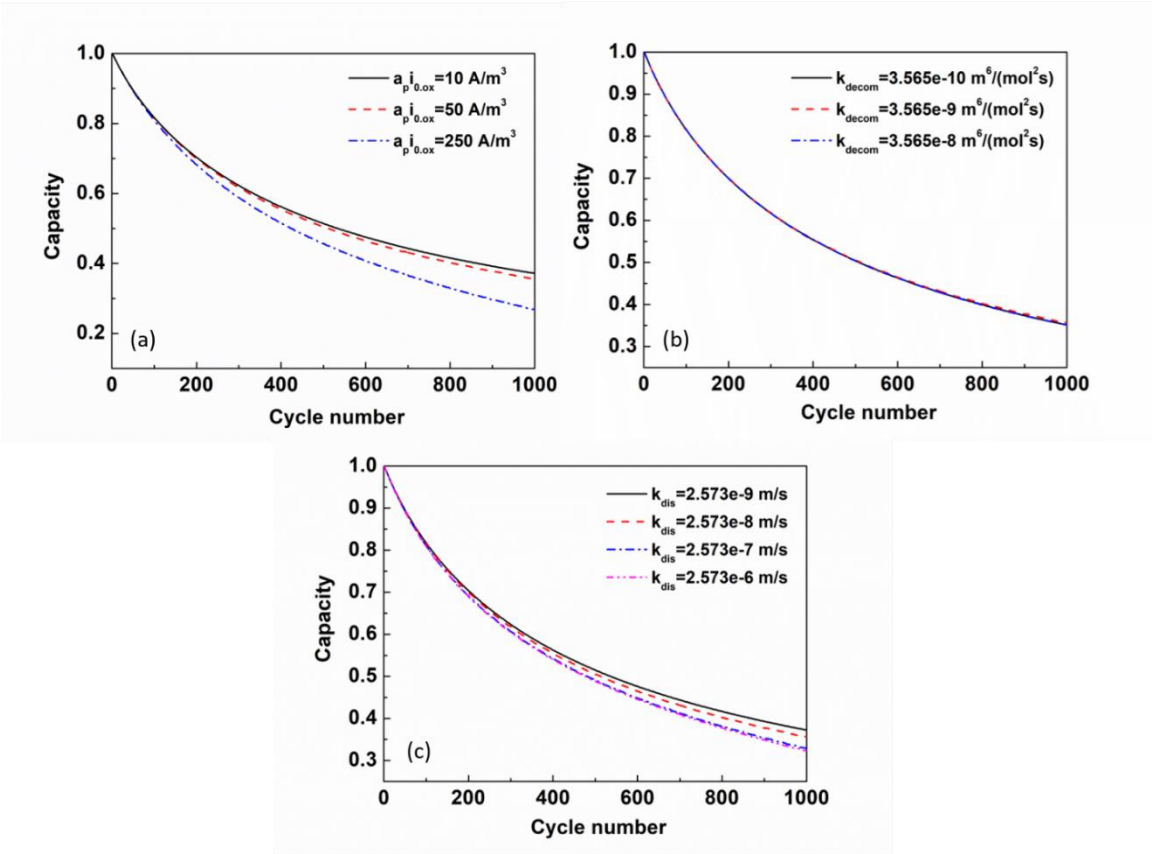

Figure 6. Capacities as a function of cycle number for (a) different solvent oxidation exchange current densities, (b) different salt decomposition reaction rate constant and (c) different dissolution reaction rate constant.

According to Eqs. 1-2, the reaction current for both SEI film and Li plating will increase as an acceleration of film growth. The depositions of SEI and Li metal were ignored in the model due to their negligible rates. Therefore, discharge current has no impact on anode side reactions.

Figure 6 shows the sensitivity study of solvent oxidation exchange current density, salt decomposition reaction rate constant, and Mn dissolution reaction rate constant. The solvent oxidation exchange current density is mainly determined by the solvent

components. For example, ethers, such as tetrahydrofuran and dimethoxyethane, are less stable while carbonates, such as ethylene carbonate propylene carbonate and diethylcarbonate, are not easily oxidized [60]. The larger the solvent oxidation exchange current density is, the less stable the electrolyte and the faster the solvent oxidation becomes. When the solvent oxidation speeds up, more protons will be generated, which triggers more intense acid induced Mn dissolution. As shown in Figure. 6(a), the capacity decreases 10.3% when the solvent oxidation exchange current density increases from 10 A/m^2 to 250 A/m^2. The salt decomposition reaction rate constant is related to the reactivity of salt. Fluorinated salts - for example, $LiPF_6$, $LiBF_4$ and $LiAsF_6$ - tend to generate F-containing anions and react with impurity water [60]. Other salts, such as Lithium bisoxalatoborate (LiBoB, $LiB(C_2O_4)_2$), have been proposed as alternatives. It was reported that concentration of Mn ions of the electrolyte after a 4-week storage of $LiMn_2O_4$ powders in 1 M LiBoB/EC:DEC (1:1) at 55 °C is 0.05 ppm, while it was 64 ppm $LiPF_6$/EC:DEC (1:1) [61]. The salt decomposition reaction, on one hand, consumes the Li ion in electrolytes and increase the cell resistance. On the other hand, it generates proton causing more Mn dissolution. It doesn't seem to have a significant impact on capacity fade within 1000 cycles. This is because solvent oxidation is a more dominant source of proton generation when compared with salt decomposition, as explained previously. Figure 6(c) shows the influence of Mn dissolution reaction rate coefficient. Mn dissolution reaction rate coefficient indicates the stability of NMC622 under acid solution. Approaches, such as bulk doping and surface modification, have been proposed for improving the cathode stability [62]. For example, A Li-bearing oxide glass Li_2O_3:B_2O_3 is applied as a surface coating layer to protect cathode material from acid attack, largely improving cells' cycling

performances [63]. In this simulation, it can be seen that the capacity fade increases 2.72% and 1.50% when the Mn dissolution reaction rate increase from 2.573e-9 m/s to 2.573e-7 m/s, respectively. However, the change of capacity fade is negligible when the Mn dissolution reaction rate varies from 2.573e-7 m/s to 2.573e-6 m/s. This is because the Mn dissolution reaction is not only limited by its reaction rate constant, but also by the proton concentration.

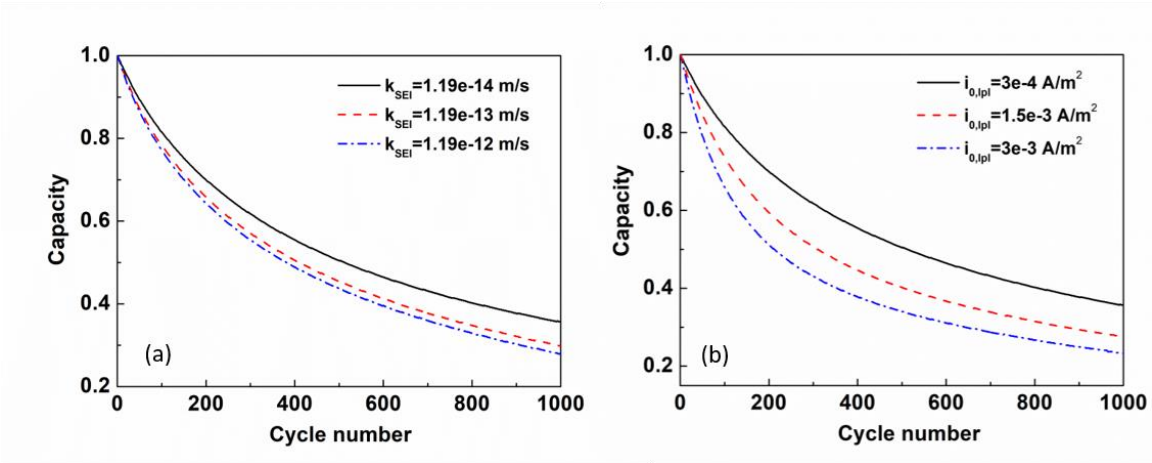

Figure 7. Capacities as a function of cycle number for (a) different SEI reaction constants, (b) lithium plating exchange current densities.

Figure 7 shows the sensitivity study of lithium plating exchange current densities and SEI reaction constants. SEI reaction takes place between the anode particle surface and the electrolyte. Therefore, the SEI constant is related to various factors, including cathode material (degree of material crystallinity, particle size, material chemical property, surface property) and electrolyte stability (salts and solvent composition, salt concentration) [64].

In Figure. 7(a), the capacity decreases by 5.83% when the SEI reaction constant increases from 1.19e-14 m/s to 1.19e-13 m/s, and it only decreases 2% when the constant changes from 1.19e-13 m/s to 1.19e-12 m/s, thus indicating the SEI constant is not the only limiting factor in the SEI layer growth. According to Eq. 1, EC concentration has an impact on the SEI reaction current because it is a main reactant for formation of SEI layer. In lithium plating, the concentration of Li ion in electrolyte, anode surface property, and electrolyte composition determine the lithium plating exchange current density. In Figure. 7(b), the capacity fade is sensitive to the lithium plating exchange current density and keeps accelerating while the parameter increases.

4. CONCLUSIONS

To predict the cell degradation and battery life of BESSs, a comprehensive degradation model - including SEI layer growth and Li plating at the anode and Mn dissolution at the cathode - has been established. The model is based on an electrolyte enhanced SP model so that it is computationally efficient for online predication. The model parameters have been identified according to the experimental data of one cell with a RMSE of 0.094. The simulation results from the obtained model showed a good match with the experimental capacity profile of another cell (RMSE=0.098). It was found that at the anode side, the deposition rate of both SEI layer and Li metal increase as the charge voltage increase. Furthermore, at the cathode side, the solvent oxidation rate determines the proton concentration that triggers the Mn dissolution reaction. As a result, active material in the cathode keeps decreasing at a gradually rising rate. As for the long cycling

test, the SEI growth plays a main role in capacity fade in the first about 2000 cycles, and Mn dissolution has a significant impact after about 1000 cycles with a capacity loss of 6.5%. It is also revealed that the mechanism that Mn dissolution cause a capacity loss is not only the loss of active material in cathode, but a consumption of Li ions in electrolyte. The current impacts on the three degradation mechanisms are analyzed separately. As observed, high charge current slows down the reaction of Mn dissolution at cathode and speed up the SEI layer growth and Li plating at anode, while high discharge current accelerates Mn dissolution. A sensitivity study of degradation parameters has been conducted against capacity fade. It shows that the capacity degradation is mostly sensitive to solvent oxidation exchange current density and Li plating exchange current density, while it is inert to salt decomposition constant. The reaction rate of Mn dissolution and SEI formation are limited by proton concentration and EC concentration, respectively; therefore, their reaction constants do not effectively impact the capacity degradation when reaching certain values.

REFERENCES

1. Smith, K., et al. Life prediction model for grid-connected Li-ion battery energy storage system. in 2017 American Control Conference (ACC). 2017. IEEE.

2. Chen, H., et al., Progress in electrical energy storage system: A critical review. Progress in natural science, 2009. **19**(3): p. 291-312.

3. Qian, H., et al., A high-efficiency grid-tie battery energy storage system. IEEE transactions on power electronics, 2010. **26**(3): p. 886-896.

4. Millner, A. Modeling lithium ion battery degradation in electric vehicles. in 2010 IEEE Conference on Innovative Technologies for an Efficient and Reliable Electricity Supply. 2010. IEEE.

5. Peterson, S.B., J. Apt, and J. Whitacre, Lithium-ion battery cell degradation resulting from realistic vehicle and vehicle-to-grid utilization. Journal of Power Sources, 2010. **195**(8): p. 2385-2392.

6. Hoke, A., et al. Electric vehicle charge optimization including effects of lithium-ion battery degradation. in 2011 IEEE Vehicle Power and Propulsion Conference. 2011. IEEE.

7. Liu, C., Y. Wang, and Z. Chen, Degradation model and cycle life prediction for lithium-ion battery used in hybrid energy storage system. Energy, 2019. **166**: p. 796-806.

8. Braithwaite, J.W., et al., Corrosion of lithium-ion battery current collectors. Journal of the electrochemical society, 1999. **146**(2): p. 448.

9. Cong, L., et al., Role of perfluoropolyether-based electrolytes in lithium metal batteries: Implication for suppressed Al current collector corrosion and the stability of Li metal/electrolytes interfaces. Journal of Power Sources, 2018. **380**: p. 115-125.

10. Yoshida, H., et al., Degradation mechanism of alkyl carbonate solvents used in lithium-ion cells during initial charging. Journal of Power Sources, 1997. **68**(2): p. 311-315.

11. Li, J., et al., Artificial solid electrolyte interphase to address the electrochemical degradation of silicon electrodes. ACS applied materials & interfaces, 2014. **6**(13): p. 10083-10088.

12. Vetter, J., et al., Ageing mechanisms in lithium-ion batteries. Journal of Power Sources, 2005. **147**(1): p. 269-281.

13. Cope, R.C. and Y. Podrazhansky. The art of battery charging. in Fourteenth Annual Battery Conference on Applications and Advances. Proceedings of the Conference (Cat. No. 99TH8371). 1999. IEEE.

14. Ahmed, S., et al., Enabling fast charging – A battery technology gap assessment. Journal of Power Sources, 2017. **367**: p. 250-262.

15. Xu, R., et al., Heterogeneous damage in Li-ion batteries: Experimental analysis and theoretical modeling. Journal of the Mechanics and Physics of Solids, 2019. **129**: p. 160-183.

16. Scrosati, B. and J. Garche, Lithium batteries: Status, prospects and future. Journal of power sources, 2010. **195**(9): p. 2419-2430.

17. Yi, T.-F., et al., Recent development and application of Li4Ti5O12 as anode material of lithium ion battery. Journal of Physics and Chemistry of Solids, 2010. **71**(9): p. 1236-1242.

18. Endo, M., et al., Recent development of carbon materials for Li ion batteries. Carbon, 2000. **38**(2): p. 183-197.

19. Verma, P., P. Maire, and P. Novák, A review of the features and analyses of the solid electrolyte interphase in Li-ion batteries. Electrochimica Acta, 2010. **55**(22): p. 6332-6341.

20. Aurbach, D., Review of selected electrode–solution interactions which determine the performance of Li and Li ion batteries. Journal of Power Sources, 2000. **89**(2): p. 206-218.

21. Aurbach, D., et al., A short review of failure mechanisms of lithium metal and lithiated graphite anodes in liquid electrolyte solutions. Solid state ionics, 2002. **148**(3-4): p. 405-416.

22. Lin, N., et al., Understanding the crack formation of graphite particles in cycled commercial lithium-ion batteries by focused ion beam-scanning electron microscopy. Journal of Power Sources, 2017. **365**: p. 235-239.

23. Vetter, J., et al., Ageing mechanisms in lithium-ion batteries. Journal of power sources, 2005. **147**(1-2): p. 269-281.

24. Nagpure, S.C., B. Bhushan, and S. Babu, Multi-scale characterization studies of aged Li-ion large format cells for improved performance: an overview. Journal of The Electrochemical Society, 2013. **160**(11): p. A2111.

25. Marcicki, J.M., Modeling, parametrization, and diagnostics for lithium-ion batteries with automotive applications. 2012, The Ohio State University.

26. Broussely, M., et al., Aging mechanism in Li ion cells and calendar life predictions. Journal of Power Sources, 2001. **97**: p. 13-21.

27. Nazri, G.-A. and G. Pistoia, Lithium batteries: science and technology. 2008: Springer Science & Business Media.

28. Li, Z., et al., A review of lithium deposition in lithium-ion and lithium metal secondary batteries. Journal of power sources, 2014. **254**: p. 168-182.

29. Perkins, R.D., et al., Controls oriented reduced order modeling of lithium deposition on overcharge. Journal of Power Sources, 2012. **209**: p. 318-325.

30. Ren, D., et al., Investigation of lithium plating-stripping process in Li-ion batteries at low temperature using an electrochemical model. Journal of The Electrochemical Society, 2018. **165**(10): p. A2167.

31. Hasan, M.F., et al., Analysis of the implications of rapid charging on lithium-ion battery performance. Journal of the Electrochemical Society, 2015. **162**(7): p. A1382.

32. Yunjian, L., et al., Electrochemical performance and capacity fading reason of LiMn2O4/graphite batteries stored at room temperature. Journal of Power Sources, 2009. **189**(1): p. 721-725.

33. du Pasquier, A., et al., An update on the high temperature ageing mechanism in LiMn2O4-based Li-ion cells. Journal of Power Sources, 1999. **81-82**: p. 54-59.

34. Lu, W., et al., Electrochemical performance of Li4/3Ti5/3O4/Li1+x(Ni1/3Co1/3Mn1/3)1-xO2 cell for high power applications. Journal of Power Sources, 2007. **167**(1): p. 212-216.

35. Gabrielli, G., et al., A new approach for compensating the irreversible capacity loss of high-energy Si/C| LiNi0. 5Mn1. 5O4 lithium-ion batteries. Journal of Power Sources, 2017. **351**: p. 35-44.

36. Su, X., et al., A new strategy to mitigate the initial capacity loss of lithium ion batteries. Journal of Power Sources, 2016. **324**: p. 150-157.

37. Golmon, S., K. Maute, and M.L. Dunn, A design optimization methodology for Li+ batteries. Journal of Power Sources, 2014. **253**: p. 239-250.

38. Ning, G. and B.N. Popov, Cycle life modeling of lithium-ion batteries. Journal of The Electrochemical Society, 2004. **151**(10): p. A1584.

39. Ramadass, P., et al., Development of first principles capacity fade model for Li-ion cells. Journal of the Electrochemical Society, 2004. **151**(2): p. A196.

40. Ramadass, P., et al., Development of First Principles Capacity Fade Model for Li-Ion Cells. Journal of the Electrochemical Society, 2004. **151**(2): p. A196-A203.

41. Ning, G., R.E. White, and B.N. Popov, A generalized cycle life model of rechargeable Li-ion batteries. Electrochimica Acta, 2006. **51**(10): p. 2012-2022.

42. Safari, M., et al., Multimodal physics-based aging model for life prediction of Li-Ion batteries. Journal of the Electrochemical Society, 2009. **156**(3): p. A145-A153.

43. Christensen, J. and J. Newman, Cyclable lithium and capacity loss in Li-ion cells. Journal of the Electrochemical Society, 2005. **152**(4): p. A818.

44. Ekström, H. and G. Lindbergh, A model for predicting capacity fade due to SEI formation in a commercial graphite/LiFePO4 cell. Journal of The Electrochemical Society, 2015. **162**(6): p. A1003.

45. Kamyab, N., J.W. Weidner, and R.E. White, Mixed mode growth model for the solid electrolyte interface (SEI). Journal of The Electrochemical Society, 2019. **166**(2): p. A334.

46. Single, F., B. Horstmann, and A. Latz, Revealing SEI morphology: in-depth analysis of a modeling approach. Journal of The Electrochemical Society, 2017. **164**(11): p. E3132.

47. Deshpande, R., et al., Battery cycle life prediction with coupled chemical degradation and fatigue mechanics. Journal of the Electrochemical Society, 2012. **159**(10): p. A1730.

48. Delacourt, C. and M. Safari, Mathematical modeling of aging of Li-Ion batteries, in Physical Multiscale Modeling and Numerical Simulation of Electrochemical Devices for Energy Conversion and Storage. 2016, Springer. p. 151-190.

49. Cannarella, J. and C.B. Arnold, The effects of defects on localized plating in lithium-ion batteries. Journal of The Electrochemical Society, 2015. **162**(7): p. A1365.

50. Ge, H., et al., Investigating lithium plating in lithium-ion batteries at low temperatures using electrochemical model with NMR assisted parameterization. Journal of The Electrochemical Society, 2017. **164**(6): p. A1050.

51. Yang, X.-G., et al., Modeling of lithium plating induced aging of lithium-ion batteries: Transition from linear to nonlinear aging. Journal of Power Sources, 2017. **360**: p. 28-40.

52. Legrand, N., et al., Physical characterization of the charging process of a Li-ion battery and prediction of Li plating by electrochemical modelling. Journal of Power Sources, 2014. **245**: p. 208-216.

53. von Lüders, C., et al., Modeling of lithium plating and lithium stripping in lithium-ion batteries. Journal of Power Sources, 2019. **414**: p. 41-47.

54. Ren, D., et al., Investigation of lithium plating-stripping process in Li-ion batteries at low temperature using an electrochemical model. Journal of The Electrochemical Society, 2018. **165**(10): p. A2167-A2178.

55. Dai, Y., L. Cai, and R.E. White, Capacity Fade Model for Spinel LiMn2O4 Electrode. Journal of The Electrochemical Society, 2013. **160**(1): p. A182-A190.

56. Park, J., et al., Numerical simulation of the effect of the dissolution of LiMn2O4 particles on Li-ion battery performance. Electrochemical and Solid-State Letters, 2011. **14**(2): p. A14-A18.

57. Li, J., R.G. Landers, and J. Park, A comprehensive single-particle-degradation model for battery state-of-health prediction. Journal of Power Sources, 2020. **456**: p. 227950.

58. Lin, X., et al., A comprehensive capacity fade model and analysis for Li-ion batteries. Journal of The Electrochemical Society, 2013. **160**(10): p. A1701-A1710.

59. Subramanian, V.R., V.D. Diwakar, and D. Tapriyal, Efficient Macro-Micro Scale Coupled Modeling of Batteries. Journal of The Electrochemical Society, 2005. **152**(10): p. A2002-A2008.

60. Jang, D.H. and S.M. Oh, Electrolyte Effects on Spinel Dissolution and Cathodic Capacity Losses in 4 V Li / Li x Mn2 O 4 Rechargeable Cells. Journal of The Electrochemical Society, 1997. **144**(10): p. 3342-3348.

61. Amine, K., et al., Improved lithium manganese oxide spinel/graphite Li-ion cells for high-power applications. Journal of Power Sources, 2004. **129**(1): p. 14-19.

62. Zhan, C., et al., Dissolution, migration, and deposition of transition metal ions in Li-ion batteries exemplified by Mn-based cathodes – a critical review. Energy & Environmental Science, 2018. **11**(2): p. 243-257.

63. Amatucci, G.G., et al., Surface treatments of Li1+xMn2−xO4 spinels for improved elevated temperature performance. Solid State Ionics, 1997. **104**(1): p. 13-25.

VI. A MODEL-BASED TEMPERATURE-DEPENDENT STATE-OF CHARGE (SOC) ESTIMATION METHOD FOR LIHTIUM ION BATTERY PACK

ABSTRACT

It is important to accurately estimate the state of charge (SOC) of a cell in order to use the battery efficiently and safely, and also to extend the life of the battery. In a pack, temperature has a significant impact on the physical behavior of individual cells, such as open circuit voltage, electrode diffusivity, and conductivity, and correspondingly these changes induce a large variation in the SOCs of the cells in the pack. A modern battery pack is usually composed of hundreds or thousands of cells. The temperature of each cell varies because of different thermal environment. In this work, a physics-based reduced-order single particle model along with a lumped thermal model is employed for SOC estimation to improve the accuracy and robustness of SOC estimation of a battery pack. To reduce the computational cost, an "average cell" SOC is firstly estimated based on the physical model, and then SOCs of individual cells are estimated by incorporating the performance divergences between the average cell and each individual cell. A hybrid approach between unscented Kalman filter (UKF) and extended Kalman filter (EKF) is proposed to enhance the accuracy and convergence rate, where UKF is used for the average cell state estimator and EKF is used for individual cells. It was observed that a drastic initial fluctuation was caused by average cell states' estimation errors in individual cell state estimation. Therefore, an extra holding time of 10 s has been added in EKF and as a result, the estimation value converges quickly in 15 s with a maximum RMSEs of 0.0186, 0.0326 and 0.6 K in cathode SOC, anode SOC and cell temperature.

1. INTRODUCTION

With the rapid development of electric vehicles and smart grids, lithium-ion batteries (LIBs) are widely used in energy storage systems owing to their high energy density, high power density, long cycle life and low self-discharge rate. [1] Due to the high nonlinear and dynamic nature of LIBs and transient vehicle operations, an advanced real-time battery management system (BMS) is in need to monitor batteries' states continuously in order to ensure a safe and efficient power management. A critical variable to be estimated is state of charge (SOC), which cannot be measured directly by electronic sensors and can only be estimated through other measurable variables, such as a terminal voltage and current. Therefore, it is important to estimate the SOC in a fast, reliable and accurate way to protect the batteries from over-discharging or over-charging and to ensure the high performance of BMS. [2, 3]

Many methods have been proposed to estimate battery SOCs in real-time. The most conventional method is Coulomb counting method, which determines cell SOC by ampere-hour integration along with a maximum discharge capacity. [4-8] However, it requires accurate knowledge of cell's initial state. And since it is an open loop method, the accumulation of initial state and current sensor error may lead to a drift away of the estimated SOC. [9] Therefore, Coulomb counting method is usually coupled with an open-circuit voltage (OCV)-based method in real applications because a battery's OCV is directly correlated with its SOC and can be used as a recalibration. [10-12] But the limitation of OCV-based method is that the battery's terminal voltage is equal to OCV only at its equilibrium state, which needs more than one hour's rest. Moreover, this method cannot work when the OCV-SOC curve is flat. Recently, a black-box method has been

reported and researched intensely. Black-box method is to develop a battery model with no knowledge of any mechanism by training input and output data with computational intelligence-based approaches. The representative approaches include artificial neural network (ANN) [13-16], support vector machine (SVM) [17-19], fuzzy logic methodology [20-22], Gauss regression process (GRP) [23, 24] and so on. Black-box method can offer a good SOC estimation accuracy under an appropriate training data set because of the effectiveness of computational intelligence in approximation of non-linear dynamics. [25, 26] However, to achieve a good performance, the training data need to be enormous so that the training process could be very computational heavy. Since its estimation performance is highly dependent on training data, the robustness and overfitting may happen in these methods. [15]

Another common type of SOC estimation is model-based estimation. Model-based methods deploy a battery model and implement an algorithm to estimate the SOC from measurable variables such as voltage and current. Conventional battery model used in this kind of methods is equivalent circuit model (ECM), which uses electrical components including resistors, capacitors, and voltage sources, to simulate battery dynamics. [27-30] Its advantage is the simple structure, which can be apply to a low-cost microcontroller easily. However, ECM lacks underlying electrochemical mechanisms so that its accuracy will becomes lower and lower due to aging, which affects the estimation precision. Physics-based battery models such as pseudo-two-dimensional (P2D) model is very accurate in describing the electrochemical reactions in cell. [31-34] However, it contains coupled, nonlinear partial differential equations (PDEs), which can be computationally expensive and unsuitable for online estimation. Single particle model (SPM) is simplified

electrochemical model which is composed only a single PDE and an algebraic equation by approximating both electrode with one particle. [35-38] By polynomial approximation, the PDE in SPM can be transformed into two ordinary equations (ODEs), which is called reduced-order SPM and largely reduce the plant model's complexity. [39] Model-based methods are usually used along with adaptive filters and state estimation algorithms, such as extended Kalman filter (EKF) [40-43], unscented Kalman filter (UKF) [2, 44-46], particle filter (PF) [44, 47-49], Luenberger observer [50-52], sliding mode observer [43, 53, 54] and so on. KF-based algorithm has the advantage that they can be designed being close loop and online so that the SOC estimation error can be self-corrected in real-time. EKF is the most preferred method for battery state estimation, which has been reported to work along with both ECM and SPM with an acceptable estimation error (<4%). [40, 41, 43] However, EKF works by linearizing the nonlinear system with Jacobian matrix, which is using partial derivatives and first-order Taylor expansion. The ignorance of higher-order terms may lead to a large estimation error and even a divergence of the filter. [55, 56] To overcome the drawbacks of EKF, UKF is introduced, which avoids the calculation of Jacobi matrix of nonlinear functions. Instead, a set of sigma points are utilized for capturing the posterior mean and covariance of variables. [57] It was reported that UKF can also work with nonlinear full order electrochemical model with an estimation error of 5%. [58] And compared with EKF, UKF shows a higher accuracy, robustness, and convergence rate. [59] KF-based estimation algorithm can only approximate the states of a non-linear system with an additive Gaussian noise. PF is a sequential Monte Carlo method and could be independent of the system model and is not subject to linearization error or Gaussian noise assumption. Recently, PF has been reported for SOC estimation based on ECM. [47, 60,

61] But PF can only achieve a high accuracy with a large number of sample particles, which needs larger computation cost.

A critical issue in SOC estimation of battery pack is the cell to cell variance. In modern battery pack, hundreds or thousands of cells are combined through series or parallel electrical connections to meet the requirement of high energy and power in applications. Individual cells will be different in initial SOC, capacity and internal resistance due to the various reasons, resulting from fabrication process, material defects, and external environment conditions. [62, 63] These differences are inevitable and could cause an inefficient usage of battery. For example, the individual cell with the lowest capacity will determine the available capacity of the pack because that cell will be the first to fully discharged in the discharge process of the pack. On the other hand, there could be a large deviation of temperature between the cells located at pack edges and in the center because of different external environment. [64-66] And the electrochemical process inside batteries could also impact the cell's thermal behavior. [67] Many battery parameters are sensitive to temperature, such as electrode diffusivity, electrolyte conductivity, and OCV-SOC curve, which would reversely impact cell capacity and internal resistance. [68, 69] High temperature could even decrease the efficiency of cells and enhancing the aging reaction. [70] To take the cell to cell variance into a consideration, to date, three approaches have been proposed. The first is "each cell" method, which is to estimate each in-pack cell's SOC and then calculate the pack SOC accordingly. [71, 72] However, considering the large number of in-pack cells, this method is highly computational expensive. The second method is so called "average cell" method. In this method, the current and "average cell" voltage are used to determine the pack's average SOC in the micro time scale first, and

then the performance divergence between the “average cell” and each individual cell are estimated to generate the SOCs for all the cells in macro time scale. [40, 62] The third method is called as “representative cell” method. The cells with special properties, such as first over-charge cell or first over-discharged cell, are selected as “representative cell”. Then the SOCs of these cells are estimated for the calculation of the pack SOC. [73, 74] However, most works mentioned above were based on ECM and didn’t consider the temperature divergences and thermal behavior of individual in-pack cells.

In this work, a combination of an average cell state estimator and several individual cell state estimators was designed to estimate cell SOCs in battery pack to reduce the computation cost. The average cell state estimator was established based on a thermal-SP model, in which the performance of UKF and EKF were compared under a dynamic loading. In individual cell state estimator, the cell SOCs’ divergences of individual cells were estimated using a discretized EKF. To improve the initial estimation performance, a 10 s holding time was added in the individual cell state estimator and its performance was compared with the estimator without time delay.

2. METHODS

2.1. BATTERY MODELING

A single particle (SP) model along with a lumped thermal model was used to describe the electrochemical dynamic as well as the internal temperature evolution in batteries. One cell is regarded as isothermal when considering the thermal effects of electrochemical reaction. The governing equations of solid phase in batteries are

$$\frac{\partial c_{s,j}}{\partial t} = D_{s,j} \frac{1}{r_j^2} \frac{\partial}{\partial r}\left(r_j^2 \frac{\partial c_{s,j}}{\partial r} \right), \tag{4}$$

with boundary conditions:

$$D_{s,j} \frac{\partial c_{s,j}}{\partial r}\bigg|_{r=0} = 0 \qquad D_{s,j} \frac{\partial c_{s,j}}{\partial r}\bigg|_{r=R_j} = -J_j \tag{5}$$

where j=p/n represents cathode/anode, respectively. R_j is the particle radius of electrodes and J_j is the molar flux of lithium ions at the electrode surface. The flux can be calculated as

$$J_p = \frac{I_{loc,p}}{F} = \frac{I_{app} R_p}{3F\varepsilon_p L_p} \qquad J_n = \frac{I_{loc,n}}{F} = -\frac{I_{app} R_n}{3F\varepsilon_n L_n} \tag{6}$$

where I_{app} is the applied current, ε_j is the solid phase volume fraction of electrodes, and L_j is the electrode thickness. The state of charge (SOC) at electrode particle surface is defined as

$$x_{j,surf} = \frac{c_{s,j,avg}\big|_{r=R_j}}{c_{s,j,\max}} \ , \tag{7}$$

where $c_{s,j,avg}$ is the average lithium ion concentration and $c_{s,j,\max}$ is the maximum lithium ion concentration of the electrode material.

The relation between overpotential η_i and flux is expressed according to Butler-Volmer equation:

$$\frac{J_j}{F} = k_j \left(c_{s,j,\max}\right)^{0.5} c_e^{0.5} \left(1 - x_{j,surf}\right)^{0.5} x_{j,surf}^{0.5} \left[\exp\left(\frac{0.5F\eta_j}{RT} \right) - \exp\left(-\frac{0.5F\eta_j}{RT} \right) \right], \tag{8}$$

and the overpotential is defined as:

$$\eta_j = \varphi_{1,j} - \varphi_{2,j} - U_j \tag{9}$$

where k_j is the intercalation reaction constant, c_e is the Li ion concentration in electrolyte, $\varphi_{1,j}$ is the solid phase potential, $\varphi_{2,j}$ is the liquid phase potential, and U_j is the open circuit voltage (OCV) which is a function of SOC and cell temperature ash shown in Figure 1.

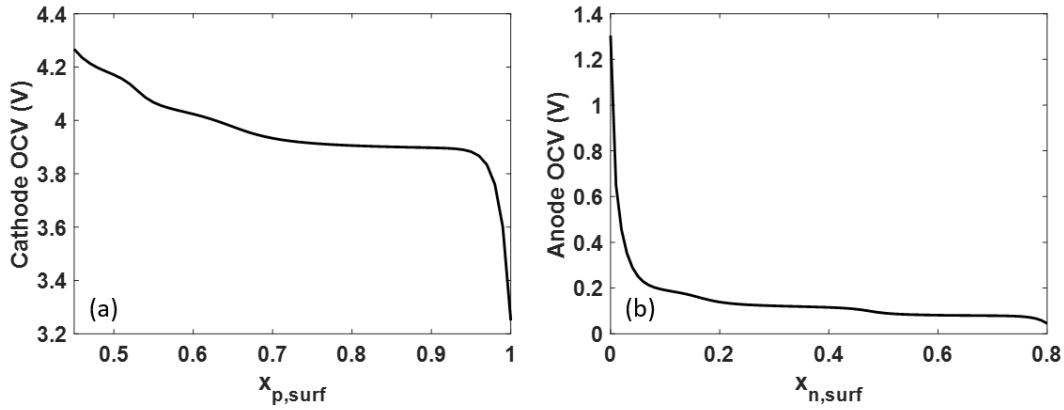

Figure 1. Plots of OCV as a function of cell SOC in (a) cathode, and (b) anode.

The terminal voltage can be derived as:

$$V_{cell} = \varphi_{1,p} - \varphi_{1,n}$$
$$= U_p - U_n + \frac{2RT}{F}\ln\left(\frac{\sqrt{m_p^2+4}+m_p}{2}\right) + \frac{2RT}{F}\ln\left(\frac{\sqrt{m_n^2+4}+m_n}{2}\right) + IR_{cell} \quad (10)$$

in which

$$m_i = \frac{I}{Fk_iL_ic_{s,i,\max}c_e^{0.5}\left(1-x_{i,surf}\right)^{0.5}x_{i,surf}^{0.5}}. \quad (11)$$

The cell temperature is calculated based on energy conservative equation:

$$\rho \upsilon C_p \frac{dT_{avg}(t)}{dt} = IT_{avg}(t)\left[\frac{\partial U_p}{\partial T}\left(x_{p,surf}\right) - \frac{\partial U_n}{\partial T}\left(x_{n,surf}\right)\right] + I\left(\eta_p - \eta_n + IR_{cell}\right) - q \quad (12)$$

where ρ is the density of cell, υ is the cell volume, C_p is the specific heat capacity, $\frac{\partial U_j}{\partial T}$ is the entropy change coefficient which is a function of SOC (Figure 2) and q is the rate of heat transfer between cell and surroundings, which can be written as $q = hA(T - T_{amb})$. Here, h is the heat transfer coefficient and A is the cell surface area.

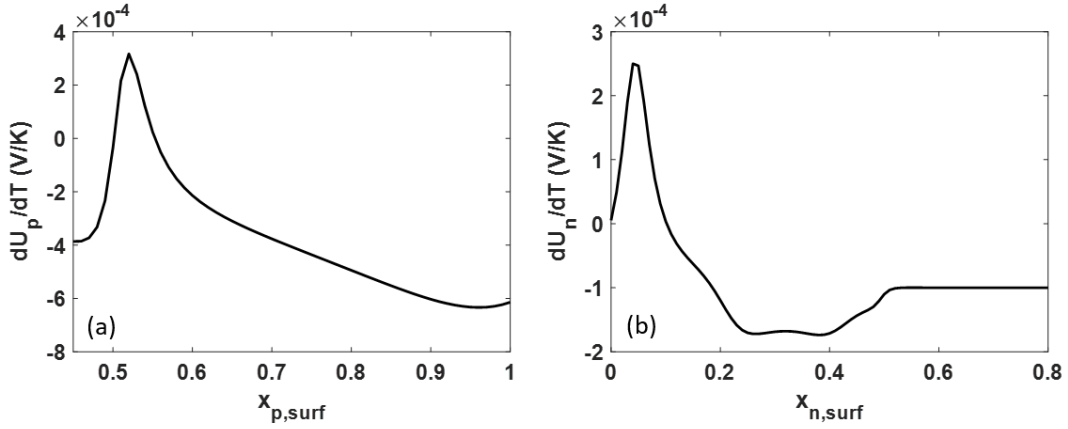

Figure 2. Plots of entropy change coefficient as a function of cell SOC in (a) cathode, and (b) anode.

The temperature-dependent coefficients in this model include solid phase diffusivity, intercalation reaction constant, open circuit voltage, and internal cell resistance, which are expressed as:

$$D_{s,j} = D_{s,j,ref} \exp\left(\frac{Ea_{D,j}}{R}\left(\frac{1}{T} - \frac{1}{T_{ref}}\right)\right) \quad (13)$$

$$k_j = k_{j,ref} \exp\left(\frac{Ea_{k,j}}{R} \left(\frac{1}{T} - \frac{1}{T_{ref}} \right) \right) \tag{14}$$

$$U_j(x_{j,surf}, T) = U_j(x_{j,surf}, T_{ref}) + \left. \frac{\partial U_j}{\partial T} \right|_{x_{j,surf}, T_{ref}} \times \left(T - T_{ref} \right) \tag{15}$$

$$R_{cell} = \theta_1 + \theta_2 \times \left(T - T_{ref} \right) \tag{16}$$

where $D_{s,j,ref}$ is the solid phase diffusivity at the reference temperature, $Ea_{D,j}$ is the activation energy of diffusivity, $k_{j,ref}$ is the intercalation rate constant in the reference temperature, $Ea_{k,j}$ is the activation energy of intercalation rate, and θ_1 and θ_2 are empirical coefficients.

To simplify the physics model, a fourth order approximation is applied to transform partial differential equations into ordinary differential equations. [39] Therefore, the battery model is described as a system of five variables: average concentration of cathode $c_{s,p,avg}(t)$, average concentration of anode $c_{s,n,avg}(t)$, average flux of cathode $q_{s,p,avg}(t)$, average flux of anode $q_{s,n,avg}(t)$ and average cell temperature $T_{avg}(t)$. The system dynamics are expressed as:

$$\frac{dc_{s,p,avg}(t)}{dt} = -\frac{3J_p(t)}{R_p} + w_1 \tag{17}$$

$$\frac{dc_{s,n,avg}(t)}{dt} = -\frac{3J_n(t)}{R_n} + w_2 \tag{18}$$

$$\frac{dq_{s,p,avg}(t)}{dt} = -30\frac{D_{s,p}}{R_p^2} q_{s,p,avg}(t) - \frac{45}{2R_p^2} J_p(t) + w_3 \tag{19}$$

$$\frac{dq_{s,n,avg}(t)}{dt} = -30\frac{D_{s,n}}{R_n^2} q_{s,n,avg}(t) - \frac{45}{2R_n^2} J_n(t) + w_4 \tag{20}$$

$$\rho \upsilon C_p \frac{dT_{avg}(t)}{dt} = IT_{avg}(t)\left[\frac{\partial U_p}{\partial T}\left(SOC_{p,surf}\right) - \frac{\partial U_n}{\partial T}\left(SOC_{n,surf}\right)\right] + I\left(\eta_p - \eta_n + IR_{cell}\right) - q + w_5 .$$

(21)

The anode SOC and cathode SOC for the average cell can be calculated as

$$SOC_{p,avg}(t) = \frac{1}{c_{s,p,\max}}\left(c_{s,p,avg}(t) + \frac{8R_p}{35} q_{s,p,avg}(t) - \frac{R_p}{35D_{s,p}} J_p(t)\right) \tag{22}$$

$$SOC_{n,avg}(t) = \frac{1}{c_{s,n,\max}}\left(c_{s,n,avg}(t) + \frac{8R_n}{35} q_{s,n,avg}(t) - \frac{R_n}{35D_{s,n}} J_n(t)\right). \tag{23}$$

The process noise is determined according to the noise of input current in the experiment. Here, the current noise is assumed in Gaussian distribution, and its mean and variance are assumed as (0, 0.25). The temperature noise is assumed as (0, 1e-4). Therefore, the process noise is $w \sim (0, Q)$, where

$$Q = diag[0.0953^2, 0.11^2, (8.9385e4)^2, (6.6014e4)^2, 1e-4]$$

The measurement is the average voltage of all the cells, which is given by

$$V(t) = U_p\left(SOC_{p,avg}(t), T_{avg}(t)\right) - U_n\left(SOC_{n,avg}(t), T_{avg}(t)\right) + \frac{2RT_{avg}(t)}{F}\left(\ln\left(m_p(t) + \sqrt{m_p{}^2(t)+1}\right) - \ln\left(m_n(t) + \sqrt{m_n{}^2(t)+1}\right)\right) + IR_{cell}\left(T_{avg}(t)\right) + v_1$$

(24)

$$m_j(t) = \frac{J_j(t)}{2k_j c_{s,j,\max} c_e^{0.5}\left(1 - SOC_{j,avg}(t)\right)^{0.5}\left(SOC_{j,avg}(t)\right)^{0.5}} . \tag{25}$$

The measurement noise is given by equipment resolution, which is $v_1 \sim (0, R)$ $R = 4e-6$.

2.2. SOC ESTIMATION ALGORITHM

2.2.1. Extend Kalman Filter (EKF) and Unscented Kalman Filter (UKF). Two kinds of Kalman filter, EKF and UKF, are implemented in this work. Table 1 shows the details of the algorithms. The variable vectors is x, k is the time step, y is the measurement, w is the state noise, and v is the measurement noise.

2.2.2. Combination of Average Cell State Estimation and Individual Cell State Estimation. The model for average cell state estimation is presented in the state-space representation in section 2.1, in which the state variable vector is $x = [c_{s,p,avg}, c_{s,n,avg}, q_{s,p,avg}, q_{s,n,avg}, T_{avg}]$ and the measurements is the average voltage of all the cells $y = V_{avg}$.

For the estimation of individual cell states, the system contains three state variables: SOC deviation from the average cell's SOC, $\Delta SOC_{i,p}$ and $\Delta SOC_{i,n}$, and temperature deviation from the average cell's temperature, ΔT_i. Now, the system dynamics is expressed as:

$$\Delta SOC_{i,p,k+1} = \Delta SOC_{i,p,k} + w_6 \tag{26}$$

$$\Delta SOC_{i,n,k+1} = \Delta SOC_{i,n,k} + w_7 \tag{27}$$

$$\Delta T_{i,k+1} = \Delta T_{i,k} + w_8 \tag{28}$$

Table 1. Algorithm for EKF and UKF.

	EKF	UKF
System	$x_{k+1} = f\left(x_k\right) + w_k$ $y_k = h\left(x_k\right) + v_k$ $w_k \sim \left(0, Q_k\right)$ $v_k \sim \left(0, R_k\right)$	
Initialization	$\hat{x}_0^+ = u_0,\ P_0^+$	
Model Forecast	$\hat{x}_k^- = f_{k-1}\left(\hat{x}_{k-1}^-\right)$ $P_k^- = F_{k-1} P_{k-1}^+ F_{k-1}^T + Q_{k-1}$ $F_k = \left.\frac{\partial f}{\partial x}\right\|_{\hat{x}_k^-}$	(1) Generate sigma points: $\hat{x}_{k-1}^{(i)} = \hat{x}_{k-1}^+ + \tilde{x}^{(i)}\ i = 1, \cdots, 2n$ $\tilde{x}^{(i)} = \left(\sqrt{nP_{k-1}^+}\right)_i^T\ i = 1, \cdots, n$ $\tilde{x}^{(i)} = -\left(\sqrt{nP_{k-1}^+}\right)_i^T\ i = 1, \cdots, n$ (2) Variable propagation: $\hat{x}_k^{(i)} = f_{k-1}\left(\hat{x}_{k-1}^{(i)}\right)$ $\hat{x}_k^- = \frac{1}{2n}\sum_{i=1}^{2n} \hat{x}_k^{(i)}$ $P_k^- = \frac{1}{2n}\sum_{i=1}^{2n}\left(\hat{x}_k^{(i)} - \hat{x}_k^-\right)\left(\hat{x}_k^{(i)} - \hat{x}_k^-\right)^T + Q_{k-1}$
Corrector	$\hat{x}_k^+ = \hat{x}_{k-1}^- + K_k\left(y_k - h_k\left(\hat{x}_{k-1}^-\right)\right)$ $K_k = P_k^- H_k^T\left(H_k P_k^- H_k^T + R_k\right)^{-1}$ $P_k^+ = \left(I - K_k H_k\right) P_k^-$ $H_k = \left.\frac{\partial h}{\partial x}\right\|_{\hat{x}_k^-}$	(1) Update predicted measurement and covariances of predicted measurement: $\hat{y}_k^{(i)} = h\left(\hat{x}_k^{(i)}\right)$ $\hat{y}_k = \frac{1}{2n}\sum_{i=1}^{2n} \hat{y}_k^{(i)}$ $P_y = \frac{1}{2n}\sum_{i=1}^{2n}\left(\hat{y}_k^{(i)} - \hat{y}_k\right)\left(\hat{y}_k^{(i)} - \hat{y}_k\right)^T + R_k$ $P_{xy} = \frac{1}{2n}\sum_{i=1}^{2n}\left(\hat{x}_k^{(i)} - \hat{x}_k^-\right)\left(\hat{y}_k^{(i)} - \hat{y}_k\right)^T$ (2) Update state variables: $K_k = P_{xy} P_y^{-1}$ $\hat{x}_k^+ = \hat{x}_k^- + K_k\left(y_k - \hat{y}_k\right)$ $P_k^+ = P_k^- - K_k P_y K_k^T$

where *i* is the cell number, *k* is the discretized time. In this way, the process model for individual cell SOC's estimation can be simplified as a linear system.

The measurements are individual cells' voltages $y = V_i$, which is predicted by:

$$V_{i,k}(t) = U_p\left(SOC_{i,p,k}, T_{i,k}\right) - U_n\left(SOC_{i,n,k}, T_{i,k}\right) + \frac{2R, T_{i,k}}{F}\left(\ln\left(m_{i,p,k}(t) + \sqrt{{m_{i,p,k}}^2(t)+1}\right) - \ln\left(m_{i,n,k}(t) + \sqrt{{m_{i,n,k}}^2(t)+1}\right)\right) + IR\left(T_{i,k}\right) + v_2 \tag{29}$$

$$m_{i,j,k}(t) = \frac{J_{j,k}(t)}{2k_j c_{s,j,\max} c_e^{0.5}\left(1 - SOC_{i,j,k}\right)^{0.5} {SOC_{i,j,k}}^{0.5}} \tag{30}$$

where $SOC_{i,j,k}$ and $T_{i,k}$ is the ith cell's SOC and cell temperature at kth time step, which are calculated by:

$$SOC_{i,j,k} = SOC_{j,avg,k} + \Delta SOC_{i,j,k} \tag{31}$$

$$T_{i,k} = T_{avg,k} + \Delta T_{i,k} \tag{32}$$

in which $SOC_{j,avg,k}$ is the SOC of average cell obtained as a function of the results of the average cell state estimator:

$$SOC_{p,avg,k}(t) = \frac{1}{c_{s,p,\max}}\left(c_{s,p,avg,k}(t) + \frac{8R_p}{35} q_{s,p,avg,k}(t) - \frac{R_p}{35 D_{s,p}\left(T_{i,k}\right)} J_{p,k}(t)\right) \tag{33}$$

$$SOC_{n,avg,k}(t) = \frac{1}{c_{s,n,\max}}\left(c_{s,n,avg,k}(t) + \frac{8R_n}{35} q_{s,n,avg,k}(t) - \frac{R_n}{35 D_{s,n}\left(T_{i,k}\right)} J_{n,k}(t)\right). \tag{34}$$

The state and measurement noises are assumed as

$$w' \sim (0, Q) \quad Q = diag[1e-8, 1e-8, 1e-4]$$

$$v_2 \sim (0, R) \quad R = 4e-6$$

3. RESULTS AND DISCUSSION

3.1 AVERAGE CELL STATE ESTIMATION

The input current profile is shown in Figure 3. The current is 1C current (1.656A) in this model, which means the battery can be fully discharged within one hour (4.2 V-2.8 V) under 1C current. The current is generated randomly (Gaussian distribution) from 0 to 1C. Positive currents indicate discharging process and negative currents indicate charging process. Each current segment lasts for 15 min. The estimator performance can be investigated under various loading conditions by using this input current.

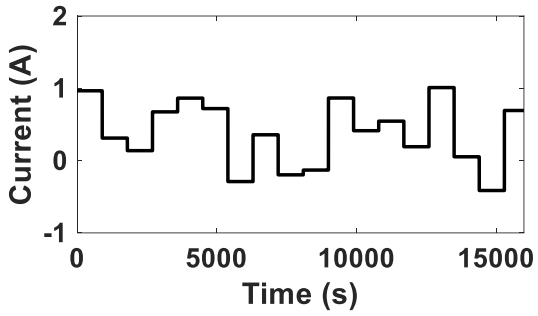

Figure 3. Input current of the battery pack.

The performances of average cell state estimators in voltage are presented in Figure 4. A time step of 1s is implemented fir average cell state estimator. First, two filters, UKF and EKF, are implemented for the average cell state estimation, and their performances are compared. As shown in Figure 4(a) and (b), the estimated voltage converges to actual voltage within 5 s in two filters, indicating a quick correction of output signal by using

UKF and EKF. The voltage estimation errors are plotted in Figure 4(c) and (d). The voltage errors are 10 mV in two filters. This error is not caused by filter inaccuracy but is induced by the model measurement noise which is set as 10 mV.

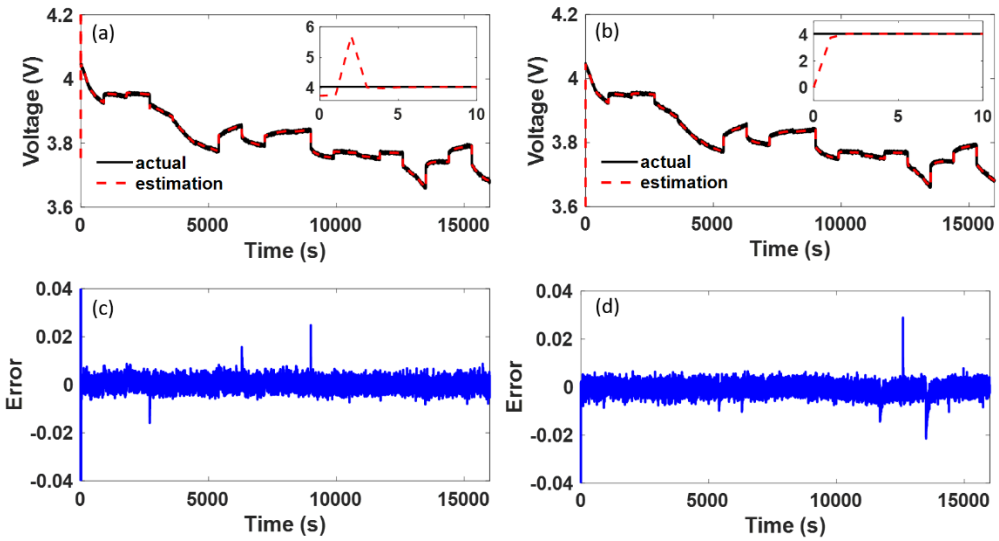

Figure 4. Actual and estimation voltage of average cell in (a) UKF and (b) EKF, voltage estimation error in (c) UKF and (b) EKF.

The estimation results in cathode SOC, anode SOC, and cell temperature estimation for the average cell are shown in Figures 5~7. It can be observed that UKF is capable of accurately estimating SOCs in both electrodes and cell temperature. The root mean square errors (RMSEs) in UKF are 0.012, 0.010 and 0.95 K for cathode SOC, anode SOC, and cell temperature, respectively. The convergence in UKF is achieved in about 5 s. In comparison, the performance of EKF is not as good as UKF. As observed, the RMSEs in EKF are 0.020, 0.129 and 1.26 K for cathode SOC, anode SOC and cell temperature,

respectively, and the filter convergence is achieved around 100 s. The filters are implemented in the estimation under loaded conditions, in which open-circuit voltage cannot be obtained from measurement. Furthermore, cell temperature change adds more complexity between the measured voltage and SOCs. Therefore, the filter functionality is critical in estimation convergence and accuracy. The physical mode for average cell state estimator is a SP model along with a lumped thermal model, which is highly nonlinear. EKF can have a great loss in the process of linearizing the model. That is why EKF cannot effectively estimate the SOCs and cell temperature, even though its output is quickly converge to the measurements. Regarding to simulation time, UKF takes 8.56 s, which is much longer than 2.07 s of EKF.

3.2. INDIVIDUAL CELL STATE ESTIMATION

In this work, it is assumed that there are 6 cells connected in series in a battery pack. The process model for individual cell is linear as introduced in Section 2.2.2. Therefore, a discretized EKF is chose for individual cells' state estimation. To reduce the computation time, a larger time scale is implemented in this filter. The time step is 5 s. Thus, the average state estimation results adopted in the individual cell estimator will be updated every 5 s.

Figure 8 shows the voltage variations in 6 cells. The voltage profiles show similar trend with certain differences in different cells. During discharge process (current is positive), voltage decreases from Cell#1 to Cell#6, while the situation is reverse in

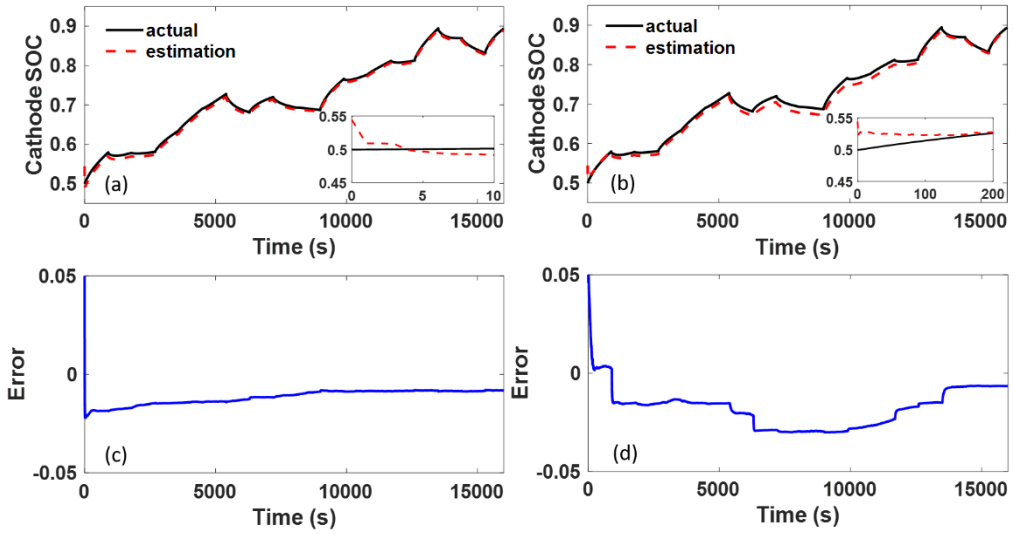

Figure 5. Actual and estimation cathode SOC of average cell in (a) UKF and (b) EKF, cathode SOC estimation error in (c) UKF and (b) EKF.

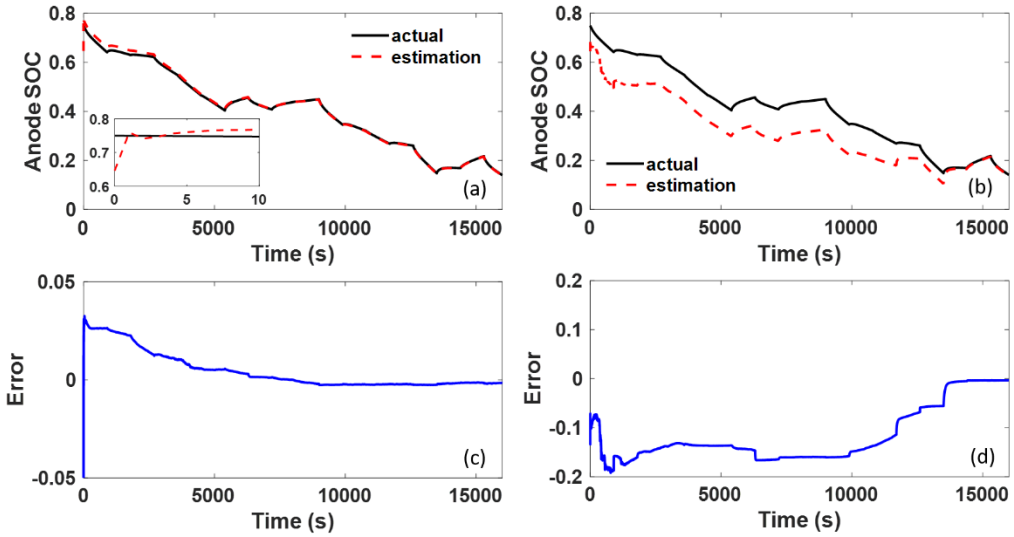

Figure 6. Actual and estimation anode SOC of average cell in (a) UKF and (b) EKF, anode SOC estimation error in (c) UKF and (b) EKF.

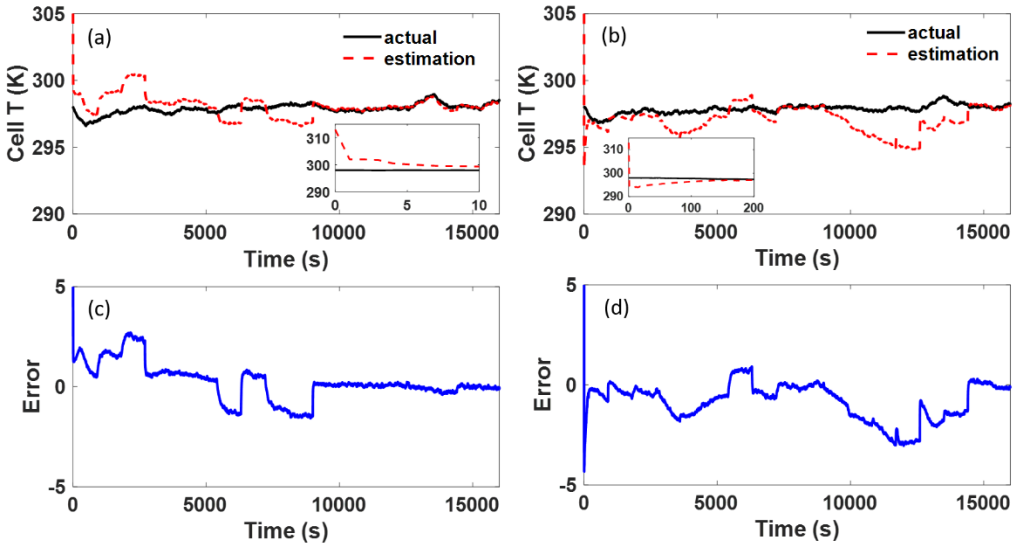

Figure 7. Actual and estimation cell temperature of average cell in (a) UKF and (b) EKF, cell temperature estimation error in (c) UKF and (b) EKF.

discharge process (current is negative). This result is the same as expected because the voltage differences from cell to cell are mainly induced by the SOC differences.

The estimation errors of cathode SOC, anode SOC and cell temperature of 6 cells are plotted in Figure 9. It can be observed that the estimation errors reached 0.09, -0.11 and -13 K for cathode SOC, anode SOC and cell temperature, respectively, in the initial 900 s, indicating a poor performance of the individual cells' filters in the initial estimation stage. The estimation errors begin to converge after 900 s for cathode SOC and cell temperature and after 5400 s for anode SOC. Although the final error decreases to about 0.02, 0.04 and 1 K in the late stage for cathode SOC, anode SOC and cell temperature, respectively, the large error in the initial stage and late converge rate are unacceptable in the state estimation. The main reason for the large estimation error in the initial stage is that the state errors of the average cell into estimation are introduced into the estimation for ΔSOCs and ΔT.

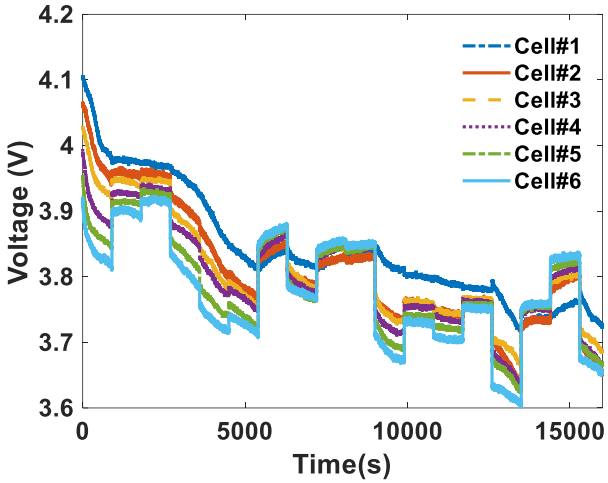

Figure 8. Cell voltage of Cell#1~Cell#6.

As shown in Section 3.1, it takes at least 5s for all the states to converge in the average cell estimator. According to Eqs. 26~29, both the average cell states' errors and individual cell states' errors are counted in the calculation of individual cell's model output, which are feedbacked in the correction of ΔSOCs and ΔT estimations. To avoid this phenomenon, a short hold time for the individual estimation is introduced until the average state estimation converges. Figure 10 shows the comparison of ΔSOCs and ΔT estimation results of individual estimators without time delay and with 10 s time delay. Take the cathode ΔSOC as an example, the initial values for cathode ΔSOCs' errors are 0.01, 0.005, -0.005, -0.015, -0.025, -0.035 for Cell#1~Cell#6, respectively. As shown in Figure 10(a), the cathode ΔSOCs' errors fluctuate drastically with a maximum value of 0.08 in the first 10 s. Then the cathode ΔSOCs' errors become stable. However, their values are still large, where Cell#6 has a maximal error of -0.05. Figure 10(b) presents the cathode ΔSOCs' errors in individual estimator with 10 s delay. It can be observed that the cathode ΔSOCs' errors

converged in about 5 s with an evident decrease after holding for 10 s, among which Cell#2 had a maximal error of 0.02. The estimation errors of anode ΔSOC and cell ΔT had a same trend with cathode ΔSOC in two kinds of individual estimators as shown in Figure 10(c)~(f). Therefore, it can be concluded that the individual estimator can effectively reduce the estimation error with 10 s delay.

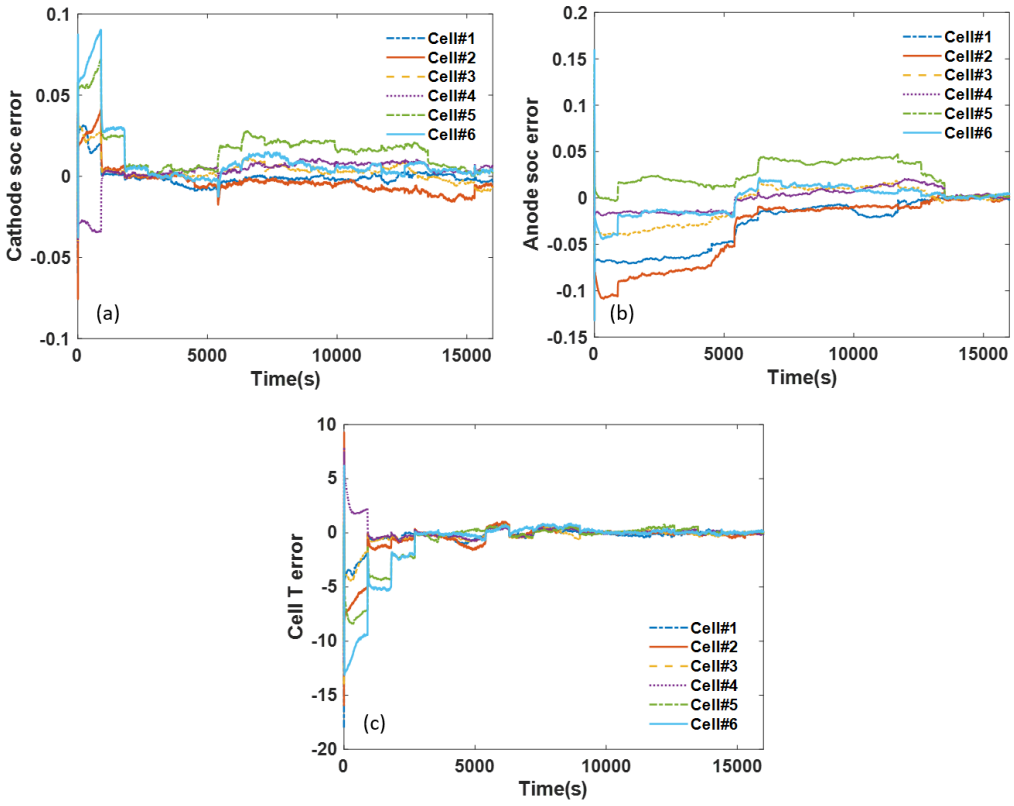

Figure 9. Estimation error in (a) cathode SOC, (b) anode SOC and (c) cell temperature of Cell#1~ Cell #6 using EKF with no time delay.

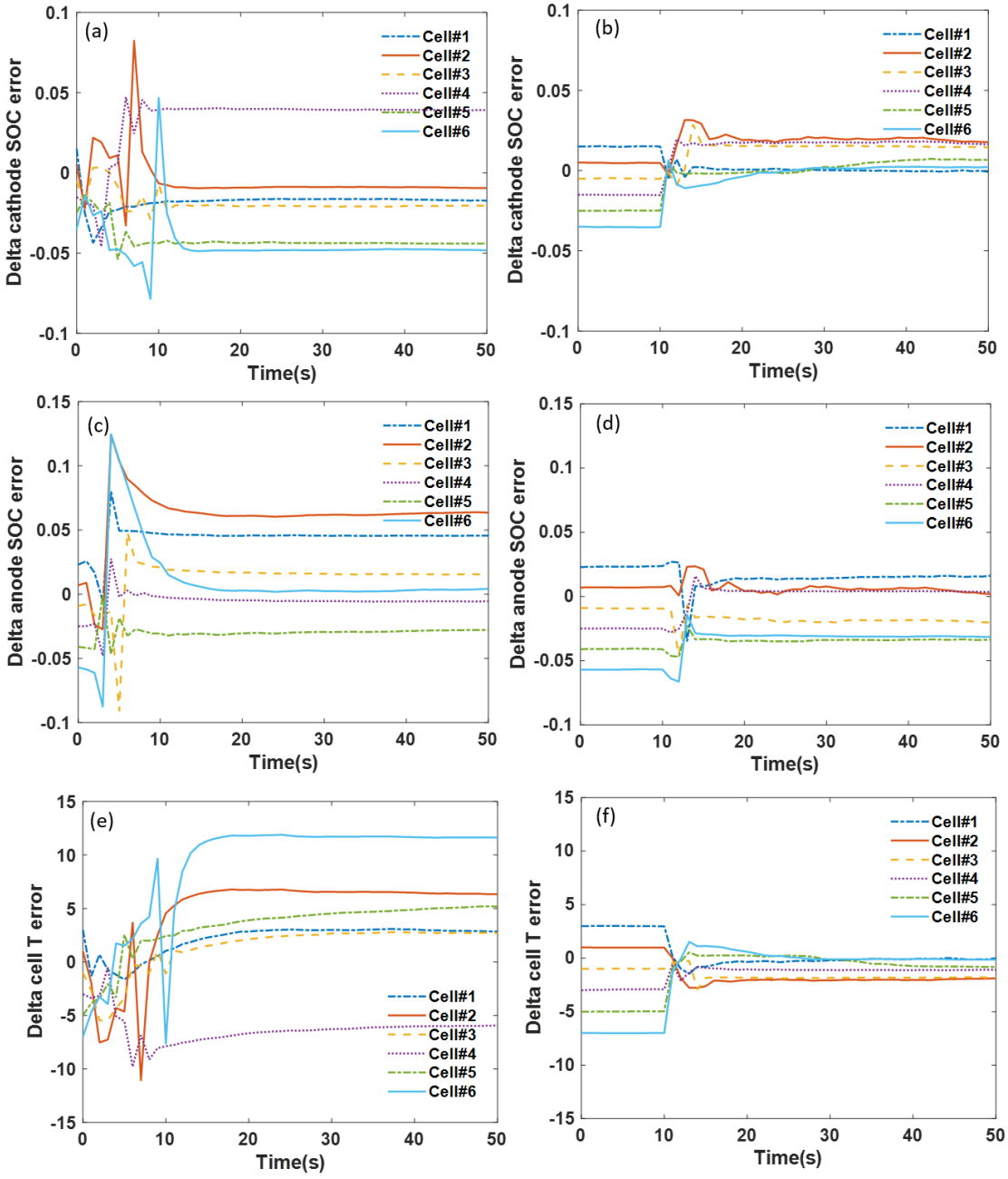

Figure 10. Estimation error in EKF with no time delay of (a) cathode SOC, (c) anode SOC and (e) cell temperature, estimation error in EKF with 10 s delay of (b) cathode SOC, (d) anode SOC and (f) cell temperature in Cell#1~ Cell#6.

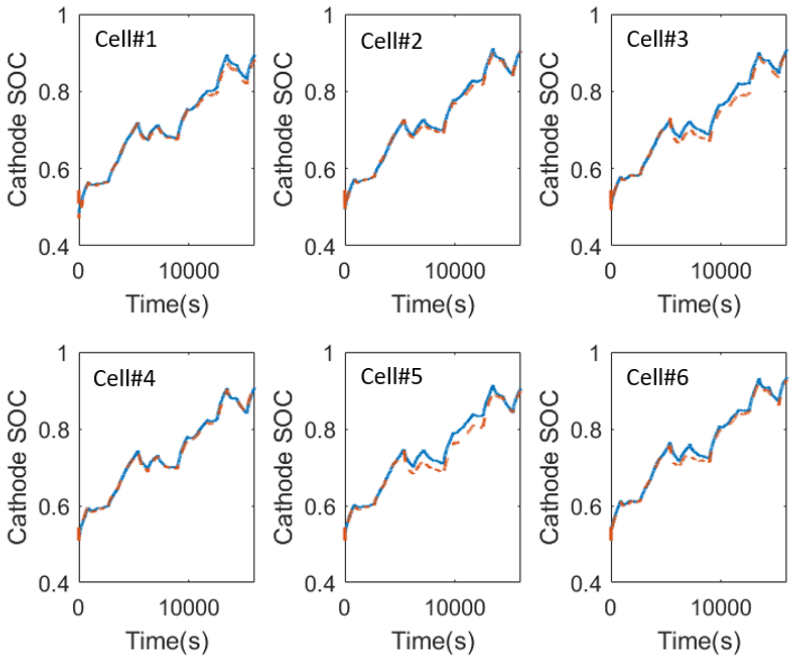

Figure 11. Comparison of actual value (blue line) and estimate value (orange dash line) of cathode SOC of Cell#1~ Cell#6.

The performance of a combination of UKF as average cell state estimator and EKF with 10 s delay as individual cell estimator is further evaluated. The comparison of actual value and estimation value of each state in 6 cells are presented in Figures 11~13. As shown, the SOC errors between true value and estimated value of Cell #3 and Cell #5 are the highest. In the setting, the initial values of ΔSOC differs from cell to cell but the initial estimation values and covariance matrixes remain same. This may be one reason for the estimation accuracy difference. As for the temperature, the true value and estimation value for all the cells match well as shown in Figure 13. The estimation errors for each state are summarized in Figure 14 and Table 1. The estimation errors of cathode SOC, anode SOC

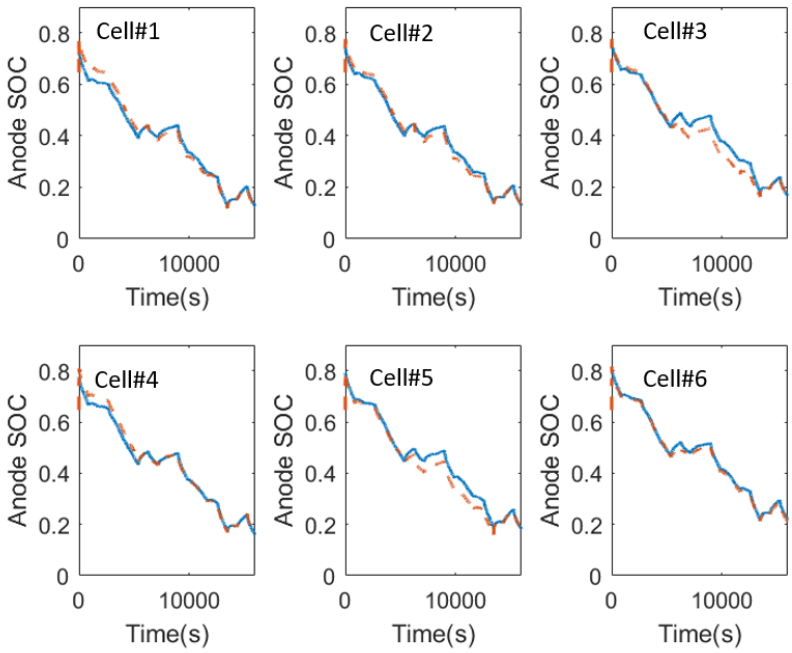

Figure 12. Comparison of actual value (blue line) and estimate value (orange dash line) of anode SOC of Cell#1~ Cell#6.

and cell temperature of individual cells converged quickly in 15 s. The maximum RMSEs are 0.0186 and 0.0326 in cathode SOC and anode SOC, respectively, indicating a good estimation accuracy (<0.04). The estimation of cell temperature also shows a high accuracy with all the estimations less than 0.6 K. The total simulation time is 15.11 s, in which the average state estimation takes 8.56 s. Averaged by the total simulation time and cell number, it takes 0.16 ms for 1 s simulation of 1 cell, which is 0.0019 % of the computation time of implementing UKF in every cell.

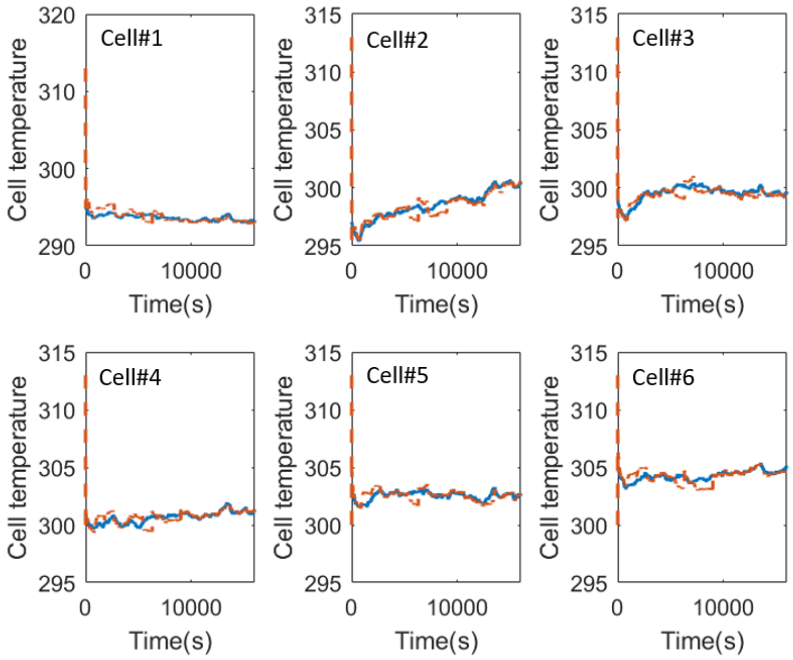

Figure 13. Comparison of actual value (blue line) and estimate value (orange dash line) of cell temperature of Cell#1~ Cell#6.

Table 2. RMSE of cathode SOC, anode SOC and cell temperature of Cell#1~ Cell #6 using filter with and without time delay.

	RMSE (SOC_pos)		RMSE (SOC_neg)		RMSE (T)	
	No delay	10 s delay	No delay	10 s delay	No delay	10 s delay
Cell#1	0.0063	0.0077	0.0383	0.0241	0.8276	0.5604
Cell#2	0.0094	0.0071	0.0484	0.0167	1.5740	0.4921
Cell#3	0.0075	0.0146	0.0202	0.0326	0.8729	0.4045
Cell#4	0.0094	0.0043	0.0118	0.0175	0.6895	0.4344
Cell#5	0.0209	0.0186	0.0281	0.0297	2.1359	0.4252
Cell#6	0.0197	0.0098	0.0153	0.0096	2.8807	0.5032

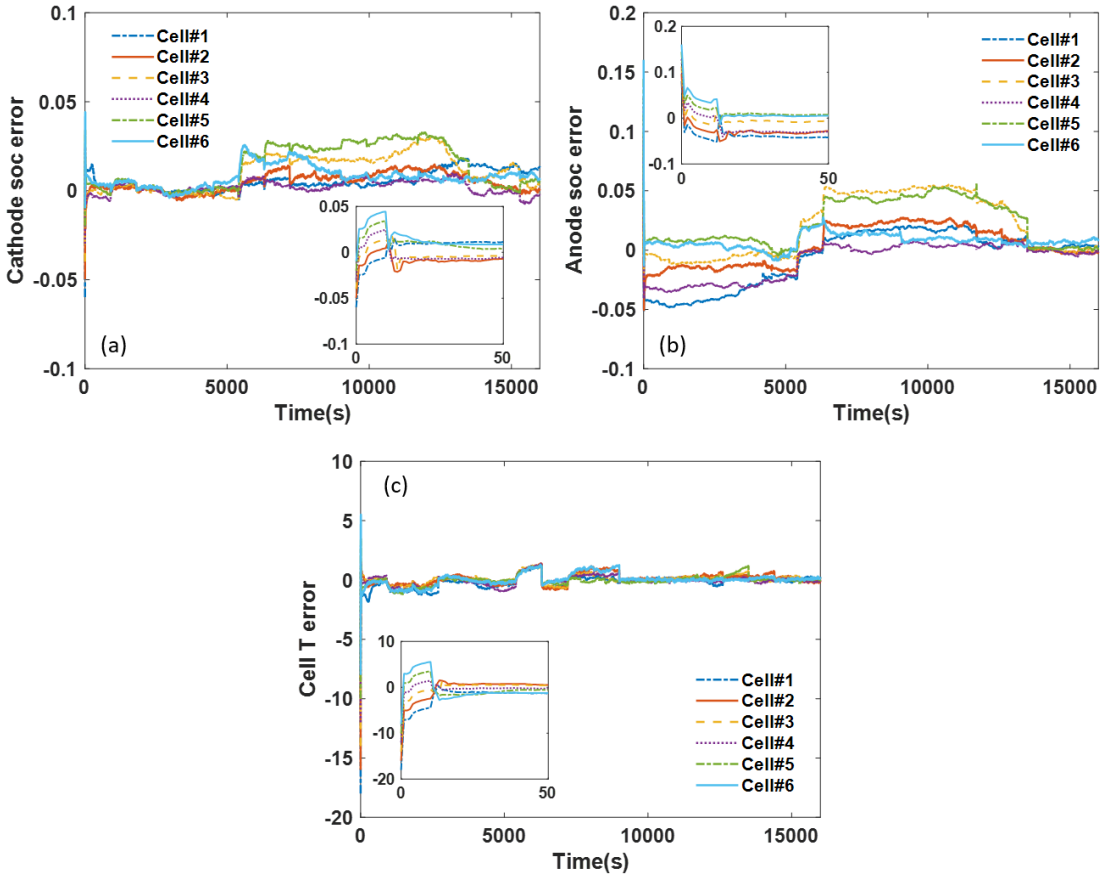

Figure 14. Estimation error in (a) cathode SOC, (b) anode SOC and (c) cell temperature of Cell#1~ Cell#6 using EKF with 10 s delay.

4. CONCLUSIONS

The cell SOCs and temperature in a battery pack are estimated by an average cell states estimator based on SP model along with a lumped thermal model, combined with individual cell states estimator which uses states' deviation from average states as variables. The performance of UKF and EKF as average cell states estimator are compared

under a dynamic loading. It turns out that EKF has a relatively poor accuracy and slow converge rate compared with UKF. The SOC estimation error in UKF are less than 0.012 and cell temperature error is less than 1 K. However, EKF has a better computation efficiency than UKF. A discretized EKF is implemented for individual cell estimation. It is found that the stability and accuracy of individual cell estimator was significantly impacted by the estimation error of the average cell states. The estimation error of the average cell states can cause a drastic fluctuation and large estimation error in the initial stage (~900 s). To avoid this problem, a holding time of 10 s has been applied in the individual cell estimator. As a result, the estimation results converge quickly in 15 s with a precise value, where the maximum RMSEs of 0.0186, 0.0326 and 0.6 K in cathode SOC, anode SOC and cell temperature, respectively. The filter design as a combination of average cell state estimator and individual cell state estimator is proved to be computation efficient that it takes 0.16 ms for 1 s simulation time in 1 cell.

REFERENCES

1. Baghdadi, I., et al., State of health assessment for lithium batteries based on voltage–time relaxation measure. Electrochimica Acta, 2016. **194**: p. 461-472.

2. Sun, F., et al., Adaptive unscented Kalman filtering for state of charge estimation of a lithium-ion battery for electric vehicles. Energy, 2011. **36**(5): p. 3531-3540.

3. Ng, K.S., et al., Enhanced coulomb counting method for estimating state-of-charge and state-of-health of lithium-ion batteries. Applied energy, 2009. **86**(9): p. 1506-1511.

4. Hansen, T. and C.-J. Wang, Support vector based battery state of charge estimator. Journal of Power Sources, 2005. **141**(2): p. 351-358.

5. Duryea, S., S. Islam, and W. Lawrance. A battery management system for stand alone photovoltaic energy systems. in Conference Record of the 1999 IEEE Industry Applications Conference. Thirty-Forth IAS Annual Meeting (Cat. No. 99CH36370). 1999. IEEE.

6. Aylor, J.H., A. Thieme, and B. Johnso, A battery state-of-charge indicator for electric wheelchairs. IEEE transactions on industrial electronics, 1992. **39**(5): p. 398-409.

7. Çadırcı, Y. and Y. Özkazanç, Microcontroller-based on-line state-of-charge estimator for sealed lead–acid batteries. Journal of Power Sources, 2004. **129**(2): p. 330-342.

8. Arun, P., R. Banerjee, and S. Bandyopadhyay, Optimum sizing of battery-integrated diesel generator for remote electrification through design-space approach. Energy, 2008. **33**(7): p. 1155-1168.

9. Liu, L., et al., Integrated system identification and state-of-charge estimation of battery systems. IEEE Transactions on Energy conversion, 2012. **28**(1): p. 12-23.

10. Lu, L., et al., A review on the key issues for lithium-ion battery management in electric vehicles. Journal of power sources, 2013. **226**: p. 272-288.

11. Tang, X., Y. Wang, and Z. Chen, A method for state-of-charge estimation of LiFePO4 batteries based on a dual-circuit state observer. Journal of Power Sources, 2015. **296**: p. 23-29.

12. Zheng, F., et al., Influence of different open circuit voltage tests on state of charge online estimation for lithium-ion batteries. Applied energy, 2016. **183**: p. 513-525.

13. CHENG, B., et al., Battery State-of-Charge Estimation Based on Chaos Immune Evolutionary Neural Network [J]. Journal of System Simulation, 2008. **20**(11): p. p2889-2892.

14. Cheng, B., et al., Ni–MH batteries state-of-charge prediction based on immune evolutionary network. Energy conversion and management, 2009. **50**(12): p. 3078-3086.

15. Sassi, H.B., et al. A comparative study of ANN and Kalman Filtering-based observer for SOC estimation. in IOP Conference Series: Earth and Environmental Science. 2018. IOP Publishing.

16. Yang, F., et al., State-of-charge estimation of lithium-ion batteries using LSTM and UKF. Energy, 2020. **201**: p. 117664.

17. Zhang, L., et al., A sparse least squares support vector machine used for SOC estimation of Li-ion Batteries. IFAC-PapersOnLine, 2019. **52**(11): p. 256-261.

18. Hussein, A.A., Derivation and comparison of open-loop and closed-loop neural network battery state-of-charge estimators. Energy Procedia, 2015. **75**: p. 1856-1861.

19. Shen, Y., Adaptive online state-of-charge determination based on neuro-controller and neural network. Energy Conversion and Management, 2010. **51**(5): p. 1093-1098.

20. Singh, P., et al., Design and implementation of a fuzzy logic-based state-of-charge meter for Li-ion batteries used in portable defibrillators. Journal of power sources, 2006. **162**(2): p. 829-836.

21. Malkhandi, S., Fuzzy logic-based learning system and estimation of state-of-charge of lead-acid battery. Engineering Applications of Artificial Intelligence, 2006. **19**(5): p. 479-485.

22. Shi, Q.S., C.H. Zhang, and N.X. Cui, Estimation of battery state-of-charge using ν-support vector regression algorithm. International Journal of Automotive Technology, 2008. **9**(6): p. 759-764.

23. Yang, D., et al., A novel Gaussian process regression model for state-of-health estimation of lithium-ion battery using charging curve. Journal of Power Sources, 2018. **384**: p. 387-395.

24. Sahinoglu, G.O., et al., Battery state-of-charge estimation based on regular/recurrent Gaussian process regression. IEEE Transactions on Industrial Electronics, 2017. **65**(5): p. 4311-4321.

25. Charkhgard, M. and M. Farrokhi, State-of-charge estimation for lithium-ion batteries using neural networks and EKF. IEEE transactions on industrial electronics, 2010. **57**(12): p. 4178-4187.

26. Lin, H.-T., T.-J. Liang, and S.-M. Chen, Estimation of battery state of health using probabilistic neural network. IEEE transactions on industrial informatics, 2012. **9**(2): p. 679-685.

27. Zou, Y., et al., Combined state of charge and state of health estimation over lithium-ion battery cell cycle lifespan for electric vehicles. Journal of Power Sources, 2015. **273**: p. 793-803.

28. Wang, Y., et al., Modeling and state-of-charge prediction of lithium-ion battery and ultracapacitor hybrids with a co-estimator. Energy, 2017. **121**: p. 739-750.

29. Sepasi, S., R. Ghorbani, and B.Y. Liaw, Improved extended Kalman filter for state of charge estimation of battery pack. Journal of Power Sources, 2014. **255**: p. 368-376.

30. Xing, Y., et al., State of charge estimation of lithium-ion batteries using the open-circuit voltage at various ambient temperatures. Applied Energy, 2014. **113**: p. 106-115.

31. Doyle, M., T.F. Fuller, and J. Newman, Modeling of galvanostatic charge and discharge of the lithium/polymer/insertion cell. Journal of the Electrochemical society, 1993. **140**(6): p. 1526.

32. Fuller, T.F., M. Doyle, and J. Newman, Relaxation phenomena in lithium-ion-insertion cells. Journal of the Electrochemical Society, 1994. **141**(4): p. 982.

33. Farrell, T.W., et al., Primary Alkaline Battery Cathodes A Three-Scale Model. Journal of the Electrochemical Society, 2000. **147**(11): p. 4034.

34. Dargaville, S. and T.W. Farrell, Predicting active material utilization in LiFePO4 electrodes using a multiscale mathematical model. Journal of the Electrochemical Society, 2010. **157**(7): p. A830.

35. Chaturvedi, N.A., et al., Algorithms for advanced battery-management systems. IEEE Control systems magazine, 2010. **30**(3): p. 49-68.

36. Tanim, T.R., C.D. Rahn, and C.-Y. Wang, State of charge estimation of a lithium ion cell based on a temperature dependent and electrolyte enhanced single particle model. Energy, 2015. **80**: p. 731-739.

37. Lotfi, N., et al. Li-ion battery state of health estimation based on an improved single particle model. in 2017 American Control Conference (ACC). 2017. IEEE.

38. Li, J., et al., A single particle model with chemical/mechanical degradation physics for lithium ion battery State of Health (SOH) estimation. Applied Energy, 2018. **212**: p. 1178-1190.

39. Subramanian, V.R., V.D. Diwakar, and D. Tapriyal, Efficient Macro-Micro Scale Coupled Modeling of Batteries. Journal of The Electrochemical Society, 2005. **152**(10): p. A2002-A2008.

40. Sun, F. and R. Xiong, A novel dual-scale cell state-of-charge estimation approach for series-connected battery pack used in electric vehicles. Journal of Power Sources, 2015. **274**: p. 582-594.

41. Xiong, R., et al., Evaluation on state of charge estimation of batteries with adaptive extended Kalman filter by experiment approach. IEEE Transactions on Vehicular Technology, 2012. **62**(1): p. 108-117.

42. Plett, G.L., Extended Kalman filtering for battery management systems of LiPB-based HEV battery packs: Part 3. State and parameter estimation. Journal of Power sources, 2004. **134**(2): p. 277-292.

43. Kim, I.-S., Nonlinear state of charge estimator for hybrid electric vehicle battery. IEEE Transactions on Power Electronics, 2008. **23**(4): p. 2027-2034.

44. Schwunk, S., et al., Particle filter for state of charge and state of health estimation for lithium–iron phosphate batteries. Journal of Power Sources, 2013. **239**: p. 705-710.

45. Li, J., et al., Multicell state estimation using variation based sequential Monte Carlo filter for automotive battery packs. Journal of Power Sources, 2015. **277**: p. 95-103.

46. Plett, G.L., Sigma-point Kalman filtering for battery management systems of LiPB-based HEV battery packs: Part 2: Simultaneous state and parameter estimation. Journal of power sources, 2006. **161**(2): p. 1369-1384.

47. Chen, Z., et al., Particle filter-based state-of-charge estimation and remaining-dischargeable-time prediction method for lithium-ion batteries. Journal of Power Sources, 2019. **414**: p. 158-166.

48. Zahid, T., et al. Sequential Monte Carlo based technique for SOC estimation of LiFePO4 battery pack for electric vehicles. in 2016 IEEE International Conference on Information and Automation (ICIA). 2016. IEEE.

49. Ye, M., et al., A double-scale and adaptive particle filter-based online parameter and state of charge estimation method for lithium-ion batteries. Energy, 2018. **144**: p. 789-799.

50. Chen, W., et al., Simultaneous fault isolation and estimation of lithium-ion batteries via synthesized design of Luenberger and learning observers. IEEE Transactions on Control Systems Technology, 2013. **22**(1): p. 290-298.

51. Tagade, P., et al., Recursive Bayesian filtering framework for lithium-ion cell state estimation. Journal of Power Sources, 2016. **306**: p. 274-288.

52. Bartlett, A., et al., Electrochemical model-based state of charge and capacity estimation for a composite electrode lithium-ion battery. IEEE Transactions on control systems technology, 2015. **24**(2): p. 384-399.

53. Xia, B., et al., A cubature particle filter algorithm to estimate the state of the charge of lithium-ion batteries based on a second-order equivalent circuit model. Energies, 2017. **10**(4): p. 457.

54. Li, G., K. Peng, and B. Li, State-of-charge estimation for lithium-ion battery using a combined method. J Power Electron, 2018. **18**(1): p. 129-136.

55. Sepasi, S., R. Ghorbani, and B.Y. Liaw, A novel on-board state-of-charge estimation method for aged Li-ion batteries based on model adaptive extended Kalman filter. Journal of Power Sources, 2014. **245**: p. 337-344.

56. He, H., et al., State-of-charge estimation of the lithium-ion battery using an adaptive extended Kalman filter based on an improved Thevenin model. IEEE Transactions on vehicular technology, 2011. **60**(4): p. 1461-1469.

57. Klass, V., M. Behm, and G. Lindbergh, Capturing lithium-ion battery dynamics with support vector machine-based battery model. Journal of Power Sources, 2015. **298**: p. 92-101.

58. Santhanagopalan, S. and R.E. White, State of charge estimation using an unscented filter for high power lithium ion cells. International Journal of Energy Research, 2010. **34**(2): p. 152-163.

59. Huang, C., et al., Robustness evaluation of extended and unscented Kalman filter for battery state of charge estimation. Ieee Access, 2018. **6**: p. 27617-27628.

60. Xu, W., et al., A multi-timescale adaptive dual particle filter for state of charge estimation of lithium-ion batteries considering temperature effect. Energy Science & Engineering, 2020. **8**(8): p. 2784-2798.

61. Xia, B., et al., A comparative study of three improved algorithms based on particle filter algorithms in soc estimation of lithium ion batteries. Energies, 2017. **10**(8): p. 1149.

62. Dai, H., et al., Online cell SOC estimation of Li-ion battery packs using a dual time-scale Kalman filtering for EV applications. Applied Energy, 2012. **95**: p. 227-237.

63. Jiayuan, W., et al., Study on the uneven cells problem of the power battery pack in the automotive application by ECM. Physics Procedia, 2012. **24**: p. 984-996.

64. Shahid, S. and M. Agelin-Chaab, Experimental and numerical studies on air cooling and temperature uniformity in a battery pack. International Journal of Energy Research, 2018. **42**(6): p. 2246-2262.

65. Azizi, Y. and S. Sadrameli, Thermal management of a LiFePO4 battery pack at high temperature environment using a composite of phase change materials and aluminum wire mesh plates. Energy Conversion and Management, 2016. **128**: p. 294-302.

66. Yang, N., et al., Unbalanced discharging and aging due to temperature differences among the cells in a lithium-ion battery pack with parallel combination. Journal of Power Sources, 2016. **306**: p. 733-741.

67. van Schalkwijk, W. and B. Scrosati, Advances in lithium-ion batteries. 2007: Springer Science & Business Media.

68. Tang, S.-X., et al., State-of-charge estimation from a thermal–electrochemical model of lithium-ion batteries. Automatica, 2017. **83**: p. 206-219.

69. Pals, C.R. and J. Newman, Thermal modeling of the lithium/polymer battery: I. Discharge behavior of a single cell. Journal of the Electrochemical Society, 1995. **142**(10): p. 3274.

70. Cicconi, P., D. Landi, and M. Germani, Thermal analysis and simulation of a Li-ion battery pack for a lightweight commercial EV. Applied Energy, 2017. **192**: p. 159-177.

71. Wei, J., et al., System state estimation and optimal energy control framework for multicell lithium-ion battery system. Applied Energy, 2017. **187**: p. 37-49.

72. Zhang, X., et al., A novel approach of remaining discharge energy prediction for large format lithium-ion battery pack. Journal of Power Sources, 2017. **343**: p. 216-225.

73. Liu, X., Y. He, and Z. Chen. State-of-Charge estimation for power Li-ion battery pack using V min-EKF. in The 2nd International Conference on Software Engineering and Data Mining. 2010. IEEE.

74. Zhong, L., et al., A method for the estimation of the battery pack state of charge based on in-pack cells uniformity analysis. Applied Energy, 2014. **113**: p. 558-564.

SECTION

2. SUMMARY AND CONCLUSION

In the first paper, it was proved that the enhanced transport property of ALD-coated particle was not attributed to the high conductivity of ALD coating layer, itself, as traditionally understood, but, rather, in the coating layer's role as a Li ion distributor enabling almost uniform intercalation through the entire particle surface despite physical blockings. The conducted simulation based on the conventional explanation showed that the CeO_2 coating layer could neither improve the capacity nor the effective diffusivity for $LiMn_2O_4$ particles when Li ion intercalation was ideally uniform. On the other hand, the model based on the proposed mechanism yielded consistent results with the experimental observation. The direct measurement of the surface area through BET and PSA indicated that the surface area of particles was partially blocked due to the agglomeration of particles and, as a result, Li ion intercalation was then limited in that region. The model confirmed that the existence of ALD coating can effectively distribute Li ions over the entire particle surface despite the physical blockings. Finally, the analysis on the influence of flux angle, current density and particle size provides deeper understanding on relationship between the coating parameters, electrode configuration, battery operating condition, and battery performance, which serves as an importance guidance for electrode and coating design strategy.

In the second paper, we carried out an exhaustive study of the effect of 3-dimensional (3D) electrode architectures on the electrochemical performance of batteries

and used the gained knowledge to determine optimized electrode structures (anodes and cathodes) for maximum areal and specific capacity. A 3-dimensional full-order electrochemical model, validated by Aerosol Jet printed open octahedral micro-lattice 3D electrodes with a two-level porosity, was used for this analysis. The impact of the electrode geometry was studied by comparing the electrochemical response of electrodes with block-, X-, cubic-structure, and a structure formed by subtracting spheres from a solid block (called 'sphere-structure'). The study revealed that: i) The primary reason for the superior performance of batteries with 3D electrode architectures is the fact that 3D structures facilitate species transport in the liquid phase. In addition, the main factors affecting battery performance are ion diffusion in the electrolyte and electron transport in the 3D electrode skeleton. ii) In 3D electrode architectures, the competition between available volume for intercalation and an easier diffusion path for ion and electron transport determines areal/total and specific capacity. Because of this competition, the maximum benefits of a 3D architecture are realized when the length of the structures' truss members is of the order of the diffusion length for the ions in the electrode (~15-20 μm in the current study). In structures with truss members smaller than this scale, the total/areal capacity is too low and discharge rates are too high (undesirable for a battery). At larger length scales, the specific capacity is too low as a result of the increasing difficulty for ion transport through the liquid. iv) Of the structures studied here, the X- and cubic-structured electrodes demonstrated a larger capacity (35% higher at 0.5C) than the inverse sphere-structured electrodes as a result of more efficient electron transport enabled specifically by the change in electrode geometry. The optimized parameters for these structures for a compromised high specific energy and high areal capacity were a thickness of 450 μm and a volume

fraction (VF) of 0.2, a thickness of 250 μm and VF of 0.4, and a thickness of 250 μm and VF of 0.4 for the X-structure, cubic-structure, and sphere-structured electrodes. v) If the electrode porosity is reduced, an insufficient diffusion of Li ions in the electrolyte causes a decrease in the electrode capacity even if the electrode volume increases. This was seen in cubic- and X-structured electrodes, where the specific capacity of 3D electrodes decreased with increasing column width and number (columns per unit length). This effect, however, becomes secondary when a bottleneck width emerges in the electrode structure which can impede electron transport through the electrode. vi) The requirement that the length scale of the truss members of optimum 3D architectures be of the order of tens of micrometers limits the availability of manufacturing methods to techniques such as aerosol jet, extrusion, or inkjet 3D printing.

In the third paper, a full order electrochemical model including two degradation physics at anode, SEI layer growth and lithium plating, was established and validated by the experiment results. The model captured the electrolyte concentration impact on both side reactions, as well as the total capacity degradation. The mechanism for how electrolyte concentration worked on each side reaction was investigated. It was found that the electrolyte concentration influenced the SEI layer and the Li plating mainly through their reaction constants and deposition overpotentials. A high salt concentration (1.5 mol/L and 2 mol/L of $LiPF_6$ in EC: DMC) suppressed the SEI layer growth and promoted Li plating. The mechanism for the interplay between the two side reactions was also analyzed. The existence of the SEI layer slowed the lithium plating rate by increasing its overpotential through ohmic resistance. In terms of charge current C-rates, a high C-rate (4C) accelerated both lithium plating and SEI layer reaction rates in terms of time. However, this

acceleration was not evident when considering charge capacity in the CC process. Comprehensively, both low electrolyte concentration and low charge current C-rate resulted in a more severe capacity degradation in the CC cycling process.

In the fourth paper, an optimized charge protocol CQtCV based on regulating Li plating current has been proposed. Li plating current is provided by a full order electrochemical model in which two main side reaction during charge process: SEI layer growth and Li plating are included. Physical parameters in the model were classified as non-degradation and degradation ones, and were identified by 1st cycle's voltage profile and capacity profile of C-rate test, respectively. The performance of two charge algorithms was evaluated based on fitted model. It was proved that the proposed charging protocol can effectively reduce charge time (>20%) and improve capacity degradation at the same time. The capacity improvement in CQtCV mainly comes from the suppression of SEI layer growth, however, Li plating would be slightly promoted in this process.

In the fifth paper, to predict the cell degradation and battery life of BESSs, a comprehensive degradation model - including SEI layer growth and Li plating at the anode and Mn dissolution at the cathode - has been established. The model is based on an electrolyte enhanced SP model so that it is computationally efficient for online predication. The model parameters have been identified according to the experimental data of one cell with a RMSE of 0.094. The simulation results from the obtained model showed a good match with the experimental capacity profile of another cell (RMSE=0.098). It was found that at the anode side, the deposition rate of both SEI layer and Li metal increase as the charge voltage increase. Furthermore, at the cathode side, the solvent oxidation rate determines the proton concentration that triggers the Mn dissolution reaction. As a result,

active material in the cathode keeps decreasing at a gradually rising rate. As for the long cycling test, the SEI growth plays a main role in capacity fade in the first about 2000 cycles, and Mn dissolution has a significant impact after about 1000 cycles with a capacity loss of 6.5%. It is also revealed that the mechanism that Mn dissolution cause a capacity loss is not only the loss of active material in cathode, but a consumption of Li ions in electrolyte. The charge current impacts on the three degradation physics are analyzed separately. As observed, high charge current slows down the reaction of Mn dissolution at cathode and speed up the SEI layer growth and Li plating at anode. A sensitivity study of degradation parameters has been conducted against capacity fade. It shows that the capacity degradation is mostly sensitive to solvent oxidation exchange current density and Li plating exchange current density, while it is inert to salt decomposition constant. The reaction rate of Mn dissolution and SEI formation are limited by proton concentration and EC concentration, respectively; therefore, their reaction constants do not effectively impact the capacity degradation when reaching certain values.

In the sixth paper, the cell SOCs and temperature in a battery pack are estimated by an average cell states estimator based on SP model along with a lumped thermal model, combined with individual cell states estimator which uses states' deviation from average states as variables. The performance of UKF and EKF as average cell states estimator are compared under a dynamic loading. It turns out that EKF has a relatively poor accuracy and slow converge rate compared with UKF. The SOC estimation error in UKF are less than 0.012 and cell temperature error is less than 1 K. However, EKF has a better computation efficiency than UKF. A discretized EKF is implemented for individual cell estimation. It is found that the stability and accuracy of individual cell estimator was

significantly impacted by the estimation error of the average cell states. The estimation error of the average cell states can cause a drastic fluctuation and large estimation error in the initial stage (~900 s). To avoid this problem, a holding time of 10 s has been applied in the individual cell estimator. As a result, the estimation results converge quickly in 15 s with a precise value, where the maximum RMSEs of 0.0186, 0.0326 and 0.6 K in cathode SOC, anode SOC and cell temperature, respectively. The filter design as a combination of average cell state estimator and individual cell state estimator is proved to be computation efficient that it takes 0.16 ms for 1 s simulation time in 1 cell.

VITA

Yaqi Zhu was born in Hubei, China. She received her bachelor degree in Material Science and Engineering in 2012 from Shanghai JiaoTong University, Shanghai, P.R. China. Then she received her Ph.D. degree in Mechanical Engineering in 2016 from National University of Singapore, Singapore, in which she worked on novel solid-state batteries for next generation energy storage devices. She worked as a battery system engineer in SAIC Motor Passenger Vehicle Company from 2017~2018. She began her 2nd Ph.D. degree at Missouri University of Science and Technology in September 2018. She worked on advanced battery modeling for interfacial phenomena and optimal charging. In July 2021, she received her Ph.D. degree in Mechanical Engineering from Missouri University of Science and Technology.